Audi
Dissertationsreihe

Hicham Tazi

Integration of Numerical Simulation Approaches in the Virtual Development of Automotive Antenna Systems

Cuvillier Verlag Göttingen

INGOLSTADT INSTITUTE DER TU MÜNCHEN

TECHNISCHE UNIVERSITÄT MÜNCHEN
Lehrstuhl für Hochfrequenztechnik

Integration of Numerical Simulation Approaches in the Virtual Development of Automotive Antenna Systems

Hicham Tazi

Vollständiger Abdruck der von der Fakultät für Elektrotechnik und Informationstechnik der Technischen Universität München zur Erlangung des akademischen Grades eines

Doktor-Ingenieurs

genehmigten Dissertation.

Vorsitzender:	Univ.-Prof. Dr.-Ing. K. Diepold
Prüfer der Dissertation:	1. Univ.-Prof. Dr.-Ing. Th. Eibert
	2. Univ.-Prof. Dr.-Ing., Dr. h.c., Dr.-Ing. E.h. W. Wiesbeck Karlsruher Institut für Technologie

Die Dissertation wurde am 13. Juni 2012 bei der Technischen Universität München eingereicht und durch die Fakultät für Elektrotechnik und Informationstechnik am 27. September 2012 angenommen.

Bibliografische Information der Deutschen Nationalbibliothek
Die Deutsche Nationalbibliothek verzeichnet diese Publikation in der Deutschen Nationalbibliografie; detaillierte bibliografische Daten sind im Internet über http://dnb.d-nb.de abrufbar.

1. Aufl. - Göttingen: Cuvillier, 2012
Zugl.: (TU) München, Univ., Diss., 2012

978-3-95404-278-4

Nonnenstieg 8, 37075 Göttingen
Telefon: 0551-54724-0
Telefax: 0551-54724-21
www.cuvillier.de

1. Auflage, 2012
Gedruckt auf säurefreiem Papier

978-3-95404-278-4

Abstract

Technische Universität München
Lehrstuhl für Hochfrequenztechnik

Tazi, Hicham
"Integration of Numerical Simulation Approaches in the Virtual Development of Automotive Antenna Systems"
June 2012

In order to satisfy the high expectations of signal reception quality for multiple multimedia services, an ever increasing number of antennas differing in location and frequency range of operation are installed in present-day vehicles. One of the greatest challenges of automotive antenna engineering is the necessity to make important decisions about the location of the antennas in early stages of development. This is essential due to the fact that many parameters, which have an important impact on the antenna functionality must be considered. The antenna evaluation can be performed if its position in the car is known, especially when antennas are in the immediate vicinity of the car body. Besides, a multitude of car types with different optional equipments are offered to satisfy the customer needs. Therefore, measurements with several prototype cars are still needed to ensure the system quality. These measurements are laborious and time consuming due to the use of expensive car prototypes in the development process. Furthermore, details relating to the car body are often discussed in the concept phase, where no prototypes are available at all. Thus, electrical engineers have started to analyze further development options to reduce measurement dependency and to allow for a faster evaluation of various system configurations.
Ever increasing computational capabilities allow very large matrix equations to be solved by utilizing numerical techniques making it possible to evaluate important antenna and **E**lectro **M**agnetic **C**ompatibility (**EMC**) decisions at an early stage of development. Antenna parameters like the scattering parameters and the radiation pattern can be reliably evaluated. In Chapter 1 of this thesis, an insight in the automotive antenna development at AUDI AG is given. In this introduction, the current automotive antennas and their operating frequency ranges are presented. Also, it will be shown, why automotive antenna system simulations are essential for the automotive antenna development.

In Chapter 2, the major development criteria for automotive antenna systems plus antenna styling and EMC criteria are described.
The most important numerical simulation approaches within commercial simulation tools for automotive antenna engineering are presented in Chapter 3. In particular, approaches based on the **M**ethod **o**f **M**oments (**MoM**) for glass antenna development, which are implemented in the simulation framework at the Antenna Department of AUDI AG, are sufficiently introduced and compared.
Algorithms that facilitate computation time optimization and modelling effort reduction are discussed in Chapter 4. These optimization methods are validated by comparison to the standard simulation methods.
In Chapter 5, important modelling details relating to the glass antenna model and its environment are discussed. The generation of accurate virtual models of the vehicle and antenna systems represents a challenge for antenna engineers and has a major influence on simulation results exactness.
Chapter 6 presents validations of the simulation models and the utilized simulation approaches for determining the antenna characteristics. This is done by the application of the methods shown in Chapter 3 for the virtual development of glass window antennas for different high frequency services.
Chapter 7 presents a new development process based on three dimensional simulation for keyless entry and keyless go systems operating in a low frequency range. The virtual development process is validated by measurements.
Last but not least, developments of very high frequency antenna systems based on simulations are illustrated in Chapter 8.
The key achievements of this thesis consist in presenting novel development processes based on simulations for several automotive antenna systems. The focus of the presented investigations is related to on glass printed antennas for a wide frequency band starting from 100 kHz up to 900 MHz. Different numerical methods based on the Method of Moments are compared to present a solution for virtual antenna development. To compare the proposed approaches, simulations using each one were performed. Furthermore, important details for antenna system and antenna environment modelling, especially those related to ground and antenna amplifiers are given. Also, keyless systems operating at low frequencies as well as roof antenna systems operating at very high frequencies beyond 700 MHz are investigated. All proposed virtual processes are validated by measurements. Valuable computation time can be saved as shown in this work by choosing adequate algorithms.

Acknowledgements

First of all, I would like to express my deepest gratitude and thanks to my Ph.D. supervisor Professor Thomas Eibert for giving me the opportunity to write my dissertation in the High-Frequency Engineering Department at the Technische Universität München. This work has been one of the most significant academic challenges I have ever had to face. This dissertation would not have been successfully completed without support, patience, and guidance from Professor Eibert who always helped me to overcome many difficult situations. I am also thankful to him for giving me the possibility to travel to several conferences around the word for presenting parts of this work.

This work would not have been possible without the financial help and support from AUDI AG. I would like to show my gratitude to my colleagues from the Antenna Department at AUDI AG especially Dr. Christoph Ullrich for his encouragement and guidance. I am deeply grateful to him and to Mr. Aurél Papp for their motivation, support, and for the multiple opportunities to show and discuss my research results. I am also grateful to many colleagues from the EMC Department especially Mr. Johannes Hippeli for the long discussions that helped me to enrich my ideas.
I owe sincere and earnest thankfulness to many people from the company EMCOS for their support, advices and very long discussions especially with Ms. Anna Gheonjian and Dr. Roman Jobava.
It is a great pleasure to thank all students that I have supervised during my Ph.D. time for their brilliant works, especially Mr. Alexander Schneider and Mr. Lukas Bochenski that I show some of our common works in parts of this thesis.
I would like to thank everyone who helped me to write my dissertation successfully especially colleagues from the High-Frequency Department, TU München.

My thanks go to all my friends and colleagues who have shared with me these past years enriching my professional and private life for their support, collaboration, encouragement, and friendship.
Last but not least, I would like to express my deepest gratitude to my family especially my parents without whom all this would not exist at all.

By three methods we may learn wisdom: First, by reflection, which is noblest; Second, by imitation, which is easiest; and third by experience, which is the bitterest.

Master Kong (551 B.C. - 479 B.C.)

List of Symbols

Symbol	Denotation	unit
β	phase constant	1/m
β_n	basis function	
Δl	length difference	m
δ	Dirac impulse	
δ_{ij}	Kronecker delta	
η	antenna efficiency	
$\Im$	imaginary part	
λ	wavelength	m
λ_0	free space wavelength	m
λ_{min}	smallest wavelength	m
μ	permeability	H/m
$\mu(f)$	frequency dependent permeability	H/m
μ_0	permeability in free space	H/m
μ_{env}	relative environment permeability	H/m
μ_r	relative permeability	
μ_{rod}	ferrite permeability	H/m
∇	Nabla operator	
ω	angular frequency	1/s
∂E_0	partial electric field	V/m
∂H_0	partial magnetic field	A/m
Φ	electrical potential	V
φ	azimuth angle	rad
φ_N	angular phase shift	rad
$\Re$	real part	
ρ	resistivity	Ω m
ρ_e	electric charge density	C/m^3
ρ_m	magnetic charge density	Wb/m^3
σ	electric conductivity	S/m
τ_N	time step	s

ϑ	elevation angle	rad
$\varepsilon(f)$	frequency dependent permittivity	F/m
ε_0	vacuum permittivity ($\approx 3 \cdot 8.85 \times 10^{-12}$)	F/m
ε_e	equivalent permittivity	F/m
ε_r	material permittivity	
$\vec{\Phi}_{ik}^{-}$	outgoing flux	
$\vec{\Phi}_{ik}^{+}$	incoming flux	
$\vec{A}$	magnetic vector potential	Vs/m
$\vec{B}$	magnetic flux density	T
$\vec{D}$	displacement current density	C/m^2
$\vec{E}$	electric field	V/m
$\vec{e}$	unit vector	
$\vec{E}^{inc}$	incident electric field	V/m
$\vec{E}^{sc}$	scattered electric field	V/m
$\overset{\leftrightarrow}{G}{}_J^E\ (\vec{r}, \vec{r}\,')$	electric dyadic Green's function	Ω/m^2
$\overset{\leftrightarrow}{G}{}_J^H\ (\vec{r}, \vec{r}\,')$	magnetic dyadic Green's function	1/m^2
$\vec{H}$	magnetic field	A/m
$\vec{J}$	current density	A/m^2
$\vec{J}^k$	mirror current density of element k	A/m^2
$\vec{J}_M$	magnetic current density	V/m^2
$\vec{n}$	unit normal vector	
$\vec{n}_k$	unit normal vector	
$\vec{r}$	position vector	m
$\vec{S}$	pointing vector	W/m^2
$\vec{v}$	velocity	m/s
${}^gC_k^{ji}$	scalar matrix coefficient element	
${}^hC_k^{ji}$	horizontal matrix coefficient element	
${}^vC_k^{ji}$	vertical matrix coefficient element	
A	surface	m^2
a	incoming wave	V/$\sqrt{\Omega}$
a_1	incoming wave in port 1	V/$\sqrt{\Omega}$
a_2	incoming wave in port 2	V/$\sqrt{\Omega}$
A_{effrad}	effective radiation antenna aperture	m^2
$A_{efftrans}$	effective transmission antenna aperture	m^2
A_J	lateral face	m^2
AF	antenna factor	1/m

b	reflected wave	$\mathrm{V}/\sqrt{\Omega}$
b_1	reflected wave in port 1	$\mathrm{V}/\sqrt{\Omega}$
B_{1n}	magnetic flux density normal component	T
b_2	reflected wave in port 2	$\mathrm{V}/\sqrt{\Omega}$
B_J	magnetic flux density	T
B_m	voltage vector elements	V
C	capacitance	F
c	light speed in material	m/s
c_0	light speed in free space ($\approx 3 \cdot 10^8$)	m/s
$C_{coplanar}$	coplanar strip line capacitance	F
c_{ii}	per unit length capacitance matrix diagonal elements	F/unit length
c_{ij}	per unit length coupling capacitance	F/unit length
C_P	parasitic capacitance	F
D	electric displacement current density	$\mathrm{C/m^2}$
d	distance	m
d_a	antenna dimension	m
div	divergence	
E	electric field	V/m
E_{tan}	electric field tangential component	V/m
f	frequency	Hz
f_0	resonant frequency	Hz
G	antenna gain	dBi
G_I	isotropic gain	dBi
G_{rad}	gain of the radiating antenna	dBi
$G_{realized}$	realized gain or practical gain	dBi
G_{trans}	gain of the receiving antenna	dBi
g_{ii}	per unit length capacitance matrix diagonal elements	s/unit length
g_{ij}	per unit length coupling capacitance	s/unit length
grad	gradient	
H	transmission coefficient	
h	thickness	m
H^*	complex transmission coefficient conjugate	
h_I	magnetic edge voltages	A
h_I	magnetic field	A/m
H^{inc}	incident magnetic field	A/m

H_{tan}	magnetic field tangential component	A/m
H_{trans}	transfer function	
I_{signal}	input signal	
I	electric current	A
I_{in}	input current	A
I_r	reflected wave current	A
J	current density	A/m^2
K	stability criterion	
k_0	free space wave number	1/m
L	inductance	H
l	length	m
L	mathematical operator	
l_{cell}	smallest cell edge	m
l_{ii}	per unit length inductance matrix diagonal elements	H/unit length
l_{ij}	per unit length coupling inductance	H/unit length
M	coupling inductance	H
n	number of coupling parameters	
O_{signal}	output signal	
P_A	available effective power	W
P_{av0}	available power	W
P_D	dissipative power	W
P_{IN}	input power	W
P_{max}	maximal power	W
p_N	amplitude amplification factor	
P_R	(effective) radiated power	W
P_R	radiation power	W
P_{rad}	radiated power	W
P_{trans}	transmitted power	W
r_1	return loss parameter	
R	Ohmic load	Ω
r	radius	m
R_E	radiation resistance	Ω
r_{ii}	per unit length capacitance matrix diagonal elements	Ω/unit length
r_{ij}	per unit length coupling capacitance	Ω/unit length
R_L	load Ohmic part	Ω

rot	rotation	
R_S	source Ohmic part	Ω
R'_{TL}	transmission line resistive load	Ω
R_V	(antenna) Ohmic loss	Ω
R_w	equivalent wire radius	m
s	curve	m
S	scattering parameter	dB
S_{11}	reflection factor at port 1	
S_{21}	transmission factor from port 1 to port 2	
s_j	mean value of the tetrahedron edges	
S_k	surface	m^2
S_r	(radial) radiation power density	W/m^2
t	time	s
T	time period	s
$\tan\delta$	dielectric loss factor	
$\tan(\delta_m)$	magnetic loss factor	
U	voltage	V
U^-	forward/backward travelling waves	V
U^+	forward/backward travelling waves	V
U_A	antenna voltage source	V
U_{in}	input voltage	V
U_L	load voltage	V
U_R	reflected wave voltage	V
U_S	source voltage	V
U_T	transmitted wave voltage	V
v	invalid tetrahedron	
V	volume	m^3
V_I	volume of the tetrahedron	m^3
v_R	receiver antenna ground speed	m/s
v_S	transmitter antenna ground speed	m/s
w	metallic strip width	m
w_m	testing function	
X_A	antenna reactance	Ω
X_L	load reactance part	Ω
X_S	source reactance	Ω
y	elements of the Y matrix	S
Z	impedance	Ω

z	propagation direction	
Z_0	reference impedance	Ω
Z_A	antenna impedance	Ω
Z_{F_0}	wave impedance	Ω
Z_{IN}	input impedance	Ω
Z_L	load impedance	Ω
Z_{matrix}	impedance matrix	Ω
Z_{MN}	impedance elements	Ω
Z_S	source impedance	Ω

List of Abbreviations

Abbreviation	Meaning
ABC	**A**bsorbing **B**oundary **C**ondition
AFS	**A**daptive **F**requency **S**ampling
AM	**A**mplitude **M**odulation
ASCII	**A**merican **S**tandard **C**ode for **I**nformation **I**nterchange
BCM	**B**ody **C**omputer **M**odule
Bilogper	**Bi**-conical **log**arithmic **per**iodical
CAD	**C**omputer **A**ided **D**esign
CATIA	**C**omputer **A**ided **T**hree- Dimensional **I**nteractive **A**pplication
CDMA	**C**ode **D**ivision **M**ultiple **A**ccess
DAB	**D**igital **A**udio **B**roadcasting
DUT	**D**evice **U**nder **T**est
DXF	**D**rawing e**X**change **F**ormat
EFIE	**E**lectric **F**ield **I**ntegral **E**quation
EIRP	**E**quivalent **I**sotropic **R**adiated **P**ower
EM	**E**lectro **M**agnetic **C**ompatibility
EMC	**E**lectro **M**agnetic **C**ompatibility
EMSL	**E**uropean **M**icrowave **S**ignature **L**aboratory
ETC	**E**lectronic **T**oll **C**ollection
FD	**F**requency **D**omain
FDM	**F**inite **D**ifference **M**ethod
FDA	**F**requency **D**istribution **A**lgorithm
FDMA	**F**requency **D**ivision **M**ultiple **A**ccess
FDTD	**F**inite **D**ifference **T**ime **D**omain
FEA	**F**inite **E**lement **A**nalysis
FEM	**F**inite **E**lement **M**ethod
FT	**F**ourier **T**ransformation
FIM	**F**inite **I**ntegral **M**ethod
FIT	**F**inite **I**ntegration **T**heory

Abbreviation	Meaning
FM	**F**requency **M**odulation
FV	**F**inite **V**olume method
FVTD	**F**inite- **V**olume **T**ime **D**omain
GO	**G**eometrical **O**ptic
GPS	**G**lobal **P**ositioning **S**ystem
GSM	**G**lobal **S**ystem for **M**obile communication
GTD	**G**eometrical **T**heory of **D**iffraction
HF	**H**igh **F**requency
IBC	**I**mpedance **B**oundary **C**ondition
IEEE	**I**nstitute of **E**lectrical and **E**lectronics **E**ngineers
IGES	**I**nitial **G**raphics **E**xchange **S**pecification
LCTL	**L**umped **C**ircuit **T**ransmission **L**ine
LED	**L**ight **E**mitting **D**iode
LF	**L**ow **F**requency
LNA	**L**ow **N**oise **A**mplifier
LoS	**L**ine **o**f **S**ight
LTE	**L**ong **T**erm **E**volution
LW	**L**ong **W**ave
MAS	**M**ethod of **A**uxiliary **S**ources
Mbps	**M**ega**b**it **p**er **s**econd
MF	**M**edium **F**requency
MFIE	**M**agnetic **F**ield **I**ntegral **E**quation
MIMO	**M**ultiple **I**nput **M**ultiple **O**utput
MoM	**M**ethod **o**f **M**oments
MoM-MAS	hybrid **M**ethod **o**f **M**oments with the **M**ethod of **A**uxiliary **S**ources
MTL	**M**ulti conductor **T**ransmission **L**ine
MW	**M**edium **W**ave
NASTRAN	**NA**sa **STR**uctural **AN**alysis System
NFSS	**N**ear **F**ield **S**ource **S**olution
NVA	**N**etwork **V**ector **A**nalyzer
ODE	**O**rdinary **D**ifferential **E**quation
OFM	**O**rthogonal **F**requency **M**ultiplexing
PBA	**P**erfect **B**oundary **A**pproximation
PDE	**P**artial **D**ifferential **E**quation
PEC	**P**erfect **E**lectric **C**onductors

Abbreviation	Meaning
PML	**P**erfectly **M**atched **L**ayers
PO	**P**hysical **O**ptic
PTD	**P**hysical **T**heory of **D**iffraction
RF	**R**adio **F**requency
SDARS	**S**atellite **D**igital **A**udio **R**adio **S**ervice
SDMA	**S**pace **D**ivision **M**ultiple **A**ccess
SM-ABC	**S**ilver **M**ueller **A**bsorbing **B**oundary **C**ondition
SERIUS	**S**ervice **I**n **US**
SISO	**S**ingle **I**nput **S**ingle **O**utput
SNR	**S**ignal **N**oise **R**atio
SPICE	**S**imulation **P**rogram **I**ntegrated **C**ircuit **E**mphasis
STEP	**S**tandard **T**emplate **E**lectronic **P**ublishing
SUV	**S**port **U**tility **V**ehicles
SW	**S**hort **W**ave
TD	**T**ime **D**omain
TDMA	**T**ime **D**ivision **M**ultiple **A**ccess
TEM	**T**ransversal **E**lectro **M**agnetic
TL	**T**ransmission **L**ine
TLM	**T**ransmission **L**ine **M**ethod
TLMM	**T**ransmission **L**ine **M**atrix **M**ethod
TPS	**T**ire **P**ressure **S**ystem
TST	**T**hin **S**heet **T**echnique
TV	**T**ele**V**ision
UMTS	**U**niversal **M**obile **C**ommunication **S**ystem
USW	**U**ltra **S**hort **W**ave
VHF	**V**ery **H**igh **F**requency
VICS	**V**ehicle **I**nformation **C**ommunication **S**ystem
WLAN	**W**ireless **L**ocal **A**rea **N**etwork

Table of Contents

1 Introduction

Many automotive engineering fields have started to use simulations profiting from the continuously increasing performance of computers in terms of computation time and memory capacity [Konr 07; Reif 11]. Computational methods are used to develop complex systems with variation of different system parameters. Simulations can also be used in different stages of development in order to achieve the best possible system performance in very short development time. However, the benefit depends on the application time as shown in Figure 1.1

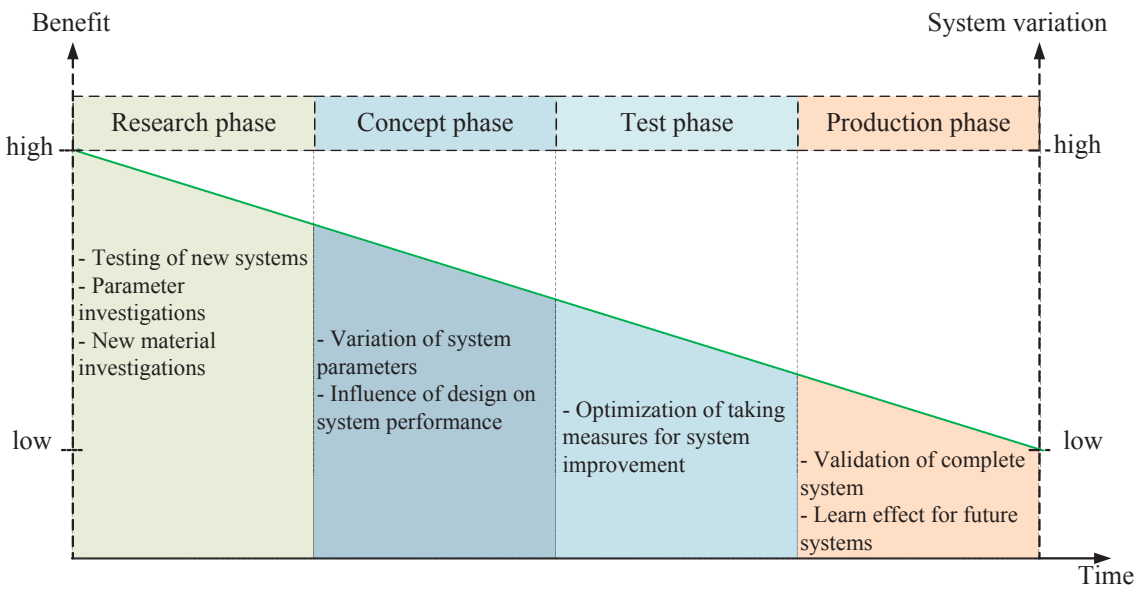

Figure 1.1: Benefit of the simulation.

[Frei 09]. When simulations are applied in the development process of automotive antenna systems, four different phases can be distinguished:

- *Research phase*: The highest benefit can be reached in this phase of development because the developer still has the possibility to change different system parameters to reach the best result. In addition, the developer has the opportunity to test completely new systems and new concepts to analyze their usability. For example, it is possible to evaluate new antenna positioning concepts in cars. The results obtained could be considered for new antenna system concepts.

- *Concept phase*: Usually, geometries of the system are already defined in this phase. The developer still has the eventuality to look for the best position of the antenna layout in the car. More than one integration location should be available in case of geometry change.
- *Test phase*: During this stage, only a few alternatives are available for the developer to improve system quality. Nevertheless, he still has a powerful tool to ensure the development of the best optimized system by changing the antenna layout.
- *Production phase*: In this stage of development only an understanding of the system performance is feasible, and troubleshooting relating to EMC problems can be performed. The results achieved could be used for development and to improve the next system generation.

1.1 Automotive Antennas

The number of the radio services offered in the automotive field has increased in recent years [Reif 11]. A need to elate customers and to differ from low cost car manufacturers leads to the integration of more and more **R**adio **F**requency (**RF**) services in cars. Initially, the only RF service offered in cars were the **A**mplitude **M**odulation (**AM**) with antennas working in **L**ow/**M**edium **F**requency (**LF**/**MF**) and **F**requency **M**odulation (**FM**) radio [Wern 06; Schn 06]. Due to a revolution in RF services worldwide [Fuji 94], further services were integrated first in luxury cars and then in regular cars. Examples for this are the introduction of telephone and navigation systems in expensive cars in the mid 90s [Talt 01]. Today, a multitude of RF systems can be found in cars, for example central locking, Bluetooth systems and **T**ire **P**ressure **S**ystems (**TPS**) [Rabi 10]. Even for multimedia services, a wide choice is available for **T**ele**V**ision (**TV**) and radio. The differences in frequency ranges in each country have to be considered. Also, differences in the technology used, such as radio based on satellite transmission or broadcast terrestrially based on LF/MF especially in the USA and Canada, or radio based on **V**ery **H**igh **F**requency (**VHF**) as it is the case in large parts of Europe. Figure 1.2 shows the development of the number of the RF services offered in cars in recent years. The number of the antennas will still increase in the years ahead and in 2015 will include some new services like Car2Car and the new mobile technology - **L**ong **T**erm **E**volution (**LTE**)- [Saut 11]. More than 20 RF services will be available in cars in the coming few years. Even taking of antenna diversity into account with two or even three antennas for some of the services offered, the number of antennas in any car could surpass 30.

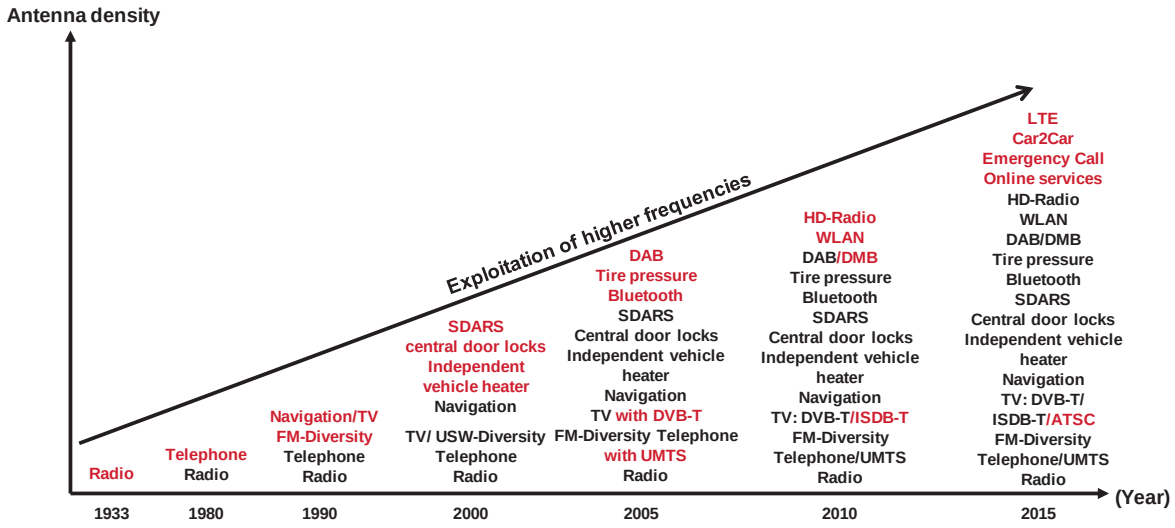

Figure 1.2: Automotive RF services evolution over the last decades.

The multiple antennas typically work in different frequency ranges. Figure 1.3 gives an overview of the diverse frequency ranges used for automotive applications. The various systems operate at frequencies starting at around 10 kHz for the keyless entry and keyless go systems and ranging up to some 10 GHz for radar systems. Several systems operate in the frequency range around 2 GHz such as the **U**niversal **M**obile **C**ommunication **S**ystem (**UMTS**), **G**lobal **S**ystem for **M**obile communication (**GSM**) [Saut 11], Bluetooth or **S**atellite **D**igital **R**adio **S**ervice (**SDARS**) [Wies 07b; Xue 04]. Radio services start with LW at 125 kHz and end at 2.4 GHz with SDARS. **D**igital **A**udio **B**roadcating (**DAB**) operating in frequency ranges starting at around 100 MHz for low band and ending at 1.9 GHz for the highest band will replace the widespread VHF system in the future [Luo 09]. The TV services operate in different bands starting at about 100 MHz for low band and ending at 1 GHz [Luo 09].

Figure 1.4 shows a typical car antenna system with the multiple positions of the antennas and the antenna amplifiers. The blue colored areas show potential positions of further antennas. Typically, several multimedia antennas, especially radio antennas operating in VHF frequency range and TV antennas, are mounted in the rear window. Side widows are often used for DAB antennas and TV.

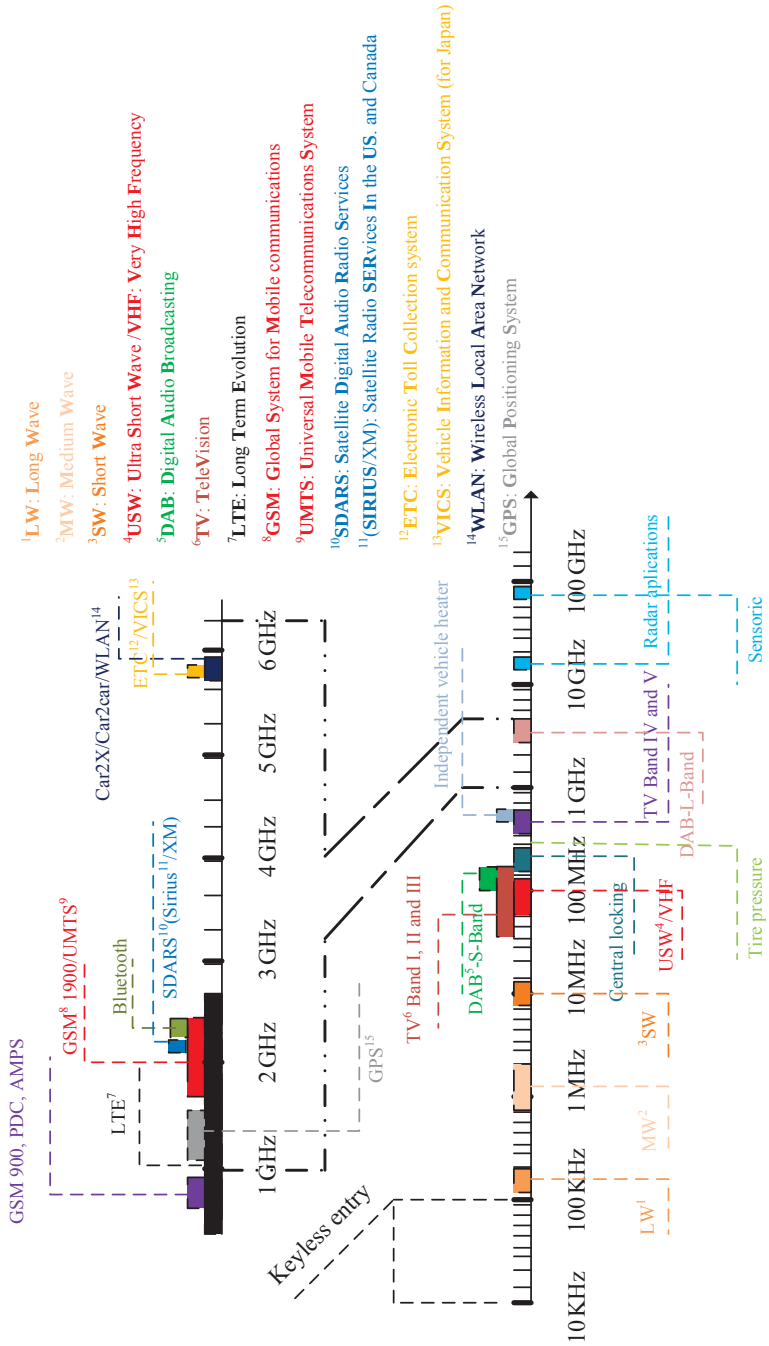

Figure 1.3: Operating frequency ranges of the multiple RF automotive services.

Sometimes an additional FM antenna is placed in the side window, for example as part of a diversity system [Kim 03]. Front windows are used often for radio and for TV in convertibles due to the small rear and side windows, which are retracted when the roof is down. Side mirrors are often used for **G**lobal **P**ositioning **S**ystem antennas **GPS** or UMTS antennas [Dode 10].

The inside mirror can also be used for this purpose. Further antennas can be hidden in the bumper as well as in the spoiler.

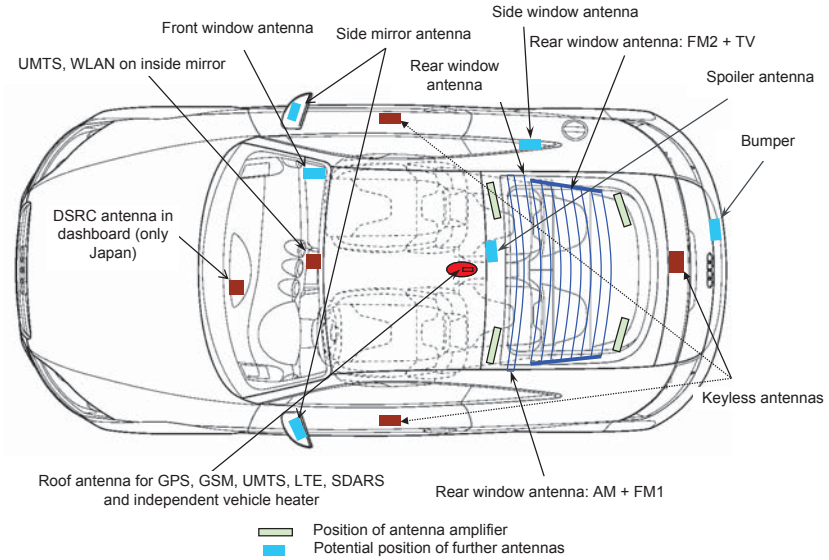

Figure 1.4: Typical car antenna system.

Keyless antennas are usually magnetic antennas, which are placed in the doors or in the luggage trunk. In limousines, several antennas operating in the high frequency range are located in the roof antenna assembly, such as GPS, GSM, UMTS and SDARS. Figure 1.5 shows a typical roof antenna system composed of two patches for GPS and SDARS and one **R**eceiving/**T**ransmitting (**Rx/Tx**) telephone antenna covering the GSM and UMTS frequency ranges.

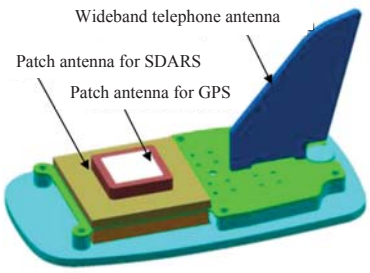

Figure 1.5: Typical roof antenna system.

Figure 1.6 shows a block diagram of a receiving system composed of a receiving antenna with a gain G_{Ant} and a **L**ow **N**oise **A**mplifier **(LNA)**, an RF cable and a receiver [Rabi 10]. The role

of the LNA is to amplify the weak received signal with preferably minimal addition of noise and it is characterized by the gain G_{LNA} and a noise factor F_{LNA}. Both, the RF cable and the receiver are also characterized by the gain G_{Cable} and G_{rec} and a noise factor F_{Cable} and F_{rec}, respectively. The LNA is connected to an input matching circuit from the antenna side and to an output matching circuit from the receiver side [Matt 80]. This is very important to ensure minimal signal loss due to the mismatching between antenna or receiver and amplifier [Russ 03]. The signal is led through the RF cable to the receiver.

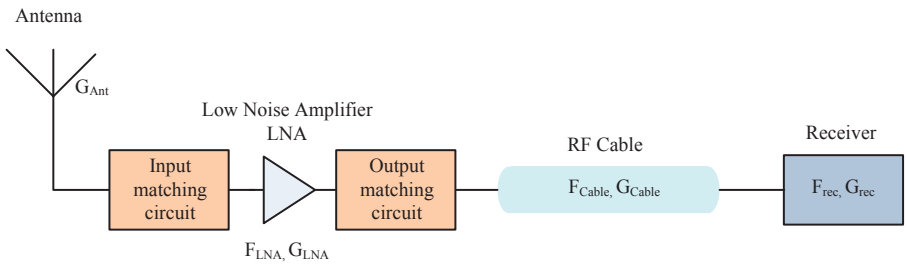

Figure 1.6: Block diagram of an automotive active antenna system.

Figure 1.7 shows a special case of Figure 1.6 [Rabi 10]. The difference between both graphs is the tuner representing a part of the car radio. The role of the tuner is to demodulate and decode the encrypted received signal.

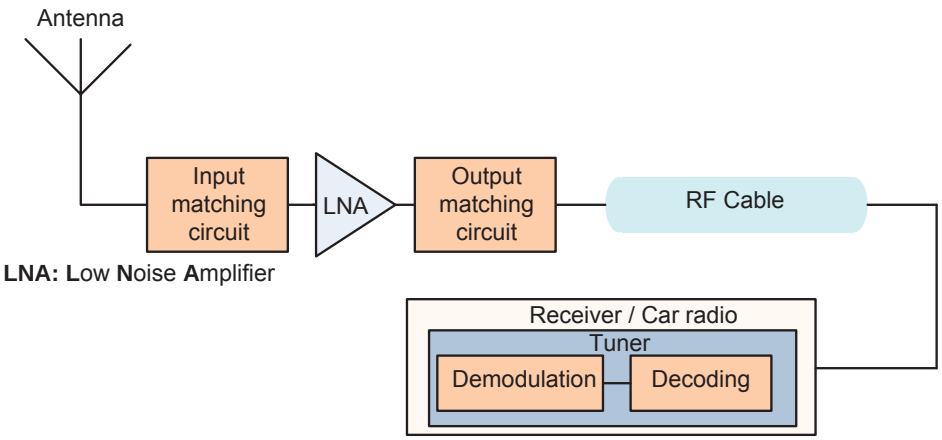

Figure 1.7: Block diagram of an automotive active multimedia antenna system.

1.2 Problem Definition

In the last three decades, the product portfolio of cars has increased rapidly. This is related to the fact that the number of the cars bought has increased strongly worldwide. Especially new

markets like China and India have shown a huge demand for cars. Car manufacturers have to be flexible and to respond to all customers' tastes, taking into account the different cultural and socio-economical backgrounds of each market. The product range goes from small city cars through limousines up to **S**ports **U**tility **V**ehicles (**SUV**s). Besides that, customers have the possibility to configure their cars with different equipment depending on their needs and budget. Figure 1.8 shows how the number of different models has developed in recent years at AUDI AG. The trend is to offer cars to all niche markets. It can therefore be expected

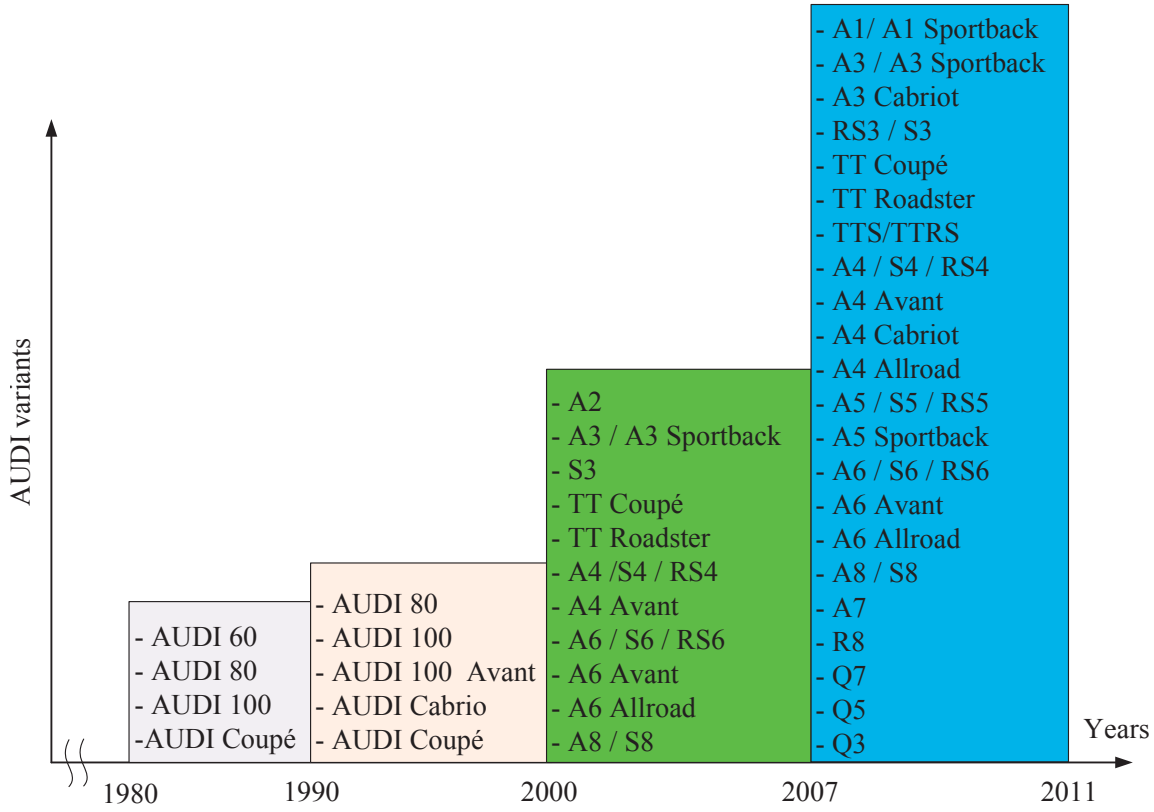

Figure 1.8: Evolution of AUDI cars in the last decades.

that the number of cars produced and of possible car configurations will increase in the years ahead. A great challenge for premium car manufacturers is to ensure the best possible quality, to be the first in the market to offer new technologies and to assure the robustness of these technologies for the car life cycle. An additional challenge is the shorter development cycle, which does often not surpass thirty-six months. Additionally, the car manufacturers try to economize resources in development such as costs related to the car prototypes, which represent an important part of the development budget of each car to stay competitive to the other car manufacturers. Thus, development time is decreasing significantly. Besides that, it is almost impossible to produce car prototypes for each potential car configuration. The application of these development challenges on the automotive antenna area makes it necessary to use new

tools based on virtual system development in order to develop antennas without the need of prototypes with decreasing time consumption and without very expensive measurements. This would give the antenna engineers the possibility to get information about system quality at a very early stage of development. However, the accuracy of the results delivered from these virtual development tools must be ensured.

1.3 Objectives

The need to use simulation tools to develop new antenna systems was recognized some years ago. Different commercial 3D simulation tools can be used in the field of the antenna and electromagnetic compatibility (EMC) engineering for system development or as a part of the development process.

The objectives of the application of simulations in the field of antenna engineering are shown in Figure 1.9. The objectives of virtual automotive antenna development can be split into four categories:

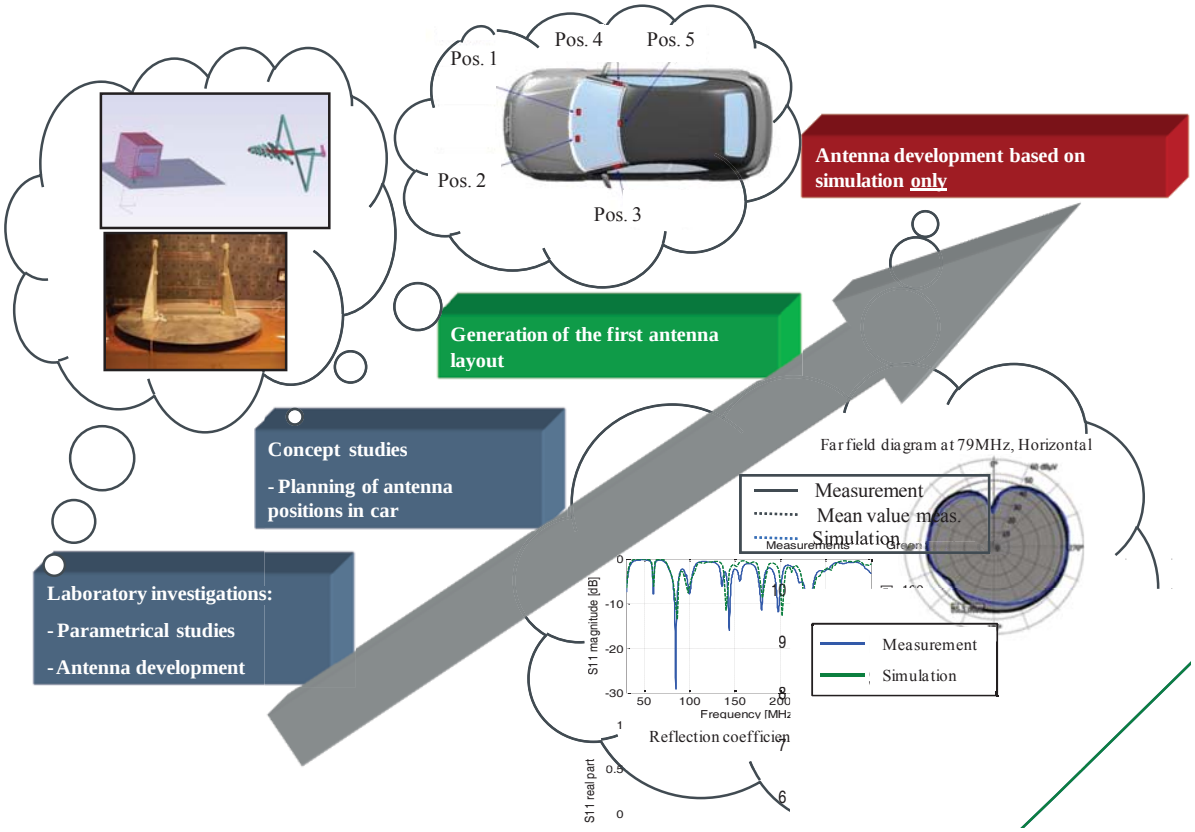

Figure 1.9: Objectives of integrating simulation into the development process.

- *Laboratory investigations*: In this development stage important investigations relating to completely new antenna concepts can be performed. Simulations can help to predict the antenna behaviour especially when parameter studies are to be realized. One example would be changing the electric parameters of the glass the antennas are printed on. This can happen if the glass supplier is changed or if new glass requirements are needed. Besides that, measurements of some simple laboratory constructions can be used to validate numerical computations of simulation methods or new features in the simulation tools.

- *Concept studies*: The antennas installed in cars have to be hidden. This is due to the strict design criteria of the car Styling Department. Consequently, new car concepts should be improved continuously to respond to all system requirements. Simulations can help engineers to find new positions in cars, where antennas could be mounted accordingly to the design criteria and system performance requirements.

- *Generation of the first antenna layout*: The development of antennas for all RF services is very laborious and time consuming. Utilizing simulation tools, it is much easier to realize many development loops. The first antenna layout can be designed in this way. However, further investigations based on measurements are still needed to validate the antenna behaviour and for fine tuning of the antenna structure.

- *Antenna development based on simulation only:* The most important goal of simulation is to be able to realize the complete development process based on simulation only without the need to verify the simulation results with measurements. This would be possible if it could be proven that simulations have been validated for all RF services and in all frequency ranges of interest. This will be achieved in the near future.

2 Antenna Characterization

In antenna engineering literature [Bala 05; Vola 07; Orfa 04; Ante 09], one can find many parameters, which are used for the characterization of antennas. Different antenna parameters are dependent on each other. In this chapter, an overview of the most important parameters in antenna engineering is given.

For a better understanding of antenna systems, equivalent circuits are used [Voge 04]. First, it can be distinguished between an equivalent circuit of an emitting system shown on the left side of Figure 2.1 and an equivalent circuit of the receiving system represented on the right side of the figure [Wies 07a; Voge 04].

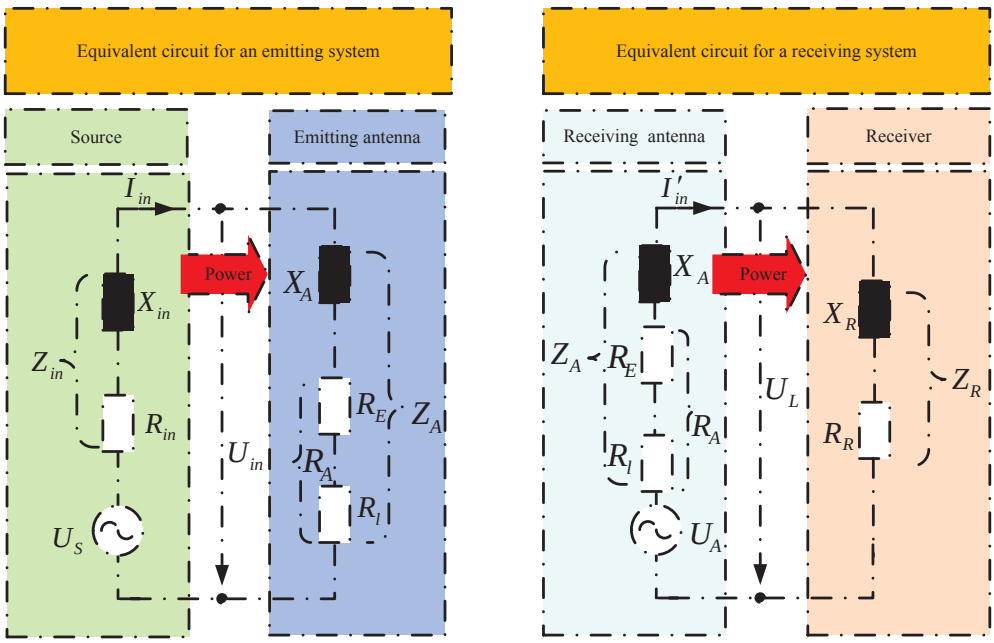

Figure 2.1: Equivalent model of an emitting and a receiving systems.

The equivalent circuit of the emitting system is composed of a source part with a source voltage U_S and a complex source impedance Z_{in}. The real part of the impedance is represented by the resistance R_{in} and the imaginary part is represented by the reactance X_{in}. Consequently, a resulting electric current I_{in} in the emitting part of the equivalent circuit can be calculated from the source voltage and the complex input impedance Z_A of the antenna. The antenna radiation power P_r can be calculated from the current I_{in} and the voltage U_{in} measured at the

source ports including the impedance Z_{in}. The current I_{in} and the voltage U_{in} at the antenna terminals are given by

$$I_{in} = \frac{U_S}{Z_{in} + Z_A} \tag{2.1}$$

and

$$U_{in} = \frac{U_S \; Z_A}{Z_{in} + Z_A} \, . \tag{2.2}$$

The blue highlighted part of the emitting system's equivalent circuit consists of the complex antenna impedance Z_A that can be split in an Ohmic part R_A and a reactance part X_A. R_A represents the sum of the antenna Ohmic losses R_l and a radiation resistance R_E.
The equivalent circuit of the receiving system is, like the emitting system, composed of a receiving antenna part and a receiver. The source voltage in the receiving antenna is represented by U_A. The receiving antenna is described in addition to the source voltage U_A with the impedance Z_A composed of X_A and the Ohmic part R_A. The receiver power can be calculated from the current I'_{in} and the voltage U_L measured at the receiver source port. The receiver part is given by the complex load impedance Z_R, which can be split in an Ohmic part R_R and a reactance part X_R.

2.1 Scattering Parameters

Figure 2.2 shows an electric circuit composed of a voltage source U_S, a source impedance Z_S and a two-port network connected to infinitesimal line sections with the wave impedance Z_0. The network is terminated by the load impedance Z_L.

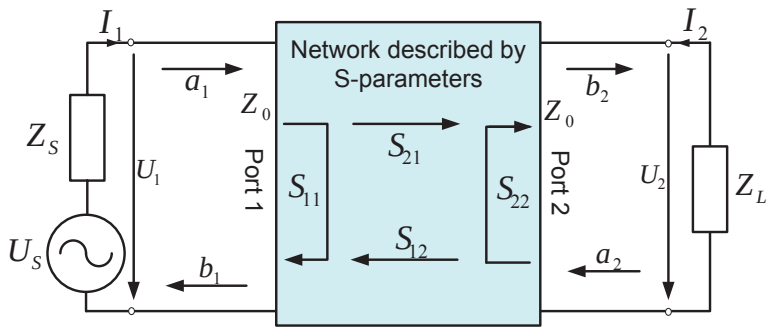

Figure 2.2: S-parameter network.

The resulting current at the input terminals of the two-port network is I_1. The voltage at port 1 is characterized by U_1. Similarly, the voltage at port 2 is characterized by U_2. Certain parts of the source energy is reflected at port 1 of the network. The rest of the energy will be transmitted to port 2 if the two port is lossless. In order to introduce the *scattering parameters*,

also called S-parameters, two new entities should be introduced. The first one is the incoming wave a and the second is the reflected wave b. The indices 1 and 2 represent the ports 1 and 2, respectively [Wies 07a; Kark 04]. The parameters of the S matrix describing the two-port network are calculated based on the normalized wave parameters a and b:

$$b_1 = S_{11}\ a_1 + S_{12}\ a_2 \tag{2.3}$$

and

$$b_2 = S_{21}\ a_1 + S_{22}\ a_2\,. \tag{2.4}$$

The four S-parameters describing the relation between incoming and reflected waves are formulated by

$$S_{11} = \left.\frac{b_1}{a_1}\right|_{a_2=0},\quad S_{22} = \left.\frac{b_2}{a_2}\right|_{a_1=0},\quad S_{21} = \left.\frac{b_2}{a_1}\right|_{a_2=0},\quad S_{12} = \left.\frac{b_1}{a_2}\right|_{a_1=0}. \tag{2.5}$$

The incoming wave a_1 at port 1 can be calculated according to

$$a_1 = \frac{U_1 + I_1\ Z_0}{2\ \sqrt{Z_0}}\,. \tag{2.6}$$

Similar to equation (2.6), the incoming wave a_2 at port 2 can be described by

$$a_2 = \frac{U_2 + I_2\ Z_0}{2\ \sqrt{Z_0}}\,. \tag{2.7}$$

The reflected wave b_1 at port 1 can be calculated according to

$$b_1 = \frac{U_1 - I_1\ Z_0}{2\ \sqrt{Z_0}}\,. \tag{2.8}$$

Similar to equation (2.8), the reflected wave b_2 at port 2 can be described by

$$b_2 = \frac{U_2 - I_2\ Z_0}{2\ \sqrt{Z_0}}\,. \tag{2.9}$$

The load impedance *return loss* parameter r_L is defined as

$$r_L = \frac{\frac{Z_L}{Z_0} - 1}{\frac{Z_L}{Z_0} + 1}\,. \tag{2.10}$$

Similarly, the source return loss parameter r_S is given by

$$r_S = \frac{\frac{Z_S}{Z_0} - 1}{\frac{Z_S}{Z_0} + 1}\,. \tag{2.11}$$

The quotient of the two voltages U_1 and U_2 is given by

$$\frac{U_2}{U_1} = \frac{S_{21}(1 + r_L)}{(1 - S_{22}\ r_L)(1 + r_1)} \tag{2.12}$$

where the return loss parameter r_1 at port 1 is defined as

$$r_1 = S_{11} + \frac{S_{12}\ S_{21}\ r_L}{1 - S_{22}\ r_L} \tag{2.13}$$

and the return loss parameter r_2 at port 2 is defined as

$$r_2 = S_{22} + \frac{S_{12}\ S_{21}\ r_S}{1 - S_{11}\ r_S}\,. \tag{2.14}$$

The *transducer power gain* of the complete system can be calculated according to

$$g_T = \frac{P_L}{P_{S\,\max}} = \frac{|S_{21}|(1 - |r_S|^2)(1 - |r_L|^2)}{|(1 - S_{11}\ r_S)(1 - S_{22}\ r_L) - S_{12}\ S_{21}\ r_L\ r_S|^2} \tag{2.15}$$

where $P_{S\,\max}$ is the maximal available source power and P_L is the absorbed power from the load impedance Z_L.

In the field of antenna engineering, the antenna return loss parameter r_{ant} delivers information about the part of the energy, which can be emitted or received from the antenna. In case of one port networks, this parameter is also called the *reflection factor* or S_{11}*-parameter* [Voge 04; Mill 05].

In antenna development, engineers first evaluate this parameter during the development process to obtain the best possible emitting or receiving antenna in the frequency range of interest.

The antenna *matching* means that the *antenna impedance* is equal to the impedance of the RF cable (transmission line) Z_{TL} as well as to the impedance of the connected transmitter and receiver depending on the antenna type (Z_L). In this case, reflections do not occur. A part of the power is transformed to thermal power due to the antenna's Ohmic part R_A and the rest of the power is radiated or received, respectively. Antenna systems have often 50 Ω or 75 Ω matching impedance. It is advisable that all antenna system parts have the same impedance or to use matching circuits to avoid impedance mismatch losses. The input impedance Z_S and output impedance Z_L are typically equal to the transmission line impedance Z_{TL}:

$$Z_S = Z_L = Z_{TL}\,. \tag{2.16}$$

In this case the antenna system is perfectly matched and the resulting return loss is equal to 0.

Related to the antenna return loss parameter r_{ant}, the ***V**oltage **S**tanding **W**ave **R**atio* (**VSWR**) gives the maximum standing wave amplitude in a relationship to the minimum standing wave amplitude. An ideally matched system has a VSWR value of 1 : 1. This parameter is often used in power electronics to define the breakdown electric field of power transistors [Voge 04]. The VSWR is calculated according to

$$VSWR = \frac{1 + |r_{ant}|}{1 - |r_{ant}|}\,. \tag{2.17}$$

2.2 Far Field Characteristics

Far field characterizes a region, where the magnetic field component $\vec{H}$ of an electromagnetic wave is in phase with the electrical component $\vec{E}$ and where both components are perpendicular to the wave direction of propagation [Bala 05]. However, in literature [Capp 01; Gave 94], depending on the field of RF engineering, different definitions determining the distance to the source, where the far field region starts can be found. For example, in the EMC field, the commonly used definition for determining the distance d to the antenna being tested, where the antenna is assumed to be located in far field [Capp 01], is

$$d \geq \frac{5\lambda}{2\pi} \tag{2.18}$$

where λ is the wavelength. For precision antennas [Whee 75; Whee 47], the distance d is calculated depending on the largest dimension D [Capp 01] with

$$d \geq \frac{50D^2}{\lambda}\,. \tag{2.19}$$

The far field region is commonly defined in automotive antenna development at distances d from the source according to

$$d \geq 2D^2/\lambda \tag{2.20}$$

with

$$\lambda = \frac{c_0}{f} \tag{2.21}$$

where c_0 is the speed of light in medium and f is the operating frequency. The electric field $\vec{E}$ and the magnetic field $\vec{H}$ are perpendicular to the wave propagation vector in the far field. $\vec{E}$ and $\vec{H}$ are combined with the wave impedance Z_{F_0} according to

$$Z_{F_0} = \frac{|\vec{E}|}{|\vec{H}|} = \sqrt{\frac{\mu_0}{\varepsilon_0}} = 120\pi\ \Omega \approx 377\ \Omega\,. \tag{2.22}$$

In order to determine the far field region, the wave number k_0 is used and is equal to $\frac{2\pi}{\lambda_0}$. The wavelength at the frequency f_0 is λ_0 where

$$k_0 d \gg 1\,. \tag{2.23}$$

2.3 Radiation Pattern of an Automotive Antenna Mounted on the Car Roof

Antenna evaluation necessitates investigation of antenna behaviour in all spatial directions. The information delivered by the return loss parameter is very important but still not enough

to evaluate antennas in the complete space. For this purpose, a further function, which delivers a statement about the three dimensional antenna behaviour is used. This function is called the *antenna radiation pattern* and is calculated according to

$$\vec{C}(\vartheta,\varphi) = \left.\frac{\vec{E}(r,\vartheta,\varphi)\,e^{j\beta_0 r}}{\left|\vec{E}(r,\vartheta,\varphi)\,e^{j\beta_0 r}\right|_{\max}}\right|_{r=const\to\infty} = C_\vartheta(\vartheta,\varphi)\,\vec{e}_\vartheta + C_\varphi(\vartheta,\varphi)\,\vec{e}_\varphi \tag{2.24}$$

where φ is the azimuth angle and ϑ is the elevation angle. It can be seen that the resulting function can be split into two components C_ϑ and C_φ in the spherical coordinate system illustrated in Figure 2.3.

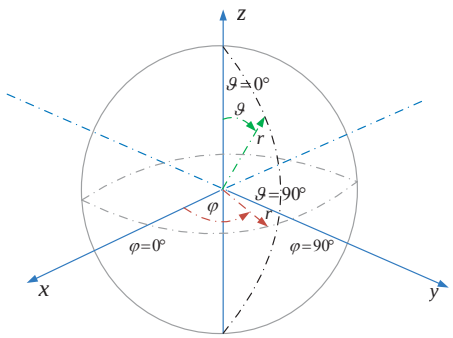

Figure 2.3: Spherical coordinate system.

The separation of these components C_ϑ and C_φ gives important information about the received or emitted signal, called *polarization* [Wies 07a; Kark 04].

There are various antenna types, which are dependent on the relationship between ϑ and φ components such as *linearly*, *circularly* and *elliptically polarized* antennas.
The investigated antenna in Figure 2.4 is mounted on the car roof. Two different axes are considered and two ordinary representations of the antenna radiation pattern types for automotive antennas are depicted in the figure. The first one, using the left green axis, delivers values in [dB] for normalized pattern in the desired elevation and azimuth angle. The same information can be read out in [dBi] by using the second representation on the right red axis. This will be annotated in the next sections.

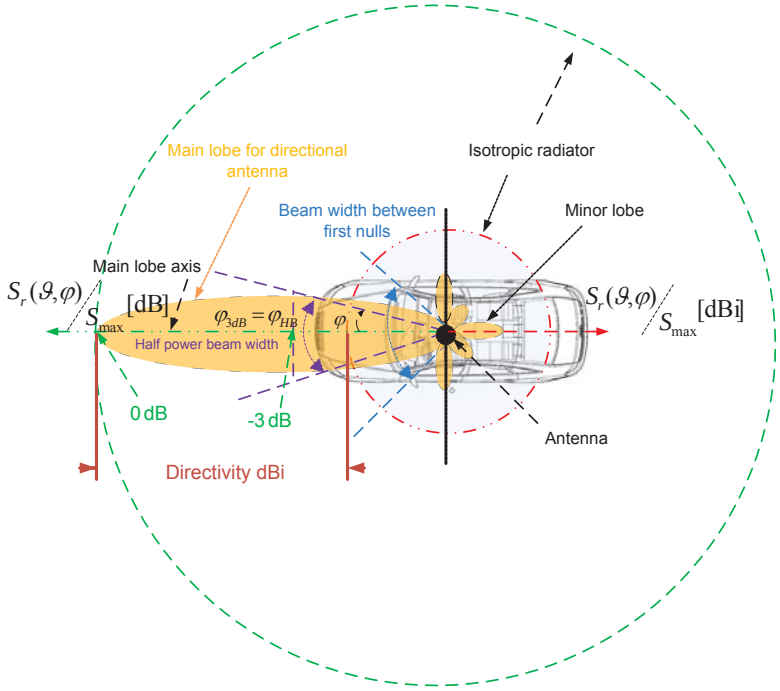

Figure 2.4: Definition of the radiation pattern for $\vartheta = 90°$.

Further information can be extracted from the presented figure like the radiation pattern *lobes,* where the antenna shows a good reception or emitting behaviour. It can be distinguished between *minor* and *main lobes.* Furthermore, we can define the *half power beam width* of the antenna pattern expressed in degrees, which gives the angle between the half power ($-3\,\text{dB}$) points of the main lobe referenced to the effective maximum radiated power of the main lobe. The antenna gain and directivity can also be extracted from the figure. The antenna gain value corresponds to the effective maximum radiated power density of the main lobe and can be given amongst others in [dB] or in [dBi].

To ensure the best possible antenna behaviour, the antenna system should have an acceptable return loss factor in the frequency range of interest. Usually engineers use $-8\,\text{dB}$ or $-10\,\text{dB}$ thresholds to define frequency ranges, where the investigated antennas deliver an acceptable return loss. However, in the automotive field, it is quite difficult to attain these values because of the very strict antenna styling criteria presented in Section 2.6. Antenna developers try to develop directional antennas depending on the antenna service of interest to ensure optimal reception or emission behaviour of the antenna system. Figure 2.5 shows three examples of different antenna radiation patterns depending on the different services. For example, for Car2Car or Car2infrastructure communications, the antenna radiation pattern should be optimized at elevations close to 90°. That means, the main lobes have to be oriented to the direction of the potential communication participants, in this case cars or infrastructure. However, it is almost impossible to avoid some minor lobes in undesirable directions.

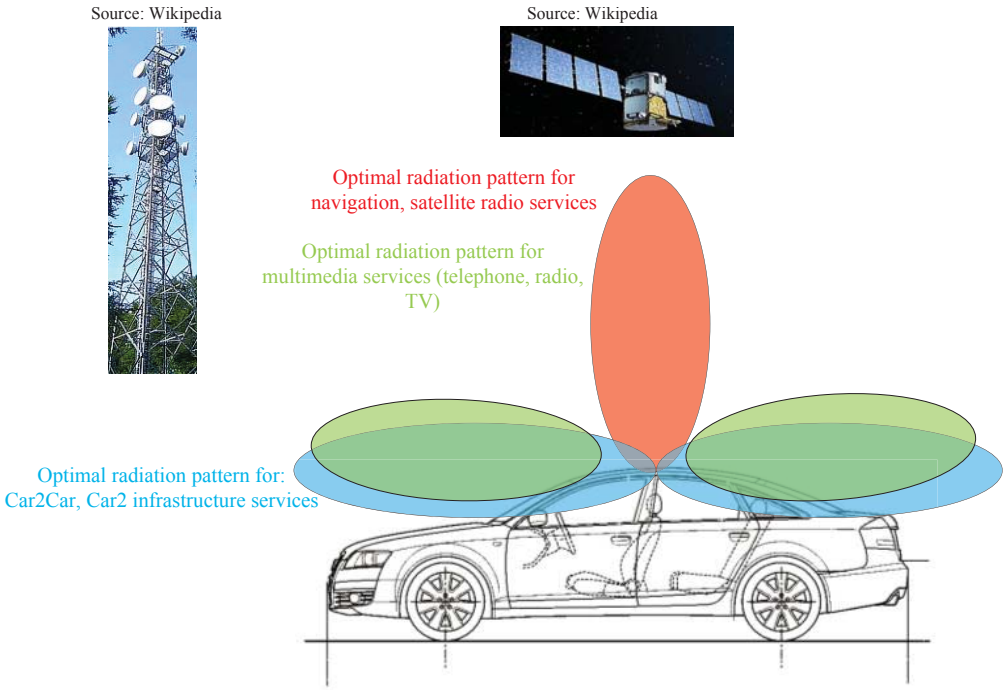

Figure 2.5: Optimal radiation patterns for different RF automotive services.

An ideal transmitting antenna is an antenna that can radiate the complete available power at its terminal without losses. In reality, a part of the available power will be transformed into thermal energy due to Ohmic and dielectric losses. Consequently, the effective radiated power P_R should be added to the dissipative power P_D to get the input power P_{in} according to equation (2.27). The *antenna efficiency* η is a parameter that describes the relationship between the input power P_{in} and the dissipative power P_D:

$$P_D = P_{in} - P_R = (1 - \eta)\, P_{in}\,. \tag{2.25}$$

Antenna efficiency can also be formulated with the *radiation resistance* R_E and the antenna Ohmic loss R_l according to

$$\eta = \frac{R_E}{R_E + R_l} = \frac{P_R}{P_{in}}\,. \tag{2.26}$$

The radiation resistance R_E in the equivalent circuit in Figure 2.1 transforms the available effective power P_A in radiation power P_R where

$$P_A = P_{in} - P_D = P_R \tag{2.27}$$

The dimension of the receiving or transmitting antenna area is important for the amount of the energy that can be radiated or received by the antenna. The parameter that describes this area is called the *antenna effective area* A_{eff} and is usually given in [m^2] [Ante 09]. It gives an equivalent area, which is orientated normally to the path of reception. The source of the

received signal is given in form of an incident electromagnetic wave with the radial radiation power density S_r according to

$$P_R = S_r \; A_{eff} \,. \tag{2.28}$$

The effective area also describes the receiving power, which an antenna can take out of the total incoming power of a certain electromagnetic power density. The effective aperture is normally smaller than the geometrical aperture and is related to the wavelength λ and the antenna gain G according to

$$A_{eff} = G \; \frac{\lambda^2}{4\pi} \,. \tag{2.29}$$

The pointing vector $\vec{S}$ is a vector that describes the radiation power flux [Kurz 08]. To determine $\vec{S}$ both the electric field $\vec{E}$ and the complex conjugate magnetic field $\vec{H}^*$ are needed according to

$$\vec{S} = \frac{1}{2}(\vec{E} \times \vec{H}^*) \,. \tag{2.30}$$

The radiation power density for an isotropic radiator can be calculated with

$$|\vec{S}| = S_i = \frac{P_R}{4\pi r^2} \,. \tag{2.31}$$

The *antenna directivity* is the quotient of the maximal radiation power density in a given direction of the antenna to the radiation power density of an isotropic radiator with the same radiating power [Wies 07a; Kark 04] according to

$$D_i = \frac{S_{r\ max}}{S_i} = 4\pi r^2 \frac{S_{r\ max}}{P_R} \,. \tag{2.32}$$

The *antenna gain* usually refers to the direction of the maximum radiation and is given as the quotient of the power required at the input of an ideal reference antenna without losses to the power supplied to the input of the real antenna in a given direction to produce the same field at the same distance [Wies 07a]. In the standards determined from the IEEE, if a direction is not fixed then the gain has to be given for the direction of the maximum radiation intensity. The antenna gain is often be expressed in [dBi], where the reference antenna is an isotropic lossless antenna. The gain can be expressed in [dBd] in cases, where a dipole antenna is used as reference antenna. Equation (2.32) makes it possible to calculate the gain including the Ohmic losses as a ratio of the maximum radiated power density in a certain direction to the average radiated power density of a spherical isotropic radiator with an input power equal to that of the antenna of interest. It is important to note that the gain does not give an amplification factor of the antenna. Gain gives a comparison of the power density of the antenna in a certain direction with the power density of an other reference radiator. The power, which is concentrated from the antenna in a certain direction is removed from other directions.
Normally, losses due to impedance and polarization mismatch are not accounted for the calculated antenna gain. The parameter that takes into account the impedance mismatch is the

realized gain $G_{realized}$, also called *practical gain*. This parameter combines the information of the return loss parameter and the normal antenna gain according to

$$G_{realized} = \left(1 - |S_{11}|^2\right) G\,. \tag{2.33}$$

Another parameter, which is quite often used is the ***A**ntenna **F**actor* (**AF**) [Joba 04]. It represents the ratio of the incident electric field E and the voltage V. This parameter can also be described with the wavelength and the realized gain for a 50Ω system [Bred 07] according to

$$AF = \frac{E}{U} = \frac{9.73}{\lambda\sqrt{G_{realized}}}\,. \tag{2.34}$$

The ***E**quivalent **I**sotropic **R**adiated **P**ower* (**EIRP**) is the product of the power supplied to the antenna and the antenna gain in a given direction relative to an isotropic antenna (absolute or isotropic gain):

$$EIRP = G\ P_{in}\,. \tag{2.35}$$

2.4 Improvement of the Signal Reception Quality

A communication system is composed of a transmitting and a receiving antenna, which are orientated towards each other to get the maximal gain in the direction of the partner. In regular reception mode, the propagation path of the signal between the communication partners is the line of sight. Both antenna systems are defined at a certain position. The maximal attainable signal transmission efficiency is calculated using *Friis Transmission formula* [Voge 04] according to

$$\frac{P_R}{P_{trans}} = \frac{A_{effrec}A_{efftrans}}{r^2\lambda^2} = \frac{G_R G_{trans}}{\left(4\pi r/\lambda\right)^2}\,. \tag{2.36}$$

The ratio of the receiving power P_R to the transmitted power P_{trans} depends on the wavelength λ, the distance between the two antennas r, the effective receiving antenna aperture A_{effrec} and the transmitting antenna aperture $A_{efftrans}$. The transmission formula can also be described using the gain of both receiving antenna G_R and transmitting antenna G_{trans}.

2.4.1 Multipath and Doppler Effect

In reality, antennas are often not fixed at a certain position. The direction of the incoming signal is usually unpredictable. Automotive antennas are especially challenging due to the fact that the car can be driven at different places like in cities, forests, highways or villages. Figure 2.6 illustrates an example of different signal propagation paths. When an **E**lectro**M**agnetic (**EM**) signal hits an object, different phenomena can occur [Povh 11; Kurz 08]:

- *Absorption*: The signal can be completely or partially absorbed by objects with high atom density and large surface cross-section.
- *Reflection*: The signal can be completely or partially reflected by objects such as buildings and metallic surfaces.
- *Scattering*: The signal can be scattered by objects with a small size or a rough surface. This happens depending on the wavelength for example when EM signals hit trees.
- *Diffraction*: This happens when a signal hits an edge or a wedge of an object.

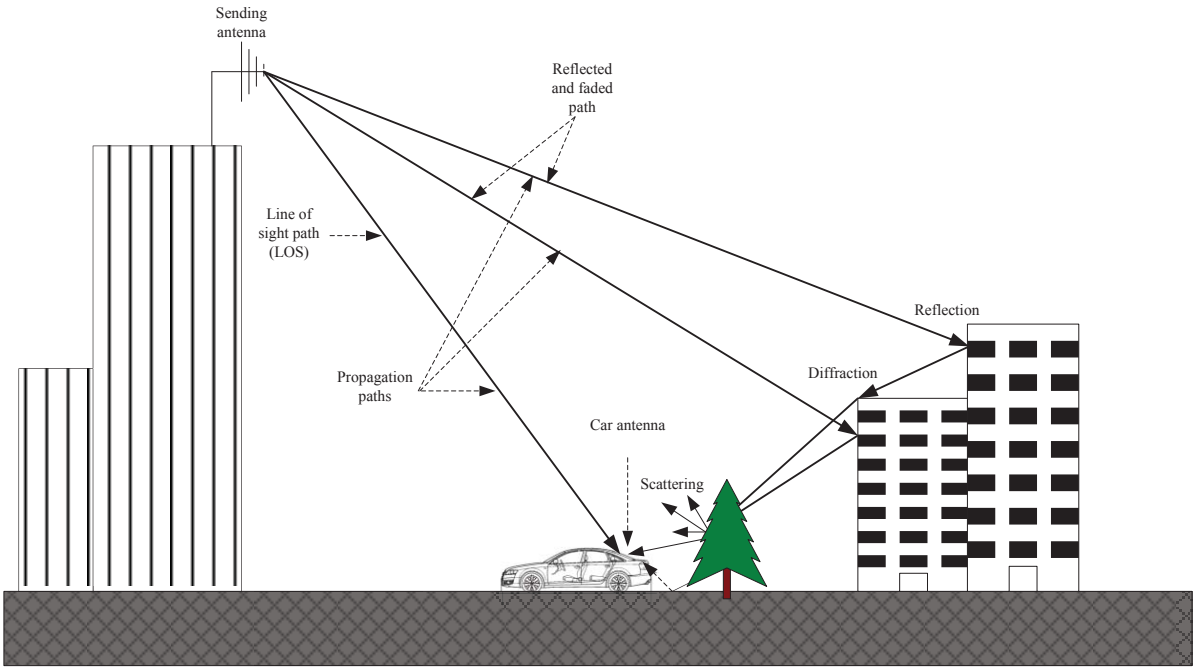

Figure 2.6: Different multipath propagation scenarios.

The car in Figure 2.6 receives all these signals overlaid on each other. In this case *multipath propagation* of the signal occurs. Depending on the signal interference type, the resulting transmitted signal may be stronger or weaker than the original transmitted signal. In the first case, *constructive interference* occurs and is responsible for the stronger signal. In the second case, the weaker is the signal due to *destructive interference*. In the case of a sent Dirac impulse δ, the resulting incoming signal $y(t)$ can be determined using

$$y(t) = \sum_{n=0}^{N-1} \rho_n e^{j\phi_n} \delta(t - \tau_n) \tag{2.37}$$

where τ_n is the delay of the nth incoming impulse, ρ_n is the amplitude amplification factor and ϕ_n represents the angular phase shift. From the presented formula, it can be seen that the

transmitted signal can be amplified or damped. The signal's angular phase can also be shifted. A further important phenomenon regarding signal propagation is the *Doppler effect*. This effect can occur if the sending and/or the receiving antenna are moved to each other or moved apart with a certain relative speed. Figure 2.7 illustrates a configuration of a moving antenna system mounted on a car with the ground speed v. The sending antenna is fixed at a certain position on ground.

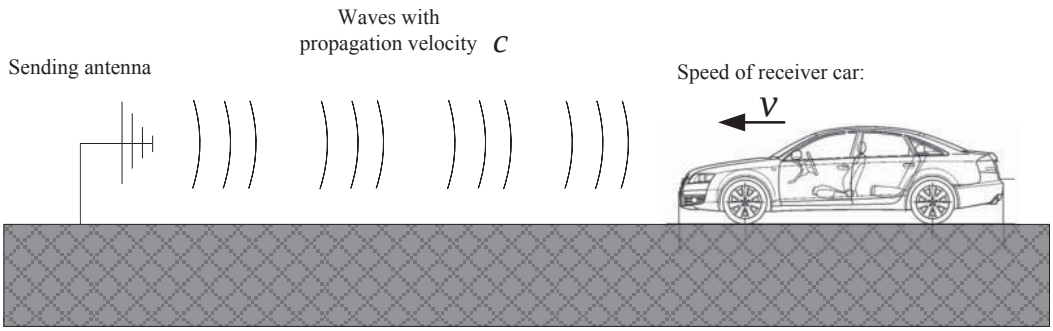

Figure 2.7: Doppler effect for moving car.

As a consequence, the frequency of the transmitted signal changes according to

$$\Delta f = \frac{v_R - v_S}{\lambda_0} = \frac{v_R - v_S}{c} f_0 \tag{2.38}$$

where Δf is the frequency difference between the signal's original frequency f_0 and the new frequency obtained due to the Doppler effect. v_R is the receiver antenna ground speed and v_S is the sending antenna ground speed. λ_0 is the free space wavelength. A combination of multipath and Doppler effects results in *fast fading* [Budd 11].

2.4.2 Diversity Systems

Optimal signal reception quality often necessitates antenna systems composed of more than one receiving antenna. In case of space diversity, the existence of several antennas with the same radiation pattern located in a distance of at least $\lambda/2$ improves the system reception behaviour. That means, if the sum of the transmitted signals does not reach the first antenna due to destructive interference, then the probability that these signals will not reach the other antennas is very small. Hence, the signal reception quality is ensured. *Diversity systems* are often utilized in antenna engineering to improve the signal reception quality [Wies 07a]. In antenna engineering, different types of diversity methods can be used. Figure 2.8 illustrates the most customary diversity methods such as polarization, code and frequency diversity. Each

method has its advantage and area of application. For automotive antennas, the most commonly used diversity systems are those based on pattern and space. On the one hand, the space diversity is quite often used for car antennas, where different antennas for the same RF service are located separately on different parts of the car (like on different glass windows). On the other hand, pattern diversity is a kind of beam forming illustrated in Figure 2.9 where radiation patterns of available receiving antennas for the same RF service are added in different manners to obtain the best possible system reception. Nowadays, analog and digital *beam forming* utilizing intelligent algorithms are used to ensure the best possible antenna receive pattern configuration [Rabi 10]. Such forming systems apply methods such as a *scan diversity* or *adaptive pattern diversity*. Figure 2.9 shows an example of a system composed of three antennas. Depending on the received signal the processor unit decides to use the sum or a part of the transmitted signals.

Phase compensation is used according to algorithms for adaptive patterns. In the last processing stage, the matching system is electronically adapted to the resulting system from the processor unit. In this way the best transmitted signal using all antennas is guaranteed.

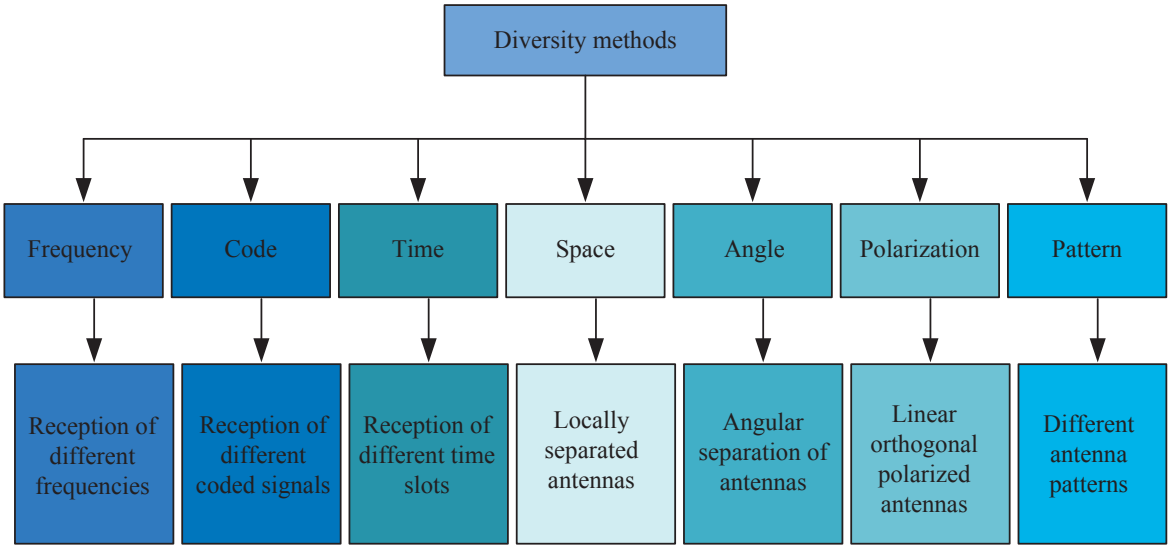

Figure 2.8: Diversity systems.

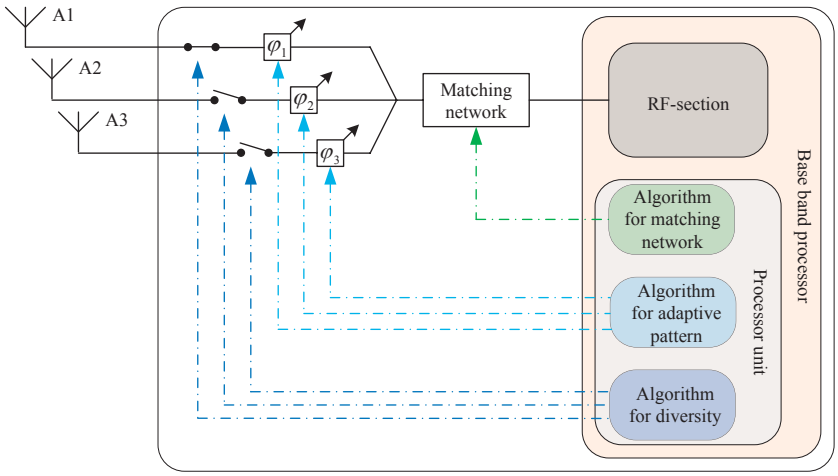

Figure 2.9: Adaptive pattern structure.

2.4.3 Multiple Input Multiple Output Systems

New telecommunication systems have improved the signal quality in terms of data rate. The currently available mobile communication standard named **L**ong **T**erm **E**volution (**LTE**) can reach effective download rates up to 100 **M**ega**b**it **p**er **s**econd (**Mbps**) and upload rates of 75 Mbps. Even the number of users for each available cell is higher than in older communication system standards like **UMTS** and can exceed a capacity of 200 active users per cell [Rabi 10]. The next mobile standard generation **LTE Extended** is even more promising and can reach effective download rates of 1 Gbps and improve cell capacity. The high data rate revolution in the communication systems mentioned can only be reached with the help of combination of the algorithm techniques in signal modulation according to Figure 2.10.

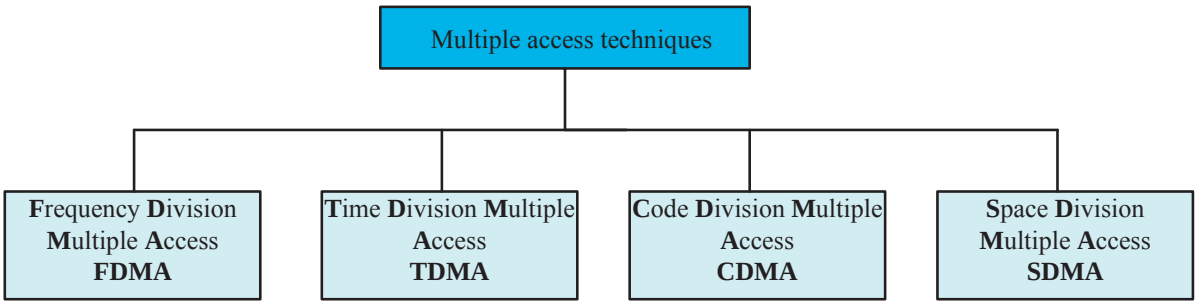

Figure 2.10: Multiple access techniques.

The new telecommunication system LTE uses in particular techniques based on **O**rthogonal **F**requency **M**ultiplexing methods and multiple antennas at both the transmitter and receiver side to increase the system performance in terms of transmitted signal energy. Figure 2.11

illustrates a simple example of a 3×3 MIMO system, where each transmitting antenna from the transmission system sends signals to each antenna of the receiver system. $\mathbf{T}$ is the matrix transmission coefficient between the two antenna systems.

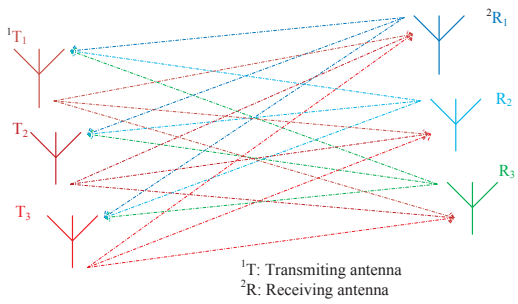

Figure 2.11: 3×3 MiMo system.

The spectral efficiency means how many bits per second per Hertz of bandwidth can be transmitted between two antenna systems. This can be improved by increasing the transmitted energy according to the *Claude Elwood Shannon* formula for **S**ingle **I**nput **S**ingle **O**utput (**SISO**) systems showing that a 3 dB increase in **S**ignal to **N**oise **R**atio (**SNR**) gives another bit/s/Hz efficiency [Wies 07b]

$$C = \log_2(1 + SNR|\mathbf{T}|^2)\,. \tag{2.39}$$

For a **M**ultiple **I**nput **M**ultiple **O**utput (**MIMO**) system with $M_{Tx} = M_{Rx} = M$ transmitting and emitting antennas, the antenna capacity grows linearly with large M according to

$$C = \log_2\{det(\mathbf{I}_{M\times N} + \frac{SNR}{M}\mathbf{T}_{M\times N}\mathbf{T}^*_{M\times N})\} \tag{2.40}$$

with $\mathbf{T}$ is the matrix transmission coefficient and $\mathbf{T}^*$ is the matrix transmission coefficient conjugate transposed and $\mathbf{I}$ is the unit matrix [Wies 07a].

2.5 Antenna Correlation

In order to evaluate diversity systems, the cross-correlation between the individual far field radiation patterns is evaluated [Lind 00; Reit 99]. Far field radiation pattern data are complex values, so, cross-correlation of the far field radiation patterns should take into account both amplitude and phase information. The general mathematical formula to calculate cross-correlation between two functions $x(t)$ and $y(t)$ is defined by [Grun 08]

$$\langle x(t) \star y(t)\rangle = \int_{-\infty}^{\infty} x(\tau)\; y(t+\tau)^* \mathrm{d}\tau \tag{2.41}$$

where $y^*(t)$ denotes the complex conjugate of the function $y(t)$ and τ is a time step. The normalized scalar product $c_{x,y}$ of both functions is given by

$$c_{x,y} = \frac{\langle x(t) \star y(t) \rangle}{\sqrt{\int\limits_{-\infty}^{\infty} |x(t)|^2 \mathrm{d}t} \sqrt{\int\limits_{-\infty}^{\infty} |y(t)|^2 \mathrm{d}t}} \,. \tag{2.42}$$

The application of equation (2.41) on the electric field functions $E_1(\varphi, \vartheta, f)$ and $E_2(\varphi, \vartheta, f)$ leads to the following formula

$$c_{1,2} = \frac{\int\limits_{\varphi=0}^{\varphi=2\pi} E_1(\varphi, \vartheta, f)\ E_2(\varphi, \vartheta, f)^* \mathrm{d}\varphi}{\sqrt{\int\limits_{\varphi=0}^{\varphi=2\pi} |E_1(\varphi, \vartheta, f)|^2 \mathrm{d}t} \sqrt{\int\limits_{\varphi=0}^{\varphi=2\pi} |E_2(\varphi, \vartheta, f)|^2 \mathrm{d}t}} \,. \tag{2.43}$$

Both functions depends of the frequency and of the angles φ and ϑ. φ is a function of the azimuth angle going from 0° to 360° and ϑ is the elevation angle. For automotive applications, correlation functions are considered only at certain elevation angles such as close to 90° for multimedia systems, where antennas should be optimized as shown in Figure 2.5. The angle φ is discretized in n steps starting from 1 to n_{max}. Besides, the correlation coefficient is split into two parts. The real part is described by

$$C_{\mathrm{Re1,2}}|_{f=const.} = \sum_{n=1}^{n=n_{\max}} (E_{\mathrm{Re1}}(n)\ E_{\mathrm{Re2}}(n)) + (E_{\mathrm{Im1}}(n)\ E_{\mathrm{Im2}}(n)) \tag{2.44}$$

and the imaginary part is given by

$$C_{\mathrm{Im1,2}}|_{f=const.} = \sum_{n=1}^{n=n_{\max}} (E_{\mathrm{Re2}}(n)\ E_{\mathrm{Im1}}(n)) - (E_{\mathrm{Re1}}(n)\ E_{\mathrm{Im2}}(n)) \,. \tag{2.45}$$

The amplitude of the correlation factor is then given by

$$|C_{1,2}| = \sqrt{{C_{\mathrm{Re1,2}}}^2 + {C_{\mathrm{Im1,2}}}^2} \,. \tag{2.46}$$

The correlation factor can be normalized by introducing the normalization factor N described by

$$N = \sqrt{\left(\sum_{n=1}^{n=n_{\max}} \left[(E_{\mathrm{Re1}}(n))^2 + (E_{\mathrm{Im1}}(n))^2\right]\right) \left(\sum_{n=1}^{n=n_{\max}} \left[(E_{\mathrm{Re2}}(n))^2 + (E_{\mathrm{Im2}}(n))^2\right]\right)} \,. \tag{2.47}$$

The normalized correlation factor is usually given in percent as

$$|c_{1,2}|_N[\%] = \frac{|C_{1,2}|}{N}\ 100\% \,. \tag{2.48}$$

In order to demonstrate the application of the correlation factor, two printed antennas on the rear window of an AUDI A5 car are investigated. Both antennas operate in the FM frequency range. Figure 2.12 presents both investigated antennas.

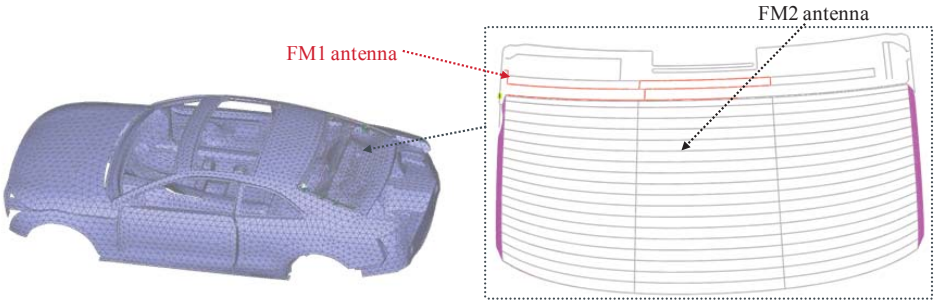

Figure 2.12: FM1 and FM2 antenna of an AUDI A5 car.

It is very difficult to decide if one or two or even more antennas are needed to ensure the optimal antenna reception characteristic without using the correlation factor. The depicted correlation coefficient curve of both antenna systems in Figure 2.13 presents an objective evaluation value for the antenna radiation pattern decorrelation. The correlation coefficient is usually given for both vertical and horizontal polarization. As an empiric value, two antenna systems are well decorrelated when the correlation factor is below 40%. It is advisable to use diversity systems only if the mentioned rule is fulfilled.

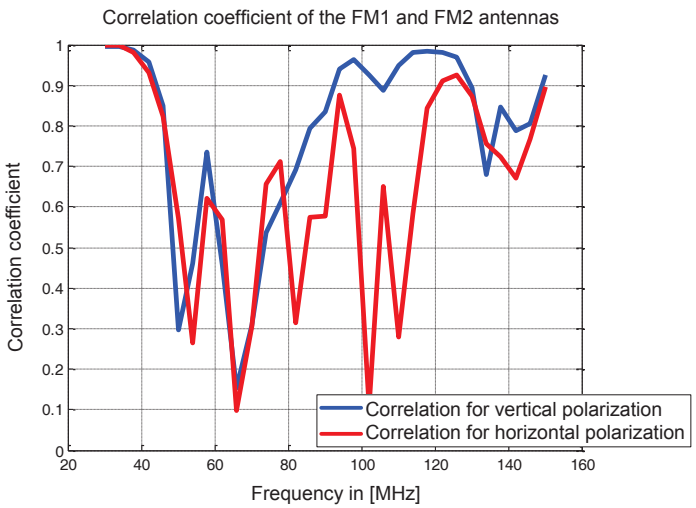

Figure 2.13: Computed correlation factor c_{12} of the two FM antennas according to Figure 2.12.

2.6 Styling Criteria

The most inconvenient criteria for automotive antenna development are those relating to the styling. The Antenna Department should always coordinate the antenna design with the

Styling Department to avoid any customer displeasure. This restricts the antenna engineer's development freedom. Since some styling rules have been established, it is possible to start early with the initial antenna draft.
Figure 2.14 shows some antenna types used in two different AUDI cars.

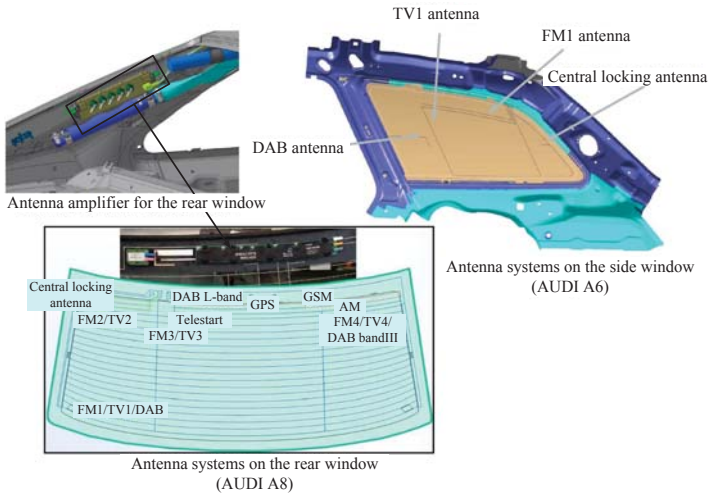

Figure 2.14: Automotive antenna glass system [AUDI AG].

As shown in the figure, most of the antennas are printed on the rear window. It is very important to keep the heating structure used for window defrosting. A further important parameter is the visual symmetry. Antennas should be as unobtrusive as possible. For an optimal positioning of the antennas on the windscreen, developers should consider the position of the antenna amplifiers. In the upper left of the figure, an example can be seen of an antenna amplifier located on the car C-pillar connected to four different antennas. On the side window different antennas for TV, FM, central locking and DAB services are printed. It is important in this case to use simple and not arbitrary forms of antenna structures. Some optimal designs created with computational algorithms and suggested in literature may not be acceptable for reasons of styling. It is also important that the antenna terminals are very close to the antenna amplifier position to avoid any signal damping and noise due to long connection pigtails.

2.7 Electromagnetic Compatibility Mechanisms

In order to ensure the best possible service quality, antenna engineers should take into account all neighbour systems of an antenna during the development process. EMC aspects become increasingly important in the automotive field due to the ever more complex systems. Electric components close to the antennas have to be considered in measurements due to their potential

influence on the antenna reception behaviour. Antennas can also be considered as susceptible devices due to indirect coupling of interference signals from other electric components [Domi 92; Gebe 03; Kais 05]. Because of this, antennas should have acceptable characteristics only in the frequency range of interest to prevent such scenarios from occurring. In this section, a short overview of EMC aspects in antenna development is presented.

2.7.1 Operation Model of an Electric Monopole

Electric monopole antennas are often used as automotive antennas for radio reception in LW/MW and USW frequency range. These antennas are usually mounted on the car roof and they are very sensitive to EM waves especially at low frequencies (LW/MW). One way to predict the EMC behaviour of these antennas is using antenna equivalent circuits. Figure 2.15 shows an example of a monopole antenna mounted on a car roof and its equivalent circuit.

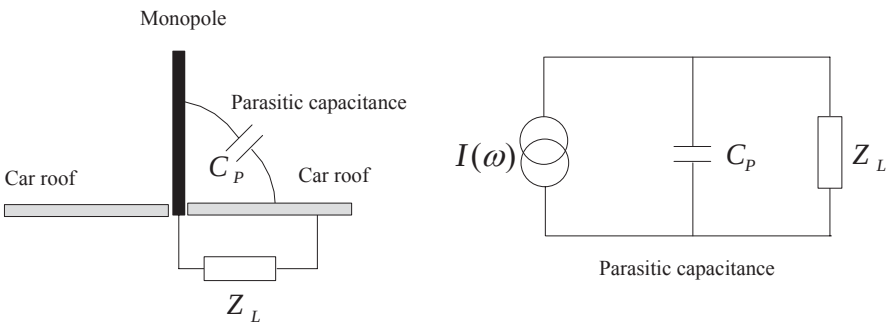

Figure 2.15: A monopole antenna mounted on a car roof and its equivalent circuit.

Electromagnetic waves with the displacement current density D induce electrical charges in the monopole. The induced current flows through the impedance Z_L and the parasitic capacitance C_P to the car roof. The car roof is considered as reference ground for the monopole antenna. The induced current can be calculated according to

$$I(\omega) = j\omega D A_{eff} \tag{2.49}$$

with the displacement current density D given by

$$D = \varepsilon_0 \varepsilon_r E = \varepsilon E \tag{2.50}$$

and

$$\omega = 2\pi f \tag{2.51}$$

where ε_0 is the vacuum permittivity, ε_r is the relative material permittivity and f is the frequency. The effective aperture surface A_{eff} is given as a relationship between the parasitic capacitance C_P and the antenna height h as [Frei 09; Tazi 08]

$$A_{eff} = \frac{C_p}{\varepsilon_0} \frac{h}{2} . \tag{2.52}$$

The parasitic capacitance C_P can be described with both antenna dimensions, the antenna height h and the radius r of the monopole by

$$C_p = \frac{2\pi\varepsilon_0 h}{\ln(h/r) - 1} . \tag{2.53}$$

2.7.2 EMC Coupling Mechanisms in Vehicles

In the automotive field different kinds of coupling can occur between an interference source and a susceptible device [Gebe 03; Domi 92; Schw 07]. In general, it can be distinguished between inductive, capacitive and galvanic coupling.

- *Capacitive coupling* occurs when electric energy is transmitted from system 1 to another system 2 through the electric capacitance existent between the two systems. This capacitance is due to the potential difference between the two systems.
- *Inductive coupling* occurs when the energy between an interference source and a susceptible device is transmitted due to the magnetic field between the two systems.
- *Conductive coupling* occurs when the current of the two systems flows through a common impedance. This common impedance is usually a common reference conductor.
- *Radiative coupling* occurs when the two systems are in a distance larger than one wavelength. The two systems act as antennas, where the susceptible device receives EM waves from the interference source.

To analyze the capacitive and the inductive coupling, the equivalent circuit represented in Figure 2.16 can be used. The electric coupling in this case is represented by the current source I_C due to the coupling capacitance C_C between the source and the susceptible device. The current I_C is given as

$$I_C = j\omega C_C U_T . \tag{2.54}$$

The magnetic coupling given by the inductance M is represented by the voltage source with

$$U_C = j\omega M I_T . \tag{2.55}$$

I_T represents the current source and M is the coupling inductance between the source and the susceptible device represented in U_C.

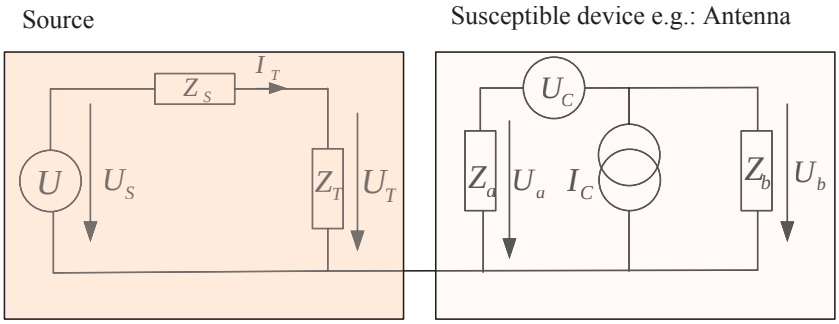

Figure 2.16: Equivalent circuit for the combined electric and magnetic coupling.

For the calculation of the voltage U_a on the impedance Z_a and U_b on the impedance Z_b, respectively, equation (2.56) and equation (2.57) can be applied:

$$U_b = \frac{Z_b}{Z_a + Z_b} \frac{U_S}{Z_s + Z_T} (j\omega C_c Z_a Z_T - j\omega M)\,, \tag{2.56}$$

$$U_a = \frac{Z_a}{Z_a + Z_b} \frac{U_S}{Z_s + Z_T} (j\omega C_c Z_b Z_T - j\omega M)\,. \tag{2.57}$$

Both coupling parameters, capacitance and inductance can be calculated analytically or approximated numerically [Schw 07].

Figure 2.17 shows an example of a direct capacitive coupling from wire 2 to the car antenna integrated in the rear window. Besides that, it can be seen in the same figure that an inductive coupling from wire 1 to wire 2 occurs to the car antenna, an indirect coupling from wire 1 to the car antenna. A multiple coupling system results when all presented coupling types are taken into account at the same time.

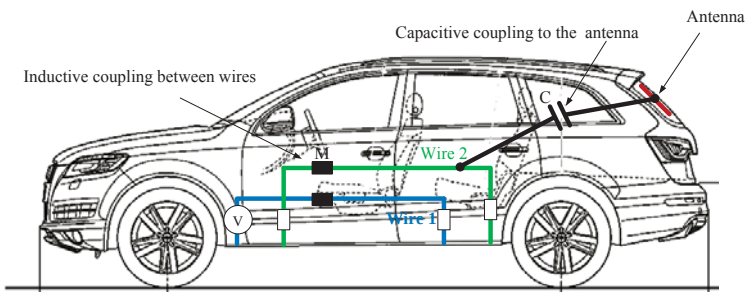

Figure 2.17: Direct and indirect coupling between wires and car antenna.

3 Numerical Approaches for Automotive Antenna Computation

James Clerk Maxwell's equations [Cler 65] represent a summary and a completion of the most important mathematical formulations related to electromagnetics such as those by Faraday and Ampere. In essence, Maxwell expanded these formulations in order to make it possible to describe all electromagnetic phenomena. Maxwell's equations can be described in both the time and the frequency domain. An overview of Maxwell's equations in both domains is given in this chapter.

In Chapter 1, multiple automotive antennas operating in various frequency ranges were presented. The frequency ranges used start from some kHz up to approximately 100 GHz. One challenge of antenna engineering is to generate virtual models of the vehicle and antenna system early enough to be able to make important decisions concerning the antenna performance and the complete EMC aspects for the complete car at an early stage of development. The computation of the electromagnetic characteristics of the different antennas requires the solution of Maxwell's equations. In several problem cases, the solution is achieved using different numerical approaches. In recent years, automotive engineering has taken advantage of the capabilities of computers and used them to solve very large matrix equations. Deploying numerical techniques, radiation and scattering problems can be calculated as shown in this chapter.

3.1 Fundamentals of Electromagnetics

The original form of Maxwell's equations is given in integral form. However, it is possible to write them using the field theory in differential form, too. Another differentiation can be done if these equations are given in the time or the frequency domain.

3.1.1 Field Theory

The field theory is used to describe EM fields relationships [Povh 11]. It gives amongst others, relations between scalar quantities and vectors. The divergence of a vector $\vec{D}$ gives a measure

of the source strength at a space point and it is calculated with the "Nabla" operator ∇ for the Cartesian coordinates x, y, z as

$$\operatorname{div}\vec{D} = \nabla \cdot \vec{D} = \frac{\partial D_x}{\partial x} + \frac{\partial D_y}{\partial y} + \frac{\partial D_z}{\partial z}\,. \tag{3.1}$$

The gradient of a scalar field Φ is a vector that shows in the direction of the strongest change of this scalar field and can be calculated according to

$$\operatorname{grad}\Phi = \nabla\Phi = \frac{\partial \Phi}{\partial x}\vec{e}_x + \frac{\partial \Phi}{\partial y}\vec{e}_y + \frac{\partial \Phi}{\partial z}\vec{e}_z\,. \tag{3.2}$$

The rotation of a vector $\vec{D}$ gives a measure of the field rotation and can be calculated as

$$\operatorname{rot}\vec{D} = \nabla \times \vec{D} = \left(\frac{\partial D_z}{\partial y} - \frac{\partial D_y}{\partial z}\right)\vec{e}_x + \left(\frac{\partial D_x}{\partial z} - \frac{\partial D_z}{\partial x}\right)\vec{e}_y + \left(\frac{\partial D_y}{\partial x} - \frac{\partial D_x}{\partial y}\right)\vec{e}_z\,. \tag{3.3}$$

The divergence of the gradient of a scalar quantity Φ is given by

$$\operatorname{div}\operatorname{grad}\Phi = \nabla \cdot \nabla\Phi = \nabla^2\Phi = \Delta\Phi = \frac{\partial^2 \Phi}{\partial x^2} + \frac{\partial^2 \Phi}{\partial y^2} + \frac{\partial^2 \Phi}{\partial z^2}\,. \tag{3.4}$$

The divergence of rotation of a vector $\vec{V}$ is equal to 0 according to due to the fact that in homogeneous field the rotation is equal to 0 because all field lines are parallel to each other.

$$\operatorname{div}\operatorname{rot}\vec{V} = 0\,. \tag{3.5}$$

Similar to the previous equation

$$\operatorname{rot}\operatorname{grad}\Phi = 0 \tag{3.6}$$

can be given.

One important result of vector analysis is described in Gauss's theorems, which give a relationship between surface and volume integrals [Kuli 09]. With help of Gauss's theorems, it is possible to rewrite some mathematical formulations, described in differential form, in integral form and vice versa. The *Gauss's first theorem*

$$\iiint\limits_V \operatorname{grad}\Phi(\vec{r})\mathrm{d}V = \oiint\limits_A \Phi(\vec{r})\mathrm{d}\vec{A} \tag{3.7}$$

states that the surface integral of a scalar quantity Φ over a closed surface A can be replaced with a volume integral of the gradient of the scalar quantity Φ over the volume V that encloses the surface A. The *Gauss's second theorem*

$$\oiint\limits_A \vec{D}(\vec{r}) \cdot \mathrm{d}\vec{A} = \iiint\limits_V \operatorname{div}\vec{D}(\vec{r})\mathrm{d}V \tag{3.8}$$

states that the scalar surface integral over a closed surface A is equal to the volume integral of the appropriate scalar field $\operatorname{div}\vec{D}$ over the volume V that encloses the surface A. $\vec{r}$ is the position vector. The *Gauss's third theorem*

$$\oiint\limits_A \mathrm{d}\vec{A} \times \vec{D}(\vec{r}) = \iiint\limits_V \operatorname{rot}\vec{D}(\vec{r})\mathrm{d}V \tag{3.9}$$

states that the vectorial surface integral of the vector field $\vec{D}$ over a closed surface A is equal to the volume integral of the appropriate rotation of the field $\operatorname{rot}\vec{D}$ over the volume V that encloses the surface A.
Stoke's equations result from differential geometry and describe the relationship between line and surface integrals. Also, based on the Stoke's theorems, it is possible to rewrite some mathematical formulations, described in differential form, in integral form and vice versa [Kuli 09]. The *Stoke's first theorem*

$$\oint_S \Phi \, \mathrm{d}\vec{s} = \iint_A \mathrm{d}\vec{A} \times \operatorname{grad}\Phi \tag{3.10}$$

states that a line integral of a scalar quantity Φ along a curve s is equal to the vectorial surface integral of the appropriate gradient field $\operatorname{grad}\Phi$ over an arbitrary surface A limited by the curve s. The *Stoke's second theorem*

$$\oint_S \vec{D}\vec{ds} = \iint_A \operatorname{rot}\vec{D} \cdot \mathrm{d}\vec{A} \tag{3.11}$$

states that a line integral of a vector $\vec{D}$ along a closed curve s is equal to the surface integral of the appropriate vector field $\operatorname{rot}\vec{D}$ over an arbitrary surface A limited by the curve s [Kuli 09].

3.1.2 Time Domain Description of Maxwell's Equations

The *Maxwell's first equation* is the extension of Ampere's law with the displacement current. The resulting Maxwell-Ampere law can be written in differential form and in time domain as

$$\operatorname{rot}\vec{H}(\vec{r}) = \nabla \times \vec{H}(\vec{r}) = \vec{J}(\vec{r}) + \frac{\partial \vec{D}(\vec{r})}{\partial t}\,, \tag{3.12}$$

where $H(\vec{r})$ is the magnetic field, $J(\vec{r})$ is the current density and $D(\vec{r})$ is the displacement current density. $\vec{r}$ represents the position vector and ∂t is the time step. The application of Stoke's first theorem on equation (3.12) gives the integral form of the equation in form of

$$\oint_l \vec{H} \cdot \mathrm{d}\vec{l} = \iint_A \left(\vec{J} + \frac{\partial \vec{D}}{\partial t}\right) \cdot \mathrm{d}\vec{A}\,. \tag{3.13}$$

The *Maxwell's second equation* is originally Faraday's law of induction. The resulting induction law can be written in differential form and in the time domain as

$$\operatorname{rot}\vec{E}(\vec{r}) = \nabla \times \vec{E}(\vec{r}) = -\frac{\partial \vec{B}(\vec{r})}{\partial t} - \vec{J_m}(\vec{r}) + \operatorname{rot}(\vec{v} \times \vec{B})\,, \tag{3.14}$$

where $E(\vec{r})$ is the electric field, $B(\vec{r})$ is the magnetic flux density and $\vec{J}_m(\vec{r})$ is the magnetic current density. $\vec{v}$ represents the velocity. The application of Stoke's first theorem (3.10) on

the differential form of Maxwell's second equation gives the integral form of the equation by neglecting the magnetic current density $\vec{J}_m(\vec{r})$

$$\oint_{\partial A} \vec{E} \cdot \mathrm{d}\vec{l} = -\iint_A \frac{\partial \vec{B}}{\partial t} \cdot \mathrm{d}\vec{A} + \oint_{\partial A} (\vec{v} \times \vec{B}) \cdot \mathrm{d}\vec{l}. \tag{3.15}$$

In the case of static objects, the second term in the equation with the velocity $\vec{v}$ will disappear and the equation can be simplified to

$$\oint_{\partial A} \vec{E} \cdot \mathrm{d}\vec{l} = -\iint_A \frac{\partial \vec{B}}{\partial t} \cdot \mathrm{d}\vec{A}. \tag{3.16}$$

The simplified equation can also be given in differential form as

$$\mathrm{rot}\, \vec{E}(\vec{r}) = \nabla \times \vec{E}(\vec{r}) = -\frac{\partial \vec{B}(\vec{r})}{\partial t}\,. \tag{3.17}$$

The *Maxwell's third equation* is in fact time and frequency independent. The formulation was first described in Gauss's law and says that the electrical charges represented by the electrical charge density ρ_e act as the source of the displacement current field $\vec{D}$. The differential form of the Gauss's law or Maxwell's third equation is given by

$$\nabla \cdot \vec{D}(\vec{r}) = \varepsilon \nabla \cdot \vec{E}(\vec{r}) = \rho_e(\vec{r})\,. \tag{3.18}$$

It should be noted that the material parameters (permittivity ε, permeability μ and resistivity ρ) used in this section in Maxwell's equations are assumed to be constant. The application of Gauss's first theorem (3.7) on the differential form of Maxwell's third equation gives the integral form of the equation in form of

$$\oiint_{\partial V} \vec{D} \cdot \mathrm{d}\vec{A} = \iiint_V \rho_e \,\mathrm{d}V = Q(V). \tag{3.19}$$

where V is the volume and $Q(V)$ is the electric charge. The *Maxwell's fourth equation*

$$\nabla \cdot \vec{B}(\vec{r}) = \mu \nabla \cdot \vec{H}(\vec{r}) = \rho_m(\vec{r}) \tag{3.20}$$

is given by Gauss's law for magnetic fields and is also time and frequency independent. The formulation says that the magnetic charges ρ_m act as sources for the magnetic flux density $\vec{B}$. The application of Gauss's theorem on the differential form of Maxwell's fourth equation gives the integral form of the equation

$$\oiint_{\partial V} \vec{B} \cdot \mathrm{d}\vec{A} = \iiint_V \rho_m \mathrm{d}V = Q_m(V)\,. \tag{3.21}$$

where $Q_m(V)$ is the magnetic charge.

3.1.3 Frequency Domain Description of Maxwell's Equations

The frequency formulation is essential for the electromagnetic description for several numerical simulation approaches, where the equations are given only in frequency domain. The angular velocity ω deduced from the frequency formula $2\pi f$ is used for this purpose. Maxwell's first equation in differential form and in the frequency domain can be written as

$$\nabla \times \vec{H}(\vec{r}) = \vec{J}(\vec{r}) + j\omega\vec{D}(\vec{r})\,. \tag{3.22}$$

Maxwell's second equation for static objects in differential form and in frequency domain can be expressed as

$$\nabla \times \vec{E}(\vec{r}) = -j\omega\vec{B}(\vec{r}) - \vec{J_m}(\vec{r})\,. \tag{3.23}$$

3.1.4 Time Domain and Frequency Domain Transformation

Maxwell's equations are given in **F**requency **D**omain (**FD**) and in the **T**ime **D**omain (**TD**). Depending on the antenna structure and the frequency range, it is expedient to use it in one and not in the other domain.
Simulations in the frequency domain are realized for each frequency and require often the same computation time for each frequency point. The system answer is computed by The excitation is often a δ-gap signal.

$$H(f) = \frac{O(f)}{I(f)} \tag{3.24}$$

accordingly to the basics in system theory with the transfer function $H(f)$, the input signal $I(f)$ and the output signal $O(f)$ [Rao 10].
$O(f)$ is equal to the transfer equation $H(f)$ when the input signal is equal to a jump function $I(f) = \Gamma(f)$.
The system answer $o(t)$ of an arbitrary input signal $i(t)$ can be calculated based on the impulse answer $h(t)$ according to

$$o(t) = \int_{-\infty}^{+\infty} i(\tau)\; h(t-\tau)\; \mathrm{d}\tau = \int_{-\infty}^{+\infty} i(t-\tau)\; h(\tau)\; \mathrm{d}\tau\,. \tag{3.25}$$

Calculations in time domain are based on the convolution [Rao 10] according to

$$o(t) = h(t) * i(t) \tag{3.26}$$

where $*$ is the convolution operator, $i(t)$ is input time dependent signal , $o(t)$ is output signal and $h(t)$ is the system answer.

Simulations in time domain are usually realized by feeding the investigated system with an excitation, often a Gaussian function in the form of energy. once the energy is completely absorbed from the system, The system answer can be calculated. The transition from the time domain to the frequency domain and vice versa is done based on the **F**ourier **T**ransformation (**FT**) [Rao 10].

3.1.5 Wave Equations for Electric and Magnetic Fields

The wave equation for a linear, source-free, homogeneous and isotropic medium can be deduced from the simplified second equation (3.17). Applying the curl on both sides of the equation leads to

$$\nabla \times \nabla \times \vec{E}(\vec{r}) = -\mu \frac{\partial}{\partial t}(\nabla \times \vec{H}(\vec{r}))\,, \tag{3.27}$$

and since $\vec{J}(\vec{r}) = 0$

$$\nabla \times \vec{H}(\vec{r}) = \varepsilon \frac{\partial \vec{E}(\vec{r})}{\partial t}\,. \tag{3.28}$$

We get

$$\nabla \times \nabla \times \vec{E}(\vec{r}) = -\mu\varepsilon \frac{\partial^2 \vec{E}(\vec{r})}{\partial t^2}\,. \tag{3.29}$$

The wave equation for electric fields can be written as

$$\nabla^2 \vec{E}(\vec{r}) + \mu\varepsilon \frac{\partial^2 \vec{E}(\vec{r})}{\partial t^2} = 0\,. \tag{3.30}$$

Similar to equation (3.30), the wave equation for magnetic fields can be written as

$$\nabla^2 \vec{H}(\vec{r}) + \mu\varepsilon \frac{\partial^2 \vec{H}(\vec{r})}{\partial t^2} = 0\,. \tag{3.31}$$

3.1.6 Material Equations

Every medium has material parameters (ε, μ and ρ), which are very important for analyzing the electromagnetic wave propagation in this medium. Generally, it can be said that the medium is *linear* if these parameters are independent of the electric field $\vec{E}$ and the magnetic field $\vec{H}$. The medium is *homogeneous* if these parameters are not functions of space variable [Chen 90; Chew 90]. The medium can be *isotropic* if the parameters are independent of the direction (scalars) [Kolu 02]. Usually all these parameters are *frequency dependent* and should accordingly be considered in Maxwell's equations in the frequency domain.

The speed of light in a material c is controlled by the speed of light in free space c_0 and by the material permittivity ε_r and permeability μ_r according to

$$c = \frac{c_0}{\sqrt{\varepsilon_r \mu_r}} \,. \tag{3.32}$$

The speed of light in a vacuum is defined as

$$c_0 = \frac{1}{\sqrt{\varepsilon_0 \mu_0}} \,. \tag{3.33}$$

The electric permittivity ε in materials is given as a relationship between the electric permittivity in free space ε_0 and the relative electric permittivity of the material ε_r according to

$$\varepsilon = \varepsilon_0 \varepsilon_r \,. \tag{3.34}$$

In electromagnetism, *four* material equations are taken into account. *The first one* describes the dependence of the displacement current density $\vec{D}(\vec{r})$ on electric permittivity ε and the electric field $\vec{E}(\vec{r})$ as

$$\vec{D}(\vec{r}) = \varepsilon \vec{E}(\vec{r}) \tag{3.35}$$

where $\vec{r}$ is the position vector. The *second material equation* describes the dependence of the magnetic flux density $\vec{B}(\vec{r})$ on permeability μ and the magnetic field $\vec{H}(\vec{r})$ according to

$$\vec{B}(\vec{r}) = \mu \vec{H}(\vec{r}) \,. \tag{3.36}$$

The permeability μ of a material is given as the relationship between permeability in free space μ_0 and the relative permeability of the material as

$$\mu = \mu_0 \mu_r \,. \tag{3.37}$$

The *third material equation* describes the dependence of the current density $\vec{J}(\vec{r})$ on the electric conductivity σ_e and the electric field strength $\vec{E}(\vec{r})$ according to

$$\vec{J}(\vec{r}) = \sigma_e \vec{E}(\vec{r}) \,. \tag{3.38}$$

The *fourth material equation* is similar to the previous formulation and describes the dependence of the magnetic current density $\vec{J}_m(\vec{r})$ on the specific magnetic conductivity σ_m and the magnetic field $\vec{H}(\vec{r})$ according to

$$\vec{J}_m(\vec{r}) = \sigma_m \vec{H}(\vec{r}) \,. \tag{3.39}$$

3.1.7 Boundary Conditions

Figure 3.1 shows the transition between two different media 1 and 2, with parameters $(\varepsilon_1, \mu_1, \rho_1)$ and $(\varepsilon_2, \mu_2, \rho_2)$, respectively. At the transition region, boundary conditions should be determined. From Maxwell's equations, the following boundary condition formulations [Karl 09] can be derived.

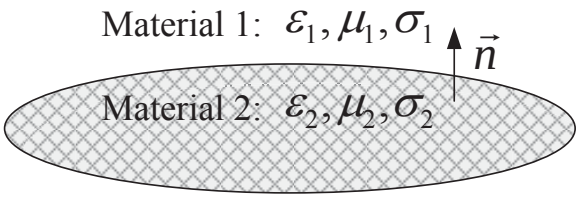

Figure 3.1: Transition between two media with different material parameters.

The *first equation*

$$\vec{n}(\vec{r}) \cdot \left(\vec{B}_1(\vec{r}) - \vec{B}_2(\vec{r})\right) = \left(\vec{B}_{1N}(\vec{r}) - \vec{B}_{2N}(\vec{r})\right) = \rho_{mA}(\vec{r}) \tag{3.40}$$

describes the relationship between the normal magnetic components at the boundaries of the two materials $\vec{B}_{1N}(\vec{r})$ and $\vec{B}_{2N}(\vec{r})$, respectively. $\vec{n}(\vec{r})$ is the surface normal vector on the boundary between the two media 1 and 2. $\rho_{mA}(\vec{r})$ is a surface magnetic charge density.
The *second equation*

$$\vec{n}(\vec{r}) \cdot \left(\vec{D}_1(\vec{r}) - \vec{D}_2(\vec{r})\right) = \left(\vec{D}_{1N}(\vec{r}) - \vec{D}_{2N}(\vec{r})\right) = \rho_A(\vec{r}) \tag{3.41}$$

describes the relationship between the displacement current field normal components at the boundaries of the two materials $\vec{D}_{1N}(\vec{r})$ and $\vec{D}_{2N}(\vec{r})$, respectively. $\rho_A(\vec{r})$ is a surface electric charge density.
The *third equation*

$$\vec{n}(\vec{r}) \times \left(\vec{E}_1(\vec{r}) - \vec{E}_2(\vec{r})\right) = \left(\vec{E}_{1tan}(\vec{r}) - \vec{E}_{2tan}(\vec{r})\right) = -\vec{J_m}A(\vec{r}) \tag{3.42}$$

describes the relationship between the electric field tangential components at the boundaries of the two materials $\vec{E}_{1tan}(\vec{r})$ and $\vec{E}_{2tan}(\vec{r})$, respectively, depend on the magnetic surface current density $\vec{J_m}A(\vec{r})$.
The *fourth equation*

$$\vec{n}(\vec{r}) \times \left(\vec{H}_1(\vec{r}) - \vec{H}_2(\vec{r})\right) = \left(\vec{H}_{1tan}(\vec{r}) - \vec{H}_{2tan}(\vec{r})\right) = \vec{J}_A(\vec{r}) \tag{3.43}$$

describes the relationship between the magnetic field tangential components at the boundaries of the two materials $\vec{H}_{1tan}(\vec{r})$ and $\vec{H}_{2tan}(\vec{r})$, respectively depend on the electric surface current density $\vec{J}_A(\vec{r})$.

3.2 Numerical Methods in Electromagnetics

The numerical solution of Maxwell's equations for arbitrarily shaped models makes it necessary to split the object into sub-domains with mathematically well described forms like cubes or tetrahedra for volumes or triangles and squares in case, where only surfaces are considered [Bayr 09]. These different shapes are chosen to ensure the best possible approximation of the original model. Numerical computation approaches in electromagnetics are used when Maxwell's equations are applied on these cells to define the electromagnetic wave propagation through these objects. The discretization rule determining the size of the smallest cell edge l is chosen to ensure that the waveform can be reconstructed in conformity to the proper waveform dependent of the desired accuracy and of the geometry. In cases where linear basis functions like RWG-functions [Glis 80] are utilized, the empiric rule

$$l \leq \frac{\lambda_{min}}{10} \,. \tag{3.44}$$

can be used. The smallest wavelength λ_{min} is controlled by the speed of light c_0 and the highest frequency of interest f_{max} according to

$$\lambda_{min} = \frac{c_0}{f_{max}} \,. \tag{3.45}$$

On the one hand the resulting step according to (3.44) is normally insufficient for the discretization of edges and angles of geometries. On the other hand, smaller discretization steps might suffice for simple shape geometries. From equation (3.45) it can be deduced that the edge size decreases with higher frequencies. For example, the smallest size of the cell edge of an antenna operating in the frequency range from 1 GHz up to 6 GHz should be smaller than 5 mm. This leads to large simulation models. In addition to the cell edge size, phenomena such as the skin effect become more important with higher frequencies and have to be taken into account.

In addition to precise **C**omputer **A**ided **D**esign (**CAD**) data, the first important aspect for the accurate approximation of the investigated antenna is the determination of the antenna environment, which should be taken into account in order to ensure the best possible realistic simulation model. Electromagnetic phenomena are governed by Maxwell's equations. However information about the investigated problem regarding both the geometry and the electromagnetic material characteristics such as permittivity ε_r, the dielectric loss factor $\tan\delta$ and the magnetic loss μ_r should be taken into consideration. Because most of these parameters depend on frequency, great care should be taken in choosing of the appropriate values. The higher the frequency range of the investigated computation problem, the more precise the simulation model should be. This can be quite problematic from the computational point of view when investigations should be realized for many problem variants and at many frequency points. In addition to the antenna geometry, the space around the investigated problem domain has to be

discretized for most of numerical computation approaches used. This means that simulations at very high frequencies are often very time consuming. The number of the mesh cells for an accurate simulation model can reach several hundred millions depending on the geometry size and on the frequency range of interest. In order to economize computation time, different simulation models are used depending on the frequency range of interest. Even compromises between accuracy of the results and the geometry area considered in simulation have to be made.

For low frequencies, phenomena like the skin effect are negligible [Bayr 09]. Therefore, information regarding the material depth can be neglected. This leads to numerical approaches permitting the computation of the electric current on surfaces without discretization of the complete investigated problem volume. In this case, so called Green's functions are used to compute the coupling between the individual dicretization surface cells [Harr 67].

In recent years, several numerical approaches differing in the interpretation of Maxwell's equations have been developed. Figure 3.2 gives an overview of the best known numerical simulation approaches used for automotive applications.

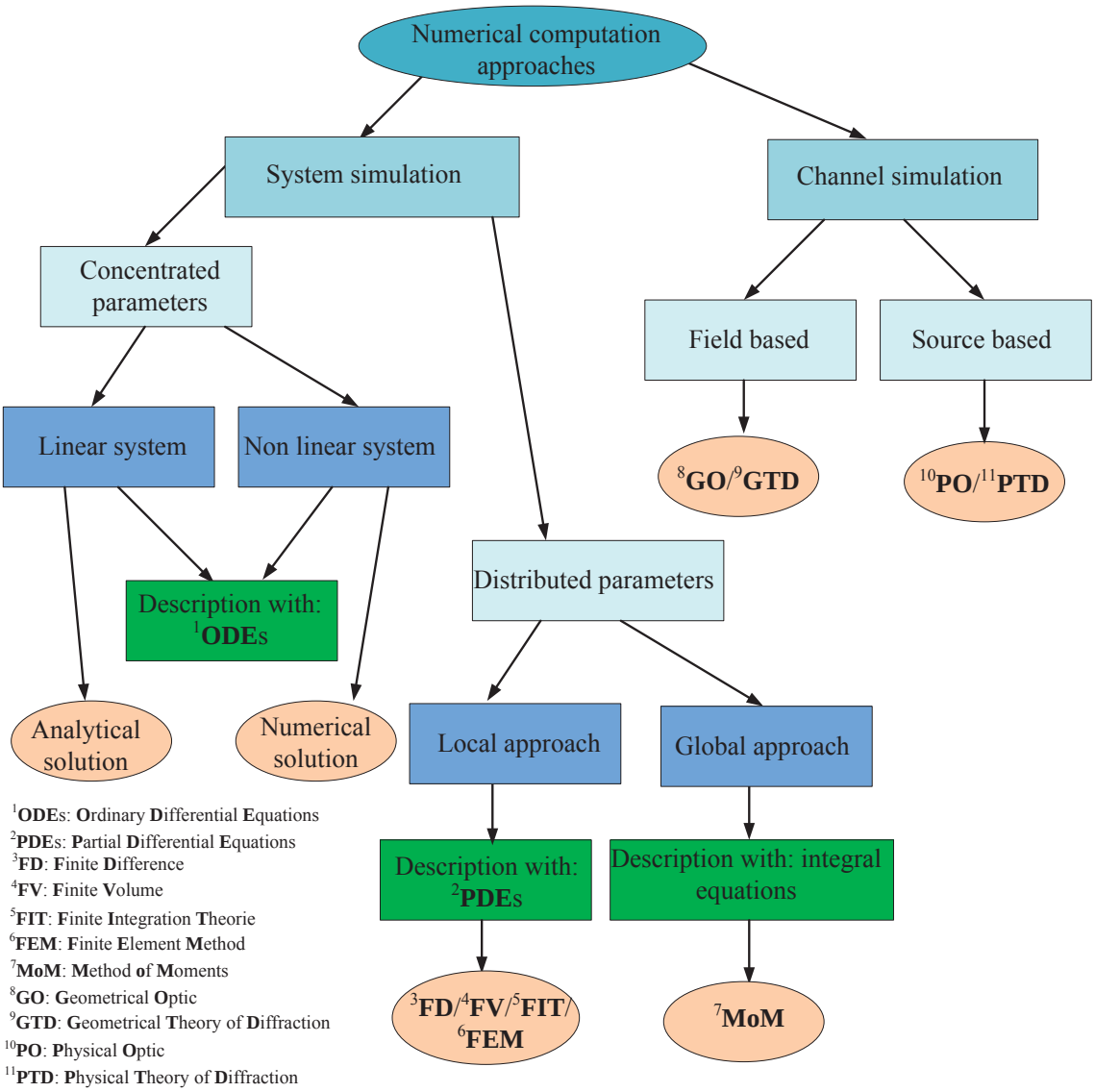

Figure 3.2: Numerical methods for automotive applications.

Numerical computational approaches can be split into two categories. The first is used for system simulation and the second one is utilized for channel simulation [Budd 11]. On the one hand, channel simulations are used to predict how antennas will act in real environment like in cities, forests or on highways to evaluate the reception behaviour of the antenna in the different situations. Hence, antenna diversity systems can be evaluated and optimized. Channel simulations can be subdivided into two groups [Eibe 03]. The first of these is field based. Examples are when **G**eometrical **O**ptic (**GO**) or **G**eometrical **T**heory of **D**iffraction (**GTD**) are used and the second concerns source based methods such as when **P**ysical **O**ptic (**PO**) or **P**ysical **T**heory of **D**iffraction (**PTD**) are used. On the other hand, system simulations are used to evaluate antenna characteristics regardless of the real antenna environment. Two

sub-categories can be considered to describe antenna systems. The first is based on concentrated elements when models are sufficiently described by simple elements like resistors R, capacitances C or inductances L. This depends on the geometry size and complexity as well as on the frequency range of interest. The solution of Maxwell's equations on the equivalent model can be delivered analytically or numerically. The second sub-category uses distributed parameters to describe the problem. This is the general case when large and complex geometries are investigated. The description can occur with integral equations for global approaches such as when the method of moments is used or with **P**artial **D**ifferential **E**quations (**PDE**s) for local approaches as in cases where **F**inite **D**ifference (**FD**), **F**inite **I**ntegration **T**echnique (**FIT**), or **F**inite **E**lement **M**ethod (**FEM**) are applied.

3.2.1 Finite Difference Time Domain Method

The **F**inite **D**ifference **T**ime **D**omain (**FDTD**) method requires the entire solution volume to be discretized. Figure 3.3 shows an example of a discretization cell used for FDTD simulations.

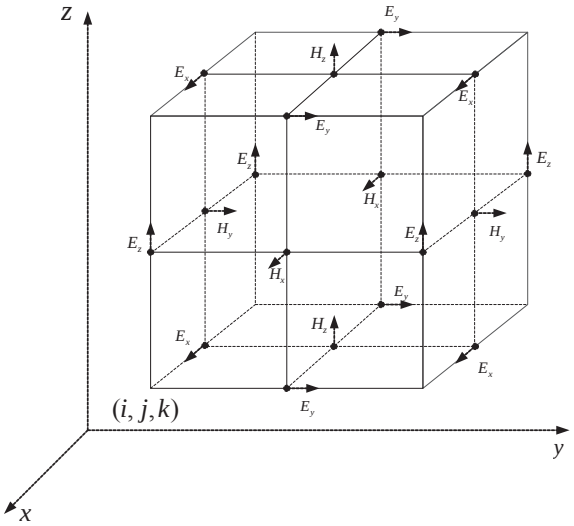

Figure 3.3: Finite difference time domain discretization cell.

Unlike the most finite element methods and the common method of moments techniques, the FDTD approach works in the time domain [Lind 96]. This makes it suitable for transient analysis problems [Bayr 09].
Similar to the finite element method, the FDTD methods are suitable for modelling complex inhomogeneous configurations. Consequently, the FDTD method is often used for modelling bounded complex inhomogeneous geometries. **A**bsorbing **B**oundary **C**ondition (**ABC**) can be used in cases where unbounded geometries are computed [Sank 07] in order to optimize the

computation time. The FDTD method represents a direct solution of Maxwell's first (3.12) and second (3.14) time dependent curl equations. It should be noted that each magnetic field vector component is surrounded by four electric field components. A first-order central-difference approximation can be expressed as

$$\frac{1}{A}[E_{x1}(t) + E_{y2}(t) - E_{z3}(t) - E_{y4}(t)] = -\frac{\mu_0}{2a\Delta t}[H_{x0}(t+\Delta t) - H_{x0}(t-\Delta t)] \tag{3.46}$$

where A is the area of the near face of the cell in Figure 3.3 with the edge size a. $H_{x0}(t+\Delta t)$ is the only unknown in this equation, since all other quantities were found in a previous time step. In this way, the electric field values at time T are used to find the magnetic field values at time $(t+\Delta t)$. A similar central-difference approximation of equation can then be applied to find the electric field values at time t from $(t+2\Delta t)$ the magnetic field values at time $(t+\Delta t)$. By alternately computing the electric and magnetic fields at each time step, fields are propagated throughout the grid. Time stepping is continued until either a steady state solution or the desired response is obtained. At each time step, the equations used to update the field components are fully explicit. No system of linear equations has to be solved. The required computer storage and running time is proportional to the electric size of the volume being modelled and the grid resolution.

3.2.2 Finite Integration Technique

The **F**inite **I**ntegration **T**echnique (**FIT**) [Clem 01; Weil 77] represents a numerical computation method to solve field problems described by Maxwell's equations. The problem domain is subdivided in small cells forming a three dimensional grid. Every cell is specified with permittivity ε_r, permeability μ_r and conductivity σ.
The edge voltage e_i as shown in Figure 3.4 is calculated from the electric field E_i for every cell edge with the size a according to

$$e_i = E_i\, a\,. \tag{3.47}$$

The magnetic flux b_j is calculated depending on the magnetic flux density B_j for the lateral face A_j according to

$$b_j = B_j\, A_j\,. \tag{3.48}$$

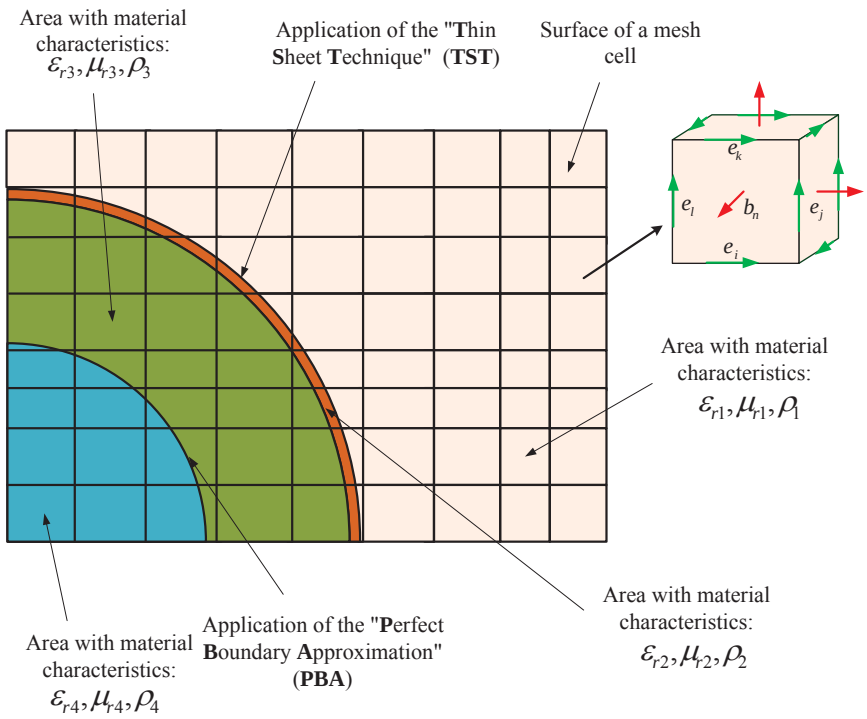

Figure 3.4: Discretization cells for simulation models computed by FIT, PBA and TST.

In addition to the first grid, a second grid orthogonal to the three dimensional grid is taken into account to calculate the magnetic edge voltages h_i depending on the magnetic field H_i for each cell edge with the size a according to

$$h_i = H_i \, a \, . \tag{3.49}$$

The electric flux d_j is then calculated depending on the electric displacement current density D_j for the lateral face A_j according to

$$d_j = D_j \, A_j \, . \tag{3.50}$$

Because of the prismatic form of the grid cells with the contour C, the electric field contour integral is simplified to

$$\oint_{C(A)} \vec{E} \cdot \mathrm{d}\vec{s} = \int_{C_1} \vec{E} \cdot \mathrm{d}\vec{s} + \int_{C_2} \vec{E} \cdot \mathrm{d}\vec{s} - \int_{C_3} \vec{E} \cdot \mathrm{d}\vec{s} - \int_{C_4} \vec{E} \cdot \mathrm{d}\vec{s} = \sum_{k=1}^{4} e_i \, . \tag{3.51}$$

The curl equation is then described as

$$\sum_{k=1}^{4} e_i = e_1 + e_2 - e_3 - e_4 = -\frac{\partial b_n}{\partial t} \, . \tag{3.52}$$

This formulation can be performed for all six grid cell surfaces. The resulting matrix is then

$$\begin{bmatrix} \cdots & \cdots & \cdots & \cdots & \cdots & \cdots & \cdots & \cdots \\ \cdots & 1 & \cdots & 1 & \cdots & -1 & \cdots & -1 \\ \cdots & \cdots & \cdots & \cdots & \cdots & \cdots & \cdots & \cdots \end{bmatrix} \begin{bmatrix} e_i \\ \cdots \\ e_j \\ \cdots \\ e_k \\ \cdots \\ e_l \end{bmatrix} = -\frac{\partial}{\partial t} \begin{bmatrix} \cdots \\ b_n \\ \cdots \end{bmatrix}. \tag{3.53}$$

The matrix has the form

$$\mathbf{C} \cdot \vec{e} = -\frac{\partial}{\partial t}\vec{b} \tag{3.54}$$

and gives a description of Maxwell's second equation. The matrix $\mathbf{C}$ has only the elements 1, 0, -1. Similar to the equation (3.54), all other matrix equations can be given. The following formulation is obtained related to Maxwell's first equation:

$$\mathbf{C}_{Dual} \cdot \vec{h} = -\frac{\partial \vec{d}}{\partial t} + \vec{j}\,, \tag{3.55}$$

$\vec{j}$ represents the current vector. For Maxwell's third equation, we obtain

$$\mathbf{S}_{Dual} \cdot \vec{d} = \vec{q} \tag{3.56}$$

where the space electrical charge vector $\vec{q}$ corresponds to the divergence of the electric displacement current density $\vec{d}$. Related to Maxwell's fourth equation, following formulation is obtained:

$$\mathbf{S} \cdot \vec{b} = \vec{0}\,. \tag{3.57}$$

The matrix $\mathbf{C}$ is the discrete representation of the analytical rotation operator and the matrix $\mathbf{S}$ of the divergence operator. The index *Dual* specifies the computation based on the second cell grid. Similar to the previous formulation, the material equations can be discretized and given as

$$\vec{d} = \mathbf{M}_\varepsilon \cdot \vec{e}\,, \tag{3.58}$$

$$\vec{b} = \mathbf{M}_\mu \cdot \vec{h}\,, \tag{3.59}$$

$$\vec{j} = \mathbf{M}_\sigma \cdot \vec{e}\,. \tag{3.60}$$

The material parameters are stored in the material matrices for permittivity $\mathbf{M}_\varepsilon$, permeability $\mathbf{M}_\mu$ and conductivity $\mathbf{M}_\sigma$. The material parameters can be directional, local and frequency

dependent. That means the method allows loss-free and lossy, isotropic and anisotropic material properties as well as frequency dependent material properties with arbitrary order for permittivity and for permeability as well as material parameter fitting functionalities. Established simulation tools such as "CST Microwave Studio" use the FIT in the time domain [Weil 77; Rien 85; CST 10]. However, very large and complex problems require a large number of grid cells for an appropriate modelling of the investigated problem, especially when models contain curve shapes and when they have multiple layers with different material parameters. Therefore, additional approaches like the **P**erfect **B**oundary **A**pproximation (**PBA**) allowing accurate and fast computation of arbitrarily shaped objects are used. Furthermore, the **T**hin **S**heet **T**echnique (**TST**) is used as a special approach for the efficient computation of thin metallic objects such as housings [Weil 77; Rien 85]. Figure 3.4 shows an example when the three approaches are used to solve an electromagnetic problem.

3.2.3 Transmission Line Matrix Method

The **T**ransmission **L**ine **M**atrix **M**ethod (**TLMM**) is based on the analogy between the field theory represented by Maxwell's equations and the transmission line theory described by Kirchhoff's equations [Russ 00; Dres 05]. The problem volume is discretized by so called TLM cells. Figure 3.5 shows an example of a TLM cell.

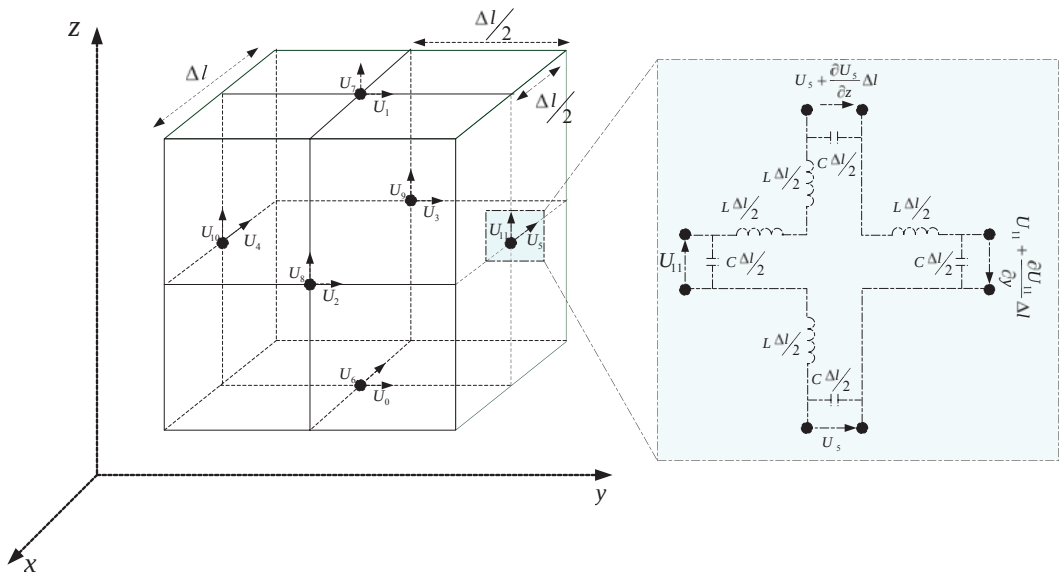

Figure 3.5: Discretization scheme of the transmission line matrix method.

The information about the material parameters of each cell is contained in their capacitances C and inductances L. The cells form a TLM network. To describe the electromagnetic behaviour

of the investigated problem domain, voltages and currents are applied on the wires of the TLM cells. It is possible to model inhomogeneous dielectrics with the TLM method, however, boundary conditions should be applied in the case of the problem volume being located in free space. The TLM method gives a solution of Maxwell's first (3.12) and second (3.14) time dependent curl equations [Krum 94; Lore 05]. A uniform inter-nodal distance of Δl is often assumed throughout the matrix (i.e., $\Delta l = \Delta x = \Delta y = \Delta z$). The relationship between network and field quantities [Russ 00] is given by

$$\frac{I_x(x-\frac{\Delta l}{2}) - I_x(x+\frac{\Delta l}{2})}{\Delta l} + \frac{I_z(z-\frac{\Delta l}{2}) - I_z(z+\frac{\Delta l}{2})}{\Delta l} = 2C\frac{\partial U_y}{\partial t} \tag{3.61}$$

and

$$\frac{U_x(x-\frac{\Delta l}{2}) - U_x(x+\frac{\Delta l}{2})}{\Delta l} = \frac{L}{2}\frac{\partial I_x(x-\frac{\Delta l}{2})}{\partial t} + \frac{L}{2}\frac{\partial I_x(x+\frac{\Delta l}{2})}{\partial t}\,. \tag{3.62}$$

The consideration of both equations (3.61) and (3.62) as well as the expansion of curl equations (3.14) and (3.12) in the rectangular coordinate system leads to the formulations

$$E_y \equiv U_x \tag{3.63}$$

$$H_x \equiv -I_z \tag{3.64}$$

$$H_z \equiv I_x \tag{3.65}$$

$$\mu \equiv L \tag{3.66}$$

$$\varepsilon \equiv 2C\,. \tag{3.67}$$

that describe the equivalences between the different quantities, where U is the voltage and I is the current. In cases in which wave propagation is considered in a periodic structure, the propagation constant $k = \alpha + j\beta$ should be taken into account according to

$$\begin{bmatrix} U_i \\ I_i \end{bmatrix} = \begin{bmatrix} e^{k\ \Delta l} & 0 \\ 0 & e^{k\ \Delta l} \end{bmatrix} \begin{bmatrix} U_{i+1} \\ I_{i+1} \end{bmatrix}. \tag{3.68}$$

3.2.4 Transmission Line Method

The **T**ransmission **L**ine (**TL**) method is a special method based on the telegrapher's equations [Goub 50]. The method is based on **T**ransversal **E**lectro**M**agnetic (**TEM**) wave propagation along conductors. The application of the TL method requires certain boundary conditions to be satisfied. By means of this, the TL method cannot be applied if vector components of the electromagnetic field exist in propagation direction. Besides that, the conductors' electrical length should be larger than their cross-sections. Furthermore, investigations show that results based on the TL method are reliable if the conductor length l is larger than about one tenth of

the shortest wavelength λ_{min}. The equivalent circuit of a TL element is represented in Figure 3.6.

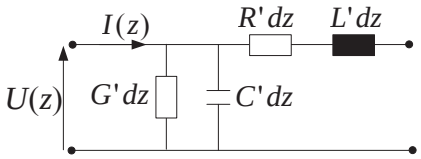

Figure 3.6: Transmission line element.

The so called telegrapher equations make it possible to calculate the voltage $U(z)$ and the current $I(z)$ dependent on z as described for the two wire conductor configuration according to

$$\frac{d^2U(z)}{dz^2} - Z'\ Y'\ U(z) = 0, \tag{3.69}$$

$$\frac{d^2I(z)}{dz^2} - Y'\ Z'\ I(z) = 0. \tag{3.70}$$

Z' and Y' stand for the impedance and admittance per unit length, respectively. The general solution of the telegrapher equations is given by

$$U(z) = U^+e^{-kz} + U^-e^{kz}, \tag{3.71}$$

$$I(z) = \frac{1}{Z_0}(U^+e^{-kz} - U^-e^{kz}). \tag{3.72}$$

U^+ and U^- stand for the forward and backward travelling waves, respectively.
The characteristic TL impedance Z_0 is defined by

$$Z_0 = \sqrt{\frac{Z'}{Y'}} = \sqrt{\frac{R' + j\omega L'}{G' + j\omega C'}}. \tag{3.73}$$

The propagation constant is given by

$$k = \sqrt{Z'\ Y'} = \sqrt{(R' + j\omega L')(G' + j\omega C')}. \tag{3.74}$$

The TL parameters such as resistances R', inductances L', capacitances C' and conductances G' are used to describe the TL. Often these parameters are given in the so called per unit length components.
The description of the formulation and analysis of the transmission line equations for lines consisting of more than two conductors is called the **M**ulti conductor **T**ransmission **L**ine (**MTL**) method and is well described in [Paul 94]. The MTL parameters are stored in the per unit length matrices for conductance $\mathbf{G}'$, capacitance $\mathbf{C}'$, resistance $\mathbf{R}'$ and inductance $\mathbf{L}'$ that describe the complete multi conductor configuration. These matrices are also called MTL

matrices. The main diagonal elements of the per unit length matrices contain the proper conductor values. Outside of the main diagonal elements are values of the coupling parameters. The number of these coupling parameters n increases with a larger number of conductors $\#wires$ according to

$$n = \#wires^2 + \#wires\,. \tag{3.75}$$

Figure 3.7 shows an equivalent circuit for a multi conductor with the length dz. The multi conductor is described by the per unit length MTL parameters.

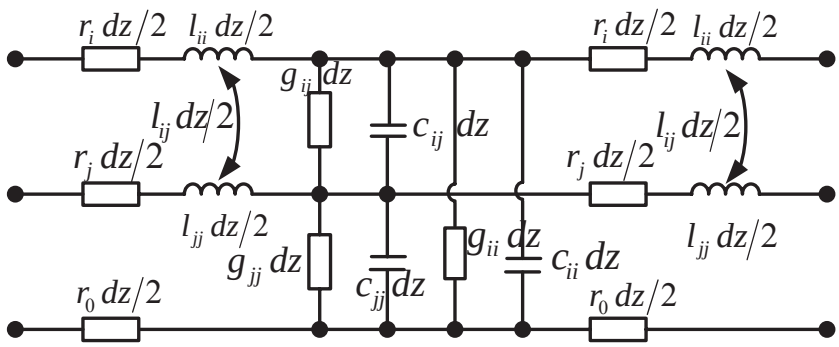

Figure 3.7: Transmission line method.

The multi conductor transmission line parameters could be determined analytically for simple multi conductor shapes or approximated numerically for complex shape. The per unit length inductance matrix $\mathbf{L}'$ contains in the main diagonal the proper per unit length inductance of the appropriate wire l_{ii} and outside the diagonal are coupling inductance l_{ij} contained with $i = 1, \cdots, n$ and $j = 1, \cdots, n$ are indices of the matrix elements. The matrix is given by

$$\mathbf{L}' = \begin{bmatrix} l_{11} & l_{12} & \cdots & l_{1n} \\ l_{21} & l_{22} & \cdots & \vdots \\ \vdots & \vdots & \ddots & \vdots \\ l_{n1} & \cdots & \cdots & l_{nn} \end{bmatrix}. \tag{3.76}$$

The structure of the per unit length capacitance matrix $\mathbf{C}'$ differs from the per unit length inductance matrix in the main diagonal, where the elements are equal to the total of the proper per unit length capacitance of the appropriate wires c_{ii} and the coupling per unit length capacitance to the other wires c_{ij} according to

$$\mathbf{C}' = \begin{bmatrix} \sum_{k=1}^{n} c_{1k} & -c_{12} & \cdots & -c_{1n} \\ c_{21} & \sum_{k=1}^{n} c_{2k} & \cdots & \vdots \\ \vdots & \vdots & \ddots & \vdots \\ -c_{n1} & \cdots & \cdots & \sum_{k=1}^{n} c_{nk} \end{bmatrix}. \tag{3.77}$$

The structure of the per unit length conductance matrix $\mathbf{G}'$ is similar to the per unit length capacitance matrix and is given by

$$\mathbf{G}' = \begin{bmatrix} \sum_{k=1}^{n} g_{1k} & -g_{12} & \cdots & -g_{1n} \\ g_{21} & \sum_{k=1}^{n} g_{2k} & \cdots & \vdots \\ \vdots & \vdots & \ddots & \vdots \\ -g_{n1} & \cdots & \cdots & \sum_{k=1}^{n} g_{nk} \end{bmatrix}. \tag{3.78}$$

The per unit length resistance r can be calculated with

$$r = \frac{\rho}{A} \tag{3.79}$$

where A stands for the wire cross-sectional area and ρ stands for the resistivity. The diagonal of the per unit length resistance matrix $\mathbf{R}'$ is composed of the appropriate wire per unit length resistance r_i and the per unit length resistance of the reference conductor r_0 according to

$$\mathbf{R}' = \begin{bmatrix} r_1 + r_0 & r_0 & \cdots & r_0 \\ r_0 & r_2 + r_0 & \cdots & \vdots \\ \vdots & \vdots & \ddots & \vdots \\ r_0 & \cdots & \cdots & r_n + r_0 \end{bmatrix}. \tag{3.80}$$

It should be noted that the per unit length matrices $\mathbf{G}'$, $\mathbf{C}'$ and $\mathbf{L}'$ are all dependent of the multi conductor geometry so that if one matrix is defined the other matrices can be calculated according to

$$\mathbf{C}' = \frac{1}{v_p^2}\mathbf{L}'^{-1} = \mu\varepsilon\mathbf{L}'^{-1}, \tag{3.81}$$

$$\mathbf{G}' = \mu\sigma\mathbf{L}'^{-1} = \frac{\sigma}{\varepsilon}\mathbf{C}' \tag{3.82}$$

where v_p is the wave phase velocity depending from the wavelength λ and the period T according to

$$v_p = \frac{\lambda}{T}. \tag{3.83}$$

Similar to the telegrapher equations given in (3.69) and (3.70) for the two conductor configuration, telegrapher equation for multi conductor configuration can be given as

$$\frac{d^2\mathbf{U}(z)}{dz^2} - \mathbf{Z}'\ \mathbf{Y}'\ \mathbf{U}(z) = 0, \tag{3.84}$$

$$\frac{d^2\mathbf{I}(z)}{dz^2} - \mathbf{Y}'\ \mathbf{Z}'\ \mathbf{I}(z) = 0 \tag{3.85}$$

where $\mathbf{U}(z)$ is the voltage vector and $\mathbf{I}(z)$ is the current vector depending on the direction of propagation z. $\mathbf{Z}'$ and $\mathbf{Y}'$ stand for the impedance and admittance matrices, respectively.

Figure 3.8 illustrates a case, where an EM field is incident on a multi conductor and the induced TL waves shall be computed.

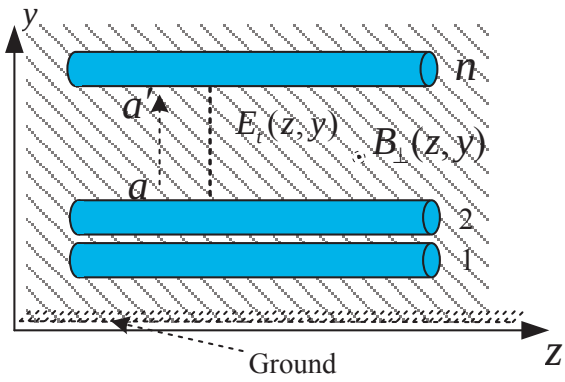

Figure 3.8: Multi conductors exposed to an EM field.

a and a' present the coordinates of two arbitrary points in the (y, z) plane and where the EM field is characterized by the electric field $E_t(x, y)$ and the magnetic flux $B_\perp(z, y)$. The telegrapher equations (3.84) and (3.85) should be extended to

$$\frac{d\mathbf{U}(z)}{dz} + \mathbf{Z}'\mathbf{I}(z) = -\mathbf{U}_F{}'(z), \tag{3.86}$$

$$\frac{d\mathbf{I}(z)}{dz} + \mathbf{Y}'\mathbf{U}(z) = -\mathbf{I}_F{}'(z). \tag{3.87}$$

The voltage vector $\mathbf{V}'_F$ the current vector $\mathbf{I}'_F$ can be calculated according to

$$\mathbf{U}'_F(z) = j\omega \begin{bmatrix} \vdots \\ \int\limits_a^{a'} B_\perp^i \mathrm{d}y \\ \vdots \end{bmatrix}, \tag{3.88}$$

$$\mathbf{I}'_F(z) = -\mathbf{Y}' \begin{bmatrix} \vdots \\ \int\limits_a^{a'} E_t^i \mathrm{d}y \\ \vdots \end{bmatrix}. \tag{3.89}$$

3.2.5 Lumped Circuit Transmission Line Method

The **L**umped **C**ircuit **T**ransmission **L**ine (**LCTL**) method is a numerical approach used in different simulation tools to describe EM propagation behaviour in multi conductors [User 05;

FEKO 07]. In this approach, a segmentation of the conductors should be done primarily according to the following rules implemented in the discretization algorithm:

- Calculation of the segmentation length with respect to the Transmission Line approach application rules described in Section 5.2.
- Identification of the critical geometrical conductor regions such as the start and end point of the conductors and branches.
- Subdividing of the conductors based on the chosen segmentation length and taking into account the critical regions.
- Subdividing of segment parts, which are in the direct vicinity of metallic parts such as housing or bodyshell in cars.
- Subdividing of basic segments, which are close to sub-segments to avoid a large variance of the segmentation steps in the same segment so that singularities are avoided in calculation. Figure 3.9 illustrates the LCTL scheme with the necessary steps to apply this approach.

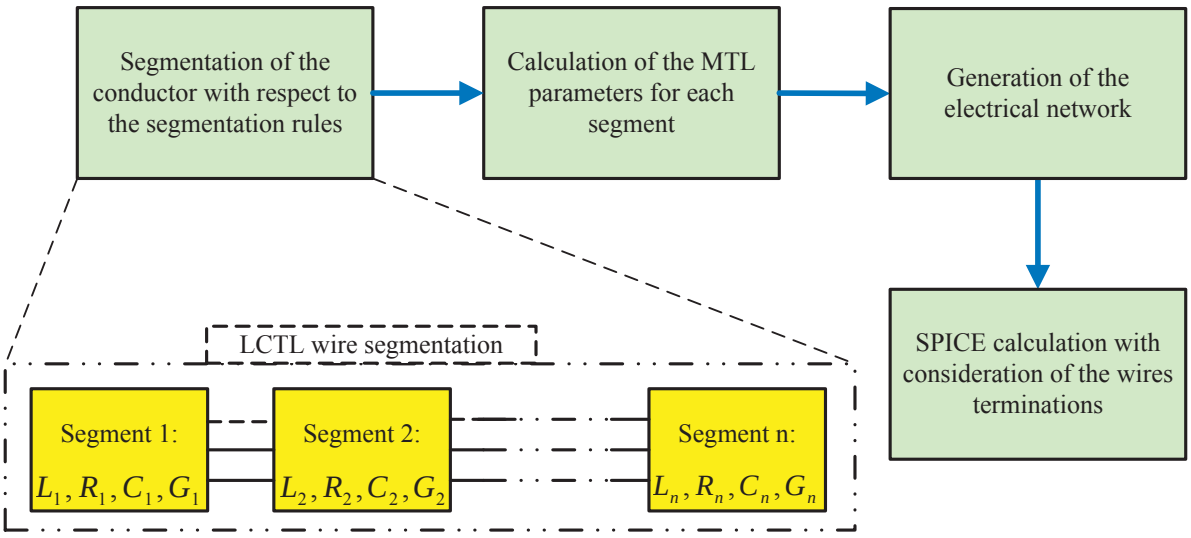

Figure 3.9: Mile stones of the LCTL approach.

Once the segmentation of the conductors is finished, MTL parameters of each segment are computed numerically. Afterwards, an electric network is built taking into account the conductor terminations and finally a **S**imulation **P**rogram with **I**ntegrated **C**ircuit **E**mphasis (**SPICE**) computation based on the Kirchhoff's circuit laws is done to calculate the currents and voltages in the complete network.

3.3 Finite Volume Method

The finite volume method [Pipe 02; Fume 06] presents a very efficient method for the simulation of unstructured meshes due to the use of tetrahedra for the discretization of the problem volume as shown in Figure 3.10. Tetrahedral mesh models give an accurate modelling with a much smaller number of cells compared to the finite difference method using Cartesian grid meshes [Bayr 09; Matt 01].

3.3.1 Finite Volume Time Domain Approach

The solution of the finite volume approach in the time domain offers many advantages such as the common time domain methods. By applying pulse excitation and building the Fourier transformation, the frequency domain characteristics can be calculated very quickly. Furthermore, no inversions of large matrix systems are required like in the frequency domain solution. However, the system solution is not accurate enough for very low frequencies. The FVTD gives a numerical solution of the Maxwell's equations (3.14) and (3.12) [Bomm 09; Fume 07].

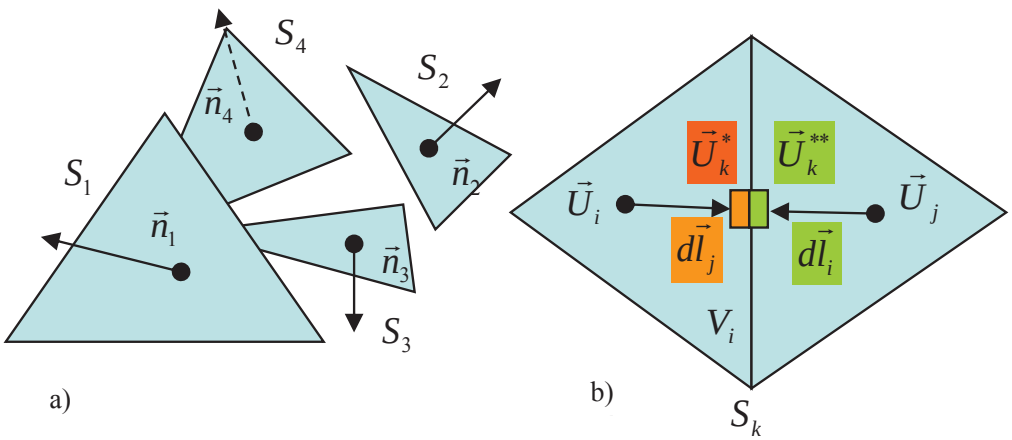

Figure 3.10: The finite volume time domain method.

The application of both Maxwell's equations (3.14) and (3.12) on the FVTD cell, Figure 3.10 (a), leads to the following equations

$$\varepsilon_i \, V_i \frac{\partial}{\partial t} \langle \vec{E} \rangle_{V_i} = \sum_{k=1}^{4} \left(\vec{n}_K \times \langle \vec{H} \rangle_{S_K} \right) S_K \tag{3.90}$$

and

$$-\mu_i \, V_i \frac{\partial}{\partial t} \langle \vec{H} \rangle_{V_i} = \sum_{k=1}^{4} \left(\vec{n}_K \times \langle \vec{E} \rangle_{S_K} \right) S_K \tag{3.91}$$

where the bracked value $\langle \cdot \rangle$ indicates spatially averaged value over the thetrahedron volume V_i with the index i or over its surface S_k. k is the index of the tetrahedral face and $\vec{n}_k$ is a unit normal to the tetrahedral surface. The expressions $\vec{n}_K \times \langle \vec{E} \rangle_{S_K}$ and $\vec{n}_K \times \langle \vec{H} \rangle_{S_K}$ describe the flux through the face S_K [Pipe 02; Fume 06]. The combination of the equations (3.90) and (3.91) gives

$$\alpha \frac{\partial \vec{U}}{\partial t} + \operatorname{div} \mathbf{F}(\vec{U}\,) = 0\,. \tag{3.92}$$

The material characteristics are considered in the material parameter matrix

$$\alpha = \begin{bmatrix} \varepsilon & 0 \\ 0 & \mu \end{bmatrix} \tag{3.93}$$

The vector $\vec{U}$ is defined as $\vec{U} = (E_x,\, E_y,\, E_z,\, H_x,\, H_y,\, H_z)^T$. The tensor $\mathbf{F}(\vec{U}\,)$ has 3 components

$$\vec{F}_1(\vec{U}) = [0,\, H_x,\, -H_y,\, 0,\, -E_z,\, E_y]^T\,, \tag{3.94}$$

$$\vec{F}_2(\vec{U}) = [H_z,\, 0,\, H_x,\, E_z, 0,\, -E_x]^T\,, \tag{3.95}$$

$$\vec{F}_2(\vec{U}) = [H_y,\, -H_x,\, 0,\, -E_y,\, E_x,\, 0]^T\,. \tag{3.96}$$

The equations (3.92), (3.94), (3.95) and (3.96) lead to

$$\alpha \frac{\partial \vec{U}_i}{\partial t} V_i = -\sum_{k=1}^{4} [\underbrace{\mathbf{F}^+(\vec{U}_k^*) \cdot n_K}_{\vec{\Phi}_{ik}^+} + \underbrace{\mathbf{F}^-(\vec{U}_k^{**}) \cdot n_K}_{\vec{\Phi}_{ik}^-}]\, S_K \tag{3.97}$$

representing a semi discrete formulation of the finite volume approach

$$\begin{cases} \vec{U}_K^* = \vec{U}_i + \nabla \vec{U}_i \cdot d\vec{l}_i \\ \vec{U}_K^{**} = \vec{U}_j + \nabla \vec{U}_j \cdot d\vec{l}_j \end{cases} \tag{3.98}$$

where ∇ is the Nabla operator. The right side of (3.97) can also be considered as an addition of the incoming flux $\vec{\Phi}_{ik}^+$ and the outgoing flux $\vec{\Phi}_{ik}^-$ illustrated in Figure 3.10 (b).

3.3.2 Validation of the Finite Volume Time Domain Approach

For the validation of the finite volume approach, investigations were performed on a wideband antenna. Figure 3.11 shows the measured antenna.

Figure 3.11: Picture of a wideband antenna.

The input impedance of the wideband antenna was measured and compared to simulations based on MoM and on FVTD as illustrated in Figure 3.12.

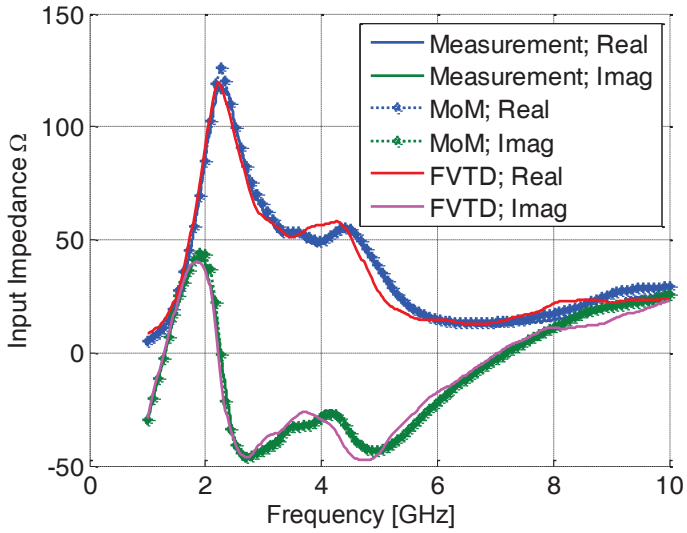

Figure 3.12: Comparison of the simulated and measured input impedance.

In addition to the input impedance, the return loss factor S_{11} was calculated with both numerical simulation approaches and compared to the measured ones. Results are presented in Figure 3.13.

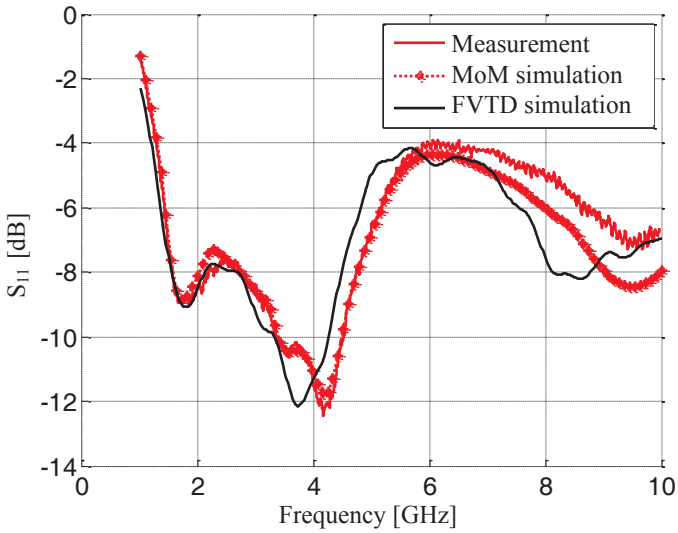

Figure 3.13: Comparison of the simulated and measured reflection factor.

From the results presented in Figure 3.12 and Figure 3.13, it can be seen that both simulations based on MoM and FVTD can give very accurate results. However, due to the fact that only one dielectric material can be taken into account when the current implemented hybrid MoM in the used simulation framework EMC Studio is used [EMCo 09], its application for complete roof antenna systems consisting of several materials with different dielectrics is restricted.

3.4 Numerical Approaches Based on the Method of Moments

The MoM often serves to solve complex integral equations [Harr 68; Wang 91; Jako 95], while relatively simple basis functions can be used for the discretization of the geometry [Wang 91].

3.4.1 Mathematical Description of the Method of Moments

The basic idea of the method of moments is to convert a linear and inhomogeneous operator equation utilizing basis and testing functions into a linear equation system [Harr 67].
The deterministic linear operator equation can be considered for the dimension x by

$$L(f(x)) = g(x) \tag{3.99}$$

where L is a linear operator, $g(x)$ is a known excitation, and $f(x)$ is unknown and to be determined. The function can be developed with basis function β_n as

$$f(x) \approx \sum_{n=1}^{N} \beta_n f_n(x)\,. \tag{3.100}$$

Combining (3.99) and (3.100), following formulation is obtained:

$$\sum_{n=1}^{N} \beta_n L(f_n(x)) \approx g(x)\,. \tag{3.101}$$

Afterwards inner products with adequate weighting functions $w_m(x)$ are built. The resulting equation is

$$\sum_{n=1}^{N} \beta_n \langle w_m(x), L(f_n(x))\rangle \approx \langle w_m(x), g(x)\rangle \tag{3.102}$$

where the angle brackets are defined for the one dimension example according to

$$\langle w_m(x), g(x)\rangle = \int_{x_1}^{x_2} w_m(x)\ g(x)\ dx\,. \tag{3.103}$$

The equation (3.102) can be written in matrix form as

$$[Z_{mn}][I_n] = [b_m]\,. \tag{3.104}$$

In cases where the MoM is utilized for electromagnetic fields, $[Z_{mn}]$ stands for the impedance matrix and $[b_m]$ stands for the voltage vector. From the current vector $[I_n]$, important information such as current distribution of the investigated model and antenna radiation pattern can be derived.

3.4.2 Deployment of the Method of Moments for Electromagnetic Fields

The magnetic vector potential $\vec{A}(\vec{r})$ and the scalar electric potential $\Phi(\vec{r})$ can be determined in space by

$$\vec{A}(\vec{r}) = \mu \iiint \vec{J}(\vec{r}\,')\frac{e^{-jk|\vec{r}-\vec{r}\,'|}}{4\pi\,|\vec{r}-\vec{r}\,'|}\mathrm{d}r'\,, \tag{3.105}$$

$$\Phi(\vec{r}) = \frac{1}{\varepsilon}\iiint \rho(\vec{r}\,')\frac{e^{-jk|\vec{r}-\vec{r}\,'|}}{4\pi\,|\vec{r}-\vec{r}\,'|}\mathrm{d}r' \tag{3.106}$$

where the electric charge density $\rho(\vec{r}\,')$ can be written as

$$\rho(\vec{r}\,') = \frac{-1}{j\omega}\ \nabla\cdot\vec{J}(\vec{r}\,')\,. \tag{3.107}$$

The contributions of (3.105) and (3.106) can be combined into the linear operator L to obtain a formulation comparable to equation (3.99) in the form of

$$\vec{E}(\vec{r}) = -j\omega\vec{A}(\vec{r}) - \nabla\Phi(\vec{r}) = L\left(\vec{J}(\vec{r})\right). \tag{3.108}$$

The MoM often serves to solve complex integral equations, whereas relatively linear basis functions can be used for the discretization of the geometry. The advantage of the method of moments compared to the finite volume method or finite element method is in the fact that only surfaces of the simulation model must be discretized to obtain the current distribution of the investigated problem. Once the current distribution is calculated, other parameters such as the near field or far field behaviour of antennas can be calculated.
The equation solved by the method of moments technique is the so called **E**lectric **F**ield **I**ntegral **E**quation (**EFIE**) given as a linear operator equation of the induced current density $\vec{J}(\vec{r})$ caused by the incident electrical field $\vec{E}^{inc}$ [Wilt 02] according to

$$\vec{E}^{inc}(\vec{r}) = L_e\left(\vec{J}(\vec{r})\right). \tag{3.109}$$

Figure 3.14 illustrates an example, where a wire is subdivided into N small segments S_N. To apply the method of moments, an incident field $\vec{E}^{inc}$ illuminates the wire. A part of this electrical field is scattered $\vec{E}^{sc}$. Consequently, a current density $\vec{J}(\vec{r})$ is induced in the wire.

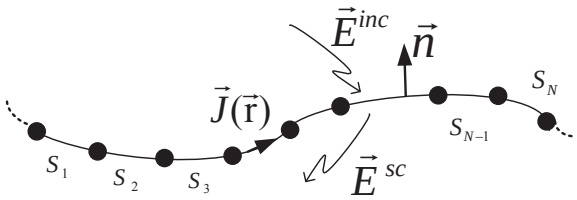

Figure 3.14: Application of the MoM on an an electric wire.

Similar to (3.109) the so called **M**agnetic **F**ield **I**ntegral **E**quation (**MFIE**) can be described and is given as a linear operator equation of the induced current density $\vec{J}(\vec{r})$ caused by the incident magnetic field $\vec{H}^{inc}$ according to

$$\vec{H}^{inc}(\vec{r}) = L_m\left(\vec{J}(\vec{r})\right). \tag{3.110}$$

Both equations are usually solved with the MoM in the frequency domain. However a MoM solution can also be given in time domain. Depending on the problem type, the EFIE or/and the MFIE should be applied to get the correct solution with the shortest computation time [Java 09]. The application of the MoM on the EFIE and the MFIE expands the induced current density $\vec{J}(\vec{r})$ as a finite sum of so called basis or expansion functions written in vector form $\vec{\beta}_n$ according to equation (3.100). Figure 3.15 illustrates an EM wave represented in the graph by a source irradiating a metallic **P**erfect **E**lectrical **C**onductors (**PEC**) volume with surface A. The source induces an electric current on the surface with a current density $\vec{J}_A(\vec{r})$ as represented in the right side of the figure.

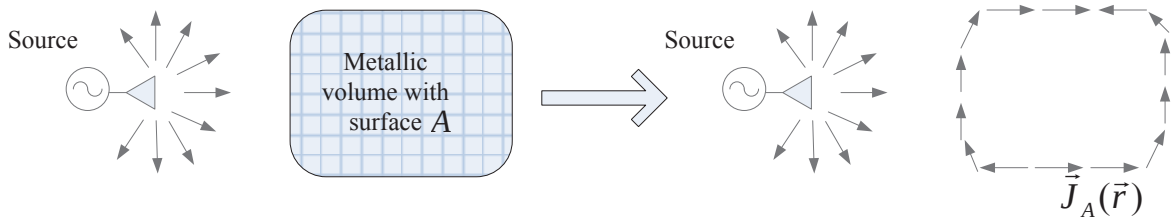

Figure 3.15: The method of moments.

The following boundary condition is applied in case of PEC problem solution:

$$\vec{n} \times \vec{E}^{inc} = -\vec{n} \times \vec{E}^{sc}, \tag{3.111}$$

with the incident field $\vec{E}^{inc}$ and the scattered field $\vec{E}^{sc}$. Consequently a current I is induced in the conductor. The boundary condition for the tangential electrical field $\vec{E}^{inc}_{tan}$ on the object surface (see Figure 3.15), gives the following EFIE formulation by utilizing the dyadic Green's function $\overset{\leftrightarrow}{G}{}^{E}_{J}\,(\vec{r},\vec{r}\,')$ [Harr 67] according to

$$-\vec{E}^{inc}(\vec{r})\Big|_{\tan} = \iint\limits_{A} [\overset{\leftrightarrow}{G}{}^{E}_{J}\,(\vec{r},\vec{r}\,') \cdot \vec{J}_A(\vec{r}\,')]\mathrm{d}a'\Bigg|_{\tan} . \tag{3.112}$$

The induced surface current density $\vec{J}_A(\vec{r})$ can be developed into basis functions according to

$$\vec{J}_A(\vec{r}_n) = \sum_{n=1}^{N} I_n \vec{\beta}_n(\vec{r}_n) . \tag{3.113}$$

Similar to (3.112) and taking into account the magnetic dyadic Green's function $\overset{\leftrightarrow}{G}{}^{H}_{J}\,(\vec{r},\vec{r}\,')$, the boundary condition for the tangential magnetic field $\vec{H}$ on the object surface gives the following MFIE formulation:

$$-\vec{H}^{inc}(\vec{r})\Big|_{\tan} = -\frac{1}{2}\vec{J}_A(\vec{r}\,') + \iint\limits_{A} [\overset{\leftrightarrow}{G}{}^{H}_{J}\,(\vec{r},\vec{r}\,') \cdot \vec{J}_A(\vec{r}\,')]\mathrm{d}a'\Bigg|_{\tan} . \tag{3.114}$$

Performing inner products of both sides of the EFIE equation described in (3.109) with adequate testing functions $\vec{w}_m$ results in a linear algebraic equation system as

$$\langle \vec{w}_m(\vec{r}_m), \sum I_n \; L_e\left(\vec{\beta}_n(\vec{r}_n)\right)\rangle = \langle \vec{w}_m(\vec{r}_m), \vec{E}^{inc}(\vec{r}_m)\rangle \tag{3.115}$$

with the discrete current vector $[I]$

$$\{I_n\} = [I] = \begin{bmatrix} I_1 \\ I_2 \\ \vdots \\ I_N \end{bmatrix} . \tag{3.116}$$

In cases where the basis functions are equal to the testing functions, the voltage vector elements are calculated according to

$$b_m = -\iint_A \vec{\beta}_m(\vec{r}_m) \cdot \vec{E}^{inc}(\vec{r}_m)\mathrm{d}a\,. \tag{3.117}$$

The discrete voltage vector is described by applying the testing functions

$$\{b_m\} = [U] = \begin{bmatrix} \left\langle \vec{\beta}_1, \vec{E}^{inc} \right\rangle \\ \left\langle \vec{\beta}_2, \vec{E}^{inc} \right\rangle \\ \vdots \\ \left\langle \vec{\beta}_M, \vec{E}^{inc} \right\rangle \end{bmatrix}. \tag{3.118}$$

The linear operator formulation given in (3.99) can be described with the matrix system equation

$$[U] = [Z]\ [I]\,. \tag{3.119}$$

The impedance elements Z_{mn} of the impedance matrix $[Z]$ are calculated according to

$$Z_{mn} = -j\frac{\omega\mu}{4\pi}\iint_A \iint_A \left[\vec{\beta}_m(\vec{r}_m) \cdot \left(\overleftrightarrow{I} + \frac{1}{k^2}\nabla\nabla\right)\frac{e^{-jk_0|\vec{r}_m-\vec{r}_n|}}{|\vec{r}_m - \vec{r}_n|} \cdot \vec{\beta}_n(\vec{r}_n)\right]\mathrm{d}a_n\mathrm{d}a_m\,, \tag{3.120}$$

where ω is the angular frequency, k_0 is the free space wave number and k is the propagation constant. $\vec{r}_m$ and $\vec{r}_n$ are position vectors, $\vec{\beta}_m$ and $\vec{\beta}_n$ represent the basis and testing functions, respectively.

The current vector elements can then be calculated by inverting the matrix equation system described in equation (3.119) as

$$[I] = [Z]^{-1}\ [U]\,. \tag{3.121}$$

To avoid long computation time problems regarding the Z-matrix inversion, mathematical techniques like the LU decomposition can be used.

3.4.3 Validation of the Method of Moments

In order to validate the method of moments, the reflection factor of an antenna is computed by the MoM implemented in EMC Studio and compared to measured results. The investigated antenna is one of the most used antennas for irradiating cars for EMC measurements and in the antenna development process for evaluating antenna reception performance. It is a chase CBL 6111D **Bi**conical **log**arithmic **per**iodical (**Bilogper**) antenna operating in frequency range from 30 MHz up to 1 GHz [Chen 03]. (See Figure 3.16).

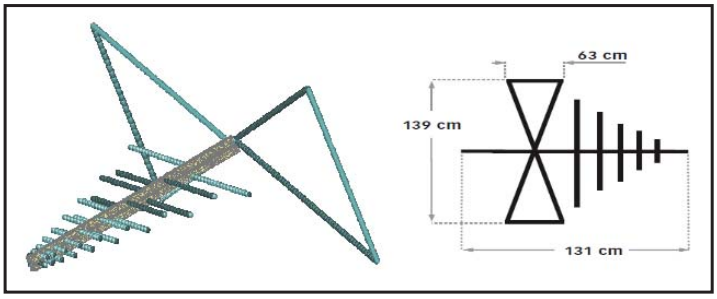

Figure 3.16: Simulation model of the Bilogper-antenna.

Figure 3.17 shows a comparison between measurement and simulation results of the Bilogper antenna.

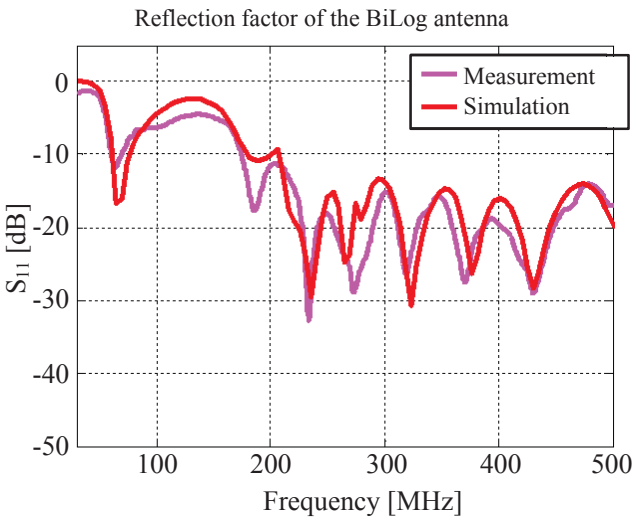

Figure 3.17: Comparison of measurement and simulation results.

Simulation results fit very well to the measurement data. This is due to the fact that all important antenna details for the simulation are taken into account, such as material parameters, geometry and the feeding point of the Bilogper antenna [Tazi 11b]. The validation of the simulation model makes it possible to use the same simulation model of the antenna in other simulations such as for susceptibility cases for EMC investigations. Figure 3.18 shows the current distribution and the far field pattern of the Bilogper antenna at different frequencies. The figure helps to give a better understanding of the mode of work of the antenna. This could be used to develop similar antennas.

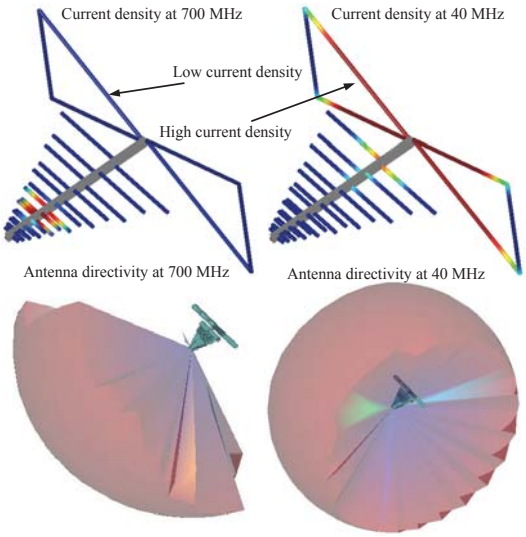

Figure 3.18: Current distribution and radiation pattern of the Bilogper antenna.

In a virtual model of the vehicle, all important parameters such as the glass of the windows have to be taken into account. Different approaches can be applied to account for these parameters appropriately. In the next three subsections, three approaches based on the MoM are discussed as solutions to this problem. By means of these, it is possible to take the antenna substrate into account, which is an improvement compared to the basic MoM.

3.4.4 Equivalent Method of Popović

Antenna structures printed on the surface of glass have complex structures. The most common vehicle antennas are placed on the rear, side or front widows of the car. Normally, the metallic strip of the antenna is located between the glass layers of the windscreen or printed on the surface. The equivalent coating approach replaces a metallic strip inside a glass with coated circular wires in free space with equivalent characteristics. Four steps are therefore needed to calculate all parameters of the equivalent model from the real model according to [Popo 91; Clar 05; Case 88] and as illustrated in Figure 3.19.

The first step is to determine the equivalent wire radius r_w. It can be calculated from the metallic strip width w [Popo 91] according to

$$r_w = \frac{w}{4} \,. \tag{3.122}$$

The second step is to find an equivalent homogeneous layer based on all layers with the thickness d_i and the permittivity ε_i composing the glass geometry. The equivalent layer has the thickness d_e, where

$$d_e = \sum_{i=1}^{N} d_i \,. \tag{3.123}$$

The equivalent electrical permittivity ε_e is given by

$$\varepsilon_e = \frac{d_e}{\sum\limits_{i=1}^{N} \frac{d_i}{\varepsilon_i}} \,. \tag{3.124}$$

The third step is to define an equivalent MoM model with the transformation of the structure in Figure 3.19 (b) into the coated wire model in Figure 3.19 (c), where

$$r_d = r_w \varepsilon^{\left[\frac{\varepsilon_{rd}}{\varepsilon_{rd}-1}\left(\ln \frac{d_e}{r_w} - \frac{\pi\varepsilon_0}{C_{coplanar}}\right)\right]} \,. \tag{3.125}$$

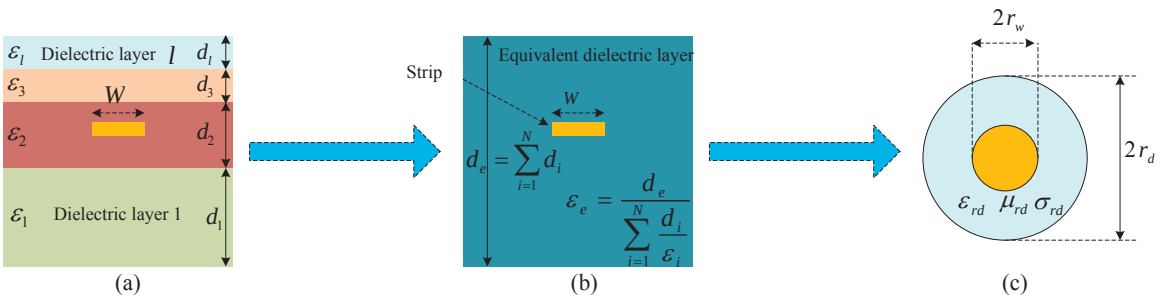

Figure 3.19: The equivalence principle of Popović.

The capacitance of the coplanar strips $C_{coplanar}$ is determined numerically for a two wire line by a highly oscillating function:

$$C_{coplanar} = \frac{\pi\varepsilon_0}{\ln \frac{d_e}{r_w} - (1 - \frac{1}{\varepsilon_{rd}})} \,. \tag{3.126}$$

Finally, an additional resistive load R'_{TL} is determined in order to account for surface waves [Chan 77] with a thermal power P_{t0}, where the current I along the equivalent wire with length l is integrated according to

$$R'_{TL} = \frac{2P_{t0}}{\int\limits_0^l |I(\xi)|^2 \mathrm{d}\xi} \,. \tag{3.127}$$

3.4.5 Thin Surface Method

Another method that can be used to take account of the dielectric parameters of glass windows is the thin surface method based on the **I**mpedance **B**oundary **C**ondition (**IBC**). The IBC is

an approximate boundary condition that makes it possible to transform a volume into a thin dielectric substrate with specific electrical properties [Karl 09]. The IBC in "Drichlet form" is given by

$$\vec{n} \times \vec{E} = Z_s \, \vec{n} \times \vec{n} \times \vec{H} \, . \tag{3.128}$$

The surface impedance approach transforms the glass into an equivalent thin dielectric substrate with specific properties according to [Harr 77; Harr 75]. When a volume V with the electrical permittivity ε in an incident field $\vec{E}^{inc}$ is considered, then the EFIE described in equation (3.109) can be rewritten as

$$L_e(\vec{J}) + \frac{\vec{J}}{j\omega(\varepsilon - \varepsilon_0)} = \vec{E}^{inc} \, . \tag{3.129}$$

The operator L_e relates the scattered field $\vec{E}^{sc}$ to the current density $\vec{J}(\vec{r})$ similar to (3.109) and (3.112) according to

$$L_e(\vec{J}) = -\vec{E}^{sc} = j\omega\vec{A} + \nabla\Phi \, . \tag{3.130}$$

The determination of $\vec{J}$ for thin dielectric shells of thickness t on a surface A can be calculated with the following formula, when the incident field $\vec{E}^{inc}$ is given

$$L_e(\vec{J}) + \frac{\vec{J}}{j\omega\Delta\varepsilon t} = \vec{E}^{inc}_{\tan} \text{ on } \quad A \tag{3.131}$$

with $\Delta\varepsilon = \varepsilon - \varepsilon_0$, the surface impedance is calculated as

$$Z_L = \frac{1}{j\omega\Delta\varepsilon t} \, . \tag{3.132}$$

The surface impedance is then derived from the previous formulations and is implemented in the used simulation framework EMC Studio to assign a dielectric impedance load to the triangles considered as dielectric layers [EMCo 09]. This load depends on the permittivity ε, the electrical loss tangent $\tan\delta$ and the thickness d of the appropriate triangle and is given by

$$Z_S = \frac{k}{2j\omega\varepsilon_0(\varepsilon_r - \varepsilon_{env})\sin({}^{kd}/_{2})} \, . \tag{3.133}$$

The propagation constant k is given as a relationship between the angular frequency ω, the free space permittivity, the free space permeability, the relative environment permeability μ_{env} and the relative permittivity ε_r in form of

$$k = \omega\sqrt{\varepsilon_0\mu_0\varepsilon_r\mu_{env}} \, . \tag{3.134}$$

3.4.6 Hybrid Method of Moments with Method of Auxiliary Sources

The hybrid MoM with the method of auxiliary sources illustrated in Figure 3.20 allows to take into account effect of dielectric losses placed close to metallic surfaces [Bogd 09a; Bogd 10; Java 09]. This permits the calculation of the current distribution of antenna structures placed on a windscreen with consideration of the glass parameters. The current density on the antenna structure $\vec{J}'$ with consideration of the glass parameters can be described as

$$\vec{J}' = \vec{J}\delta_{ij} + \sum_k \{{}^vC_k^{ji}(\vec{J}_k\vec{n})\vec{n} + [{}^hC_k^{ji}[\vec{J}_k - (\vec{J}_k\vec{n})\vec{n}]\}\,. \tag{3.135}$$

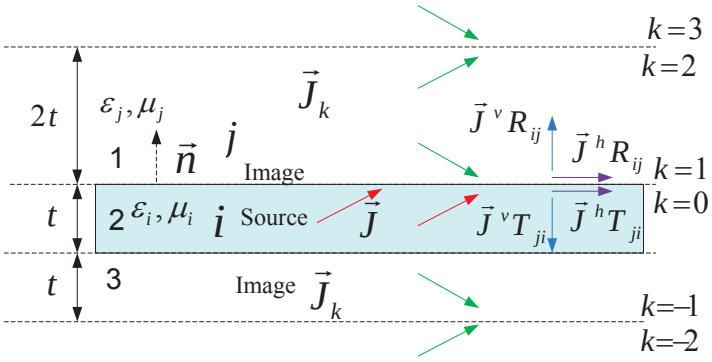

Figure 3.20: Hybrid method of moments with the method of auxiliary sources.

$\vec{J}_k$ is the image current density in layer k, δ_{ij} is the Kronecker delta, and $\vec{n}$ is the unit normal on the dielectric surface. For the current density $\vec{J}$ in the region i (Figure 3.20), an electromagnetic field at the observation region $j = 1, 2, 3$ is composed of the field of the original current $\vec{J}$ (if $j = i$) and that produced by its mirror images $\vec{J}_k$. The amplitudes of the current density are calculated by taking into account ${}^vC_k^{ji}$, ${}^hC_k^{ji}$ for vertical and horizontal components of vector potentials and ${}^qC_k^{ji}$ for scalar potentials. The reflection and transmission factors for each polarization are calculated by using following formulas [Bogd 09a]:

$${}^qR_{ij} = {}^vR_{ij} = \frac{\varepsilon_i - \varepsilon_j}{\varepsilon_i + \varepsilon_j}, {}^hR_{ij} = \frac{\mu_j - \mu_i}{\mu_i + \mu_j} \tag{3.136}$$

and

$${}^qT_{ji} = {}^vT_{ji} = \frac{2\varepsilon_j}{\varepsilon_i + \varepsilon_j}, {}^hT_{ji} = \frac{2\mu_i}{\mu_i + \mu_j} \tag{3.137}$$

resulting in

$${}^tC_{-k}^{12} = {}^tT_{12}{}^tR_{21}^k, k = 0, 1, 2, \dots, \tag{3.138}$$

$$ {}^{t}C_{k}^{22} = {}^{t}R_{21}^{|k|}, k = \pm 1, \pm 2, \dots , \tag{3.139} $$

and

$$ {}^{t}C_{k}^{32} = {}^{t}T_{12}\,{}^{t}R_{21}^{k}, k = 0, 1, 2, \dots . \tag{3.140} $$

Considering $\Re$ as an imaging operator, $\vec{J}_k$ can be described by

$$ \vec{J}_k = \Re_k(\vec{J}) . \tag{3.141} $$

The current density described in (3.135) can be derived with the introduction of a transformation operator $\Im$ according to

$$ \vec{J}' = \Im(\vec{J}) . \tag{3.142} $$

Similar to the previous formula, excitation can be rewritten as

$$ \vec{b}_k = \Im(\vec{b}) . \tag{3.143} $$

The MoM should be fitted with the new described transformation operator as

$$ L\Im(\vec{J}) = \Im\vec{b} . \tag{3.144} $$

The application of the hybrid MoM-MAS method for a glass antenna car problem necessitates consideration of the complete geometry. The geometry is subdivided into the basic part B and the antenna part A [Bogd 10] according to

$$ G = \{B, A\} . \tag{3.145} $$

The antenna part is composed of the antenna lines and the glass. The basic part can be modelled with the traditional MoM and the antenna part is modelled by the MoM-MAS hybrid method. Figure 3.21 illustrates the MoM/MoM-MAS scheme used to calculate the antenna behaviour in automotive simulations.

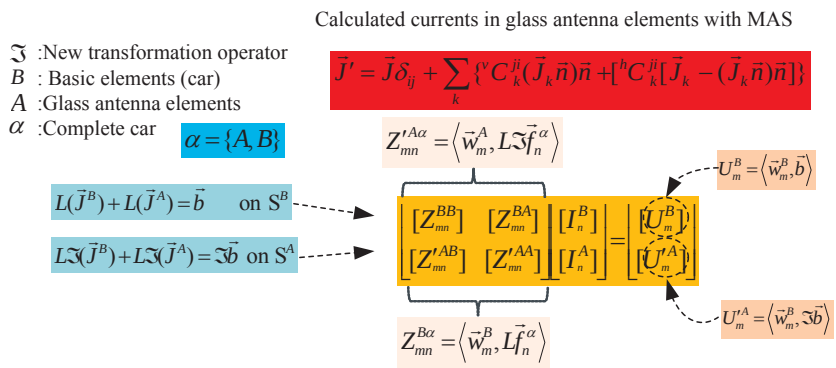

Figure 3.21: Hybrid method of moments with the method of auxiliary sources scheme.

3.4.7 Comparison of the Presented Simulation Methods Based on MoM

In the case of printed antennas on glass, the equivalent coating approach can be applied only when the coupling between adjacent antenna lines is negligible. This is the case when the antenna lines are thin and located at a considerable distance to each other. This approach does not take into account the coupling between antenna lines, which are directly adjacent. This coupling can be taken into consideration with the surface impedance approach. The surface impedance approach can be used for modelling glass around antenna lines. However, a dielectric under an antenna cannot be modelled by applying this approach. The hybrid MoM approach allows the complete printed antenna structure to be taken into account using accurate description for electromagnetic and geometrical characteristics of the glass.
Figure 3.22 describes the differences between the three presented approaches. It can be seen how the dielectric under the antenna structure is considered in the different approaches.

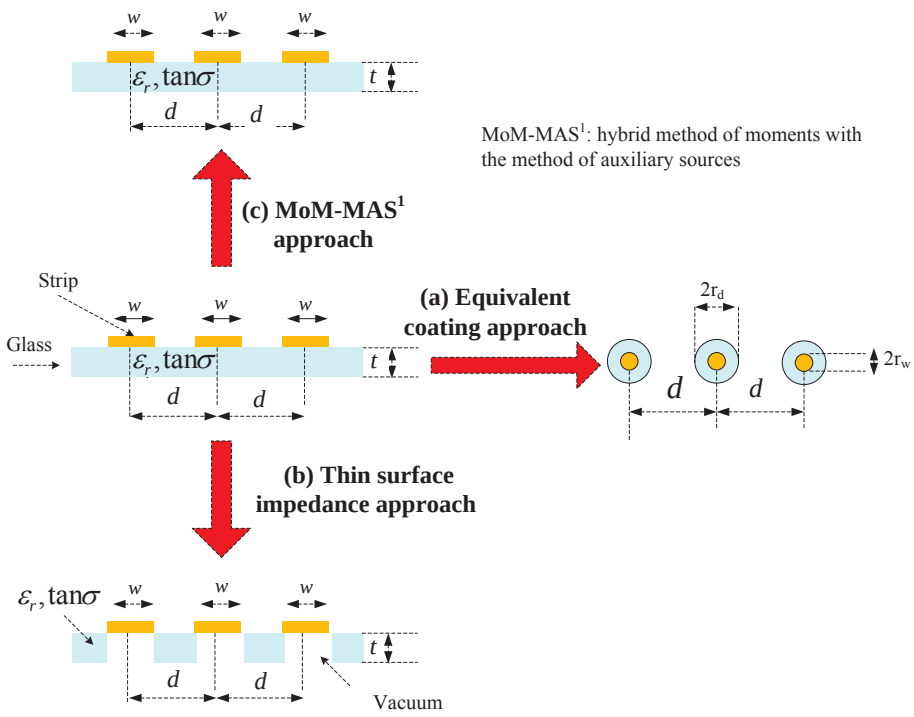

Figure 3.22: Numerical methods based on MoM for simulations of antennas printed on glass.

Today, simulations based on the hybrid method of MoM and method of auxiliary sources present an integral part of the development process of window antenna systems to improve antenna performance and to make important decisions about the location of antennas in early stages of development [Tazi 09; Tazi 10d; Tazi 11c].

In order to compare the three approaches based on MoM presented in Figure 3.22, a curved rear window antenna on an AUDI A5 was considered. Figure 3.23 shows a rear window antenna excited by an EM plane wave. The wave propagation is chosen in a way that the electric field $\vec{E}$ irradiates the rear window.

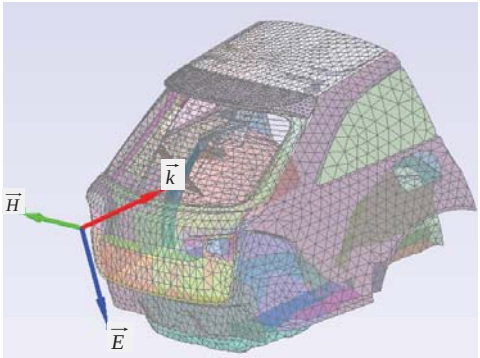

Figure 3.23: Rear window with an incident plane wave.

The coupled voltage in the AM antenna structure (printed on the rear window) was calculated. The voltage was observed in a frequency range from 200 kHz to 1.8 MHz. A comparison of simulation results obtained using dielectric triangles, the equivalent coating and the hybrid MoM approach for the car model is presented in the Figure 3.24.

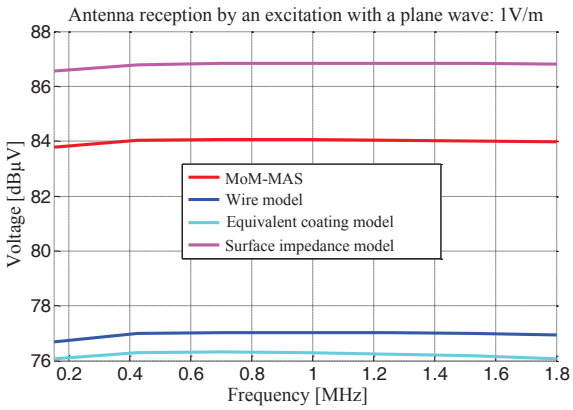

Figure 3.24: Comparison of the numerical simulation approaches in AM frequency range.

From the obtained results, it can be seen that there are large differences between the different approaches in comparison to the standard wire model (without taking into account of the glass material) represented by the blue curve. The results differ even between the surface impedance approach and the hybrid MoM approach. For a larger frequency range, larger differences could be expected. Therefore, great care should be taken in the modelling of the glass windows. The

last approach was successfully validated by measurement results in a wide frequency range as will be shown in Chapter 6. Performed validation of hybrid MoM for modelling of glass antennas shows good agreement of simulation results with measurements. In contrast to the surface impedance approach in glass antenna simulations there are no restrictions on distance between antenna lines and thickness of glass.

For an additional validation and comparison of the three approaches, an antenna structure printed on a 50 cm x 50 cm window was considered, see Figure 3.25. Measurements of antenna reflection coefficients were performed in the AUDI EMC Centre in the frequency range from 30 MHz to 300 MHz. Simulation models of all methods used: dielectric triangles, the equivalent coating, the hybrid MoM approach and for the antenna prototype are presented in Figure 3.25.

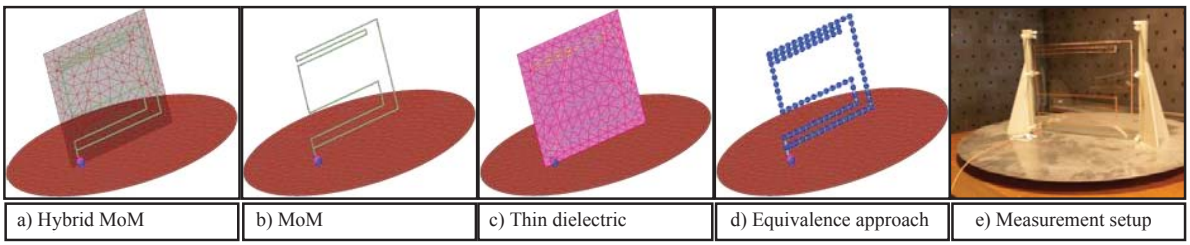

Figure 3.25: Prototype and simulation models of the window antenna.

Figure 3.26 shows a comparison of the different numerical results. From the graph, it can be seen that almost all methods have the same tendency as the measurement. Nevertheless, simulation results obtained with the hybrid method are the closest to the measurement results. This is due to the fact that this method takes into account the influence of the glass under and between the antenna lines.

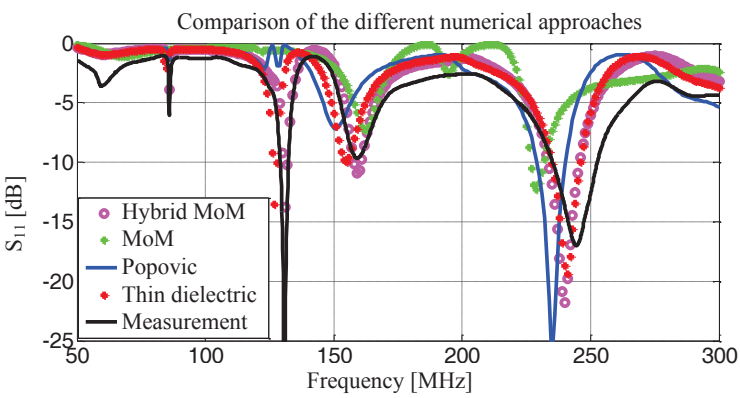

Figure 3.26: Comparison of the different numerical results to measurement results.

3.4.8 Incorporation of Electrical Networks into the Simulation Models

It is time consuming and not necessary to consider the complex electrical details from the internal structure of the electronic devices for EM simulations. Devices in close vicinity to antenna structures can be treated as black boxes, which can be described with N-port network parameters [Bogd 10]. The incorporation of electronic devices, e.g. antenna amplifiers in the MoM calculation necessitates to extend the basic MoM to allow the accounting of multi port networks [Bogd 07]. Figure 3.27 illustrates a black box considered as an N-port network connected to a MoM segment. Each network port i is characterized with an electric current I_i and a voltage U_i.

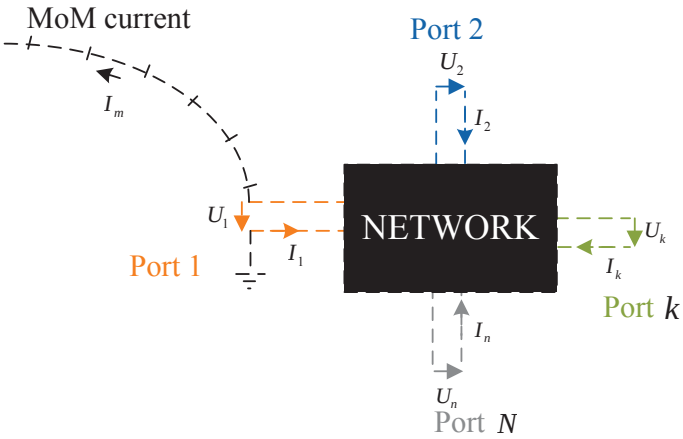

Figure 3.27: Incorporation of N-port network in MoM.

In electrical engineering, different forms of network parameters relating currents to voltages can be considered to describe electrical circuits. The widely used forms in EM simulations are listed below [Wing 08]:

- Description with impedance matrices $\mathbf{Z}^{Net}$ with matrix elements Z_{mn}^{Net}, the relationship between current and voltage is given by

$$\mathbf{U} = \mathbf{Z}^{Net}\mathbf{I}\,. \tag{3.146}$$

- Description with admittance matrices $\mathbf{Y}^{Net}$ with matrix elements Y_{mn}^{Net}.
- Circuit networks described with scattering matrices $\mathbf{S}^{Net}$ with matrix elements S_{mn}^{Net}. The relationship between normalized incoming waves a_i and reflected waves b_j is described in Section 2.1.

- **T**ransmission **L**ines (**TL**) are often used to describe the electrical length of adapters used in measurements or pigtails connected to antenna structures. The electrical length l_e of cables or adapters can be calculated by taking into account the geometrical length l_g and the surrounding electric permittivity ε_r according to

$$l_e = \frac{l_g}{\sqrt{\varepsilon_r}} \,. \tag{3.147}$$

The incorporation of the network equations into the MoM system [Yarm 08] makes it necessary to relate both the MoM vector matrix and the network vector matrix elements [Bogd 07; Bogd 09b]. First, it can be distinguished between free port networks, which are controlled with voltage sources and mixed ports composed of free and forced ports. In the first case the port current vector $\mathbf{I}$ is related to the MoM segment current vector $\mathbf{I}_m$ according to

$$\mathbf{I} = -\mathbf{I}_m \,. \tag{3.148}$$

The segment voltage vector $\mathbf{U}_m$ is composed of external voltage source vector $\mathbf{U}_m^S$ and the network voltage vector $\mathbf{U}$ in form of

$$\mathbf{U}_m = \mathbf{U}_m^S + \mathbf{U} \,. \tag{3.149}$$

The insertion of equation (3.146) and equation (3.148) in equation (3.149) leads to

$$\mathbf{U}_m = \mathbf{U}_m^S - \mathbf{Z}^{Net}\mathbf{I} \,. \tag{3.150}$$

Taking into account of the MoM formulation in equation (3.150) gives the hybrid MoM and network algebraic system formulation:

$$(\mathbf{Z}^{MoM} + \mathbf{Z}^{Net})\mathbf{I} = \mathbf{U}_m^S \,. \tag{3.151}$$

In case of mixed ports the equation can be rewritten in

$$(\mathbf{Z}^{MoM} + \mathbf{Z}^{'Net})\mathbf{I} = \mathbf{U}_m^S + \mathbf{U}_m^{add} \tag{3.152}$$

where $\mathbf{Z}^{'Net} = (\mathbf{Y}^{'Net})^{-1}$ is the free port impedance matrix of the N-port network. The additional voltage vector $\mathbf{U}_m^{add}$ describes the forcing ports according to

$$\mathbf{U}_m^{add} = -\mathbf{Z}^{'Net}\mathbf{Y}^{''Net}\mathbf{U}^S \tag{3.153}$$

where $\mathbf{Y}^{'Net}$ and $\mathbf{Y}^{''Net}$ are the free-port and mixed-port network admittance matrices, respectively. To determine the network parameters of the antenna amplifier, the measurement setup illustrated in Figure 3.28 can be used. The amplifier is fed by a 12 V voltage source and both amplifier ports are connected to a vector network analyzer to measure the network scattering matrix $\mathbf{S}$. From the $\mathbf{S}$ matrix, further network parameters such as the impedance matrix $\mathbf{Z}$ and the admittance matrix $\mathbf{Y}$ can be derived.

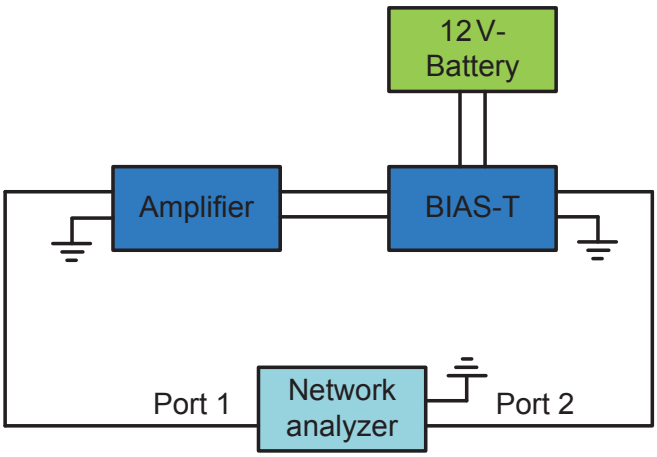

Figure 3.28: Measurement of the S-parameters of an antenna amplifier.

3.5 Near Field Source Solution

Modelling of metallic parts of the car body can be efficiently done by using method of moments. However, simulations of complex devices such as ferrite antennas may require an extended analysis approach. One possibility for simplifying the simulation model is to simulate or measure the field distribution in close vicinity to the antenna and introduce this field data to the model of the remaining part as sources. This can facilitate the modelling of the antennas and allows the substitution of all antennas, which shall be accounted in the simulation model by near field sources [Tazi 10a]. The change of the placement of these sources in the simulation model is much easier than to use the real geometry model of the ferrite antenna. Besides, the computation time with the introduced near field sources is much faster since the Z matrix contains fewer elements than in case of the real geometry of the antenna. This near field source solution is based on the field equivalence principle [Bala 05]. This states that the original electric current $\vec{J}$ and magnetic current sources $\vec{M}$, which produce the electrical field $\vec{E}$ and the magnetic field $\vec{H}$, Figure 3.29 (a), can be replaced by equivalent sources, see Figure 3.29 (b).

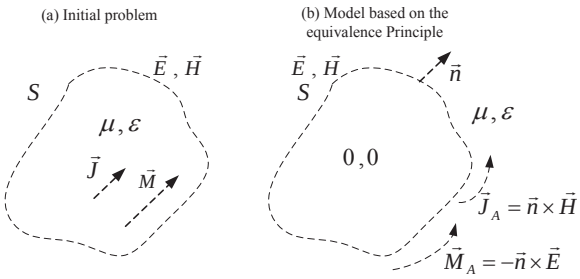

Figure 3.29: Equivalence principle.

The imaginary closed surface S surrounding the original sources is defined. $\vec{n}$ is the unit normal to the surface S. The field outside an imaginary surface is produced by equivalent electric and magnetic currents on the surface S. The current densities are chosen so that the field inside the closed surface S containing sources is assumed to be zero and outside it is equal to the radiation produced by the original sources. In order to get correct results for near field sources it is necessary to have full information about simulated or measured $\vec{E}$ and/or $\vec{H}$ fields (x, y, z real and imaginary components, phase). Also, it should be mentioned that mutual coupling between the replaced antenna and the car body is no longer accounted for. Figure 3.30 shows a simulation model of a car, where the ferrite antenna is considered by an equivalent near field source.

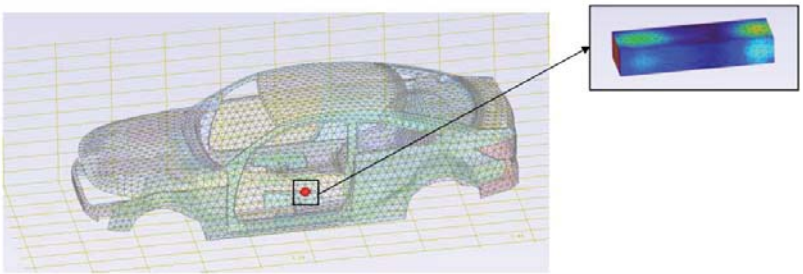

Figure 3.30: A car with a keyless antenna simulation model based on the equivalent principle approach.

MoM simulation of the ferrite antenna was validated by comparing simulation results with measurement results. For magnetic field investigations two simulation models of the ferrite antenna were considered as shown in Figure 3.31.

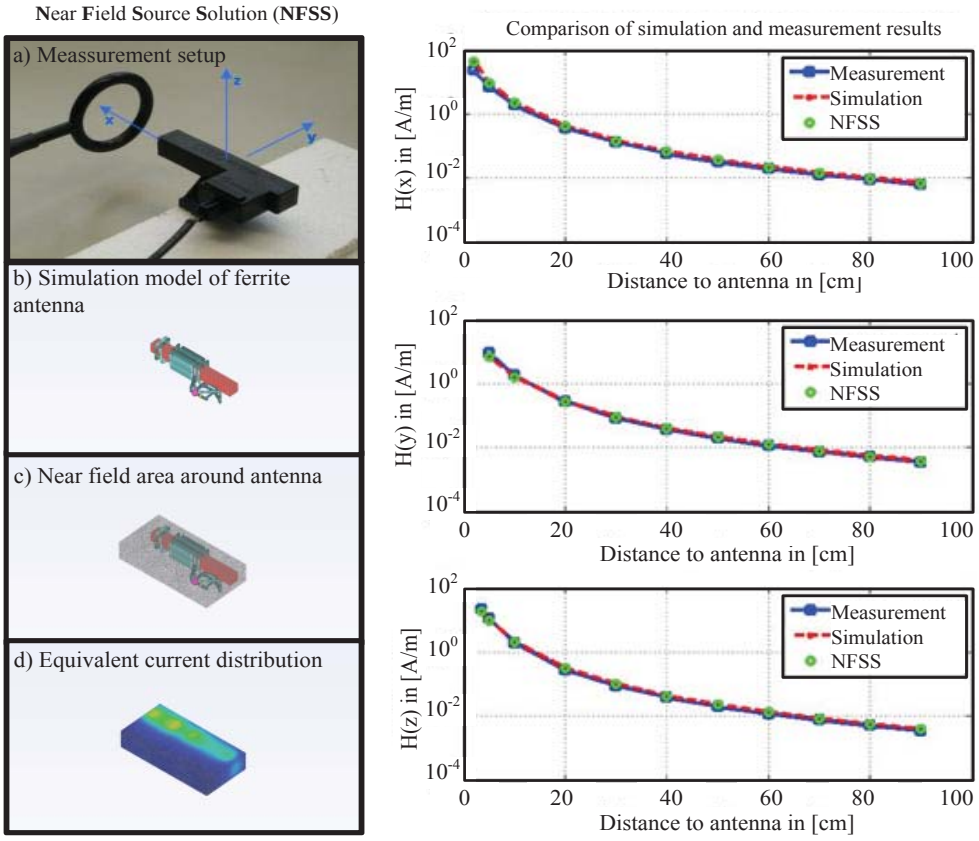

Figure 3.31: Comparison of simulation and measurement results.

At first, the complete geometry of the antenna was modelled then the **N**ear **F**ield **S**ource **S**olution (**NFSS**) model of the antenna was realized. The simulations are performed for a coil antenna, which is placed in free space, where the magnetic field is observed along three perpendicular directions. Both the simulation models and comparison of the two simulation and the measurement results are shown in Figure 3.31. From the results shown in Figure 3.31, it can be seen that magnetic field simulations with the MoM solver (EMC Studio) using the surface integral approach is in very good agreement with measurement results and simulation results realized with the NFSS model.

4 Computation Time Optimization for MoM

In order to integrate simulations into the automotive antenna development process, several algorithms leading to computation time optimization and modelling effort reduction are used, some of which will be introduced in this chapter.

4.1 Multi Excitation Approach

It is common to evaluate different antennas, which are located in close vicinity to each other in the automotive antenna optimization process by ensuring the best possible antenna reception for the whole antenna system. This requires sequential analysis of the behaviour of all antennas. The standard MoM simulation requires the simulation of all antennas. Hence, the simulation time increases in direct proportion to the number of the antennas investigated. Obviously, simulation of a full matrix with corresponding inversion and solution for each task is time consuming. In the multi excitation approach, first the matrix is filled, inverted and saved on disk and then used for computations in different excitation cases as illustrated in Figure 4.1. Excitation vectors are exchanged depending on the simulation model.

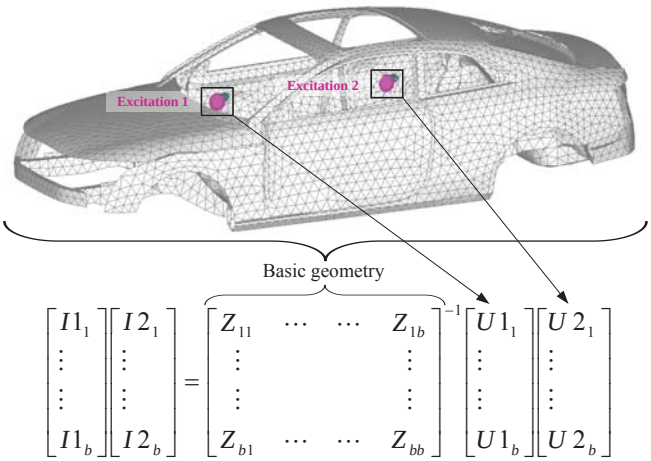

Figure 4.1: Multi excitation approach scheme.

This method allows much time to be saved for this kind of problem [Bogd 10; User 05]. For the correct utilization of this approach sufficient memory resources should be available for storage

of the matrix elements [Tazi 10a; schn 10]. Therefore, if M is the memory required to solve the problem, then the space required to store temporary matrices is $S = M \cdot F$, where F is the number of frequency points defined in the simulation task. To utilize the multi excitation approach, the main problem will be split into base geometry and additional excitations. In the EMC Studio simulation framework used, it is possible to specify each excitation with help of layers. At first, the problem with the base layer will be solved. The MoM simulation is used to fill and invert the system matrix for each frequency defined in a simulation problem [Bogd 09a; Wang 91]. Afterwards, different right sides of the matrix equation are considered to solve the problem for each combination of the applied excitations (layers) see Figure 4.1. The solutions can be found without repeating the inversion of the matrix. Thus, much time can be saved especially if there is a large number of unknowns. Simulation of keyless entry systems presents a perfect case, where the multi excitation approach can be used to save much computation time. Since for fixed geometry, different excitations are observed, the multi excitation approach can deliver solutions for the entire simulation model in a short time.

4.2 Multi Partitioning Approach

In the vehicle design development process, it often happens that a considerable part of geometry remains the same in different simulations [Bogd 10]. This is the case when comparing characteristics of different antennas mounted in a rear window of the same car model (see Figure 4.2).

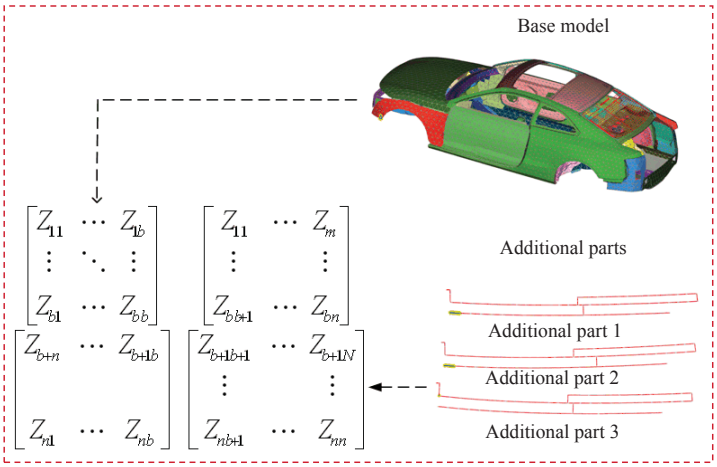

Figure 4.2: Application of the matrix partitioning method to develop rear window antennas.

Also, this is the case when considering an optimization problem regarding the optimal dimensions and position of certain antennas, which should be installed inside or on the surface of

the vehicle. A partitioned MoM scheme is intended to effectively handle series of geometries having a predominant common part [Bogd 05; Frei 06]. This scheme is based on a partitioned calculation and inversion of unvarying (main) and differing (additional) parts of the impedance matrices to quickly obtain solutions to EM problems on a series of geometries [Tazi 10b]. The multi-partitioned MoM scheme is hybridized with MAS and can be used for glass antenna simulation problems. Unlike the usual partitioned scheme [Bogd 05], a series of different partitioned geometries may be specified, and all the computations for the main and additional modes are performed in a single flow. This allows to perform a simultaneous solution of a series of antenna problems. Moreover, both the main and additional partitioned matrices may contain both the traditional MoM elements to take into account the basic car geometry, and the modified elements to include the dielectric effect on glass antenna elements. If a k-series of simulation model geometries $G_1, G_2, \ldots, G_K$ is considered with a common basic geometry part G^b where

$$G^b = \bigcap_{k=1}^{k} G_k \,. \tag{4.1}$$

Each geometry G_k can be described as a sum of the common basic part G^b and a specific additional part G_k^a according to

$$G_k = G^b + G_k^a \,. \tag{4.2}$$

The basic MoM matrix formulation can then be rewritten in

$$\begin{bmatrix} \mathbf{Z}^{bb} & \mathbf{Z}^{ba} \\ \mathbf{Z}^{ab} & \mathbf{Z}^{aa} \end{bmatrix} \begin{bmatrix} \mathbf{I}^b \\ \mathbf{I}^a \end{bmatrix} = \begin{bmatrix} \mathbf{U}^b \\ \mathbf{U}^a \end{bmatrix} \tag{4.3}$$

where $\mathbf{Z}^{bb}$ represents the matrix elements describing the coupling between the basic parts and the coupling between the additional parts is given by $\mathbf{Z}^{aa}$. $\mathbf{Z}^{ba}$ and $\mathbf{Z}^{ab}$ represent the impedance coupling elements between the additional and the basic parts. The number of the equation unknowns N is the sum of the additional element parts N^a and the basic parts N^b. The LU decomposition of the partitioned MoM impedance matrix leads to

$$\begin{bmatrix} \mathbf{I}_b \\ \mathbf{I}_a \end{bmatrix} = \begin{bmatrix} \mathbf{U}^{bb} & \mathbf{U}^{ba} \\ \mathbf{0} & \mathbf{U}^{aa} \end{bmatrix}^{-1} \begin{bmatrix} \mathbf{L}^{bb} & \mathbf{0} \\ \mathbf{L}^{ab} & \mathbf{L}^{aa} \end{bmatrix}^{-1} \begin{bmatrix} \mathbf{U}_b \\ \mathbf{U}_a \end{bmatrix} . \tag{4.4}$$

The $\mathbf{Z}$ matrix obtained from the LU decomposition shows that the basic block matrix $\mathbf{Z}^{bb} = \mathbf{L}^{bb}\mathbf{U}^{bb}$ remains the same as the one obtained from the basic geometry G^b.

In the matrix partitioning algorithm, the basic part is at first considered and the inverted basic L^{bb} and U^{bb} parts are calculated and stored. Afterwards, the additional blocks of the partitioned impedance matrix are considered and calculated successively. The complete $\mathbf{Z}$ matrix can now be described as

$$\begin{bmatrix} \mathbf{Z}^{bb} & \mathbf{Z}^{ba} \\ \mathbf{Z}^{ab} & \mathbf{Z}^{aa} \end{bmatrix} = \begin{bmatrix} \mathbf{L}^{bb} & \mathbf{0} \\ \mathbf{L}^{ab} & \mathbf{L}^{aa} \end{bmatrix} \begin{bmatrix} \mathbf{U}^{bb} & \mathbf{U}^{ba} \\ \mathbf{0} & \mathbf{U}^{aa} \end{bmatrix} . \tag{4.5}$$

The solving time is optimized when the matrix partitioning scheme is used, especially if the common part between the calculated geometries is much larger in comparison to the additional parts. The obtained solution time gain G can be calculated [Harp 40] according to

$$G = \frac{1}{(1-\beta)/(k+\beta)} \tag{4.6}$$

where $k = 1/[(1-(1-\alpha)^3]$ and $\alpha = N^a/(N^a + N^b)$. β is the additional time required for a direct task computation.

4.2.1 Matrix Partitioning for Front Window Antenna Investigations

The illustration in Figure 4.3 shows a front window of an AUDI A5, where different structures of antennas are printed on the upper left side of the front window. Nine different antenna structures are modelled. In all models a large geometry part remains unchanged (car body, glass and a part of the antenna). The table shown in Figure 4.3 illustrates the differences between all simulation models.

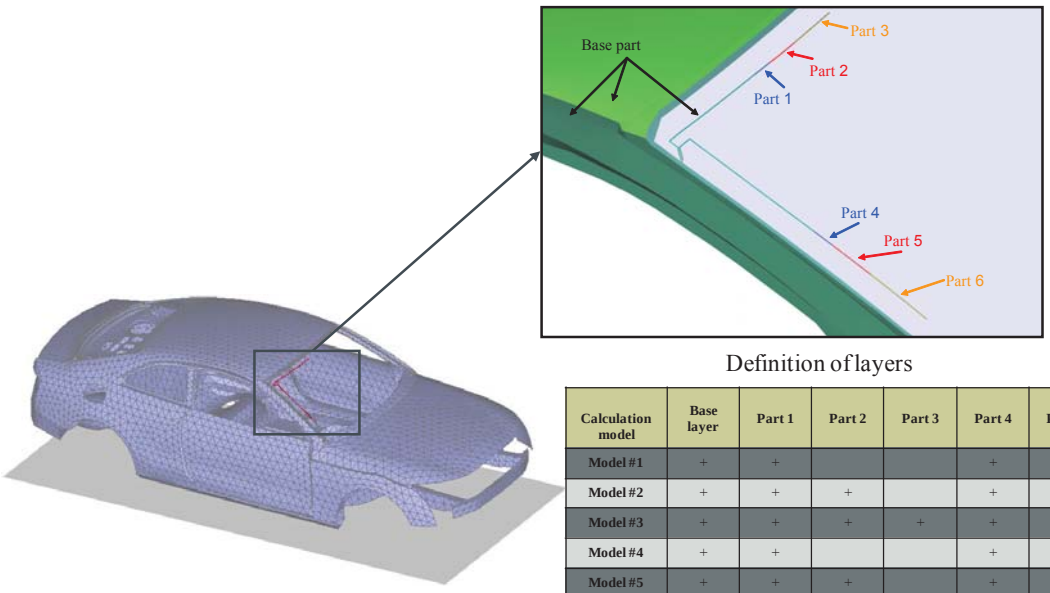

Definition of layers

Calculation model	Base layer	Part 1	Part 2	Part 3	Part 4	Part 5	Part 6
Model #1	+	+			+		
Model #2	+	+	+		+		
Model #3	+	+	+	+	+		
Model #4	+	+			+	+	
Model #5	+	+	+		+	+	
Model #6	+	+	+	+	+	+	
Model #7	+	+			+	+	+
Model #8	+	+	+		+	+	+
Model #9	+	+	+	+	+	+	+

Figure 4.3: Matrix partitioning for different front window antennas.

To validate the matrix partitioning method, simulation models based on the direct solution and on the matrix partitioning solution of the different front window antennas were realized. The obtained reflection coefficient of the different antennas is compared with the two solutions in a frequency range from 30 MHz up to 150 MHz. Figure 4.4 shows both simulation models of Model 1 and Model 2 and the simulation results obtained with the direct and the matrix partitioning solution. On the one hand, Model 1 is composed from the base layer and part 1 highlighted in blue in Figure 4.3. On the other hand Model 2 is composed from the base layer and part 1, 2 and 4 as shown in Figure 4.3. It can be seen that the same results are obtained with both solutions.

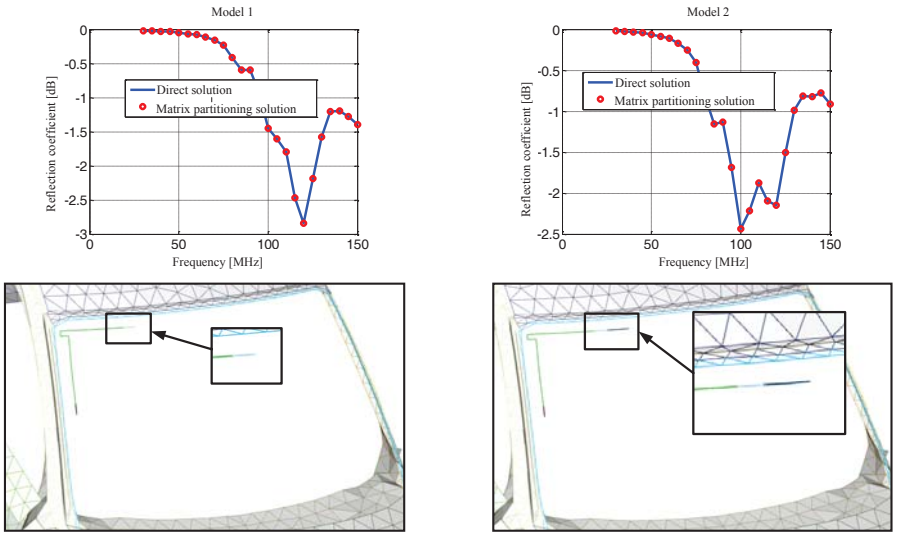

Figure 4.4: Comparison of direct and matrix partitioning solution for Model 1 and Model 2.

Figure 4.5 shows both the simulation models of Model 4 and Model 5 and the simulation results obtained with the direct and the matrix partitioning solution. Model 4 is composed from the base layer and part 1 and 4 shown in Figure 4.3. Model 5 is composed from the base layer and part 1, 2, 4, and 5 as shown in Figure 4.3.

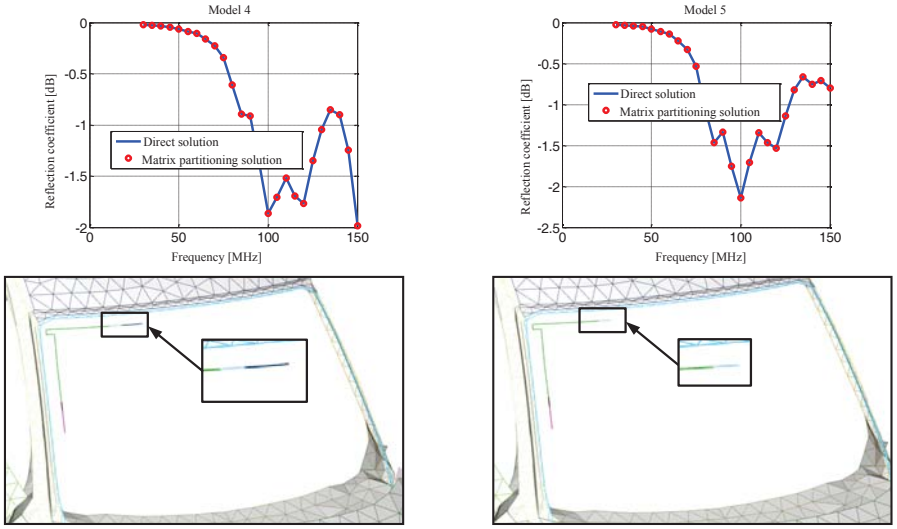

Figure 4.5: Comparison of direct and matrix partitioning solution for Model 4 and Model 5.

The results obtained confirm the previous results presented in Figure 4.5. Validated simulation results of the reflection coefficient from all investigated configurations are compared and presented in Figure 4.6. In this way, the optimal obtained antenna structure that corresponds to Model 6 in this investigation can be defined. Besides that, the antenna gains achieved from the different configurations are compared and presented.

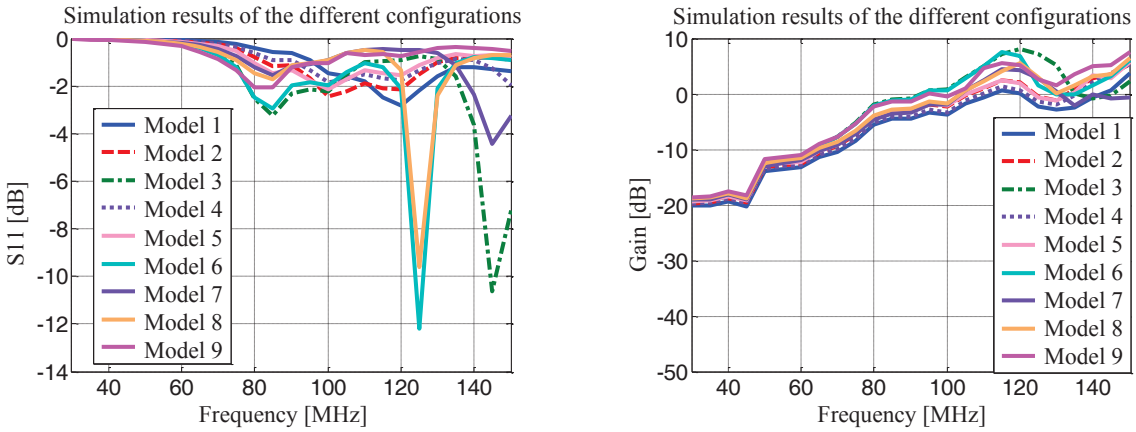

The time efforts required for direct and matrix partition solution (25 sample points) are listed in table. Calculations were performed on 2-core Xeon 3.0 GHz, 2CPU, 16 GB RAM.

Solution type	Computational time for one frequency point
Direct solution (9 tasks)	261 min (29 min per task)
Matrix partitioning (9 partitions)	51 min (32 min for basis + 19 min for 9 partitions)

Figure 4.6: Simulation results of the different configuration by comparison of the computation time of both solution types.

Furthermore, the figure shows a comparison between the simulation time needed for the direct and the matrix partitioning solution. It can be seen, that the simulation time benefit is very important. On the one hand 261 min are needed to calculate the nine different tasks for 25 frequency points. On the other hand, only 51 min are needed for all tasks and for the 25 frequency points to get the same results with the same accuracy. Both solutions are obtained with simulations on the same hardware with details indicated at the bottom left corner of Figure 4.6.

4.2.2 Matrix Partitioning for Glass Window Parameter Investigations

Due to the fact that supplier can change from car model to car model and that the glass parameters can change between the glass delivered, the matrix partitioning method can be used to investigate the impact of the glass parameters on the antenna characteristics. Various glass types form different suppliers were measured. The results are shown in the table illustrated in Figure 4.7. The relevant parameters are the glass permittivity ε_r, the dielectric loss factor $\tan\delta$ and the glass thickness d.

Glass	Thicknes s	Permittivity	Dielectric Loss Factor
Glass1	3.5 mm	6.8	0.02
Glass2	3.0 mm	6.8	0.02
Glass3	4.0 mm	6.8	0.02
Glass4	3.5 mm	7.0	0.02
Glass5	3.5 mm	7.5	0.02
Glass6	3.5 mm	6.8	0.015
Glass7	3.5 mm	6.8	0.005

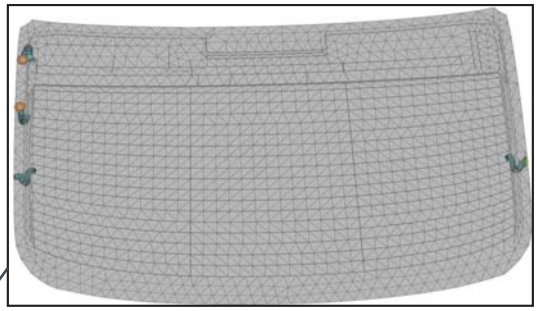

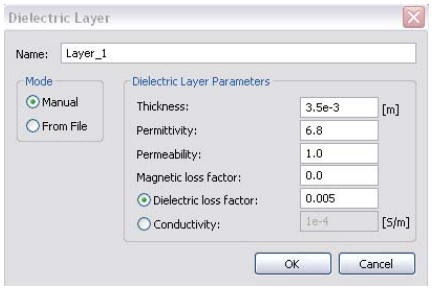

Figure 4.7: Matrix partitioning for different front window antennas.

The results obtained from the glass parameter investigations are presented in Figure 4.8. From the shown results, it can be seen that the different parameters can affect the antenna reflection factor. This impact remains negligible in most of the investigated configurations. However, to avoid any inconvenience in the results, it is advisable to take into account the precise glass parameters.

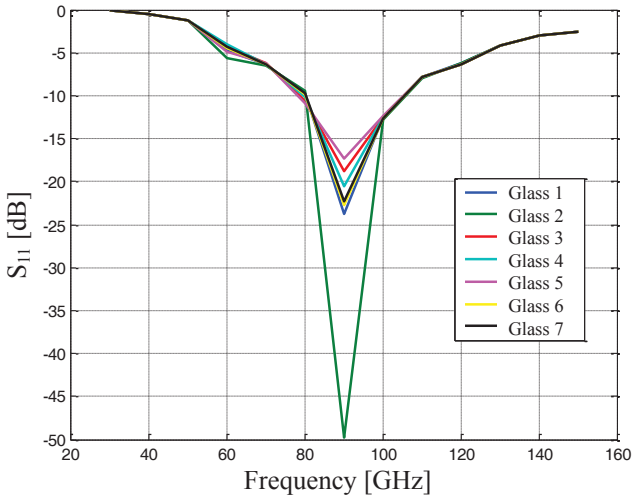

Figure 4.8: Matrix partitioning for different rear window antennas.

4.2.3 Matrix Partitioning for Rear Window Parameter Investigations

A further application of the matrix partitioning method is to optimize rear window antennas, where a large part of the simulation model of all investigated configurations remains unchanged as shown in Figure 4.9.

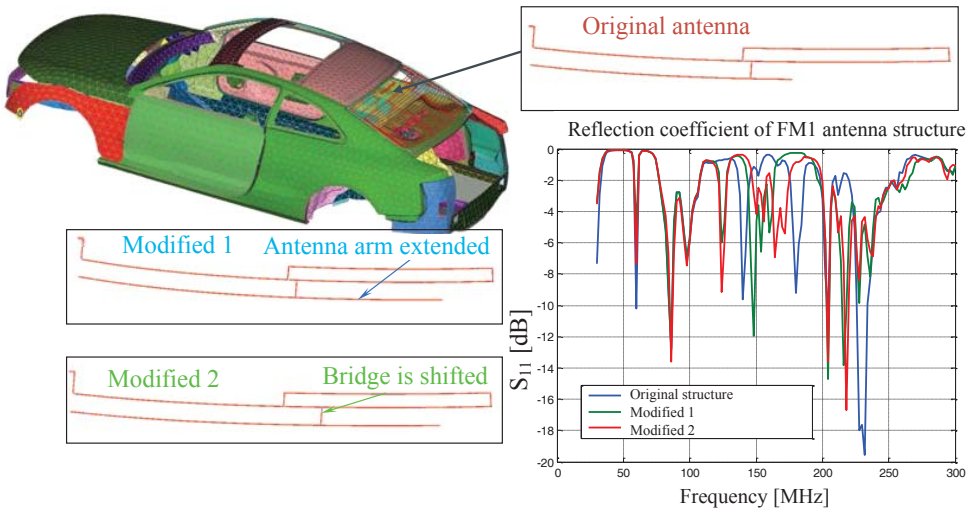

Figure 4.9: Optimization of printed antenna on the rear window.

The results obtained show that slight changes in the antenna structure can cause shifting of the reflection factor. With small changes in the antenna structure, antennas can be optimized to reach the best possible antenna characteristic in the desired frequency range.

4.3 Multi Partitioning and Multi Excitation Approach

An effective antenna optimization process should not only take all antenna structures into consideration during the development process but also the antenna characteristics of all available antennas should be controlled for each optimization loop. By means of this, the antenna characteristics of each antenna has to be simulated. This necessitates to change the voltage sources on the antenna terminations for each configuration. Fortunately, it is possible to combine the multi excitation approach and the multi partitioning method to reduce computation time. The scheme illustrated in Figure 4.10 shows an example of an optimization process of three different antennas, which are located very close to each other. During the optimization of any one of these three antennas, the multi partitioning approach is used for the computation and at the same time, the multi excitation approach is used to check how the antenna behaviour of all antennas changes during the optimization of one of the antennas.

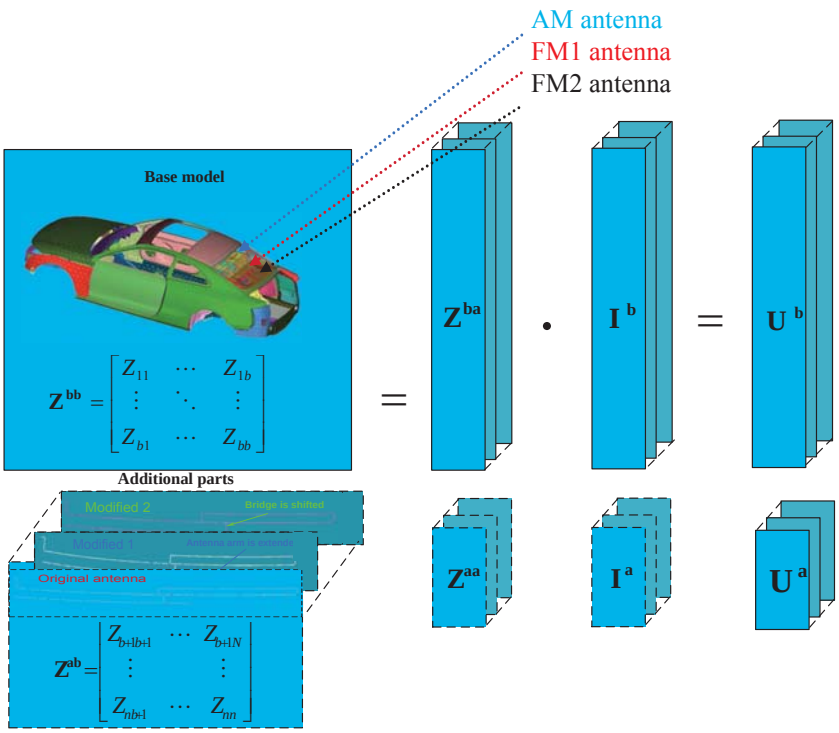

Figure 4.10: A combined multi partitioning and multi excitation approach.

An advantage of the presented scheme is furthermore demonstrated by comparison of the simulation results and computation times in a real AUDI A5 FM antenna optimization [Bogd 10]. In this investigation, a chain of simulation models with different mounted antenna amplifiers based on the multi partitioning and multi excitation approaches are carried out. The illustration in Figure 4.11 shows a vehicle exposed to electromagnetic plane waves positioned at

different elevation angles to determine the antenna radiation pattern for both vertical and horizontal polarization at the region of interest. Additional simulation details concerning the antenna pigtails connecting the amplifiers to the antenna structures are illustrated in the table shown in the figure.

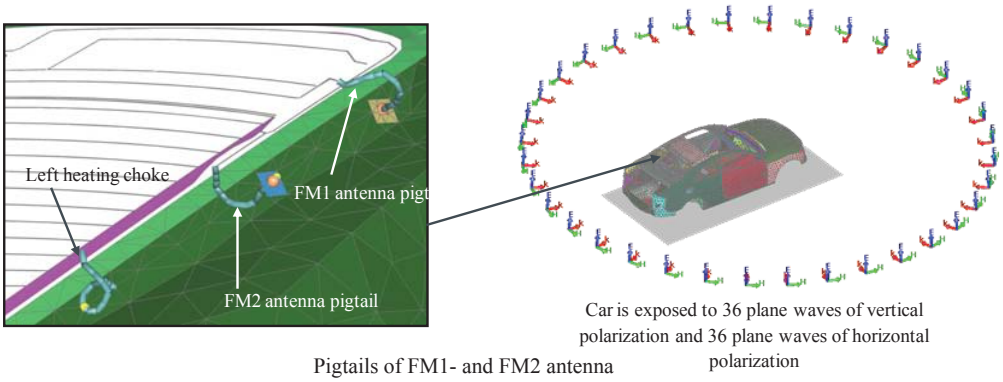

Pigtails of FM1- and FM2 antenna

	Parameter	FM1 antenna	FM2 antenna
Pigtail	length, [cm]	10	8
	radius, [mm]	0.3	
	Insulation radius, [mm]	0.3	
	permittivity	2.3	

Figure 4.11: Far field investigation by different antenna amplifiers.

Figure 4.12 illustrates the obtained results, where the effect of the different antenna amplifiers suitable for different frequency ranges can be seen. The two antenna amplifiers for DAB and TV services are operating at 177.5 MHz and 184.5 MHz. Hence, the highest obtained coupling voltage to the antenna system is obtained in configurations with both antenna amplifiers.

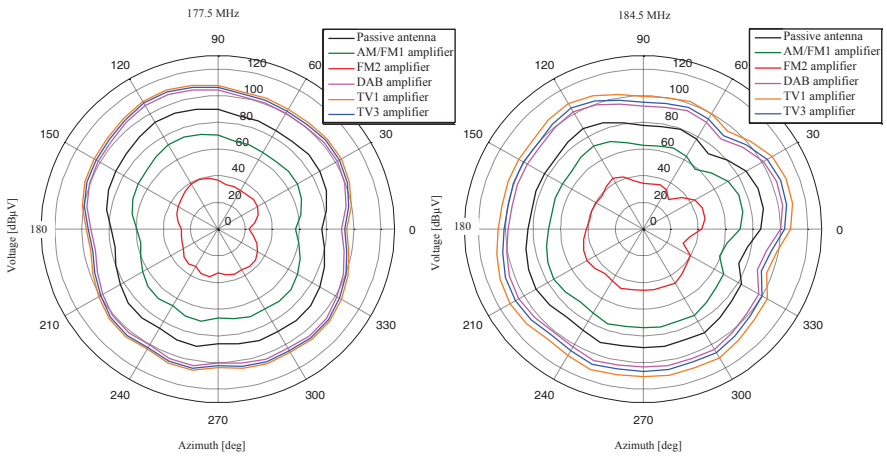

Figure 4.12: Far field results of the different antenna amplifiers.

4.4 Further Methods for Computation Time Optimization

An additional computation time optimization is given by the **A**daptive **F**requency **S**ampling (**AFS**) and the **F**requency **D**istribution **A**lgorithm (**FDA**) [User 05; FEKO 07].
The AFS algorithm allows to define the maximum number of calculated frequency points between the limits of the calculation frequency range of interest. The algorithm defines the calculating frequencies not from the lowest to the highest frequency but rather in loops. The first frequency loop starts with the lowest frequency and ends with the highest one from the complete calculation frequency range. A sampling between the two frequencies is chosen controlled by the maximum defined number of frequency samples and by the size of the frequency range. An additional important parameter in the AFS is the accuracy, which controls the fitting error limit for controlling convergence of the fitting model. The default value used in EMC Studio is set to 5% [User 05]. The algorithm compares the obtained results between two adjacent frequencies. If the difference between the two calculated values (impedance) is higher then the defined accuracy value, an additional frequency point will be set between those frequencies for calculation. This procedure is repeated until either the maximum set sampling frequency number is reached or the accuracy condition is satisfied. Once all frequencies are calculated, the calculated values are interpolated and give the final result. The first stopping condition in the AFS is the accuracy parameter. By means of this, the AFS algorithm stops the simulation when the accuracy parameter is satisfied even if the maximum number of the sampling frequency points is not reached.
The FDA is used in particular when simulations are performed on multiprocessors, especially for clusters and parallel computers with sufficient storage memory [Yavo 05]. The algorithm makes it possible to perform each frequency on one processor. This approach is more effective if the memory required for the computational task can be predicted. This memory can be estimated according to the number of unknowns in the MoM equation derived from the number of simulation model elements (triangles and segments). According to the required memory, many simulations at different frequencies can be allocated simultaneously to the available processor nodes. Hence, the required simulation time is reduced considerably.
A further method for optimizing computation time, in case of the method of moments, is the **M**ulti **L**evel **F**ast **M**ultipole **M**ethod (**MLFMM**), which allows large simulation models to be handled while keeping the same accuracy as the standard MoM [Kone 05]. However, it is difficult to implement the MLFMM in the available MoM codes containing additional hybrid methods such as the MAS or the incorporation of network elements in the MoM while keeping the same accuracy.

5 Generation of the Simulation Model

5.1 General Rules for Simulation Model Generation

The **C**omputer **A**ided **D**esign (**CAD**) model quality is of crucial importance in electromagnetic simulations for obtaining good agreement between simulation and measurement results [West 10; Joba 03a]. For this reason, the majority of simulation frameworks currently available offer several possibilities for obtaining precise virtual models. The consideration of geometrical details increases the accuracy of results. Figure 5.1 shows an example of a simulation model adapted for glass antenna investigations.

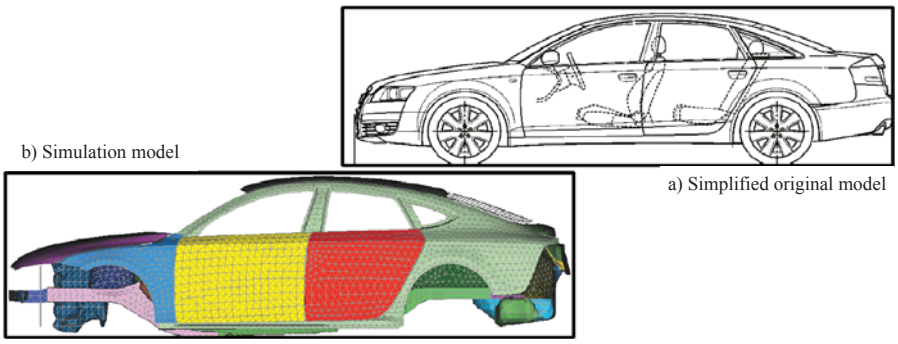

Figure 5.1: Generation of an adequate simulation model.

The model building represents the first step in the simulation process [Anto 05]. Especially for higher frequencies, the model accuracy can have a decisive impact on the accuracy of the simulation results [Mart 05; Marh 02]. Simulation models can differ depending on the computation approach used [Maur 06; Maur 01]. For example, on the one hand, MoM simulation requires models based on surfaces to apply the Green's function. On the other hand, FEM simulations are performed with volume simulation models, where the complete volume is discretized. Also, depending on the Green's functions used for MoM simulations, different meshes must be chosen such as triangles or rectangles. The process is described in Figure 5.2. Usually, this process takes a long time at the start of each new problem description to guarantee that system development can be done based on simulation only.

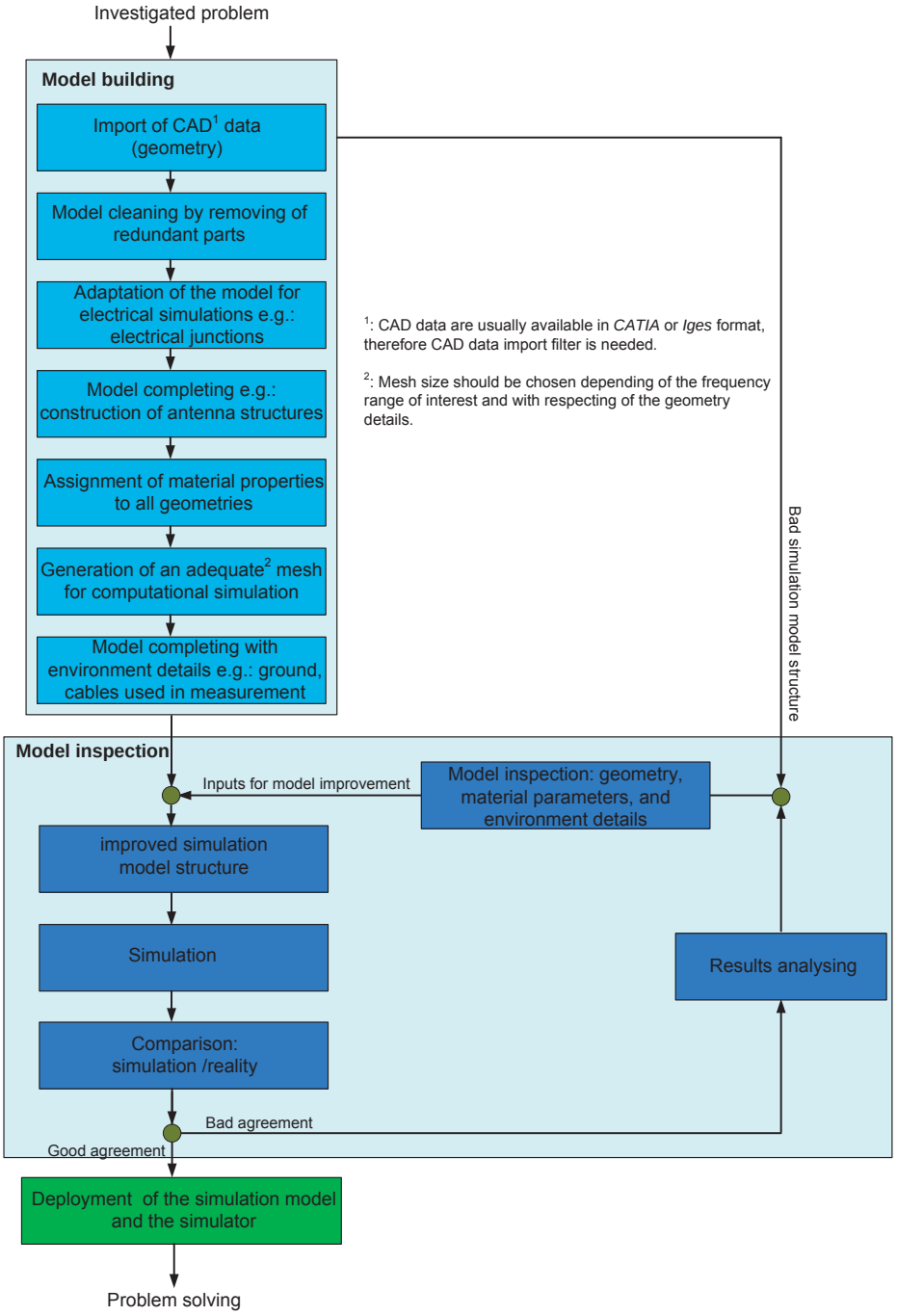

Figure 5.2: Simulation model building process.

This process can be subdivided in the following steps described in Figure 5.2.

1. Import of CAD data: The geometry of the investigated problem should be imported in the CAD data format convenient to the simulation framework. For this, several CAD import filters are available in the different simulation tools. Usually, CAD data are available in the following popular formats [Vajn 09].

- **C**omputer **A**ided **T**hree-Dimensional **I**nteractive **A**pplication (**CATIA**) data format are encountered in a CAD software developed by the Dassault Systemes company [CATI 11].
- The **I**nitial **G**raphics **E**xchange **S**pecification (**IGES**) is an additional file format that allows the digital exchange of CAD information.
- The 3D **ACIS** Modeler (ACIS) format also called **SAT** files arises in a 3D modelling kernel owned by Spatial Corporation ACIS and represents an underlying 3D modelling functionality for different CAD tools.
- **NA**sa **STR**uctural **AN**alysis system (**NASTRAN**) is a **F**inite **E**lement **A**nalysis (**FEA**) developed in the late 1960s for NASA. Nastran files are often used by simulation tools to describe a model mesh and can be exchanged between the different commercial simulation tools.
- The 3D **ACIS** Modeler is a computer-aided design 3D modelling kernel owned by Spatial Corporation.
- **S**tandard **T**emplate for **E**lectronic **P**ublishing (**STEP**) is also used for CAD data exchange.
- **D**rawing e**X**change **F**ormat (**DXF**) is a CAD data file format developed by Autodesk enabling data exchange between AutoCAD and other CAD or simulation programs [Auto 11].

2. Cleaning phase: The next step is to eliminate all redundant data. The available CAD data contain more model information than needed for the EM simulations.
3. Modification of the simulation model for EM simulations: In this step, the right junctions between object parts are mandatory. The current distribution in the simulation model can be affected in case of incorrect junctions.
4. Model completion: In this step, missing information in the simulation model should be completed. In case of antenna simulations, it is quite often the case that only the glass surface is available and sometimes the heating structure in the form of lines is also existent. For an appropriate antenna simulation, the antenna model should be generated based on the available data [Titt 91; Abou 98].
5. Assignment of material parameters: Once the geometry model is finished, the developer can start by assigning the material parameters. The most important parameters are [Bowl 06]:

- the permittivity ε_r,
- the electrical loss factor $\tan\delta$,
- the permeability μ_r,
- the magnetic loss factor $\tan\delta_m$,
- the resistivity ρ or the conductivity σ,
- the material thickness for glass screens. In case of wires with coating, both geometry data and material parameters for the inner radius as well as for the outer radius should be considered.

6. Generation of an adequate mesh for computational simulation: The segment or the cell edge size depend on the frequency range of interest or from the time steps in time domain. Discretization should be realized by taking into account the geometry information, which should be reflected as precisely as possible with the discretized model.

7. Model completion with environment details: Usually, simulation models are validated by measurements. The obtained measurement results can be influenced by the measurement setup such as the measurement cables and the general measurement environment such as the ground. To obtain an optimal agreement between measurement and simulation results, these details should be considered while generating the simulation model.

8. Model inspection: Once the simulation model is completed, calculations can be carried out by using the appropriate simulator. After the first simulation, comparison between simulation and measurement results should be realized. Afterwords, results have to be analyzed to be able to explain any discrepancy between the obtained results. Consequently, the simulation model should be improved. This improvement loop should be applied until the agreement between the results is satisfactory.

9. Deployment of the simulation model and the simulator: When the simulation model is validated, the development process based on simulation of the investigated problem (antenna, device...) can start. Many simulations can be performed to investigate the impact of geometry or material parameters with the objective of developing the best possible device e.g.: an antenna.

5.2 Discretization Rules for MoM Simulation

In addition to the fact that the mesh size should be chosen in a manner that the geometry model is not infringed, accurate mesh model generation for the simulations requires certain discretization rules, which should be respected when linear basis functions for the MoM solution are used. The following segmentation rules are derived from multiple MoM simulation experiences summarized in [Tazi 08] to reach an acceptable accuracy when the simulation framework EMC Studio is used.

- The segment length and the triangle edge length should be smaller than one tenth of the smallest wavelength $\lambda_{\min}$ according to

$$l_{element-length} < \frac{\lambda_{\min}}{10} \tag{5.1}$$

  where $\lambda_{\min} = \frac{c_0}{f_{\max}}$, c_0 is the speed of light and $f_{\max}$ is the highest frequency. In case of a maximal frequency of 300 MHz the smallest wavelength is $\lambda_{\min} = 1\,\mathrm{m}$. Therefore, the smallest mesh size should be smaller than 10 cm.

- In cases where the distance between two elements (segments or triangles) is a, a mesh size of $l_{segment} \leq 2\,a$ should be chosen.

- For wire modelling, if the wire diameter (including insulation) is d then it should be ensured that the segment length $l_{segment} \geq 3\,d$.

- When the distance from a wire to a metallic plate is h then the segment lengths and the edge sizes of triangles located directly under the wires should fulfil the following rule:

$$l_{segment} = l_{edge-length} \leq h\,. \tag{5.2}$$

- The length difference between two adjacent elements has to be smaller than three times of the smallest element length.

5.3 Glass Antenna Model Generation

Usually, the glass geometry is imported in CATIA format. Fortunately, simulation tools used nowadays contain different CAD import filters, which make it easy and flexible for antenna development engineers to use different available CAD data formats.
Similar to all raw CAD data, available glass CAD data contain more information than it is needed for automotive antenna simulations. Therefore, CAD data have to be cleaned and reduced.

In addition to the cleaning phase stated, the process of mesh generation for the computational model needs further steps, which can be summed up in the following scheme [Gheo 11b; Gheo 11a; Gheo 09]:

- Import of CAD data. Figure 5.3 a) shows an example of imported raw CATIA CAD data for a particular glass geometry.

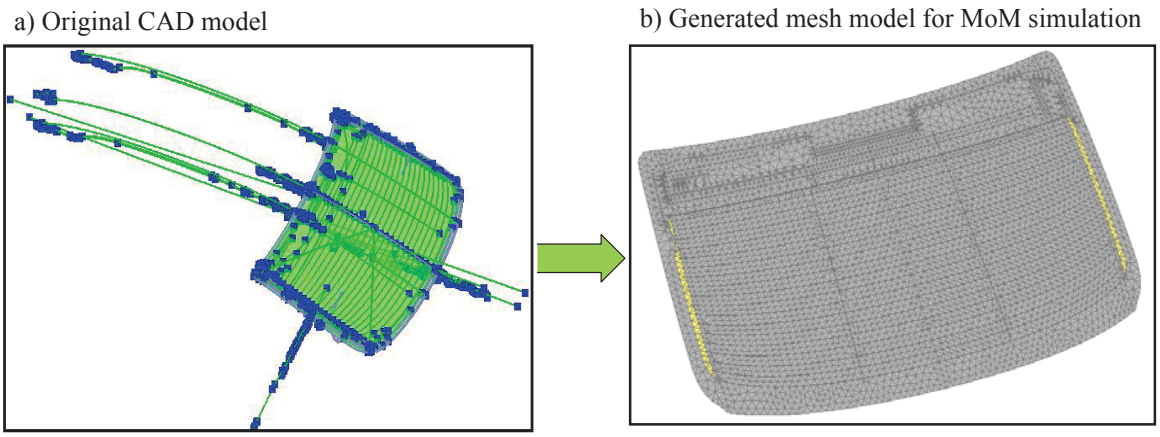

Figure 5.3: Generation of the glass antenna model for a car rear window.

- Geometry cleaning by removal of volumes, surfaces and curves, which are redundant for the antenna computational model.
- Construction of the antenna structure by merging curves and creating surfaces for metallic strips on curves.
- Projection of antenna structure to glass surface to obtain a correct geometry model.
- Removal of the antenna structure.
- Assignment of the material parameters for glass and the metallic antenna structure.
- Mesh model generation including choosing the correct mesh steps with respect to the mesh rules for the MoM simulations stated in Section 5.2.

Figure 5.3 b) shows an example of generated mesh for MoM simulations. Accurate simulations based on the hybrid MoM-MAS requires two different mesh files for both the model of the printed antenna on glass and for the actual glass. The antenna structure has to be saved separately, where triangles that do not belong to the antenna should be removed as illustrated in Figure 5.4 a). The second file contains the glass structure with all triangles generated during the process of mesh generation according to Figure 5.4 b).

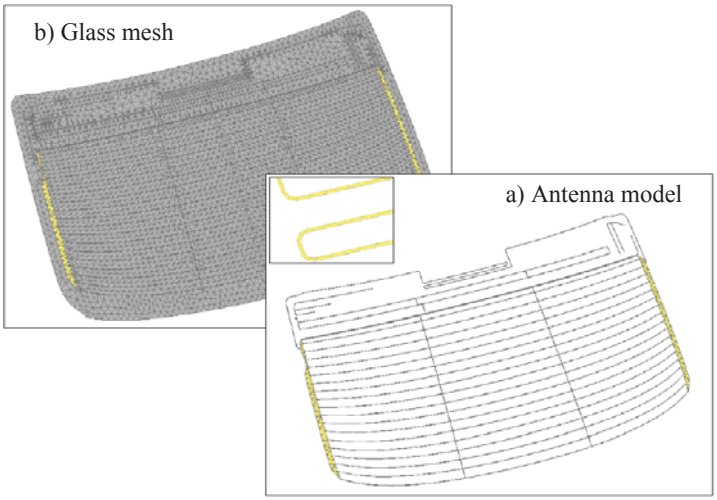

Figure 5.4: Generation of the antenna and glass model.

5.4 Modelling of Electrical Networks

In addition to antenna structures and the car body, further electronic devices such as antenna amplifiers and electronic control units can affect the RF signals [Rabi 10]. Figure 5.5 shows a mounted antenna amplifier in a car serving to amplify and to transmit the received signals from the antennas to the signal processing units.

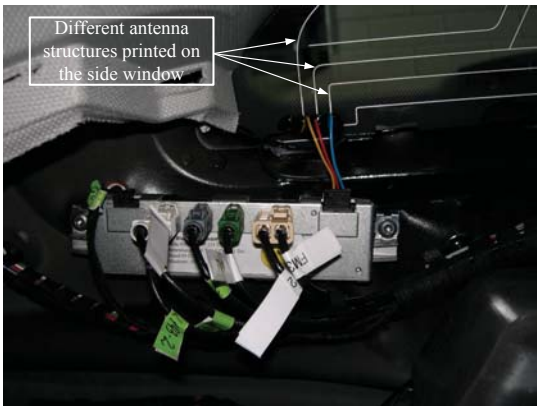

Figure 5.5: Picture of an antenna amplifier installed in a car.

Figure 5.6 illustrates a case of glass antennas using the heating structure to extend the antenna length. To separate the RF signal from the DC current, electric filters and chokes are used. The electrical networks and chokes used can be often described according to Figure 5.6 with simple electric components such as resistances, inductances and capacitances.

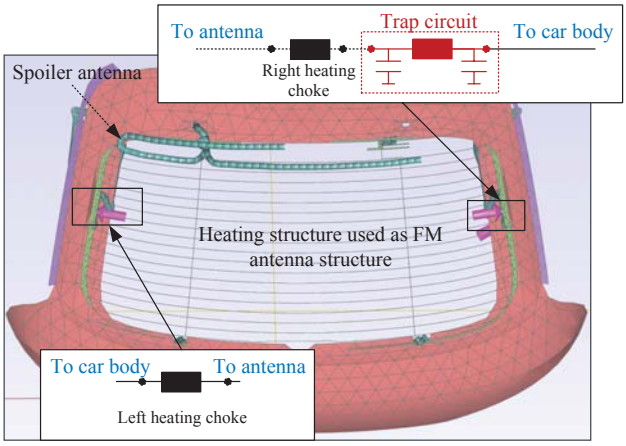

Figure 5.6: Filter structure modelling.

Depending on the simulation purpose, different ways of integrating antenna amplifiers in simulation models can be used. It is obvious that the antenna amplifier input impedance often differs from the antenna input impedance and consequently changes the antenna return loss. It is sufficient to describe the antenna amplifier network only with a complex input impedance in cases, where the goal of the simulation is to take into account the influence of the antenna amplifier on the antenna return loss. However, in the automotive antenna development process, engineers are generally interested in the antenna gain as well as in the antenna return loss. To calculate the complete antenna system gain, it is necessary to take into account the whole antenna amplifier scattering matrix in the simulation. The antenna installed in the car will be irradiated with electromagnetic plane waves located at fixed elevation angles and for each polarization according to the simulation model illustrated in Figure 5.7. The radiation pattern of the investigated antenna can be constructed from the coupled voltage at the receiving antenna input impedance from each plane wave. From the coupling voltage different antenna radiation patterns characteristics can be derived like the antenna gain or antenna directivity. It is laborious and time consuming to make both simulations of the radiation pattern and the antenna return loss separately. This is due to the fact that two different simulation models should be prepared in the simulation preprocessing phase. Moreover, simulation data evaluation of the multiple simulation result files in the post-processing phase is also laborious because of the multiple radiation plane waves needed to calculate the antenna radiation pattern.

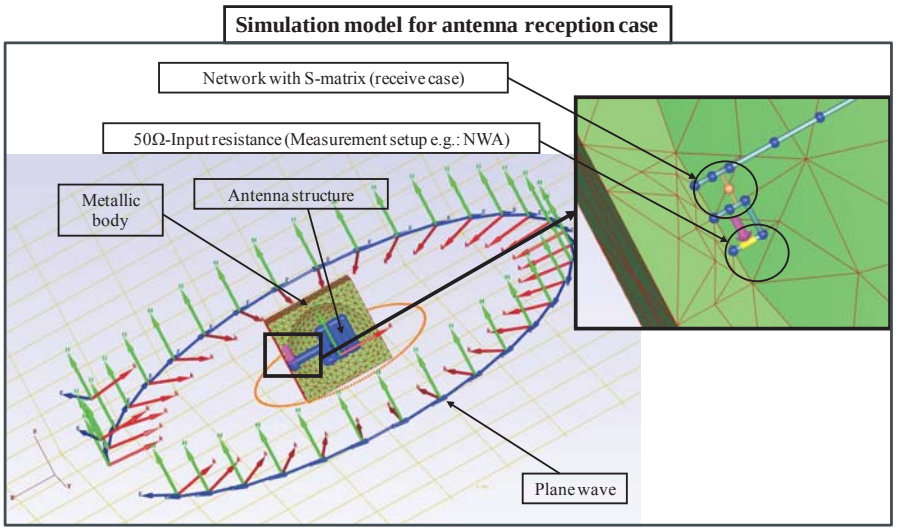

Figure 5.7: Simulation model for antenna receiving case.

It is obvious that antenna characteristics in the emitting case remains the same in the antenna receiving case for passive antenna systems because of the antenna reciprocity [Bala 05]. Unfortunately, it is different in the case of automotive antenna systems because of the active elements in the antenna amplifiers. The simulation model illustrated in Figure 5.8 presents a solution to overcome this simulation model generation dilemma. The system considered is in the emitting case. This can be modelled with a 1 V voltage source at the antenna termination. The antenna amplifier network is normally described with a $\mathbf{Z}$ matrix according to

$$\mathbf{Z} = \begin{bmatrix} z_{11} & z_{12} \\ z_{21} & z_{22} \end{bmatrix} . \tag{5.3}$$

However, to generate a simulation model suitable for both return loss calculation and radiation pattern determination, the inner network impedance matrix parameters z_{12} and z_{21} are exchanged and the network is described with the modified $\mathbf{Z}'$ matrix according to

$$\mathbf{Z}' = \begin{bmatrix} z_{11} & z_{21} \\ z_{12} & z_{22} \end{bmatrix} . \tag{5.4}$$

To validate the emitting case method, simulation models based on the voltage source method (emitting case) and the plane wave method (receiving case) of the shown antenna structure in Figure 5.7 and Figure 5.8 are generated. Radiation pattern results obtained from both methods are compared.

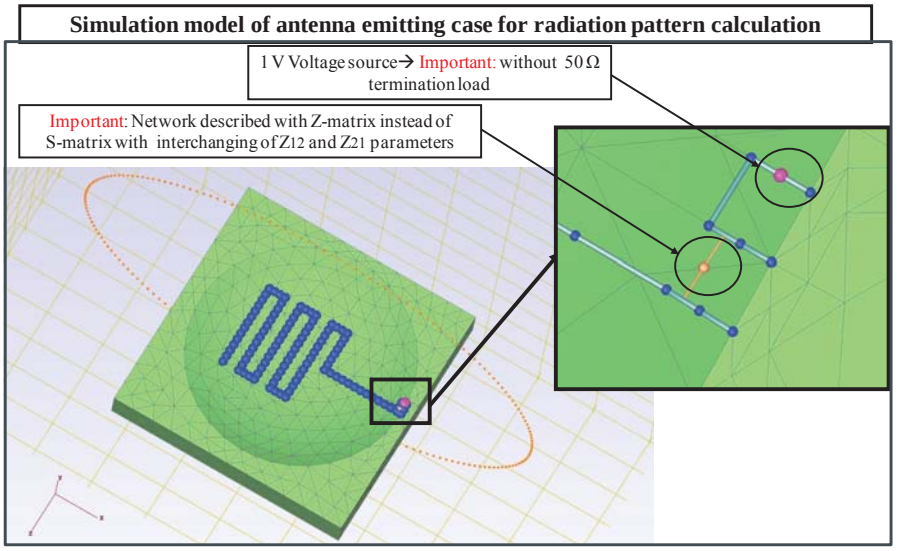

Figure 5.8: Simulation model for antenna emitting case.

From the simulation results shown in Figure 5.9, it can be seen that both methods deliver the same antenna radiation pattern. Validation is performed for different frequencies.

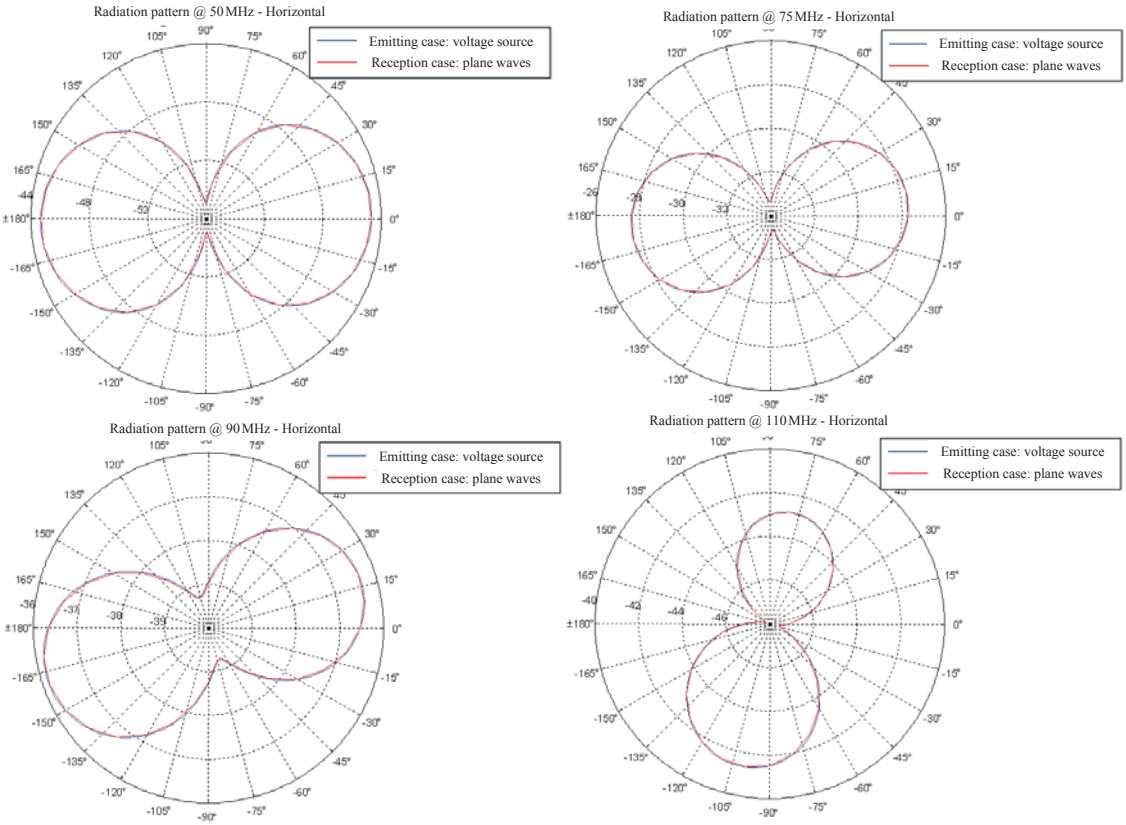

Figure 5.9: Validation of the emitting case for far field calculation.

Figure 5.10 gives the physical background that explains why both methods lead to the same results. The starting point is the antenna factor, which remains the same in the case of emitting and receiving antenna system when the antenna mismatching is taken into account. The radiation pattern of the antenna in terms of received voltage from each plane wave depends on the impedance antenna termination Z_{load}, the free space wave impedance Z_0, the wavelength λ as well as from the calculated antenna gain G_0 based on the network modified impedance network Z'.

- The antenna factor remains the same in reception and emitting case with accounting of the antenna mismatching.
- The antenna mismatching factor $\eta_{mismatch}$ is given by

$$\eta_{mismatch} = 1 - |S_{11}|^2$$

- The received voltage is calculated with accounting of the antenna mismatch and antenna factor as follows:

$$V_{recieved} = \frac{E_{incident}}{\sqrt{\frac{480\pi^2}{Z_{load}\eta_{mismatch}\lambda^2 G_0}}}$$

- Z_{load} :Impedance at antenna termination
- Z_{F_0} :Free space wave impedance $120\pi\,\Omega = 377\,\Omega$
- A_{eff} : Effective receiving antenna, [m²]
- G_0 : Antenna gain

$$AF = \frac{E_{incident}}{V_{recieved}} = \sqrt{\frac{Z_{F_0}}{Z_{load}\eta_{mismatch}A_{eff}}} = \sqrt{\frac{Z_{F_0}}{Z_{load}\eta_{mismatch}\frac{P_{available}}{S_{inc}}}} = \sqrt{\frac{Z_{F_0}}{Z_{load}\eta_{mismatch}\frac{\lambda^2}{4\pi}G_0}} = \sqrt{\frac{480\pi^2}{Z_{load}G_0'\lambda^2}} = \sqrt{\frac{480\pi^2}{Z_{load}\eta_{mismatch}\lambda^2 G_0}}$$

Figure 5.10: Calculation of the received voltage with taking into account the antenna factor and mismatch.

5.5 Ground Modelling

Measurements of the far field radiation pattern performed at the AUDI AG measurement test site illustrated in Figure 5.11 are done by setting the **D**evice **U**nder **T**est (**DUT**) on a turntable in a free space measurement range [Tazi 11a; Ullr 10]. This is limited to an elevation angle of about eighty-six degrees due to the fixed position of the sending antenna in the measurement setup. The transmission factor between the fixed antenna and the DUT is measured continuously during rotation of the turntable over the complete azimuth. Objects in close vicinity to the automotive antennas such as the car's bodyshell or the ground can influence the antenna behaviour [Bala 82]. Hence, accurate modelling of the environment of the investigated antenna should be provided [Tazi 11a; Ullr 10; Ullr 09]. On the one hand, it is important to

consider the maximum amount of detail, which can affect the antenna characteristics such as the turntable and the ground. On the other hand, it should be ensured that all details are correctly interpreted by the simulation framework and that there are no restrictions due to the implemented algorithms in the modelling from the simulation tool side [Hune 05]. Great care should be taken while modelling a real ground, which is approximated by the commonly used simulation frameworks. In [Delg 89; Awad 78], several recommendations are given for ground modelling, permitting an accurate evaluation and development of antennas. Furthermore, investigation results concerning the influence of the glass curvature and the bodyshell on the antenna performance are presented.

Figure 5.11: AUDI AG radiation pattern measurement setup.

The gain of the automotive antennas is measured in the far field as described in Section 2.2 by setting the car on a turntable according to Figure 5.12. Measurements of the far field radiation pattern of automotive antennas are performed by setting the device being tested on a turntable. Figure 5.13 shows how the measured car will be set on a turntable, which is positioned at a distance of 75 m from the transmitting antennas. These antennas are located at an elevation angle of 86° for the horizontal and the vertical polarization.

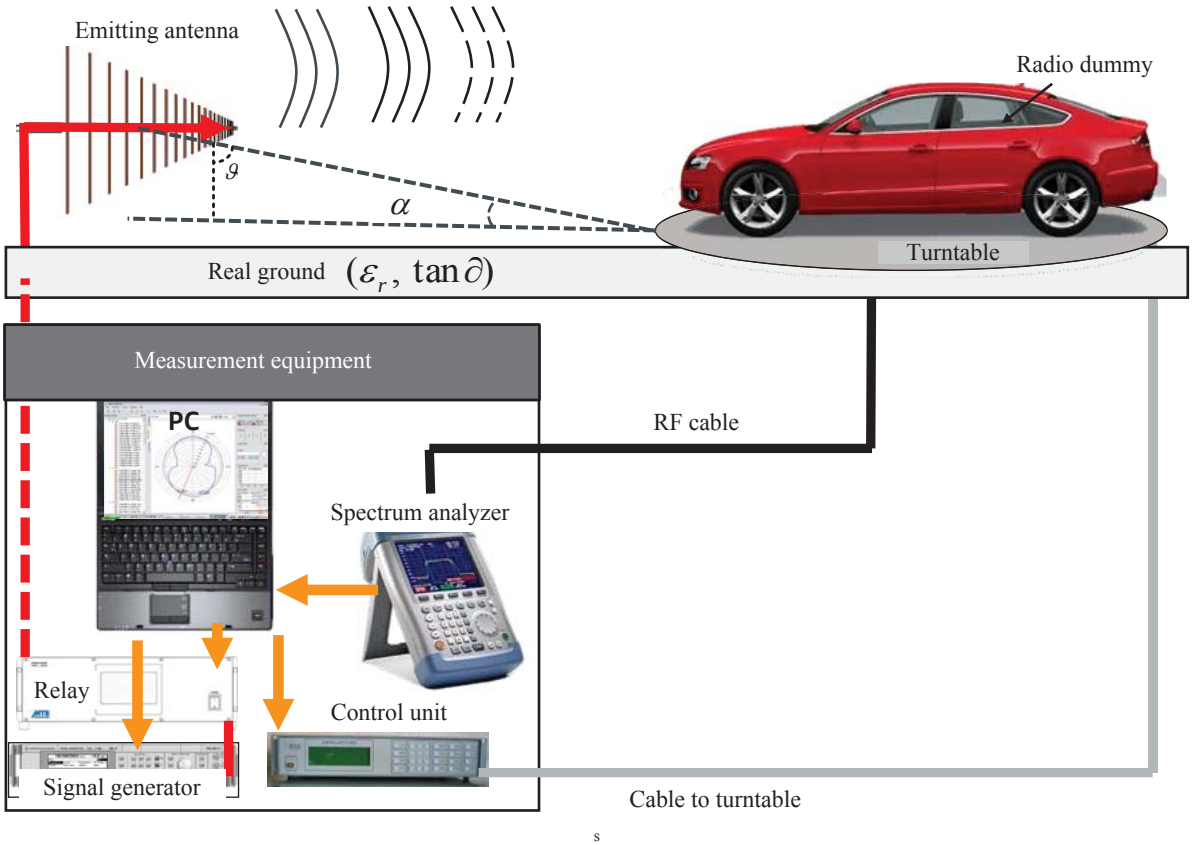

Figure 5.12: AUDI AG radiation pattern measurement setup.

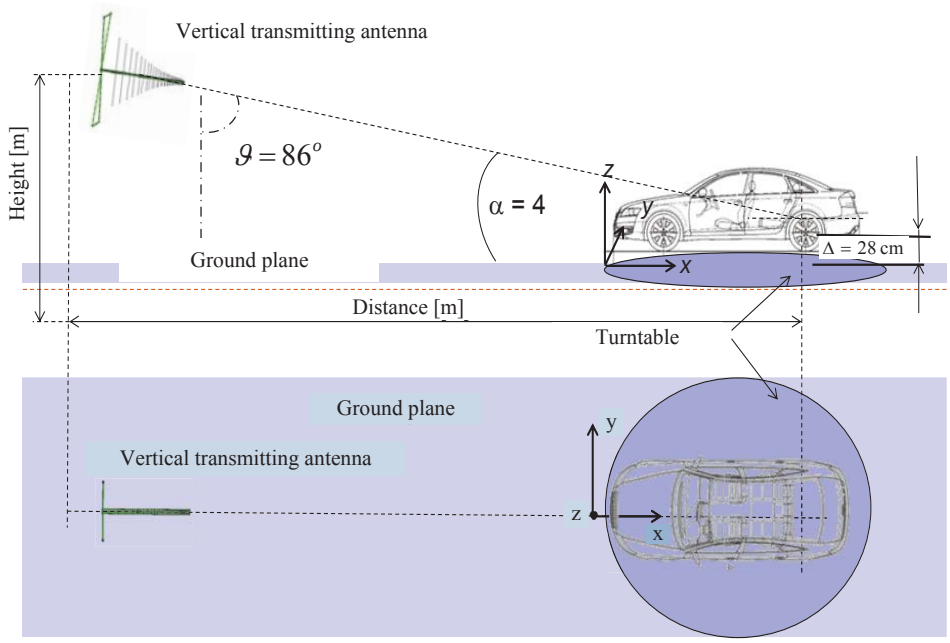

Figure 5.13: Far field measurement at AUDI AG measurement setup.

Figure 5.14 shows how the CAD coordinate system is defined at the Volkswagen Group. It is very important for this to be defined in advance in order to avoid any errors caused by different coordinate systems when measurement results from different car companies are compared or when measurements and simulations are compared.

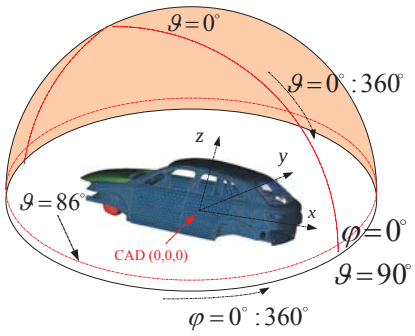

Figure 5.14: Far field definition for simulation and measurement.

Moreover, the modelling of the metallic turntable and the real ground should be taken into account due to their non negligible effects on the far field behaviour. In order to investigate the turntable and the real ground effects, six different simulations were performed. A printed antenna on the car side window was simulated under these configurations. Figure 5.16 shows the difference in the return loss between the individual configurations. This difference is relatively small between all configurations except for configuration *a) Turntable with real ground*. In this configuration, it can be observed that the resonant frequency is shifted slightly to a higher frequency.

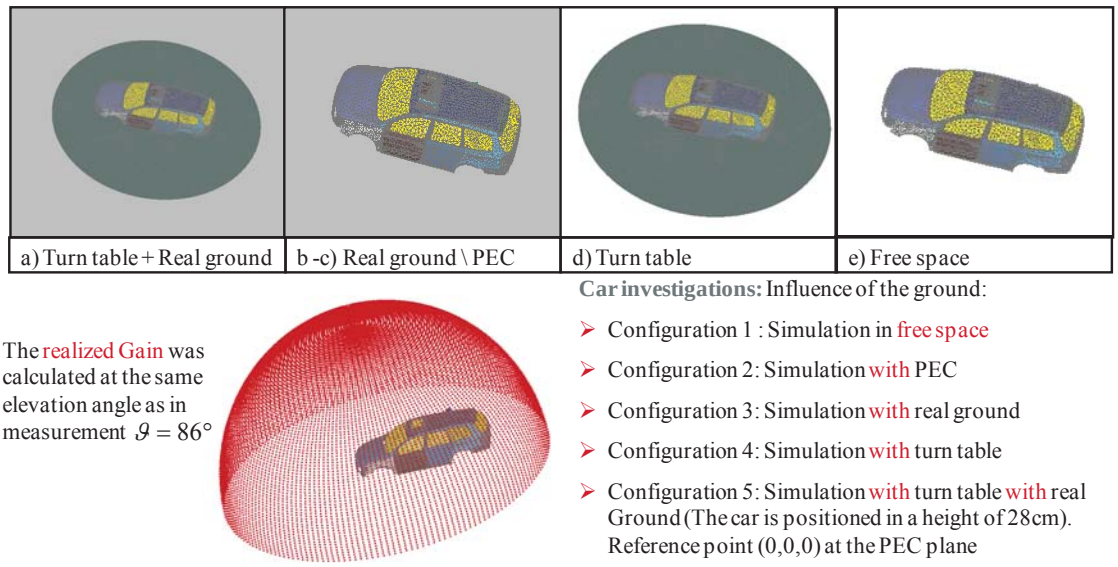

Figure 5.15: Ground modelling investigation.

Figure 5.15 illustrates simulation models of the considered configurations. Both the return loss and the gain in terms of coupled voltage were compared between the different configurations.

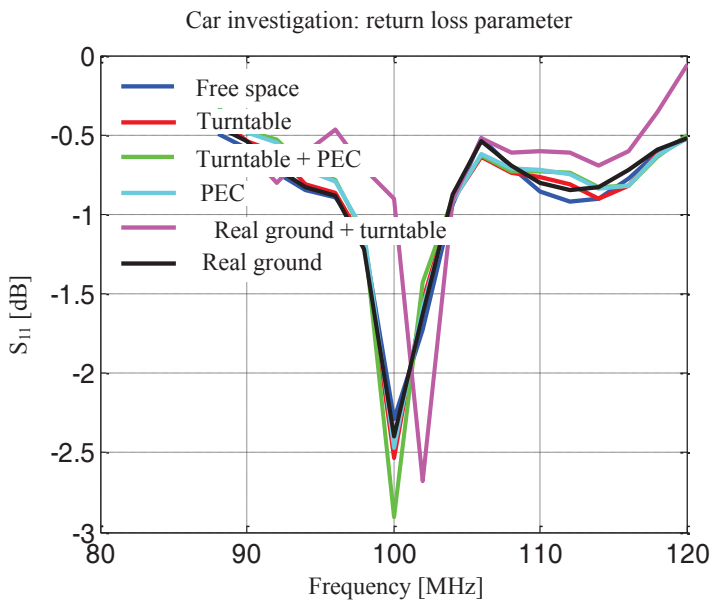

Figure 5.16: Ground modelling investigation results (Reflection factor).

Figure 5.17 shows the influence of the ground and turntable on the far field performance of the car antennas in the six different configurations shown in Figure 5.15. The mean value of the coupled voltage to the antenna from the transmitting antenna over all elevation angles or azimuth angles is presented. Results for different values of the elevation angle ϑ and the azimuth angle φ are compared. It can be seen that the difference between the individual configurations is not negligible for the different angles. In the worst case, this difference can reach values of 30 dB. Some configurations show the same results like the configuration *d) PEC alone* and configuration *b) PEC with turntable* for all presented cross-sections. The difference between configuration *e) Turntable* and Configuration *f) free space* is relatively small. Unusual results are obtained with configuration *b) Turntable with real ground*. This is attributed to the fact that the used simulation tool (EMC Studio) gives incorrect numerical results for the interpretation of this case, where the metallic part (turntable) is in very close vicinity to the real ground. The height from the turntable to the real ground is 1 cm. Because of this, great care should be taken for modelling such problems. Therefore, the correct interpretation of the simulation model by the simulation framework is very important for obtaining correct results. It is important to note that all configurations except configuration b) show the same tendency. This is very important for the development of antennas under consideration of the measurement environment (real ground and turntable). The results from 5.17 show that the only difference between the simulation in free space and the others is a given offset. Therefore,

for the purpose of design, it is possible to consider the free space case in order to simplify modelling and reduce computation time required for the simulation.

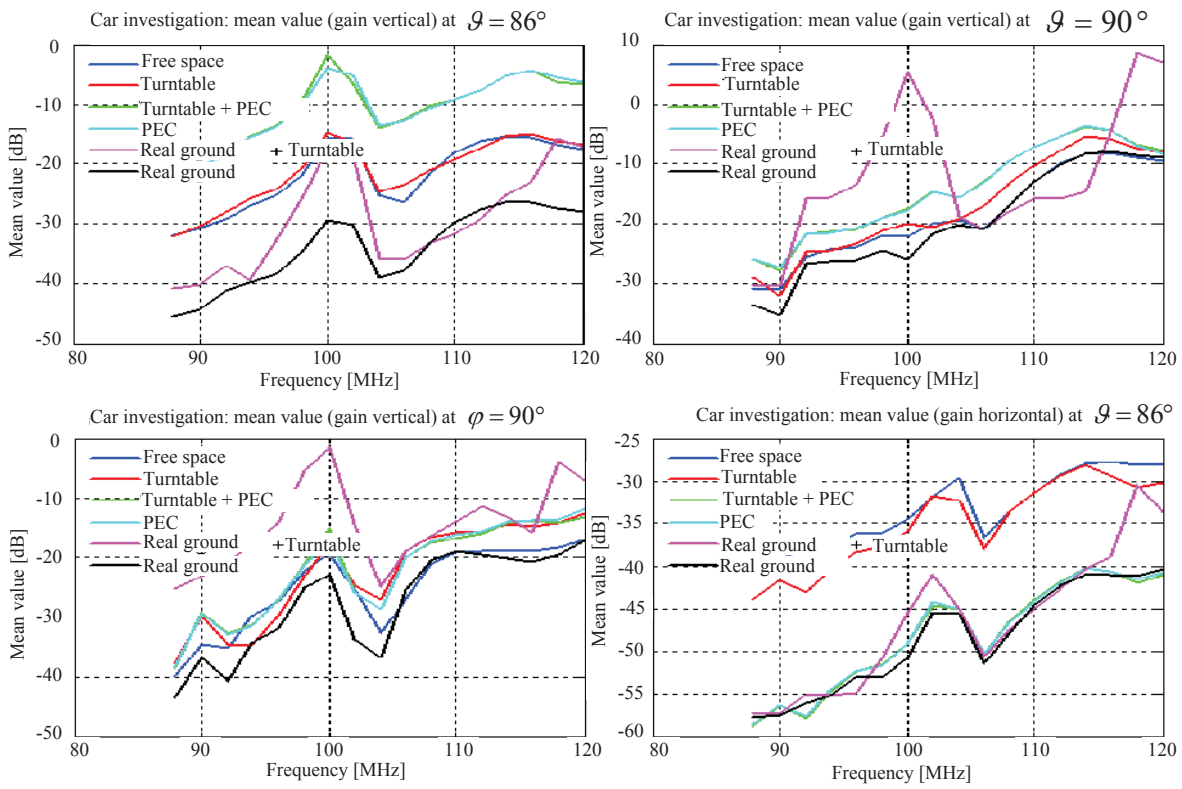

Figure 5.17: Ground modelling investigation results (Gain mean value).

Further investigations should be performed to improve the modelling of very close metallic parts to a real ground for a correct interpretation from the simulation framework. Implementation of Sommerfeld's equations to take account of ground effects could help to obtain successful results [Somm 09].

6 Virtual Development of Glass Antenna Systems

Sometimes printed antennas on flat glass are used in order to predict the antenna behaviour of the same structure on slightly curved glass antennas such the car windows [Tazi 11b]. To ensure that the antenna performance of printed antennas on flat glass is the same as that printed on curved glass, investigations with both variants were performed. Figure 6.1 illustrates the investigated configurations. In the first comparison the two antennas printed on different glass geometries were compared a) and b). In the second comparison, the two antennas without glass were investigated c) and d).

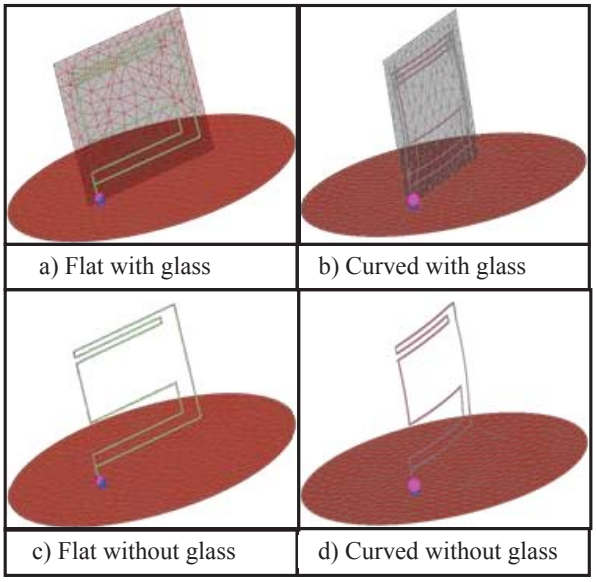

Figure 6.1: Flat and curved glass investigation.

From the simulation results in Figure 6.2, it can be observed that the influence of curvature on the return loss of the antenna is negligible in both cases. However, the return loss of the antenna with glass differs from the one of the antenna without glass. This is due to the dielectric effect of the glass. These results show that the development of glass antennas with slight curvature can be performed without considering the glass curvature. The modelling effort for the simulation and the laborious process of printing antennas on curved glass in real development can thus be reduced.

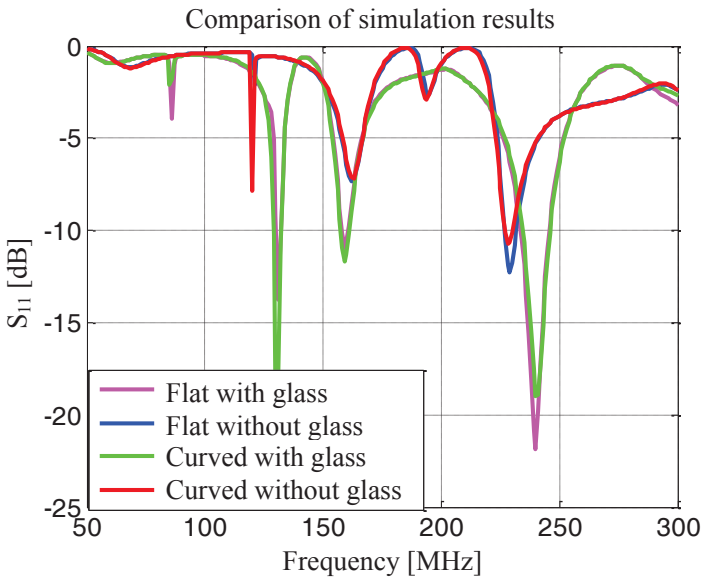

Figure 6.2: Flat and curved glass investigation results.

Besides the use of an adequate numerical simulation approach, the key to achieving accurate and reliable simulation results is the generation of a precise simulation model as shown in Chapter 5.

Figure 6.3 shows an example of a simulation model of an AUDI Q3 used for the virtual optimization of several antennas located on the vehicle rear end. It is important to assign the correct electromagnetic parameters for the windscreens and antenna structures. Investigations performed by the AUDI AG Antenna Department indicated that it is sufficient to assign PEC for most of the car's metallic parts for simulations in the frequency range between 1 MHz and 1 GHz, including the operation frequencies of glass printed antenna systems.

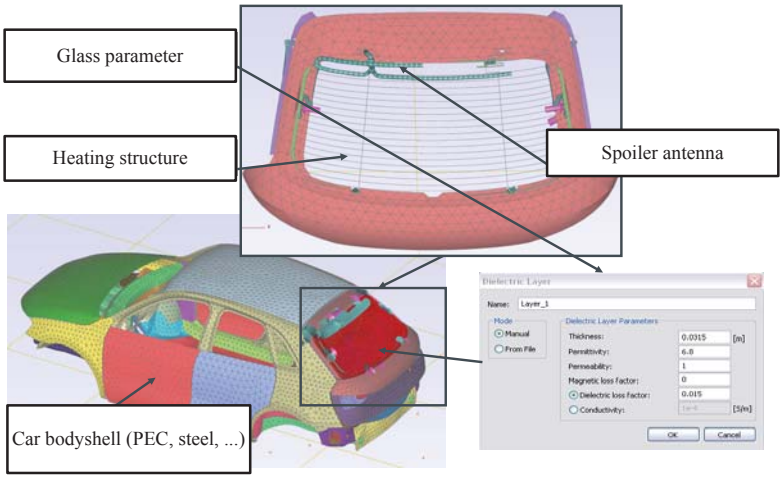

Figure 6.3: Q3 rear window glass antenna simulation model.

Figure 6.4 illustrates all antenna systems installed on the rear end of the Q3 model. Effective development of all antenna systems can only occur if all systems are taken into account simultaneously. In the development process, improvement of the antenna characteristics of the RF services operating at the lowest frequency range is usually done at the beginning. After this, antenna systems operating in higher frequency ranges are optimized, taking the already optimized systems into account.

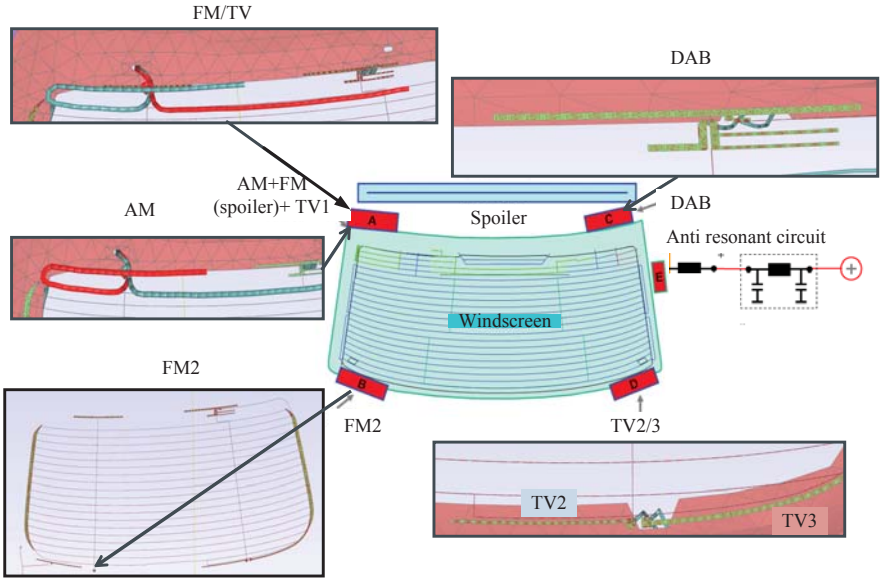

Figure 6.4: Rear antenna system of an AUDI Q3.

When all antenna systems are optimized, one final simulation can be carried out in the frequency ranges of all operating antenna systems. The computational resources can be used optimally if the algorithms presented in Chapter 4 for reducing of simulation time and computational resources are used carefully.

6.1 Strip-line Investigations

The main task of an automotive antenna system is to ensure the optimal reception for the different multimedia services [Tazi 10c]. The LW/MW frequency band is still important for radio reception in several countries such as USA and Canada. One procedure for measuring antenna performance is to excite cars with a well defined homogeneous EM plane wave. AM antenna structure is, like most antenna systems, placed on the car windows. In this section a new procedure for calculating the antenna reception with help of a virtual strip-line is presented. The application of this simulation procedure was validated based on measurements under the strip-line [Tazi 10c].

Figure 6.5 shows the principal overall configuration of measurement and simulation. As it can be seen, an EMI test receiver with integrated generator was used to sweep through the required frequency range. The generator has a fixed output voltage $U = 96\,\mathrm{dB}\mu\mathrm{V}$, with an internal resistance $R_i = 50\,\Omega$.

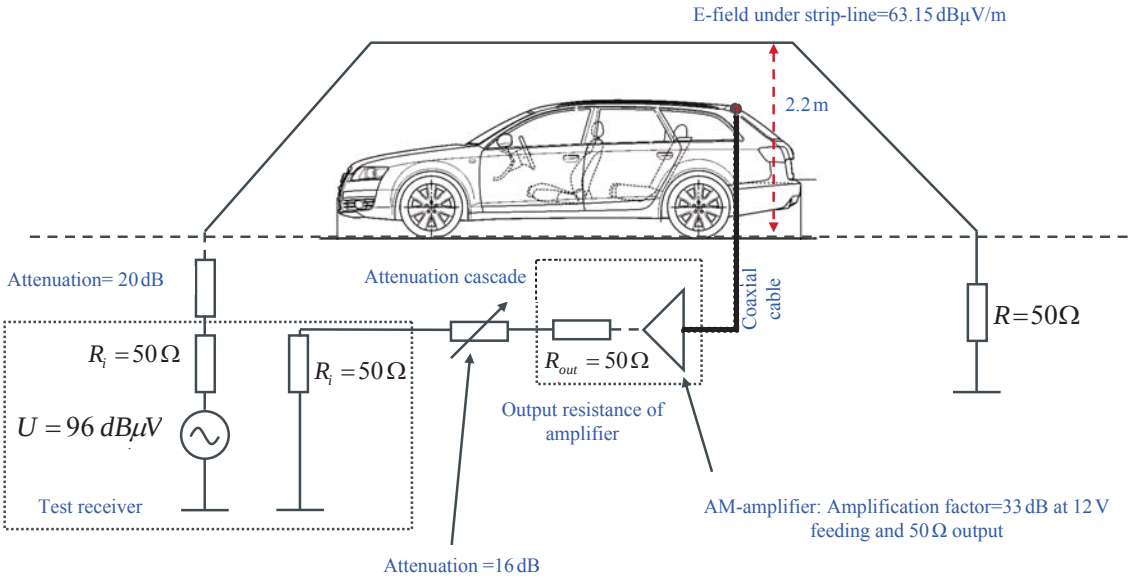

Figure 6.5: Strip-line measurement setup.

The voltage divider between the source impedance R_i and the $50\,\Omega$ termination of the strip-line ($-6\,\mathrm{dB}$), together with the used attenuation of $20\,\mathrm{dB}$ reduces the strip-line voltage level to $70\,\mathrm{dB}\mu\mathrm{V}$. If the space under the strip-line is free, there will be a relatively homogeneous E-field of $63.15\,\mathrm{dB}\mu\mathrm{V/m}$. The receiving port of the EMI receiver is connected to an attenuation cascade and the output of the used antenna amplifier. The high impedance input of the used amplifier is directly connected to the AM antenna structure, which works as a short electric monopole. The car body acts as a reference for the antenna and amplifier. To compare measurements with simulations, the whole setup with all used terminations, amplifications and attenuations must be taken into account. MoM computation is used to identify the transfer function in the frequency range between the port of the strip-line and the antenna termination. The antenna was modelled using the hybrid MoM approach. In the post processing, all other parameters can be taken into account. Figure 6.5 shows an exemplary simulation model of a complete car under a strip-line. One important detail for the simulation model is the ground connection between the feeding point of the strip-line and the amplifier case as illustrated in Figure 6.6.

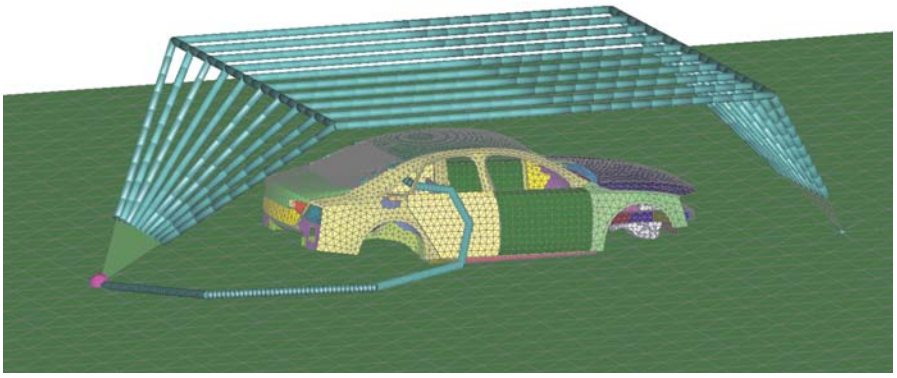

Figure 6.6: Strip-line simulation model with ground connection.

This connection results from the use of the EMI receiver in the measurement, which connects the car body to the metallic floor via the outer connector of the coaxial cable. This influence was also tested in comparison to a setup with an external signal generator, where the ground connection did not exist. Figure 6.7 shows that the correct modelling of glass antennas and a strict consideration of all measurement equipment, metallic geometries, antenna terminations (including adjacent antenna terminations) and ground connections lead to very good simulation results.

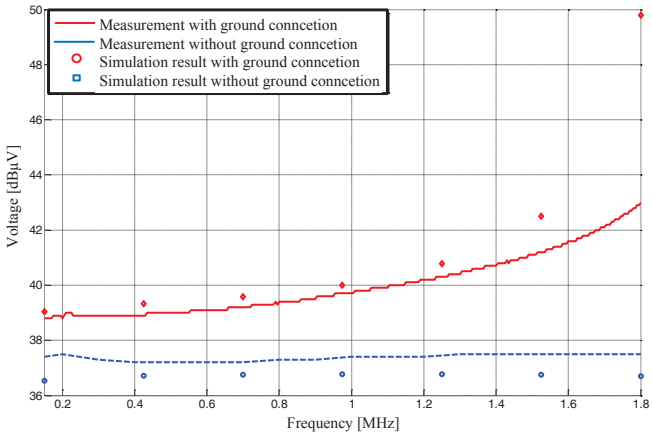

Figure 6.7: Strip-line investigation results.

An accuracy better then 1 dB was achieved in the AM frequency range. The difference between the two curves in the case of the setup with ground connection results from the poor modelling of cable parasitics, which become resonant at higher frequencies. The overall method for considering dielectric glass antennas is thus successfully validated. Figure 6.8 shows how the

difference in coupled voltage in the AM antenna structure can be explained when the car is located under the strip-line.

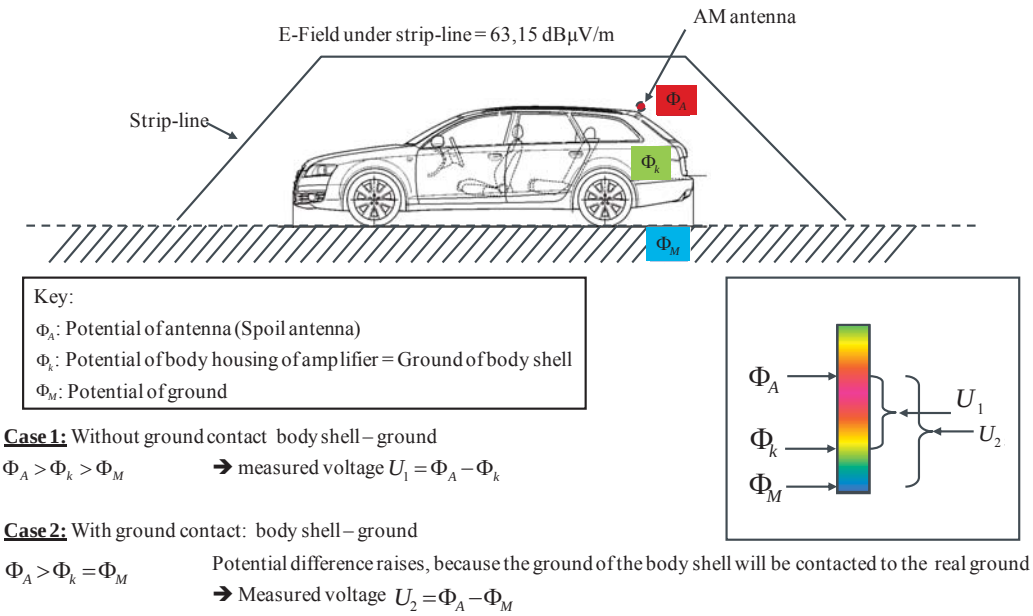

Figure 6.8: Coupled voltages in the car antenna under the strip-line.

The difference between the two measured cases is the reference electrical potential set to the car body in case 1 without modelling of the measurement cable. In case 2, where the measurement cable is taken into consideration in the simulation, the reference voltage or electrical potential is set to ground contact. Even if the measured electrical potential at the antenna is unchanged in both cases, the subtraction of the reference electrical potentials leads to different measured coupling voltages in the antenna. Computation of the antenna reception in LW/MW frequency range can be anticipated with high accuracy when the hybrid MoM presented in Section 3.4.6 is used. The procedure for calculation of the antenna reception with simulations is also verified for different antenna structures. All investigated simulations with hybrid MoM show a very good agreement to the measurement results. Reliable simulations in LW/MW frequency range can thus be realized for the evaluation of vehicle glass antennas. The strip-line method can be used to develop AM-antennas. Figure 6.9 shows an example of different AM-spoiler antennas, which are investigated on the basis of strip-line simulations.

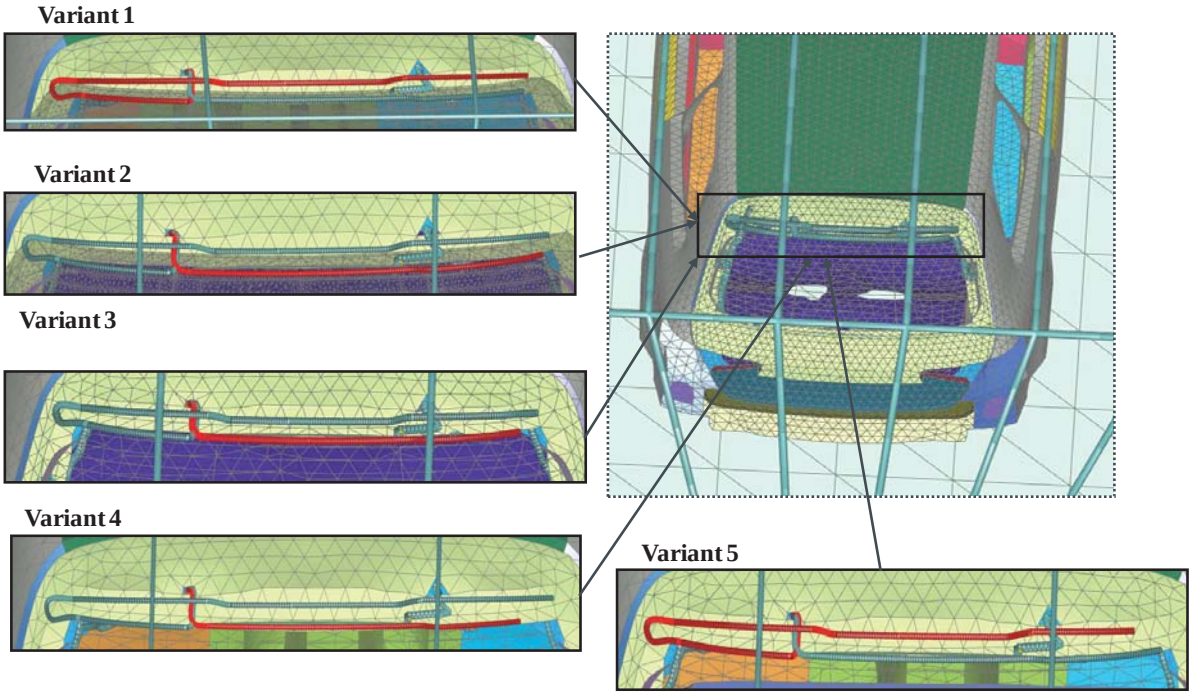

Figure 6.9: Strip-line simulation models of different AM antennas.

Figure 6.10 presents the obtained results, where the coupling voltages in the different spoiler antennas are compared. From the presented results it can be seen that the highest coupling voltages are obtained with the antenna variants 5 and 6 with an improvement of around 4 dB in comparison to variant 2 and 3. This investigation shows how strip-line simulations can be used in the automotive antenna virtual development process to evaluate vehicle antenna systems in the LW/MW frequency range.

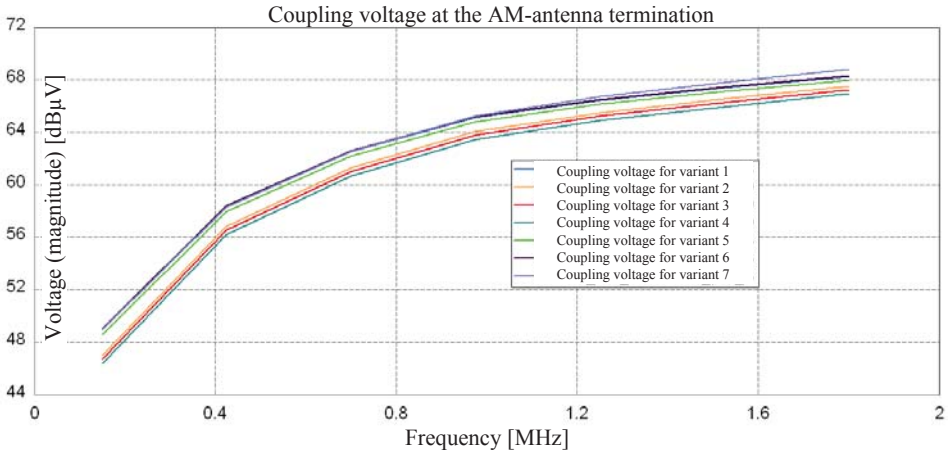

Figure 6.10: Strip-line simulation results of different AM antennas.

6.2 Far Field Investigations

For further validation of the MoM-MAS method [Gheo 08], investigations of the antenna gain with the same glass antenna were performed. The glass antenna was mounted on a metallic box according to the illustration in Figure 6.11 d). The antenna gain measurements were performed at the AUDI AG far field measurement test site as shown in Figure 5.13. The coupling voltage on the antenna termination was measured and compared with the simulation results.

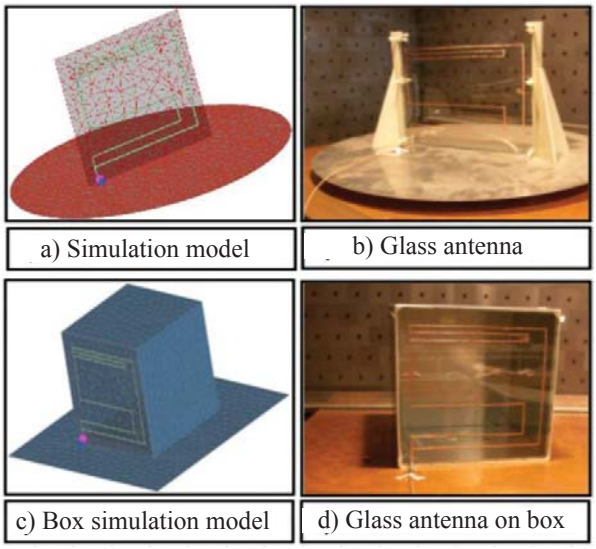

Figure 6.11: Investigated glass antenna configurations.

It is important to note that the bodyshell of cars affects the automotive glass antenna behaviour for all high frequency services offered [Joba 03a]. In order to investigate the impact of the influence of the bodyshell on the antenna, the return loss S_{11} was measured and simulated for different configurations. The glass antenna shown in Figure 6.11 b) was measured with and without a box to simulate the car bodyshell effect. The investigation was performed for a frequency range from 50 MHz up to 300 MHz. Figure 6.11 shows the investigated cases. From the results shown in Figure 6.12, it can be seen that the simulation results agree well with the measurement results. The box effect is visible and therefore the bodyshell, in this case the box, should not be neglected in either the simulation or the measurements during the development process.

The radiation pattern is presented in terms of coupled voltage from the fixed transmitting antenna at the elevation angle of 86° to the glass antenna terminals. From the results shown in Figure 6.13, it can be seen that even the measured far field behaviour of the antenna fits

well with the simulation results for both vertical and horizontal polarizations and at different frequencies.

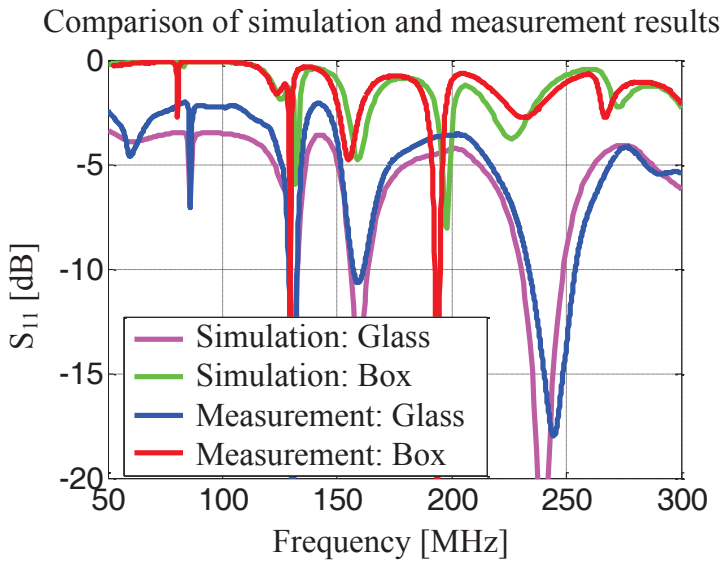

Figure 6.12: Influence of the box on the return loss of the glass antenna.

In this case the box was placed on the turntable according to the measurement setup shown in Figure 5.13

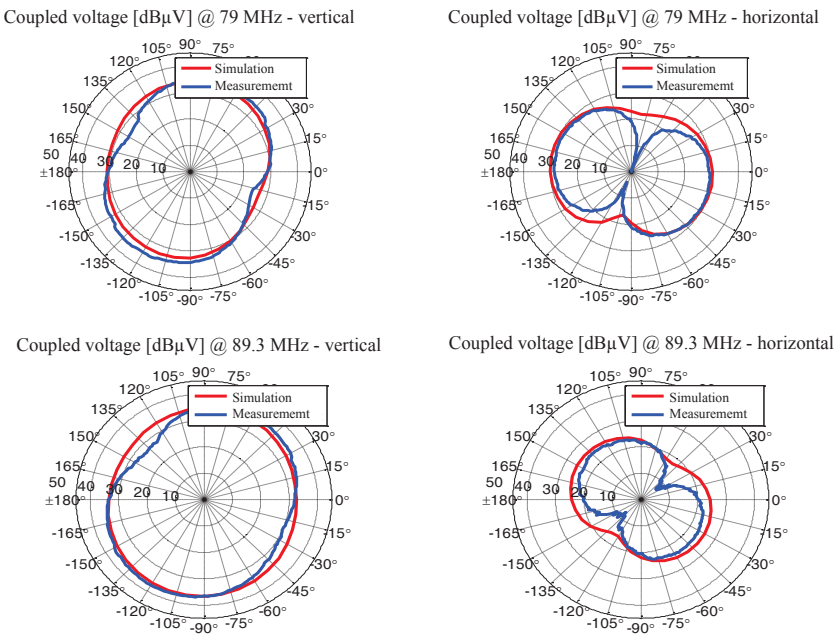

Figure 6.13: Box far field investigation results.

6.3 Development Process of Rear Window Antennas

The rear window, with the heating structure, presents a suitable arrangement, which can be used to integrate several antenna elements. Primarily, because of strict styling criteria, antenna engineers do not have much development freedom and cannot arbitrarily change the heating structure style. Antenna characteristic tuning can be achieved by extending the heating structure with additional antenna elements as shown in Figure 6.14.

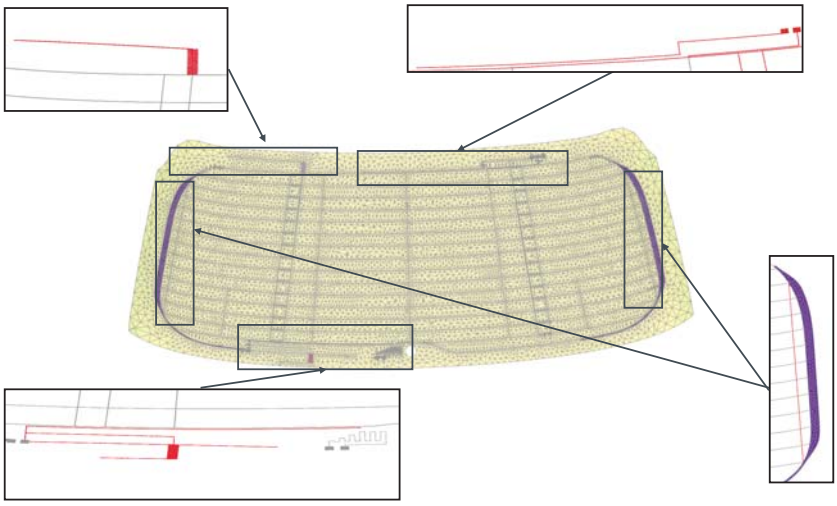

Figure 6.14: Modelling of the rear window antenna (1).

The additional elements are highlighted in red. A distinction can be made between two kinds of additional elements. On the one hand, the most commonly used one is the galvanic coupling, which represents a direct antenna length extension. On the other hand, a further rather less popular method is the capacitive coupling of the additional elements to the heating structure. However, the latter method can be risky due to possible ion migration between the antenna elements. In the case where this scenario occurs, antenna reception quality cannot be guaranteed. Another way of tuning the antenna characteristics is illustrated in Figure 6.15.

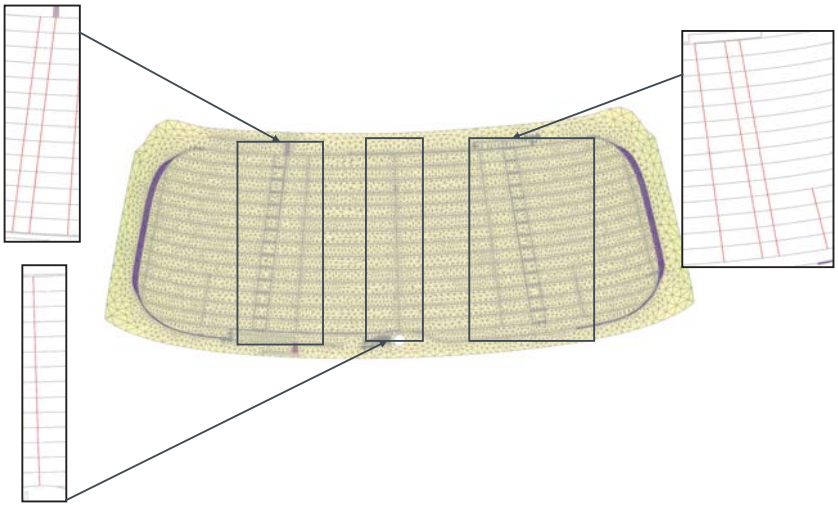

Figure 6.15: Modelling of the rear window antenna (2).

Additional vertical antenna elements could be placed on the heating structure with respect to the model symmetry.
Regarding simulation of the proposed antenna models, it is time-consuming to carry out simulations at many frequency points for all designed models. Simulations are therefore performed only at certain frequency points belonging to each RF service frequency range as shown in Table 6.1.

FM range	DAB range	TV range (band III)
79 MHz	174 MHz	177.5 MHz
89.3 MHz	198 MHz	184.5 MHz
93.6 MHz	253 MHz	191.5 MHz
100 MHz		198.5 MHz
106.6 MHz		209.5 MHz
		212.5 MHz
		219.5 MHz
		226.5 MHz

Table 6.1: List of calculated frequency points.

The chosen frequency points are the same such as those chosen during the antenna measurement process. This makes it possible to compare the obtained simulation results with the measurement results at any time .

7 Keyless Entry Systems

Keyless entry systems allow the driver to open the door and activate certain electrical systems while being outside the vehicle. Also, keyless entry systems allow the driver identification by the car electronics and starting of the engine without a mechanical key [Take 98; Hira 98]. The commonly used antennas for automotive smart or keyless entry systems are ferrite antennas, which work in the low frequency range [Kimu 06]. Operation of the system is usually realized at two defined frequencies: 21.8 kHz for transmission mode, and 433 MHz or 315 MHz for receiving mode. Figure 7.1 illustrates the functionality principle of the keyless entry system. Keyless entry systems are becoming more and more important and belong nowadays to standard automotive equipment for premium cars. These systems require a high level of security for the car entry and start engine permission. The keyless go system should enable to start the engine only if the key is recognized inside the car. This is important to ensure that the car cannot be started misleadingly. The system is composed of two parts, the first of which is represented by several antennas placed in the car.

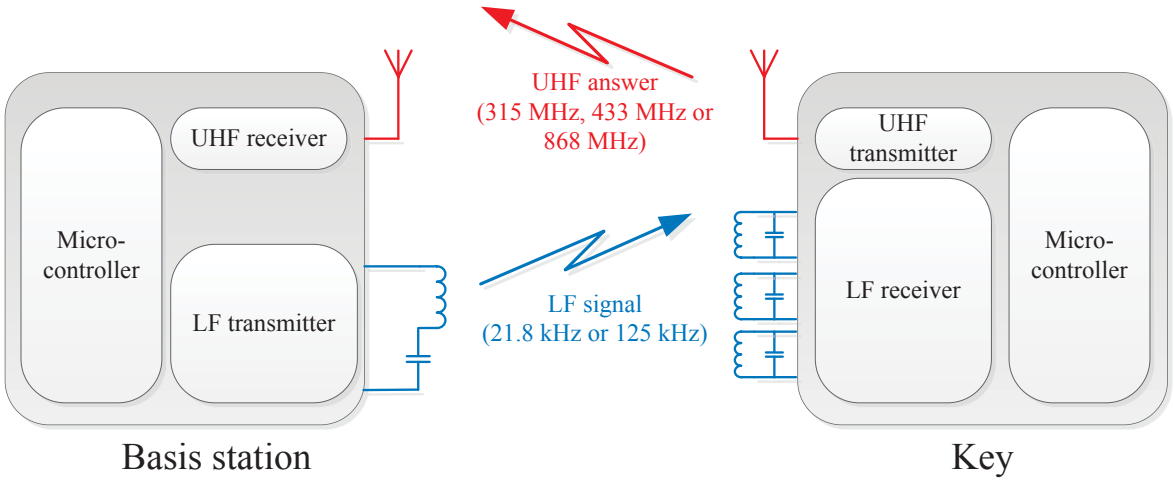

Figure 7.1: Functionality of keyless entry systems.

The second part is the driver remote key. The characterization of the field behaviour inside and outside the vehicle is of prime importance for evaluating and optimizing the system [Roy 94; Suga 07; Sato 99]. Figure 7.2 illustrates both areas, where the car key has to be detected to

allow the driver to enter the car and the area, where the key should be detected to permit the driver to start the engine.

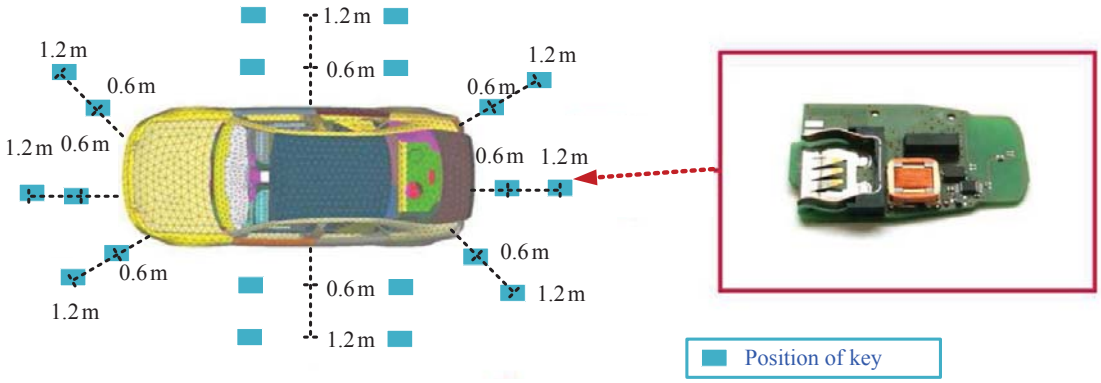

Figure 7.2: Areas where the key should be recognized from the keyless entry system.

Measurements used for this purpose need a long time for the system to be evaluated. 3D field simulation can be used to optimize the placement of the appropriate antennas. Figure 7.3 shows how simulations can be deployed to predict the antenna system performance at an early stage of development. This would facilitate the development process of these antenna systems. Besides that, the need for costly and time consuming prototype measurements can be reduced.

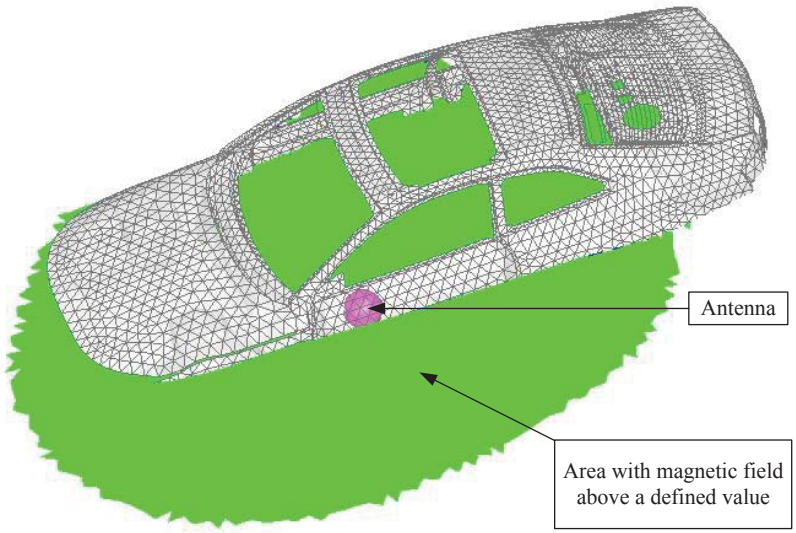

Figure 7.3: Application of the EM simulation for keyless entry system evaluation.

In addition, the number of antennas needed could be reduced while maintaining an equivalent system performance. In many cases, there is still a need of such optimization in order to find out the best antenna positioning in the vehicle [Tazi 10a].

One way to model the ferrite antennas, which are responsible for detecting the key is to use the equivalent near field sources [Tazi 10a]. Those sources allow substitution of the antenna geometry in a relatively simple way taking into account the environment of the antenna. By means of this, the modelling of the antenna structure can be simplified. The multi excitation approach is deployed in order to save computation time when the complete geometry of the simulation model is the same and the effect of different sources are to be be investigated. That is the case in automotive keyless antenna systems, when the radiated field of active antennas from the same car should be calculated with different combinations of source excitation. In this chapter, simulation results of the keyless antenna systems are presented. Furthermore, magnetic field measurements inside and outside the car serve to validate the presented simulation procedure of the keyless antenna systems.

7.1 Laboratory Investigations

In this section, two different smart entry system antennas are investigated. The difference between the two antenna systems is the transmission frequency of data from vehicle antenna to the key antenna. The first presented antenna concept uses loop antennas permitting data transmission at 125 kHz and the second system is based on ferrite antenna systems working at a lower frequency of 21.8 kHz.

7.1.1 Loop Antennas Systems

The loop antenna illustrated in Figure 7.4 (a) is produced by Siemens and operates at 125 kHz. The antenna consists of 74 windings of copper wires with a diameter of $d = 0.2\,\text{mm}$. The antenna is of an elliptic form with the radii $r_1 = 3.2\,\text{cm}$ and $r_2 = 5.2\,\text{cm}$. The plastic housing is used only to stabilize the antenna form and to facilitate the mounting of the antenna in cars. Figure 7.4 (b) shows an example of an opened loop antenna, where the windings are visible.

(a) (b)

Figure 7.4: Loop antenna for keyless systems.

According to the antenna data sheet [schn 10], the operating antenna current is $I < 300\,\mathrm{mA}$. The antenna parameters lead to an inductance of $1.2\,\mathrm{mH}$ $\pm 10\%$ with a resistance of $12\,\Omega$ $\pm 2\,\Omega$. To feed the antenna with a current of $300\,\mathrm{mA}$, a voltage of $286\,\mathrm{V}$ has to be applied to the antenna impedance according to

$$U = (R + jX_L)\ I = (R + j2\pi f\ L)\ I \tag{7.1}$$

$$= (12\,\Omega + j2\pi\ 125\,\mathrm{kHz}\ 1.2\,\mathrm{mH})\ 300\,\mathrm{mA} \approx 286\,\mathrm{V}\,. \tag{7.2}$$

The simulation model of the loop antenna consists of one equivalent winding of the 74 windings to avoid any modelling problems due to the fact that the huge number of windings are very close to each other. However, the compensation of the winding number is ensured by multiplying the antenna feeding current by the number of windings. The parasitic capacitances and inductances between the windings are negligible and should not be taken into account in the antenna simulation model. The obtained simulation model shown in Figure 7.5 takes into account the antenna geometry data.

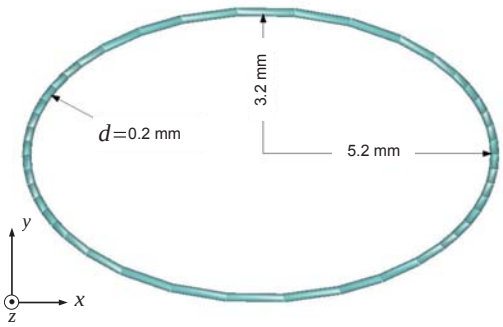

Figure 7.5: Simulation model of the loop antenna.

To validate the simulation model, the magnetic field of the loop antenna is measured with a probe connected to a test receiver at different distances from the antenna and compared to the

values calculated with the simulation model. The probe is located in a way that the maximum magnetic field component of the three axes (x, y, z) can be measured (see Figure 7.6). The z-component correlates with the highest measured magnetic field for this setup. The probe surface should therefore always be set parallel to the x-y-plane to measure the magnetic field z-component.

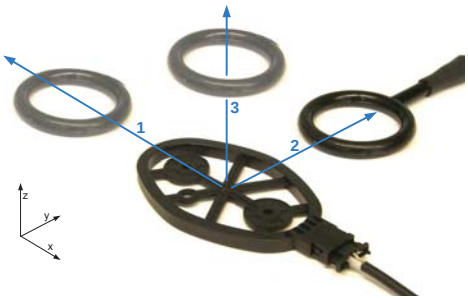

Figure 7.6: Magnetic field measurement setup for the loop antenna.

The loop antenna simulation model is extended by setting field probes on the three antenna axes to get the magnetic field values at the same positions as in the measurement. The antenna is fed by a signal generator with a voltage of 20 V on a 50 Ω impedance. The resulting current in one winding of the loop antenna is 11 mA according to equation (7.2). Figure 7.7 shows the simulation model of the measurement setup, where a current source of 814 mA is used according to the multiplication of 11 mA by 74 windings as explained above.

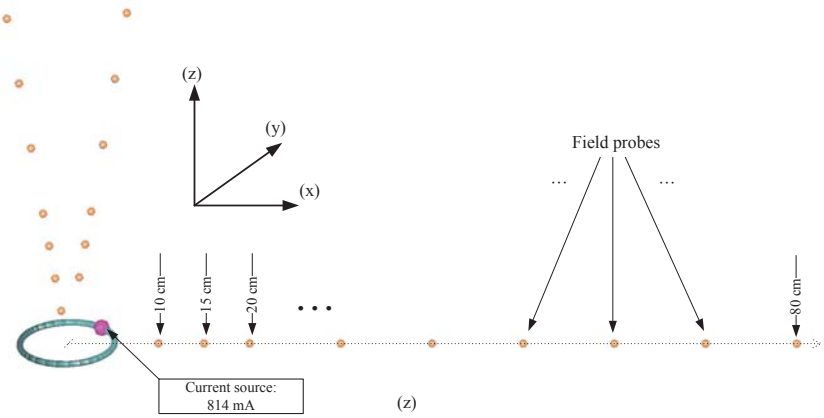

Figure 7.7: Simulation model of the loop antenna measurement setup.

Simulations are performed for the system operating at 125 kHz, where the obtained z-components of the set field probes are compared with the appropriate measurement values. Figure 7.8 shows the obtained results.

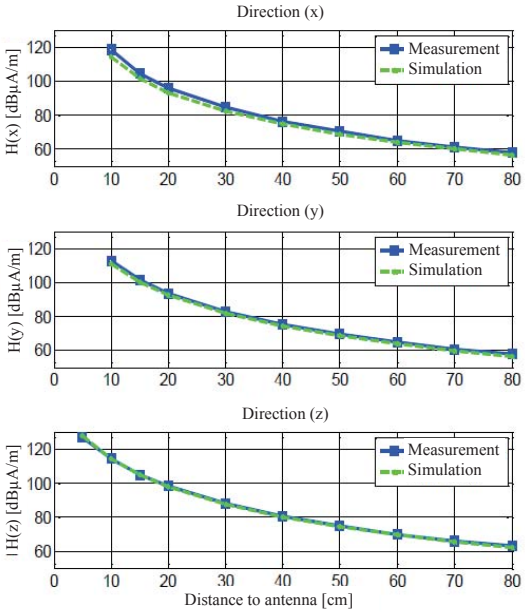

Figure 7.8: Validation of the loop antenna simulation model.

From the graph, it can be seen that the simulation results agree very well with the measured data for the three axes and at all distances from the loop antenna. Hence, the loop antenna model is validated and can be used for car simulations.
Since the loop antenna is not common in current AUDI models, more detailed investigations on cars with the presented antenna are not performed in this work.

7.1.2 Ferrite Antenna Systems

Coil antennas with ferrite are used very often in keyless entry systems. For analysis of problems related to smart entry systems, accurate simulations of the magnetic field produced by the antenna is required. For this purpose, the parameters of the antenna should be well known. The ferrite core has high magnetic permeability (μ_r from 100 to 4000). This core is surrounded by a large number of wire turns, which represent the antenna structure. The operating frequency of the system is very low and usually varies from 20 kHz up to 125 kHz. Figure 7.9 shows a ferrite core with copper windings used as a magnetic antenna operating at 21.8 kHz for keyless entry systems from the company Marquardt [Marq 10].

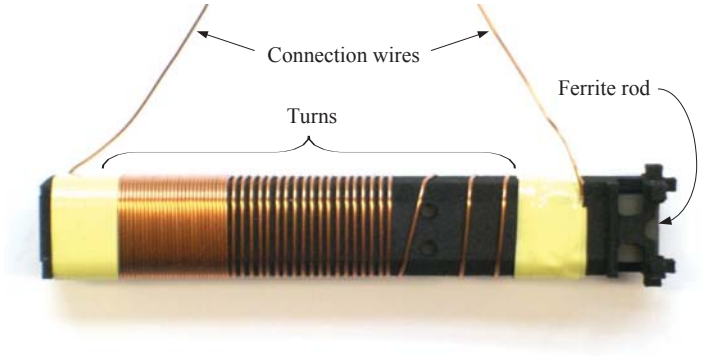

Figure 7.9: Ferrite core with copper windings used as magnetic keyless antenna.

In addition to the inductance of the coil, a capacitance is usually added to obtain an LC resonance with a peak at the required frequency, for example 21.8 kHz. To tune the LC resonance to the required frequency, the value of the antenna inductance should be known. The presence of the ferrite rod increases the sensitivity of the antenna to the external magnetic fields, but usually not by the value of the relative magnetic permeability of the core. μ_{rod} is the relative 'rod' permeability and represents the effective magnetization of an external magnetic field. μ_{rod} can be calculated according to [Cros 01] as

$$\mu_{rod} = \left(\frac{l}{d}\right)^{\frac{5}{3}} + 2.5 \tag{7.3}$$

where l is the length of the rod and d is the diameter of the rod for a rod with circular cross-section. In case of a core with rectangular cross-section, width a and height b, the following formulation can be considered by

$$d = \sqrt{\frac{a\ b}{\pi}}\ 2\,. \tag{7.4}$$

For small l/d the following approximation formula pursuant to [H 04] can be applied:

$$\mu'_{rod} = \frac{\mu_{rod}\ \mu_r}{\mu_{rod} + \mu_r}\,. \tag{7.5}$$

The first step to build the antenna simulation model is to verify the indicated parameter by way of measurement. The utilized measurement setup for this purpose consists of the impedance analyzer Agilent 4294A serving to measure the frequency dependent input impedance of the ferrite antenna as depicted in Figure 7.10. Table 7.1 shows a comparison between the indicated and measured values.

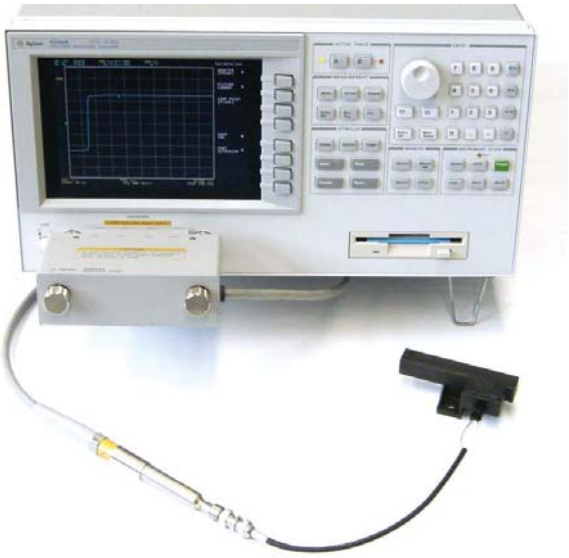

Figure 7.10: Parameter measurement with the impedance analyzer.

Parameter	Indicated values	Measured values
Capacitance C of the capacitor	$0.33\,\mu$F	$0.33\,\mu$F
Inductance L of the coil	$161.5\,\mu$H $\pm 10\%$	167 to $171\,\mu$H
Resistant R in resonance case	$< 0.35\,\Omega$	$0.3\,\Omega$
Diameter d	0.5 mm	0.5 mm
Geometry of ferrite core	$90 \times 10 \times 7.5$ mm	$90 \times 10 \times 7.5$ mm
Resonant frequency f_0	21.8 kHz $\pm 2\%$ (at $23\,^o$C)	21.3 kHz
Number of windings N	45	45

Table 7.1: Comparison of measured and indicated values of the ferrite antenna.

As shown in Table 7.1, the measured parameters agree well with the indicated values or are within the tolerance interval.

The next step is to create a simulation model according to the values given in Table 7.1. The permeability value can be read out from the antenna specification sheet as $\mu_r = 2400$. In addition, the capacitance and resistance values given in Table 7.1 should be applied to the wire segment elements as a complex impedance. The obtained simulation model can be seen in Figure 7.11.

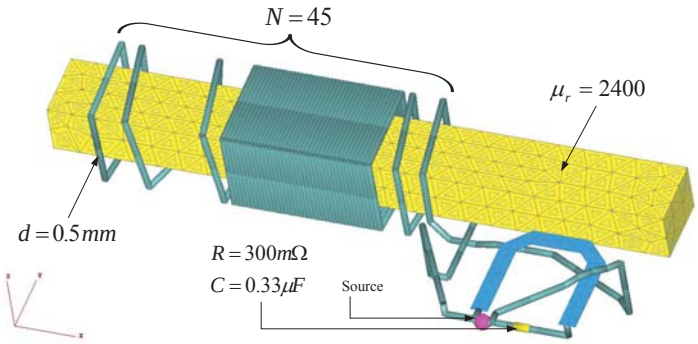

Figure 7.11: Simulation model of the ferrite antenna.

The ferrite core antenna is connected to a 0.33 μF capacitor to obtain a resonant frequency at 21.8 kHz. The resonant frequency of $f_0 = 21.8\,\text{kHz}$ can be calculated with Thomsons's oscillation equation

$$f_0 = \frac{1}{2\pi\sqrt{LC}} \tag{7.6}$$

with an obtained resistance value at the resonant frequency of 350 mΩ according to

$$f_0 = \frac{1}{2\pi\sqrt{161.5\,\mu\text{H}\,0.33\,\mu\text{F}}} = 21.8\,\text{kHz}\,. \tag{7.7}$$

Figure 7.12 shows that more accurate results are achieved when the ground is taken into consideration in the simulation model. Therefore, it is recommended to include the ground in the ferrite antenna simulation model to avoid any inconvenience in comparison of simulation and measurement results especially when the ferrite antenna simulation model is used in complex configurations such as those with a complete car.

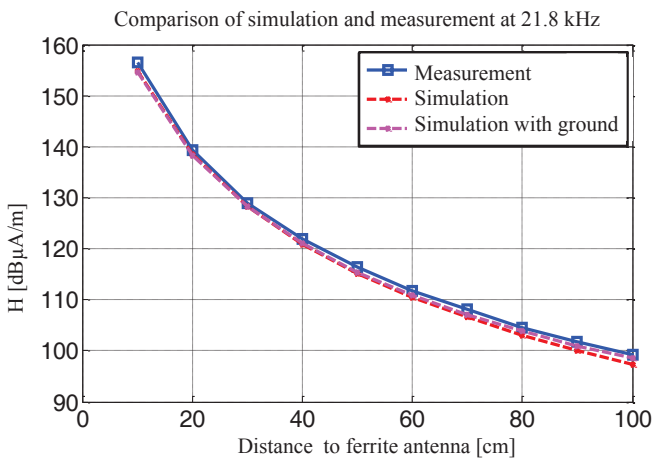

Figure 7.12: Validation of the ferrite antenna simulation model.

Ferrite antennas are placed near the car body. In order to take into account the influence of the metallic surface of the car body on the magnetic field behaviour of the antenna, further simulation models of the ferrite antenna near a metallic plate were done. Figure 7.13 (a) shows a ferrite antenna in a height of 3 cm from the metallic plate. The magnetic field was calculated in the z-direction. Further investigations were performed to examine the effect of the ground on the accuracy of the simulation results. Figure 7.13 (b) shows a simulation model of the ferrite antenna, where an endless PEC ground is considered.

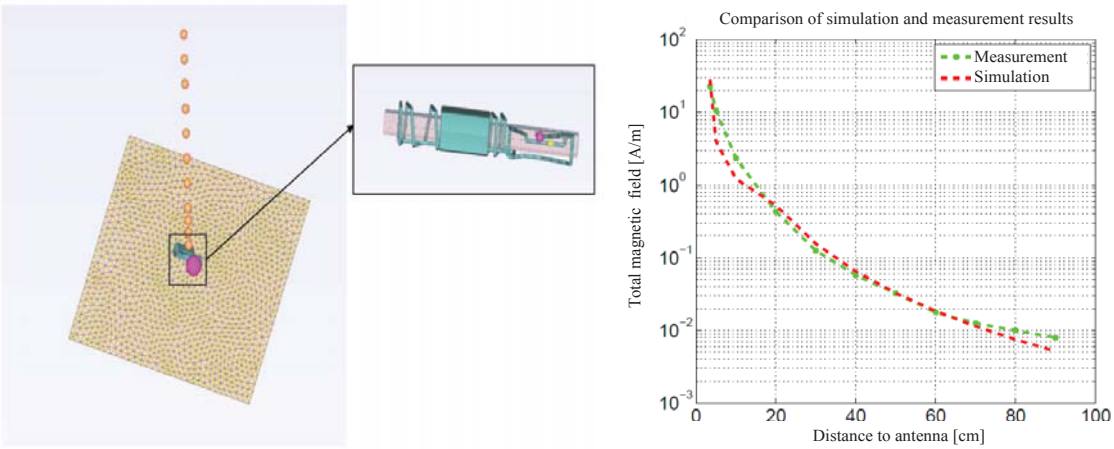

(a) (b)

Figure 7.13: Validation of simulation model of the ferrite antenna over a metallic plate.

Investigations of the z-component of the magnetic field at different distances from 5 cm to 90 cm from the ferrite antenna were carried out. From the obtained results, it can be seen that an accurate system modelling of the ferrite antenna with the metallic plate leads to good agreement between measurement and simulation results.

7.1.3 Ferrite Antenna Sensitivity Determination

Usually, the key magnetic field sensitivity is not given in system specifications [schn 10]. Even with the very sensitive equipment available at the AUDI AG EMC and Antenna Departments, it is not possible to determine the minimal LF receiving signal that can be recognized from the key antenna.

With help of simulation and a modified **B**ody **C**omputer **M**odule (**BCM**), the sensitivity value could be determined. Normally, the ferrite antenna keyless entry system is conceived such that a processor unit sends an LF signal only when certain incidents happen, for example when the system is woken up because of a key approaching the car. On the other hand, the key is

programmed to answer the incoming signal with a flashing **L**ight **E**mitting **D**iode (**LED**). Figure 7.14 shows the used BCM instead of a processor unit, which is programmed so that it permanently sends an encoded signal to the ferrite antenna with a maximal current of 8 A.

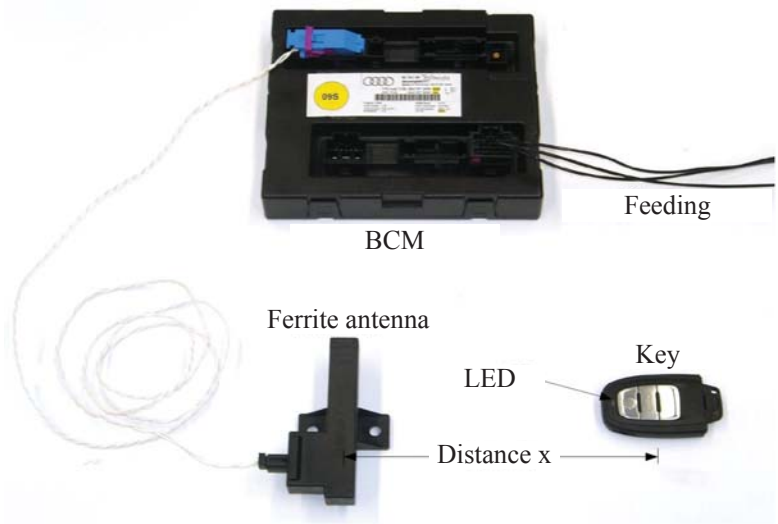

Figure 7.14: Setup to determine the key magnetic field sensitivity.

To determine the sensitivity value, the key is positioned at a distance to the antenna, where the LED is barely flashing properly. At greater distances, the LED flashing gradually decreases until a distance of 7.80 m where the LED no longer flashes at all.
The simulation model depicted in Figure 7.15 can be used to illustrate a ferrite antenna in free space with two field probes 1 and 2 located at the points determined by measurement.

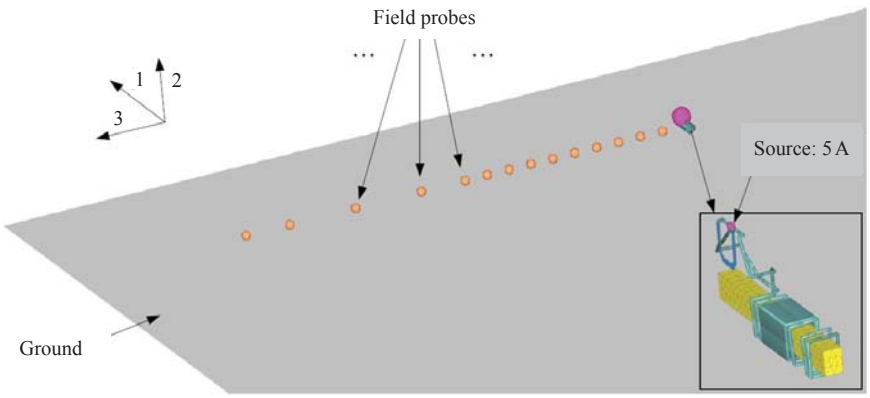

Figure 7.15: Keyless entry antenna ground simulation model.

The two field probes are at a distance to the antenna of 6.10 m and 7.80 m, respectively. The antenna is fed in both simulation and measurement by a current of 8 A. The simulation is carried

out at the antenna system operating frequency of $f = 21.8\,\text{kHz}$. The calculated magnetic field at probe 1 and 2 is $32.85\,\text{dB}\mu\text{A/m}$ and $26.56\,\text{dB}\mu\text{A/m}$, respectively. Hence, the sensitivity of the ferrite antenna system is determined and can be used for car investigations.

7.2 Virtual Development of Keyless Entry Systems

In this section, three different investigations are presented. Firstly, a simulation model of the ferrite antenna mounted on a car door will be validated. After that, the simulation model will be extended with consideration of the complete car bodyshell. Simulation models are validated with measurements performed in the EMC Department chamber. Last but not least, multi excitation approach is used to facilitate the integration of the simulation in the keyless system development process.

7.2.1 Ferrite Antenna Mounted in Car Door

The keyless system development can be achieved only if the complete car body, which affects the magnetic field of the ferrite antenna, is taken into account during the development process. The proper incorporation of the car body in the keyless system simulation model requires the system complexity to be increased in steps. First step concerning simulation model validation of the ferrite antenna above a metallic plate was realized and presented in Section 7.1.2. After that, the ferrite antenna will be mounted at two different positions on the car door. The picture in Figure 7.16 shows both mounting positions of the ferrite antenna on an AUDI A5 Coupé driver's door at a distance of $h = 19\,\text{cm}$ above the ground. In position 1, the antenna is directly mounted on the door sheet metal. In position 2, the antenna is fixed on a wooden staff in the door cavity.

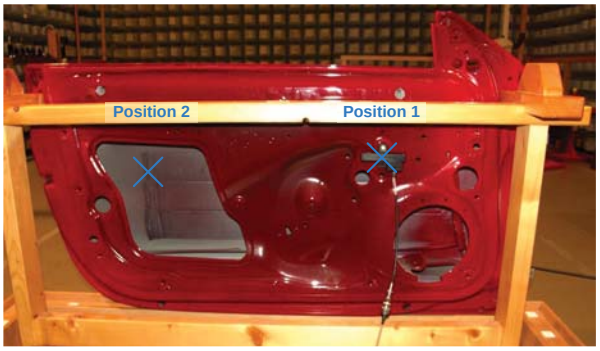

Figure 7.16: Ferrite antenna mounting positions on an AUDI A5 driver's door.

The antenna is connected directly to an amplifier, which is fed by a sinusoid signal generator. The amplifier is used to boost the low current signal generator to 5 A required for the high power in keyless systems. The magnetic field are measured at different distances from the ferrite antenna with help of magnetic field probes connected to a test receiver. The magnetic field loop is positioned perpendicular to the ferrite antenna at different distances from the antenna to measure the highest magnetic field component, which corresponds to the x-component. To consider the shielding effect of the door, investigations of the ferrite antenna irradiated magnetic field are performed in the internal space as shown in Figure 7.17 (a) and in the external space as illustrated in Figure 7.17 (b).

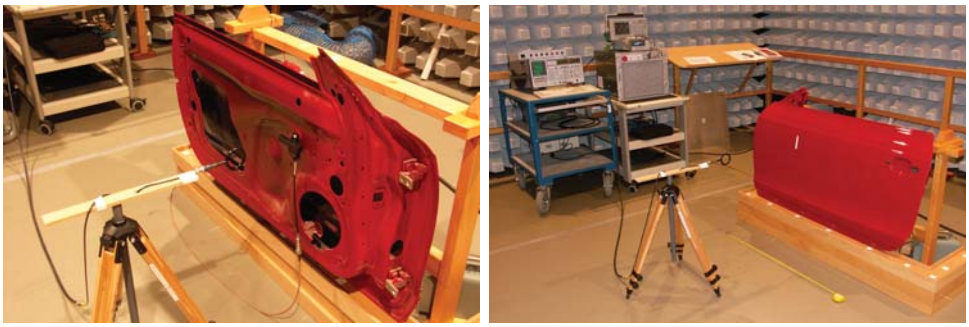

(a) (b)

Figure 7.17: Measurement setup for internal space (a) and for external space (b).

Figure 7.18 illustrates the corresponding simulation model to the measurement setup shown in Figure 7.17.

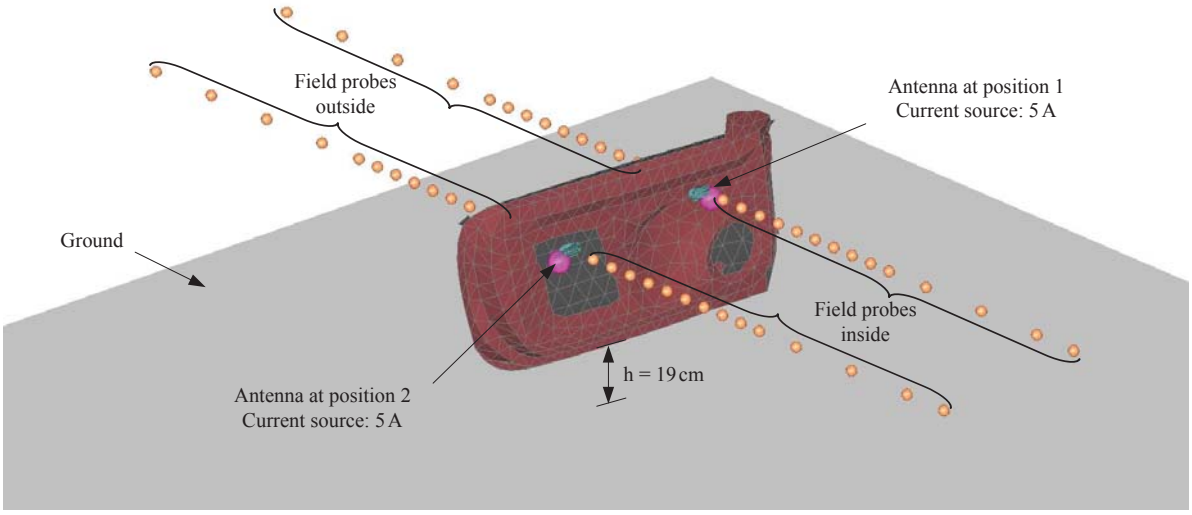

Figure 7.18: Simulation model of the keyless system door investigation.

The field probes are positioned at distances to the ferrite antenna, which correspond to the measured magnetic field positions. Both antenna configurations are modelled according to Figure 7.18. Two simulations at a frequency of 21.8 kHz are carried out, where one of the modelled antennas is fed by 5 A while the other one is passive.

The simulation results obtained for the first antenna configuration are plotted in Figure 7.19. The related measurement results of both antenna positions are also presented. Besides that, the measurement results of the ferrite antenna in free space at the same distances to the antenna like in this door investigation are also plotted to visualize the door shielding effect. For the internal space, the results obtained are very close to the results of the antenna in free space. This can be explained with the non-existing shielding effect of the door in the internal space. Therefore, magnetic field distribution in the internal space could be approximated by a ferrite antenna simulation model in free space.

From the obtained results, it can be seen that the measurement results agree well with the simulation results for both the internal and the external space. Besides that, it can be mentioned that the magnetic field radiation of the antenna in the external space is much lower in comparison to the results obtained of the ferrite antenna in free space. This is evident due to the metallic shielding effect of the vehicle door.

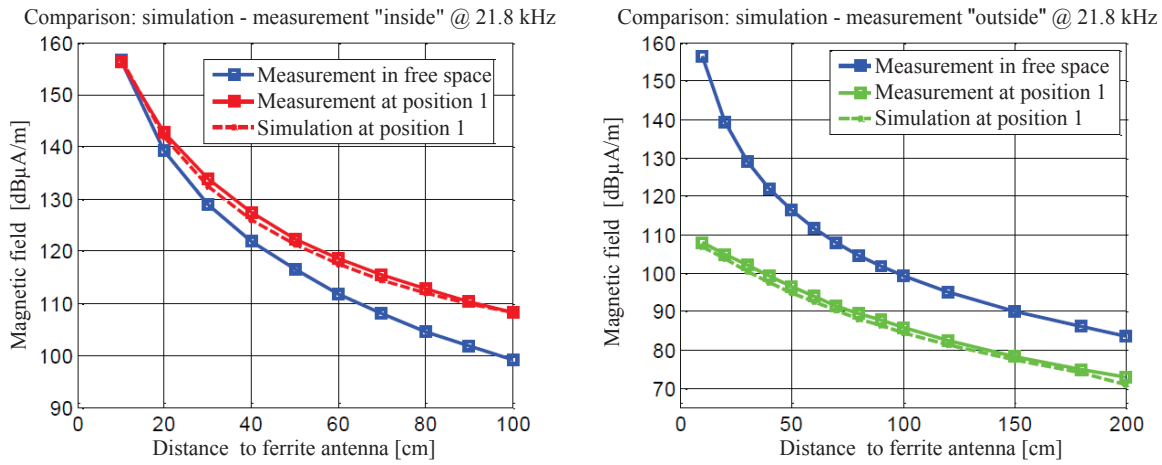

Figure 7.19: Validation of the simulation model in position 1.

Figure 7.20 illustrates both obtained results in external space of the two investigated antenna positions.

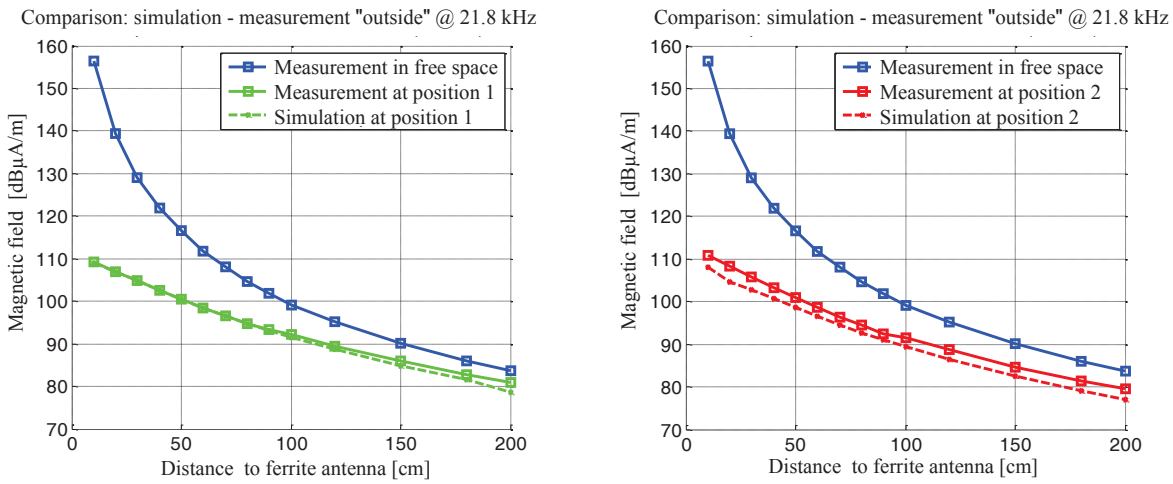

Figure 7.20: Validation of the simulation model for both positions.

The obtained results with position 2 confirms the obtained results with position 1 shown in Figure 7.19. Hence, a further validation of the ferrite antenna was achieved and the keyless entry system complexity can be elevated.

7.2.2 Ferrite Antenna Mounted in Vehicle Car Bodyshell

Next, the ferrite antenna model is integrated to a complete AUDI A5 Coupé car bodyshell. Figure 7.21 illustrates the measurement setup used. The investigated antenna positions are the same as those in the previous driver's door investigations. The antennas are fed with a current of 5 A with the previously mentioned sinusoidal signal produced from the signal generator and amplified with an amplifier at a frequency of $f = 21.8\,\text{kHz}$.

Figure 7.21: Measurement setup of the keyless car body investigation.

Initially, the ferrite antenna is mounted at position 1. Measurements are performed at a complete distance of 2 m from the car body. Measurements are performed in the external

space of the car on an axis perpendicular to the ferrite antenna in the same way as in the measurement in the previous investigation. Afterwards, investigations are realized with the ferrite antenna mounted on position 2. Measurements are performed in the same way as the previous investigation with the driver's door.
A suitable simulation model for the measurement setup shown in Figure 7.21 is illustrated in Figure 7.22. All accounted details in the simulation model can be read out from the door simulation model.

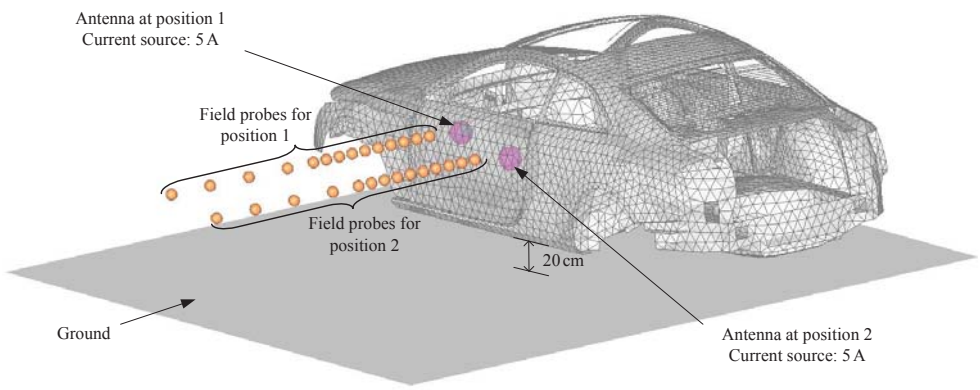

Figure 7.22: Simulation model of the keyless system car body investigation.

From the obtained results shown in Figure 7.23, very good agreement between simulation and measurement results is achieved even with the complex car model. For antenna position 2, the small difference between measurement and simulation can be explained with the imprecise antenna position in simulation. However, even this difference is still acceptable for the development of keyless antenna systems.

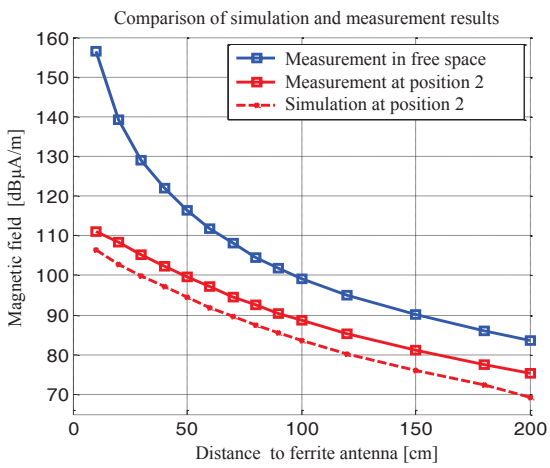

Figure 7.23: Validation of the car body simulation model.

7.2.3 Integration of the Keyless System Simulation in the Development Process

Keyless entry system simulations could be utilized to predict the electromagnetic field distribution caused by the ferrite antennas installed in car. In this way, system antennas could be placed efficiently in the car so that the best system performance can be ensured with the maximum level of car access and car starting security. Furthermore, problem regions related to EMC, where a car control unit should not be placed in the vicinity of the ferrite antennas could be predicted at an early stage of development so that optimal compromises can be found.
The depicted simulation model shown in Figure 7.24 presents the keyless entry simulation model on the AUDI A5 Coupé. The model consists of seven different ferrite antennas placed at different positions in the car. The seven positions could be reserved for ferrite antennas.

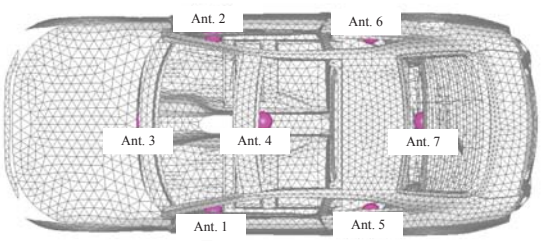

Figure 7.24: Positions of the ferrite antennas in multi excitation approach.

The goal of this investigation is to predict the number and the position of the ferrite antennas in order to predict the optimal system performance in term of security. First of all, simulations with only one ferrite antenna in each case were performed. After this, different antenna combinations were investigated. Table 7.2 shows the different investigated antenna combinations. In sum, 17 different antenna combinations were proposed. The multi excitation approach described in Section 4.1 was used to optimize the necessary computational time. To visualize the field distribution [Gheo 10], three near field areas were placed at distances of 50 cm, 65 cm and 80 cm from the ground in addition to the different modelled antennas as shown in Figure 7.25. An infinite PEC ground plane was considered in the simulation model. Because of the model size, simulations were performed on a cluster with 40 processor units and a maximal storage capacity for 160 GByte.

	Ant.1	Ant.2	Ant.3	Ant.4	Ant.5	Ant.6	Ant.7
Configuration 1	x						
Configuration 2		x					
Configuration 3			x				
Configuration 4				x			
Configuration 5					x		
Configuration 6						x	
Configuration 7							x
Configuration 8	x	x	x	x			
Configuration 9	x	x					
Configuration 10						x	x
Configuration 11					x	x	x
Configuration 12	x	x		x			
Configuration 13	x	x	x				
Configuration 14			x	x		x	
Configuration 15	x						x
Configuration 16		x			x		
Configuration 17	x	x	x	x	x	x	x

Table 7.2: Investigated antenna combinations.

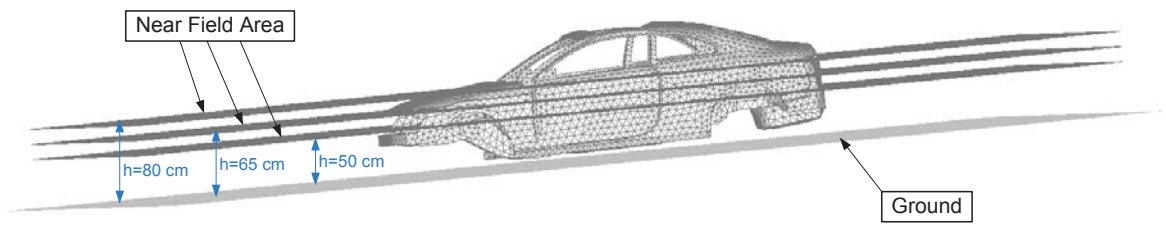

Figure 7.25: Simulation model with near field areas.

Table 7.3 shows simulation details of two configurations, the first one, with only one antenna and the second one with seven antennas. Information about the required computation time and storage capacity and about the number of elements can be extracted from the table.

	Number of elements	Required storage capacity	Computation time
1 antenna	26331	24.6 GByte	26 min
7 antennas	30004	44.7 GByte	50 min

Table 7.3: Simulation details of the calculated cases.

The total computation time required for all configurations presented in Table 7.2 on said cluster is 500 min when simulations are performed in sequence. If the multi excitation approach is used, the computation time on the same cluster for all configurations is reduced to 116 min. That means 85% of computation time can be saved.
It should be mentioned that contrary to the basis MoM simulation models, multi excitation approach simulation models contain antennas, which would not exist in reality depending on the considered simulation case. These antennas are then passive structures. However, antenna elements such as the ferrite antenna could influence the simulation results. Therefore, further comparisons between simulations based on normal MoM solutions and those based on the multi excitation approaches were performed. Figure 7.26 shows the obtained results of magnetic field distribution for a field area with and without passive antennas.

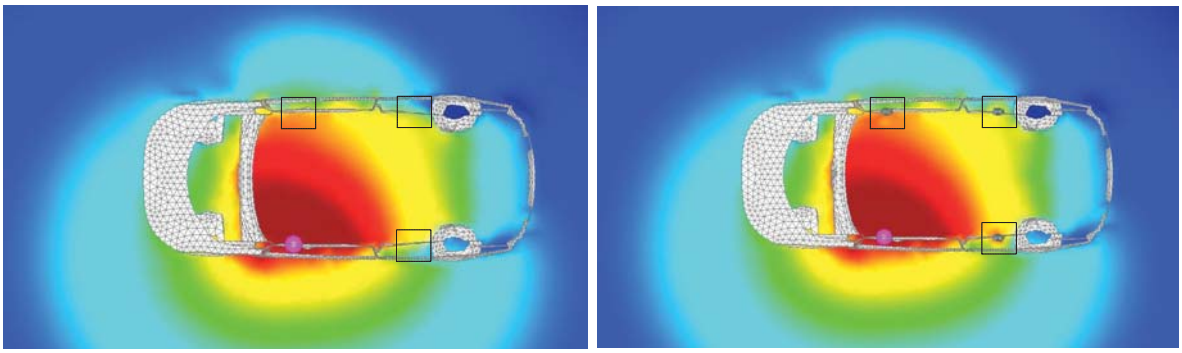

(a) (b)

Figure 7.26: Comparison of magnetic field distribution of simulations without (a) and (b) with passive Antennas in the near field area at $h = 65\,\text{cm}$.

From the results obtained, it can be seen that at areas marked with boxes, where passive antennas are located, high magnetic field distribution could be registered. This is due to the fact that passive antennas contain ferrite elements, which concentrate the magnetic field. Nevertheless, this effect is still negligible in comparison to the complete field distribution caused by active antennas. Besides that, these areas are directly connected to the passive antenna positions. Therefore, simulations based on the multi excitation approach, where additional passive antennas are taken into account are not falsified by the passive antennas. The two

color magnetic field representation presents a further simulation setting option to facilitate the definition of regions, where keyless entry system recognizes whether the key is in the right area to allow car to start or to be accessed [Gheo 10; schn 10]. It is possible in this way to define a magnetic field level so that only regions above or under this threshold are visualized in one color according to Figure 7.27(b).

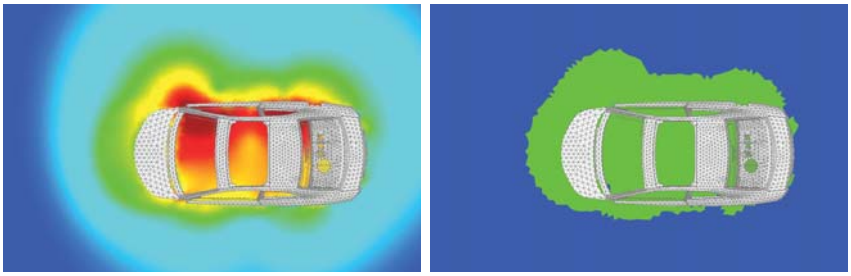

(a) (b)

Figure 7.27: Magnetic field distribution on a near field area (a), with definition of a threshold value (b).

Figure 7.28 shows the results for the case that both antennas 2 and 5 are excited. The arbitrarily chosen reference level is 10 mA/m. The green area shows the value of the magnetic field, which is higher or equal to the given reference value. The blue region represents field areas below 10 mA/m. Keyless entry system development can be performed according to Figure 7.28, where different areas are positioned in car to calculate the magnetic field.

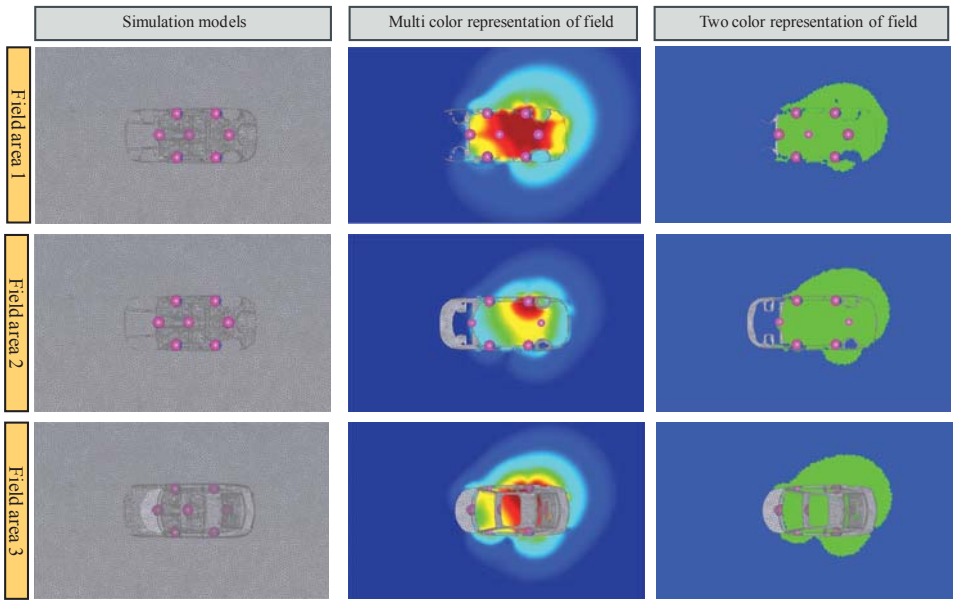

Figure 7.28: Smart entry two color representation investigation.

8 Development of Very High Frequency Antenna Systems

The integration of the high frequency services in present-day vehicles requires antennas, which often have to be placed very close to each other. This is the case with roof antennas that operate in different frequency ranges for GSM, UMTS, GPS and SDARS applications [Tazi 11c; Rabi 10]. The depicted roof antenna assembly in Figure 8.1 shows an antenna system comprising three antennas: an UMTS antenna emitter and two patch antennas for SDARS and GPS services.

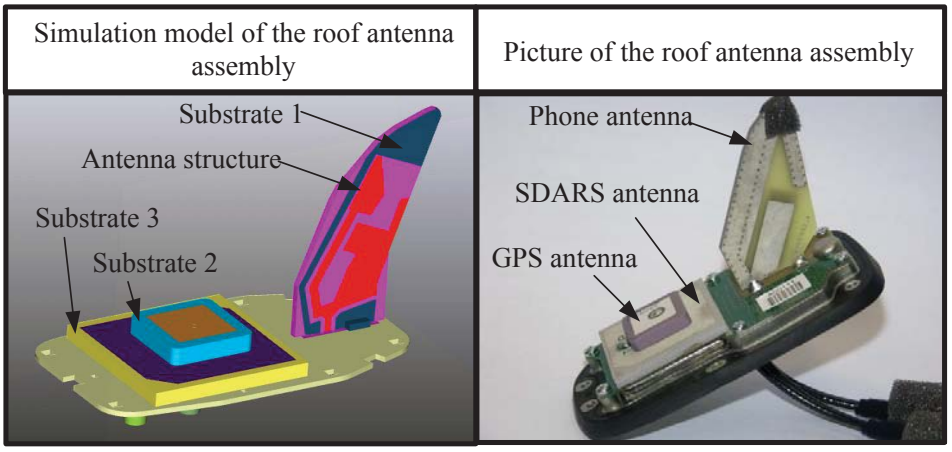

Figure 8.1: Prototype and simulation model of a roof antenna system.

Both, antenna and the equivalent CAD data of the antenna system are presented. The development of such antenna systems poses a new challenge due to the fact that more antennas should occupy the same space reserved for existing systems as that the exterior design remains unchanged. This will be the case with the additional integration of LTE, WIMAX and Car-2-X antennas. Besides that, the performance of individual services should be kept constant regardless of the antenna system configuration. In other words, a customer should have the possibility to order a system without one or more services, the remaining antennas must retain the same individual performance.

In order to expedite the development process and reduce the costs relative to the use of prototype cars, numerical computations based on the surface discretizing method of moments are

successfully used for the development of different glass antenna systems as shown in Chapter 6. However, for roof antenna systems, volume discretizing simulation approaches appear to be a better choice. The implementation of the method of Finite Volume Time domain [Pipe 02; Fume 06] described in Section 3.3.1 into the used simulation framework requires that a complete system evaluation based on simulations using volume discretization to be accurately performed. In this chapter, a comparison between simulations realized with the standard MoM solution used in EMC Studio and simulations based on the FVTD method will be presented. In addition, the simulation results are validated by measurements. Furthermore, potential coupling between different antennas is investigated. Besides that, suggestions for optimal individual antenna positions inside the roof antenna system are given. Finally, 3D field measurement results are used to investigate the car roof influence on the antenna characteristics.

8.1 Roof Antenna Systems

Several RF services use antennas located on the roof. Figure 8.2 and Figure 8.3 show a roof antenna assembly consisting of patch antennas mounted on a ground plane (GPS, SDARS) and a radiating structure (GSM, UMTS). In order to integrate more antennas on the roof permitting the working of the new RF services, antenna systems have to be extended by keeping the same roof antenna assembly size [Tazi 11c]. Such system extensions can be performed only if the system integrity of the existing antennas is not affected. Besides that, sufficient space should be found to accommodate these additional antennas. In other words, the existing antennas should eventually be miniaturized while keeping the same performance.

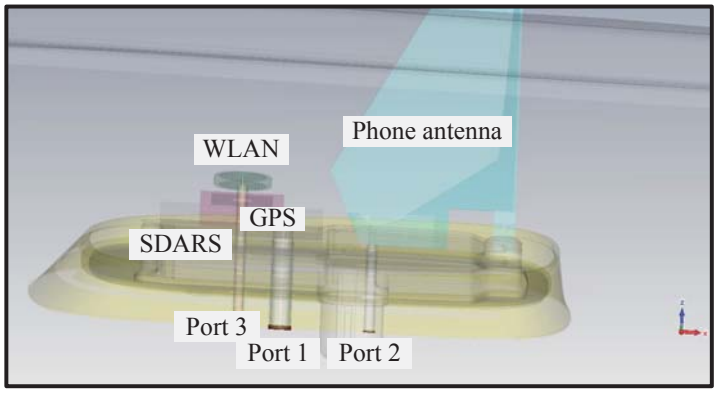

Figure 8.2: Position of different antennas in the roof antenna assembly.

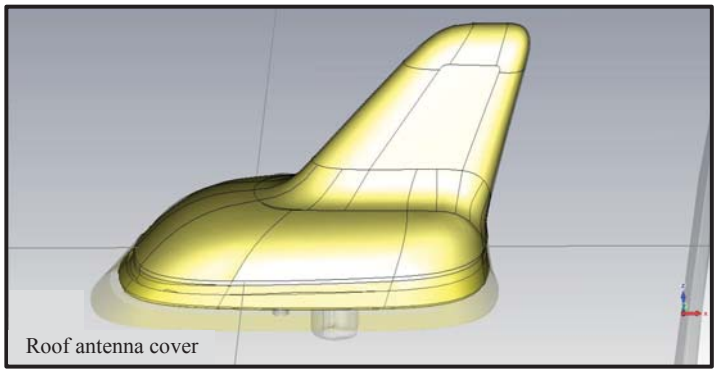

Figure 8.3: Model of cover of the roof antenna system.

Because of strict styling restrictions, further antenna systems such as LTE antennas, WLAN and Car-2-X antennas should also be placed in the roof antenna assembly without enlarging the cover, which represents a boundary condition that cannot be changed.

8.2 Application of the Finite Volume Approach for RF System Development

In Section 3.3, simulations based on the FVTD were validated with measurements and simulation approaches based on MoM and hybrid MoM.
The next important step to integrate the FVTD simulations in the roof antenna development process is to increase the simulation model complexity. This can be achieved by considering real roof antenna CAD data. Available roof antenna CAD data contains several geometry details, which may complicate the simulation model.
Simulations of RF systems in this chapter are calculated with the FV-Modeller, which is a simulation tool from the company EMCoS based on the Finite Volume Time Domain method presented in Section 3.3.1. The simulation tool is used for the virtual development of an antenna with a very high frequency range. Simulations are performed in the following steps:

1. *Data import*: Firstly, CAD data such as ACIS data that support the cleaning and simplification of the geometry should be imported into the simulation tool.

2. *Meshing*: The second step consists of determining the frequency range of interest to define the minimum required mesh steps. Generally, CAD data contains several hundreds of surfaces, volumes and edges for modelling small geometry details. Consequently, mesh generators may produce very small tetrahedra with a large ratio between the tetrahedral surfaces. The mesh steps should be fitted in certain areas to the geometry requirements

of complex shaped models. Great care should be given by modelling of coaxial cables with small inner and outer radii to avoid poor meshes. The most important criterion when analyzing mesh quality is the stability criterion presented in [Fume 08; Fume 06] as

$$\Delta t \leq \Delta t_{\max} = \frac{1}{c} \min \left(\frac{V_i}{\sum_{k=1}^{4} (A_k)} \right) . \tag{8.1}$$

V_i and A_i are the ith tetrahedral volume and surfaces, respectively. The equation states that the smallest tetrahedral edge defines the computation time step $\Delta t_{\max}$. Poor meshes might contain very small tetrahedral surfaces, which might affect the simulation time. The computation time step should be controlled by the smallest tetrahedron and not by the poorest one in terms of relationship between tetrahedral faces. Analyzer tools make it possible to show invalid tetrahedra by setting a reference value, which does not fall below the regular tetrahedron volume by a factor of 100 times. A regular tetrahedron is characterized by a value of

$$v = \frac{\min(\overline{MF_K})}{s_j} \tag{8.2}$$

where M is the midpoint of a tetrahedron and $\overline{MF_K}$ is the edge between M and its projection on the kth tetrahedral face. s_j is the mean value of the tetrahedral edges.

3. *Material parameters assignment*: In the third step, material parameters such as the permittivity ε_r and permeability μ_r are assigned. These parameters can be given as frequency dependent functions $\varepsilon_r(f)$ and $\mu_r(f)$, respectively.

4. *Boundary box modelling*: The complete space is discretized in the FV method. The boundary box is used to limit the simulated device environment and should model the infinite space expansion. Figure 8.4 shows an example of a boundary box model for a Bluetooth antenna simulation model. The box is placed empirically in $\lambda_{\min}/2$ distance to the antenna borders. $\lambda_{\min}$ represents the smallest wavelength in the material with the highest material permittivity $\varepsilon_{r_{\max}}$ controlled by the maximum frequency of interest $f_{\max}$ and the free space, c_0 is the speed of light according to

$$\lambda_{\min} = \frac{c_0}{f_{\max} \sqrt{\varepsilon_{r_{\max}}}} . \tag{8.3}$$

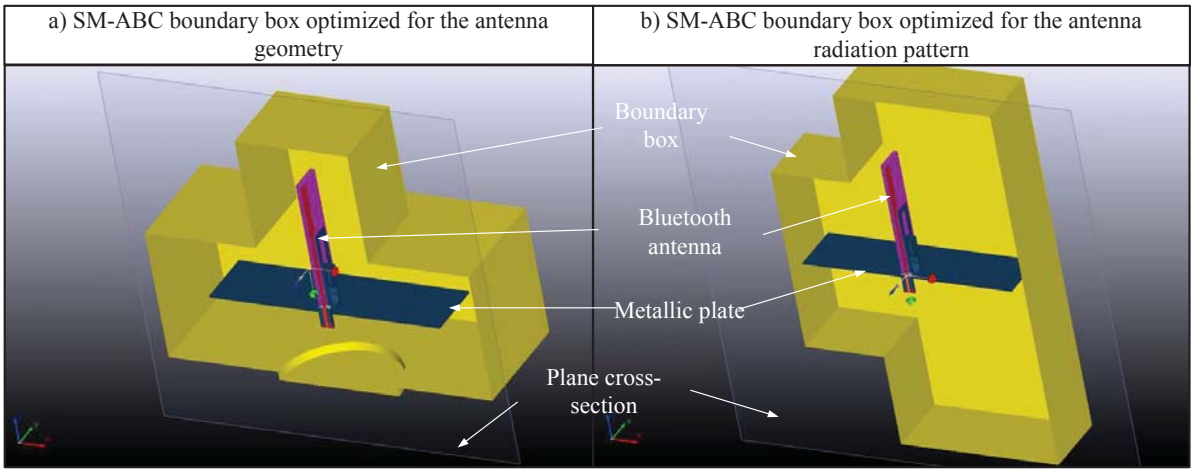

Figure 8.4: Modelling of the SM-ABC boundary box.

There are different approaches for modelling the boundary box. The method implemented in the used simulation framework is the **S**ilver-**M**ueller **A**bsorbing **B**oundary **B**ox (**SM-ABC**) method [Sank 07]. This approach reduces wave reflections on the boundary box surfaces to 50 dB when the incident wave fronts are perpendicular to the boundary box surface. Otherwise, the reflection can be higher, which means that energy is sent back to the system, falsifying the system characteristics. Hence, to ensure reliable simulation results, it is advantageous to model the SM-ABC taking into account the estimated radiation pattern of the antenna.
The **P**erfectly **M**atched **L**ayer (**PML**) is a better method for modelling the boundary box, which is independent of the antenna excited wave fronts and has a better wave reflection factor exceeding 80 dB [Sank 05; Fume 05]. This method will be implemented in a further version of the used simulation tool.

5. *Lumped circuit settings*: Often, lumped circuits are used to tune antenna characteristics or to filter undesired signals. In this case, it is possible to complete simulation models with concentrated RLC parameters.

6. *Port determination*: Antenna feeding points should be determined for calculating antenna parameters of interests such as the return loss parameter. The designed points are excited by electrical signals quantified by electrical energy. System characteristics such as the system reflection factor or system transfer function can be calculated when the feeding energy is completely swung off and converges to zero. The FVTD method and all numerical methods in time domain are therefore not generally suitable for systems with resonant characteristics because the system energy will probably be conserved inside the system and will never converge to zero.

The reflection factor of an automotive patch antenna deployed in a car information communication system service in Japan (see Chapter 1) is calculated by both MoM-MAS and FVTD methods and measured in a simulation range from 3 GHz to 10 GHz. Both simulation models and the real patch antenna are illustrated in the Figure 8.5.

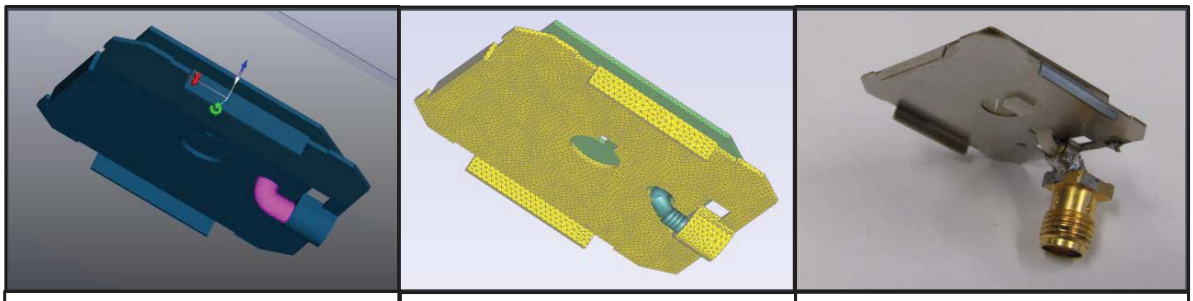

a) FVTD simulation model	b) MoM simulation model	c) Patch antenna model

Figure 8.5: Picture and simulation models of the patch antenna.

Figure 8.6 shows the obtained results confirming the previous validation investigation shown in Section 3.3. Both simulation curves fit well with the measurement curve in the whole frequency range. The MoM results show a deeper resonance than in measurements. This means that the MoM input impedance differs from the measured one. This can be attributed to the MoM simulations that do not take the skin-effect into account.

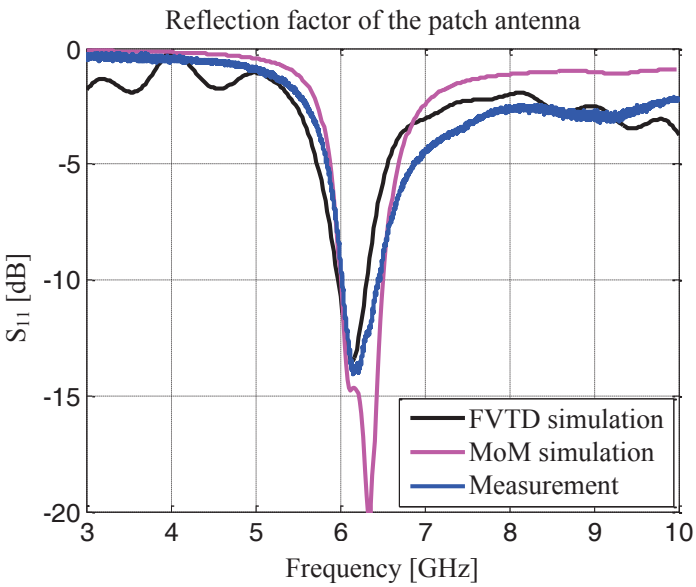

Figure 8.6: Validation of the simulation model of the patch antenna.

In addition to the patch antenna, a Bluetooth antenna is investigated with both numerical simulation approaches. The FVTD simulation model and a picture of the Bluetooth antenna are illustrated in Figure 8.7.

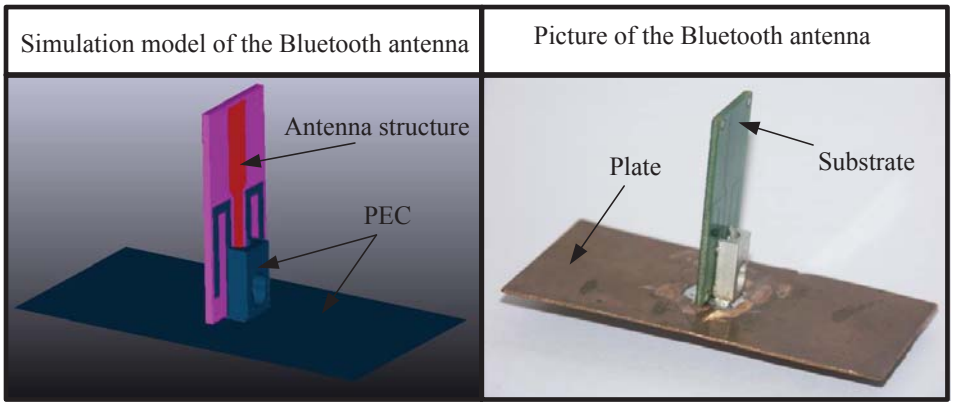

Figure 8.7: Picture and simulation model of the Bluetooth antenna.

Figure 8.8 shows the results obtained with the FVTD methods, which agree well with the measurement results. The simulation results obtained by the MoM-MAS method show a discrepancy to the measurement results. This can be explained by the metallic strips printed on both sides of the Bluetooth substrate, which cannot be taken into account properly by the imaging method of the auxiliary sources used in the MoM-MAS method.

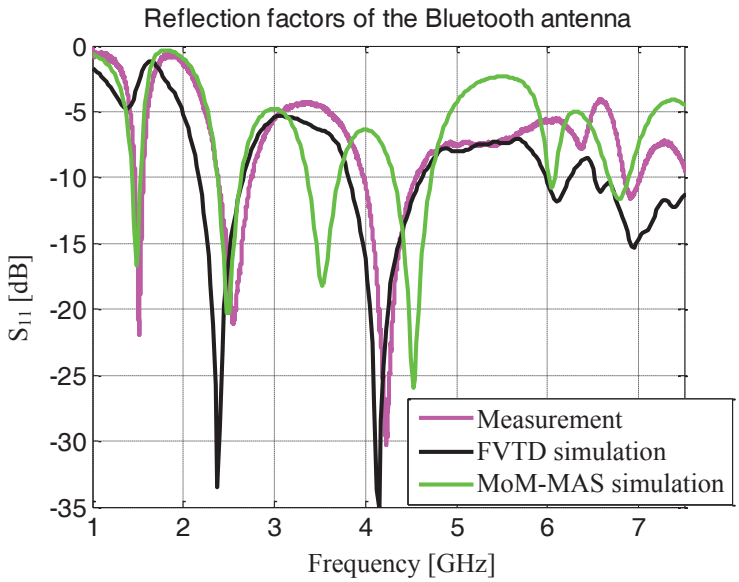

Figure 8.8: Validation of the simulation model of the Bluetooth antenna.

8.3 Influence of the Antenna Environment on the Antenna Performance

In order to reduce the simulation model complexity in relation to roof antenna systems several investigations based on measurements were carried out [Boch 11].
Usually, roof antenna assemblies with the same antenna system are placed on different car models. An additional objective of the said investigations is to explore the influence of the antenna environment on both the antenna radiation pattern and the antenna return loss. On the one hand, return loss parameter measurements were performed at the AUDI AG antenna laboratory. On the other hand the 3D antenna radiation pattern was measured at the **E**uropean **M**icrowave **S**ignature **L**aboratory (**EMSL**) in Ispra, Italy. Figure 8.9 illustrates a 3D radiation pattern measurement setup for a roof antenna mounted on an AUDI A8 car. The measurement setup consists of a hemispherical absorbing chamber with a diameter of 20 m. A platform is positioned in the center of the chamber, where a complete car with a maximal weight of 3 t could be placed.

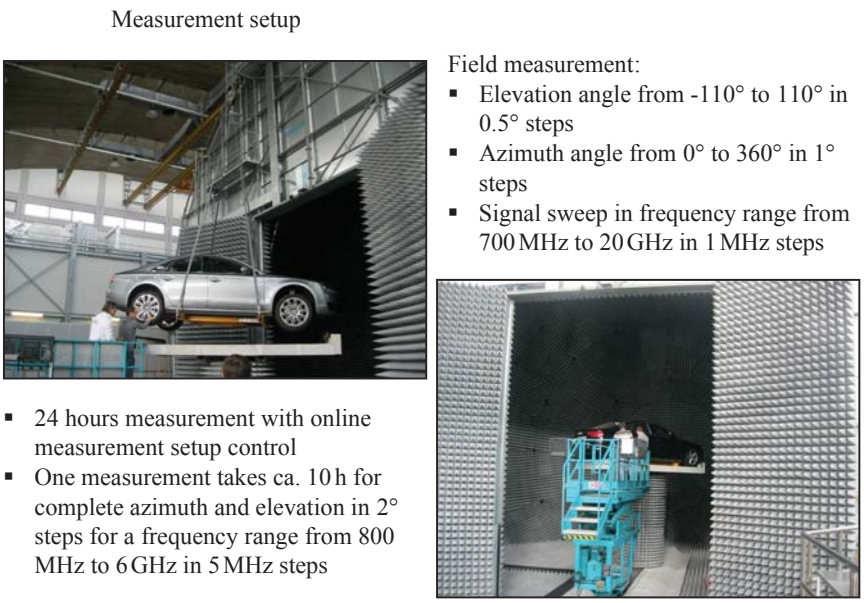

Figure 8.9: Picture of the radiation pattern measurement setup in Ispra.

The platform can be rotated in $\varphi = \pm 180°$ so that 3D radiation pattern measurements are possible as shown in Figure 8.10.

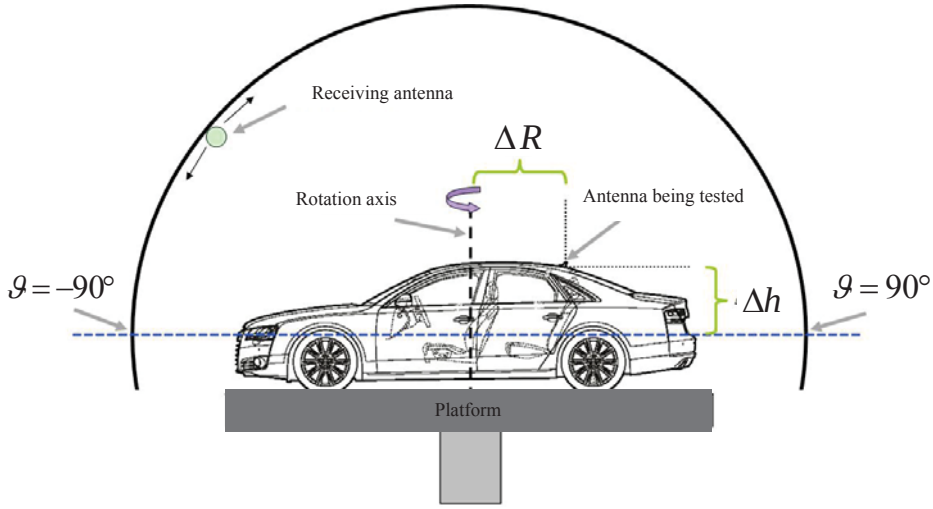

Figure 8.10: Radiation pattern measurement setup at EMSL.

The chamber contains two separate TX/RX antenna modules fixed on two sleds permitting a coverage of an angle interval of ±115°. Both the antenna being tested, in this case the sending antenna, and the receiving antenna are connected to a **N**etwork **V**ector **A**nalyzer (**NVA**) sending a frequency sweep from 500 MHz to 20 GHz. At each measuring point, the receiving antenna measures the vertical and horizontal polarization components separately at the same time.

The system is calibrated at the start of each new measurement configuration with a reference antenna to deliver a calibration parameter when analyzing the measurement results. Besides that, measurement errors related to the fact that the antenna being tested is not positioned in the center of the chamber should be investigated. Usually, the reference antenna is positioned in the center of the chamber during the measurement setup calibration process. The antenna being tested corresponds to the roof antenna mounted on a car and it is located at 60 cm height from the skid level at $\vartheta = 90°$ and $\vartheta = 270°$, respectively and at a distance of 1 m from the chamber center according to Figure 8.10. Firstly, the case in which the height difference between the two antennas is set to zero to define the maximum antenna position caused a horizontal error. Afterwards, the worst case is considered for all azimuth angles $\varphi = \pm 180°$. The distance between the antenna being tested and the receiving antenna is $d = R_0 + \Delta R =$ 9.5 m+1 m=10.5 m. Assuming that the investigated case corresponds to the far field and the field decreases relative to the distance r in the far field with $1/r$, the horizontal measurement error for both directions corresponds to $\pm 20 \log_{10}(9.5\,\text{m}/10.5\,)\text{m} = \pm 0.87\,\text{dB}$. Similar to the maximum horizontal error, the maximal vertical antenna position, which causes an error can be calculated. For the measurement at $\vartheta = 180°$ with consideration of the height difference of 0.6 m in the worst case, the distance is calculated by $d = R_0 + \Delta h = 9.5\,\text{m}$-0.6 m=8.9 m. The obtained measurement error is 0.57 dB.

The executed investigations comprised the following antenna environment parameters, which may affect the antenna characteristics:

- Roof antenna cover
- Roof curvature
- Roof size
- Roof material

Figure 8.11 shows a measured roof antenna system equipped with a WLAN antenna while keeping the same roof antenna assembly size of a regular AUDI antenna.

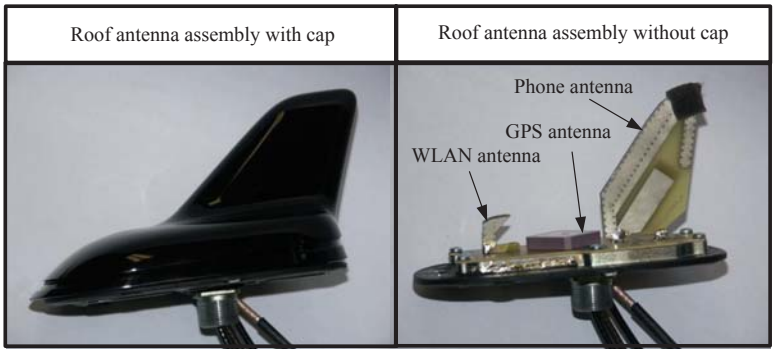

Figure 8.11: Investigated roof antenna assembly with and without cover.

Normally, roof antenna systems are developed without much attention being paid to the roof antenna cover. The goal of the first measurement is to investigate the effect of the cover on the roof WLAN antenna performance. Figure 8.12 shows the S_{11} measured curves for the WLAN antenna with and without cover. From the results obtained, it can be seen that the difference between the two configurations is negligible in a frequency range up to 4.7 GHz.

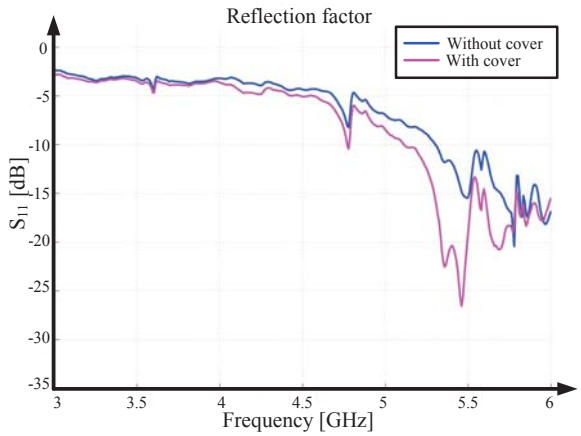

Figure 8.12: Influence of the roof antenna cover on the S_{11}-parameter.

The realized antenna gain of both configurations for different elevation angles was measured and averaged over all azimuth angles and plotted as function of frequency f to facilitate the comparison of the measured configurations. Figure 8.13 shows the results obtained for both elevations at $\vartheta = 100°$ and $\vartheta = 80°$.

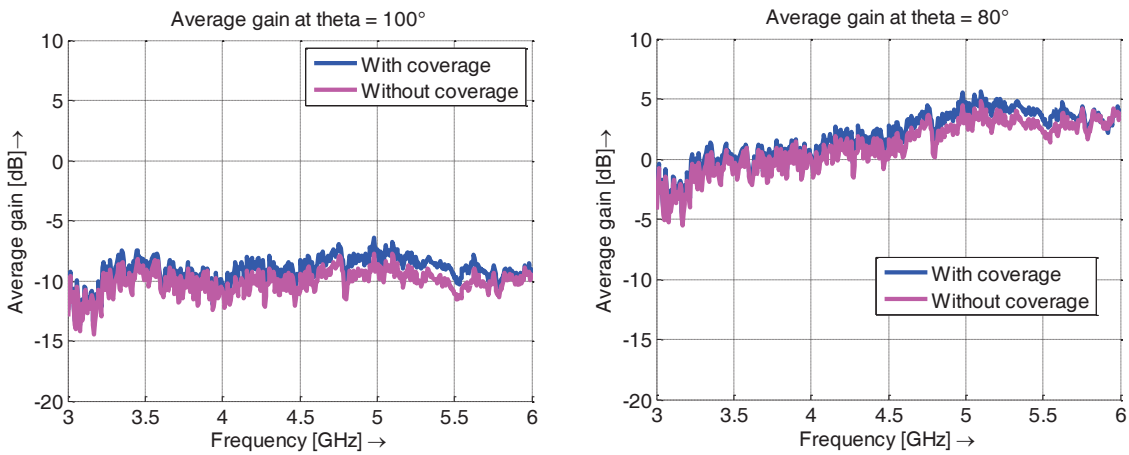

Figure 8.13: Influence of the roof antenna cover.

For higher frequencies, a remarkable improvement in the configuration with antenna cover can be detected. This can be explained by the fact that the antenna cover presents an additional capacitance that improves the return loss parameter at this frequency range. Both elevation angles are very important for Car2Car applications, where the antenna performance should have its best radiation pattern characteristics. For both angles, it can be observed that the measured configuration with roof antenna cover has a better performance especially at frequencies greater than 4 GHz, which can be explained by the fact that the return loss factor is

included in the formulation for the realized gain calculation $G_{realized}$ according to the antenna gain G formula:

$$G_{realized} = G\left(1 - |S_{11}|^2\right). \tag{8.4}$$

Hence, reliable system evaluation requires the roof antenna cover to be taken into account during the system development process at least for the return loss parameter. For the radiation pattern in terms of antenna gain, simulation models could be simplified by reducing the cover from the geometry model complexity, which can reduce the calculation time significantly.
In the second step, the effect of the roof curvature on the roof antenna system performance is investigated. For this purpose, another antenna type is considered. The wideband antenna used was developed at the Volkswagen research center as part of a Masters thesis and shows very good antenna characteristics for most installed automotive roof antenna service requirements (GSM, LTE, Car2Car, GPS, SDARS) [Kwoc 10]. Since this antenna has only one port, it can easily be used for measurement at the different frequency ranges. This antenna is used for the next investigations concerning the roof curvature, roof material and roof size.
Both the used roof antenna and the wideband characteristic of the return loss parameter in a frequency interval from 1 GHz to 6 GHz are illustrated in Figure 8.14.

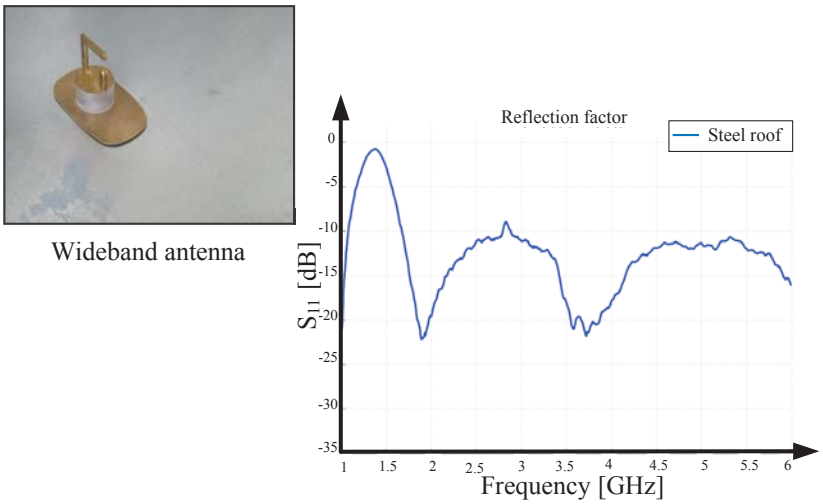

Figure 8.14: Picture and return loss of the wideband antenna used.

In order to investigate the effect of the car roof curvature on the antenna performance, the wideband antenna was mounted on a roof section with a size of 70 cm × 100 cm and on a flat plate with the same size and material of the roof section to get comparable setup to the car measurements. Both mounted antenna configurations are depicted in Figure 8.15.

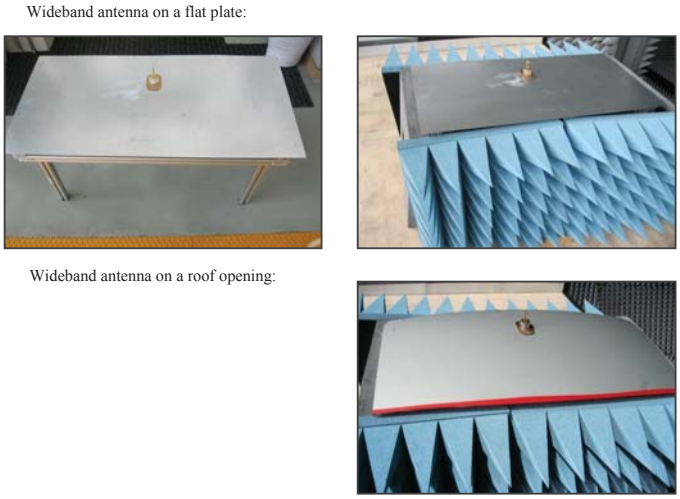

Figure 8.15: Mounted antennas on a roof section and on a flat plate.

Both the car roof section and the plate are placed on a stand covered with absorbent materials as shown in Figure 8.15. Figure 8.16 presents the measured return loss parameters in the frequency interval from 1 GHz to 6 GHz for both configurations.

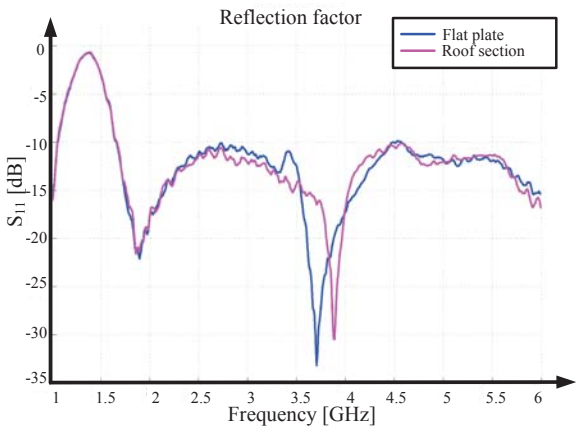

Figure 8.16: Influence of the curvature of the car roof.

From the obtained results, it can be seen that both curves are very similar except for a small discrepancy in the frequency range from 3.5 GHz to 4 GHz, where the third antenna resonance appears. Due to the fact that this difference affects levels smaller than −15 dB, it can be assumed that this difference is negligible and can be attributed to measurement uncertainty in the measurement setup. Hence, antenna development in terms of the reflection factor could be simplified in both measurement and in simulations taking into account flat shapes as a reference electrical ground of the roof antenna system. Figure 8.17 shows the average realized antenna

gain measured average realized antenna gain measured the two configurations at $\vartheta = 60°$ and $\vartheta = 90°$ as function of the frequency f.

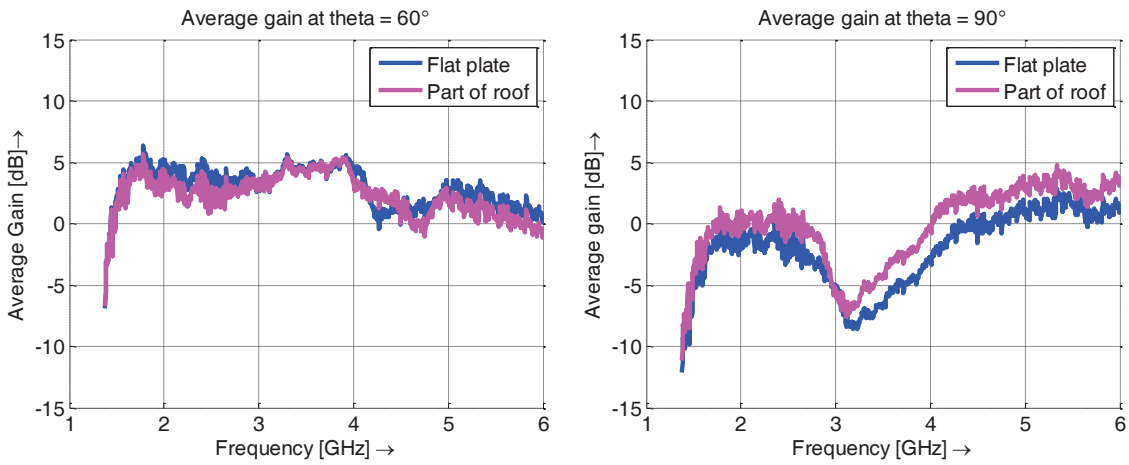

Figure 8.17: Influence of the roof curvature.

The results obtained at both elevation angles show the same curve shape. For both configurations, the two measured curves differ from each other and a difference value of 3 dB is achieved. Since the measured return loss parameter for both configurations is very similar, this effect can only put down back to the geometry model showing a curvature difference. Therefore, to evaluate the real antenna radiation pattern, the roof curvature should be taken into account during the system development. The third investigation is related to the impact of the model reduction on the antenna characteristics. By means of this, two different configurations are considered. In the first one, the antenna system is mounted on the whole car and measured. In the second configuration, the antenna is mounted on the roof section used in the second investigation. The goal of this investigation is to see if it is possible to reduce the system model to an antenna mounted on reference ground for the roof antenna system development. Figure 8.18 presents the return loss parameters measured in the frequency interval from 1 GHz to 6 GHz for both configurations.

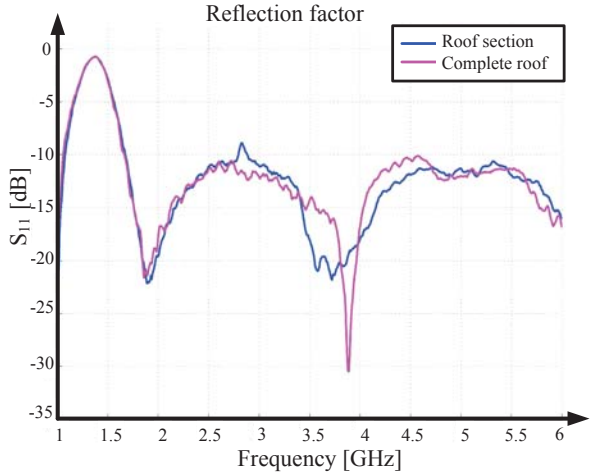

Figure 8.18: Influence of the roof size on the S_{11}-parameter.

Similar to the S_{11} results obtained in the previous investigation, it can be seen that both curves are very similar except for a small discrepancy in the frequency range from 3.5 GHz to 4 GHz for the third antenna. That means, a system reduction does not affect the accuracy of the results for the return loss parameter. From the obtained results of the average realized antenna gain measured over all azimuth angles of both configurations at $\vartheta = 60°$ and $\vartheta = 90°$ shown in Figure 8.19, it can be seen that for both configurations, the two measured curves differ from each other and reach values of approximatively 5 dB apart.

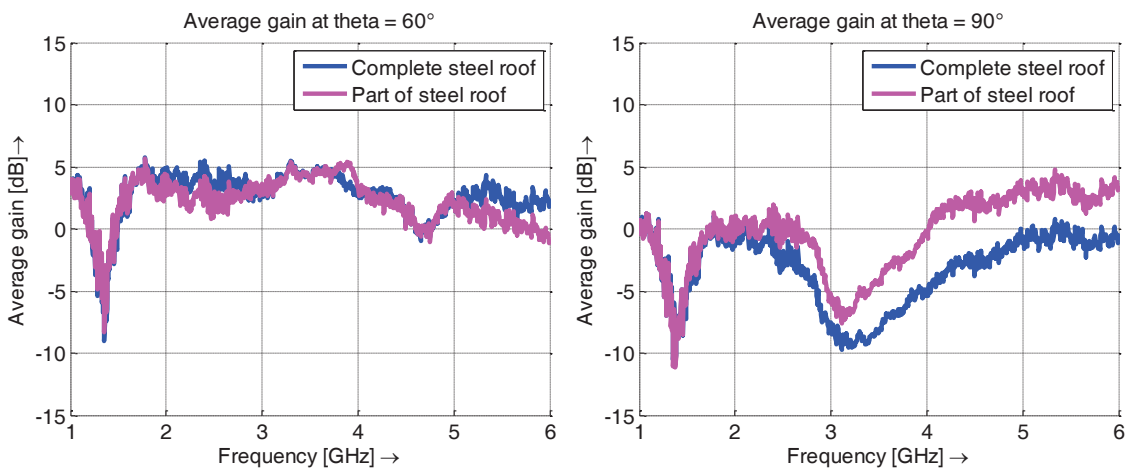

Figure 8.19: Influence of the roof size.

Therefore, to evaluate the correct antenna radiation pattern, the complete car should be taken into account during the virtual system development process. Simulations can be used in a first step to optimize the best antenna configuration with a reduced simulation model. In this case,

it is sufficient to use models with a part of steel roof instead of complete car. This system reduction is done in order to save computation time. The results of the different antenna configurations could be compared to give a statement about the best optimized system, which fits with the one developed on the basis of measurements. In order to evaluate the real system performance in the field, a complete car should be taken into account in last step of the system simulation process.

In the next investigation, the influence of the roof material on the antenna performance is taken into account. This is important for the system developer to know how the antenna behaves on cars with different roof configurations. In this investigation, two different AUDI A8 cars are used. The first with a steel roof while the second is equipped with a sliding glass roof. Gain in terms of realized gain is measured and compared.

The obtained radiation pattern results for the vertical antenna pattern cut is presented in Figure 8.20.

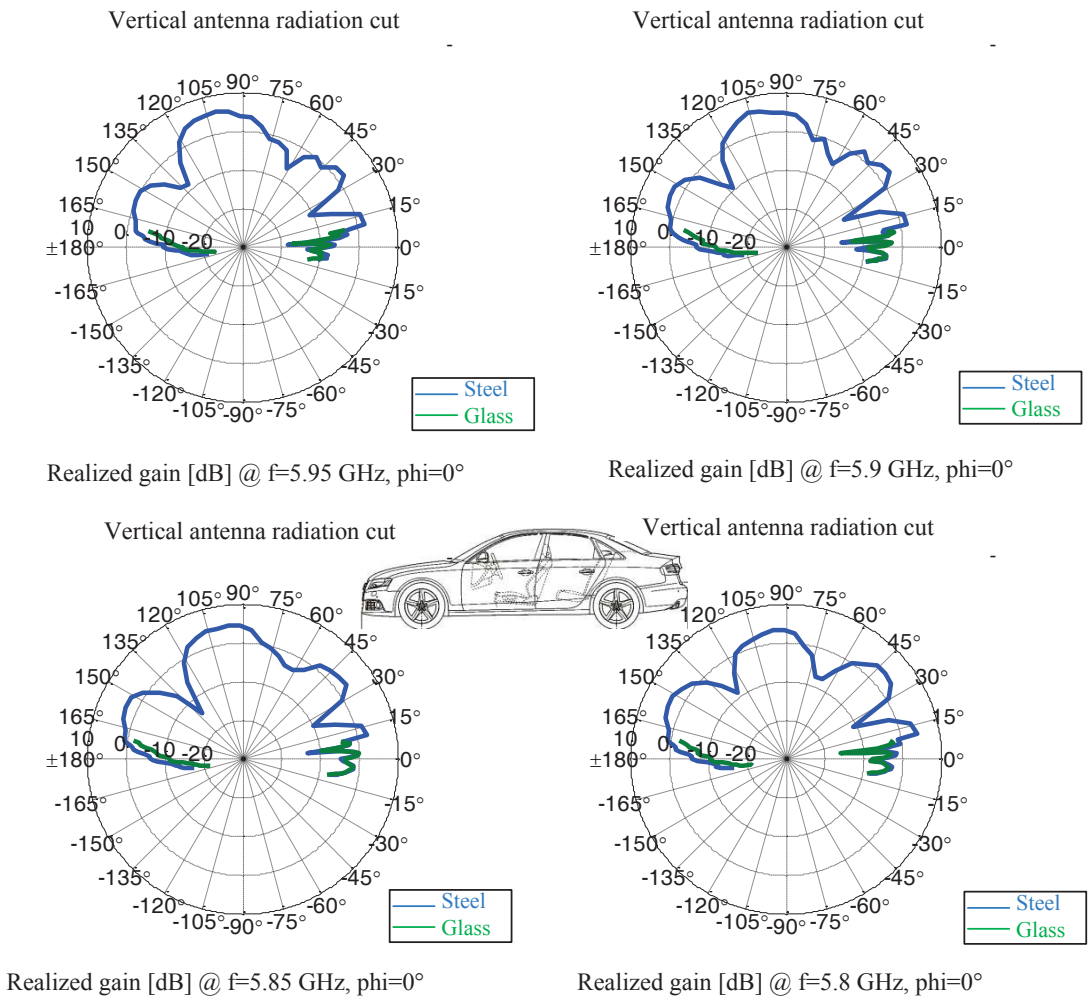

Figure 8.20: Influence of the roof material on the vertical antenna pattern cut.

The presented measurements were realized at frequencies relevant for Car2Car applications. The vertical antenna pattern cut measurement was performed for the azimuth angle $\varphi = 0°$ and the elevation angles from $\vartheta = -100°$ to $\vartheta = 100°$ in 1° steps for the steel roof and from $\vartheta = -100°$ to $\vartheta = -80°$ and from $\vartheta = 80°$ to $\vartheta = 100°$ in 1° steps for the glass roof. The measurement angle limitation for the glass roof configuration is due to measurement time restrictions, which did not permit to extend the measurement interval to be extended in the complete upper side of the vertical antenna pattern cut. However, the obtained results are sufficient to evaluate both configurations for Car2Car applications. From the results depicted in Figure 8.20, it can be seen that all realized gains measured for the glass antenna are lower than the ones measured with the steel roof for the elevation angle interval $\vartheta = -100°$ to $\vartheta = -80°$. For Car2Car applications, this interval is one of the most important regions allowing the antenna to communicate with antennas installed in cars in the front. The difference between the two configurations can reach more that 4 dB. Besides that, the obtained radiation pattern results for the horizontal antenna pattern cut are illustrated in Figure 8.21.

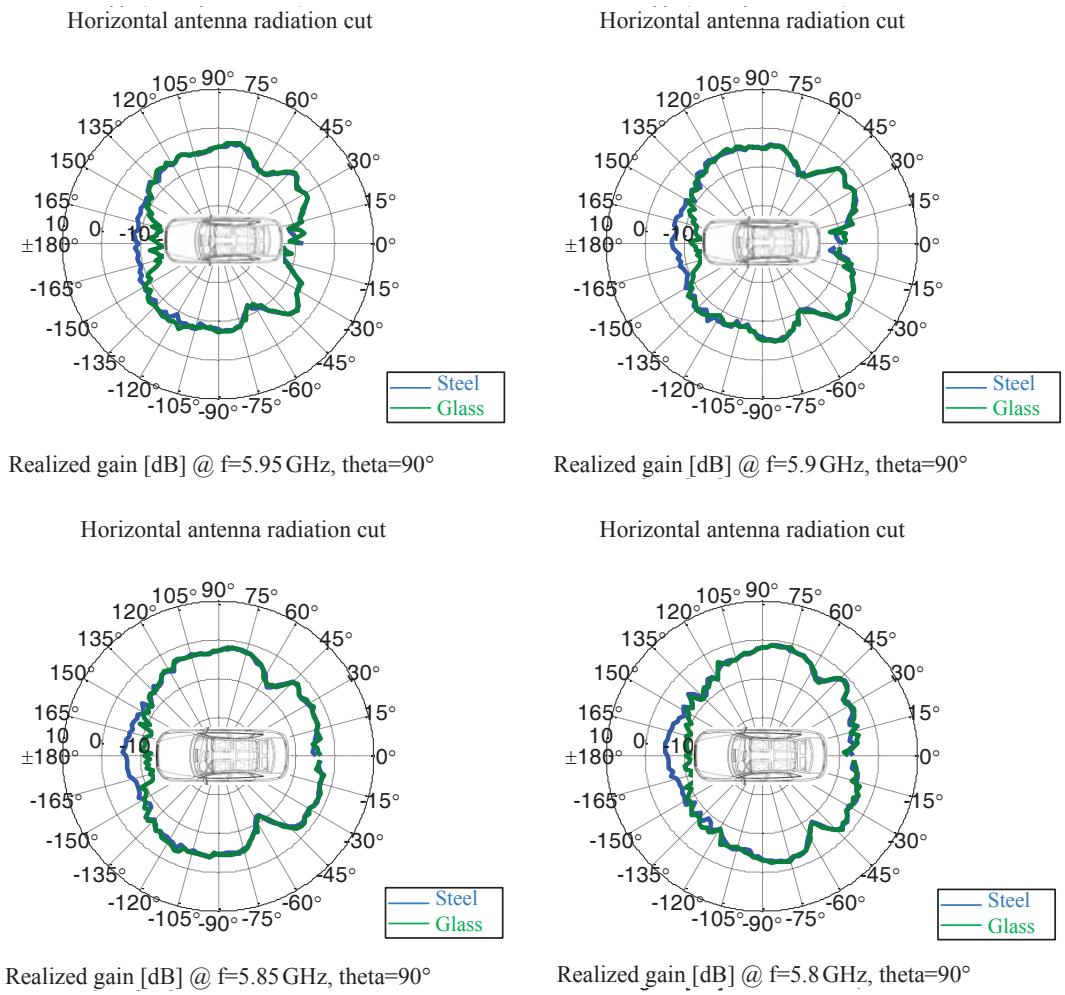

Figure 8.21: Influence of the roof material on the horizontal antenna pattern cut.

The horizontal antenna pattern cut measurement was performed at the elevation angle $\vartheta = 90°$ and for the azimuth angles from $\varphi = 0°$ to $\varphi = 360°$ in 1° steps. Similar to the results presented in Figure 8.20 the results depicted in Figure 8.21 show that all realized gains measured for the glass antenna are lower than the measured ones with the steel roof for the azimuth angle interval from $\varphi = 150°$ to $\varphi = 210°$. That means that the glass roof antenna performance is very poor compared to the steel roof configuration for Car2Car applications, where the azimuth angle interval from $\varphi = 150°$ to $\varphi = 210°$ plays a major role because of diverse Car2Car communication scenarios. The difference between the two configurations can exceed 8 dB. From the results obtained for both antenna pattern cuts, it can be deduced that much attention needs to be paid when roof antenna systems developed close to a certain part of roof material. Hence, roof material parameters should be taken into account in the simulation to ensure a reliable antenna development process.

8.4 System Development

In this section, it will be shown how simulations based on the FVTD method can be deployed to predict roof antenna system characteristics at very high frequencies.
Figure 8.22 shows an antenna assembly comprising three different antennas operating in different frequency ranges:

1. UMTS + GSM transmitter for mobile applications consisting of strips printed on a substrate according to Figure 8.22
2. GPS patch antenna used for the positioning system
3. SDARS patch antenna used for satellite radio service

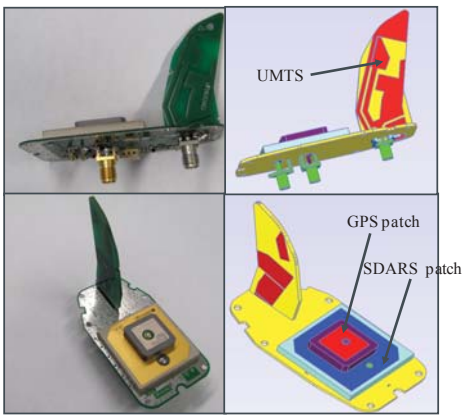

Figure 8.22: Roof antenna assembly.

In the first stage of development, it is advisable to investigate the difference between the antenna characteristics of the single antenna and the same antenna integrated in an antenna assembly. Figure 8.23 shows an SDARS antenna mounted on a metallic plate and its corresponding FVTD simulation model [Boch 11]. The antenna feeding point remains unchanged in comparison to the antenna mounted in a roof antenna assembly.

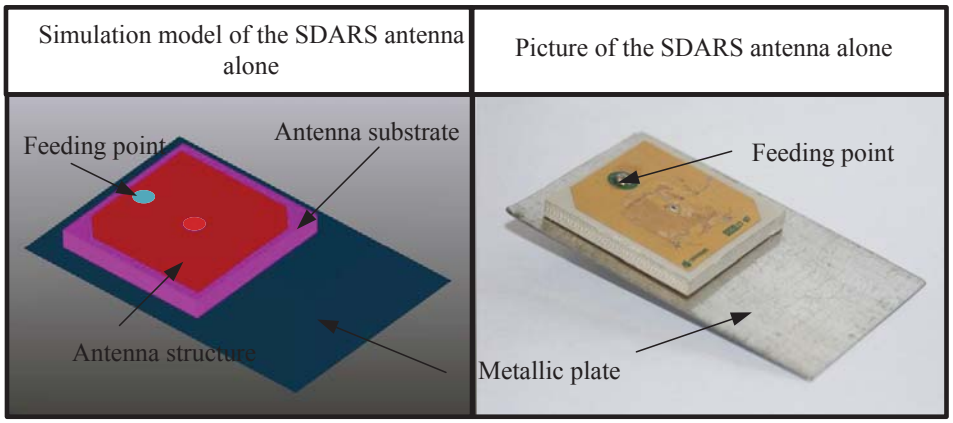

Figure 8.23: Picture and simulation model of the SDARS antenna alone.

From the presented results of the antenna reflection factor in a frequency range from 1 GHz to 5 GHz depicted in Figure 8.24, we can see that the simulation results agree well with the measurement results. Both curves indicate resonances at two frequency points, 2.4 GHz and 4.7 GHz. The SDARS service operates at 2.4 GHz.

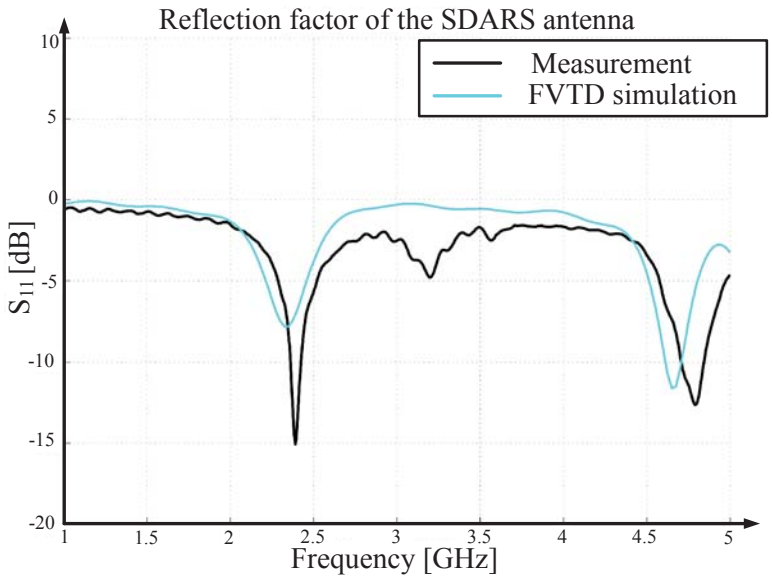

Figure 8.24: Validation of the FVTD simulation results of the SDARS antenna alone.

In a second step, it is interesting for antenna development engineers to investigate the interaction between two antennas, which are stacked such as the previous SDARS patch antenna and the GPS patch antenna as shown in Figure 8.25 [Iche 01]. Both antennas are mounted on a metallic plate.

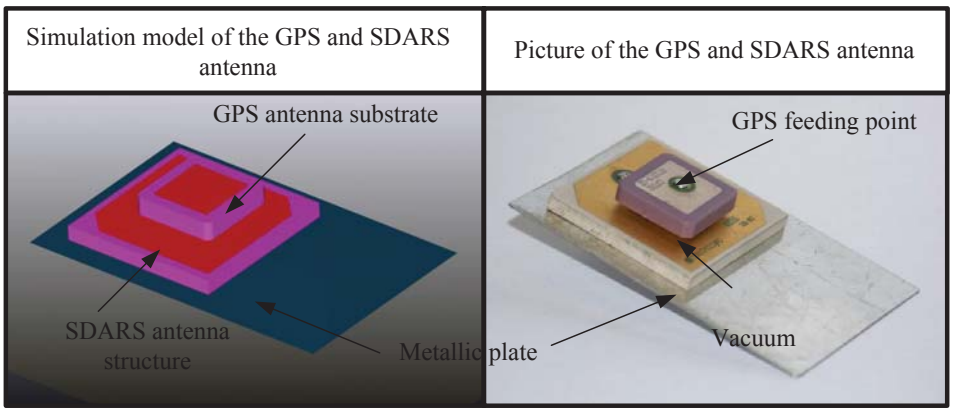

Figure 8.25: Picture and simulation model of the SDARS stacked with GPS antenna (1).

From the results presented in Figure 8.26 concerning the reflection factor S_{11} in a frequency range from 1 GHz to 5 GHz, we notice that the influence of the mounted GPS patch antenna on the SDARS antenna is negligible. Obtained simulation results based on the FVTD show good agreement with the measurement results.

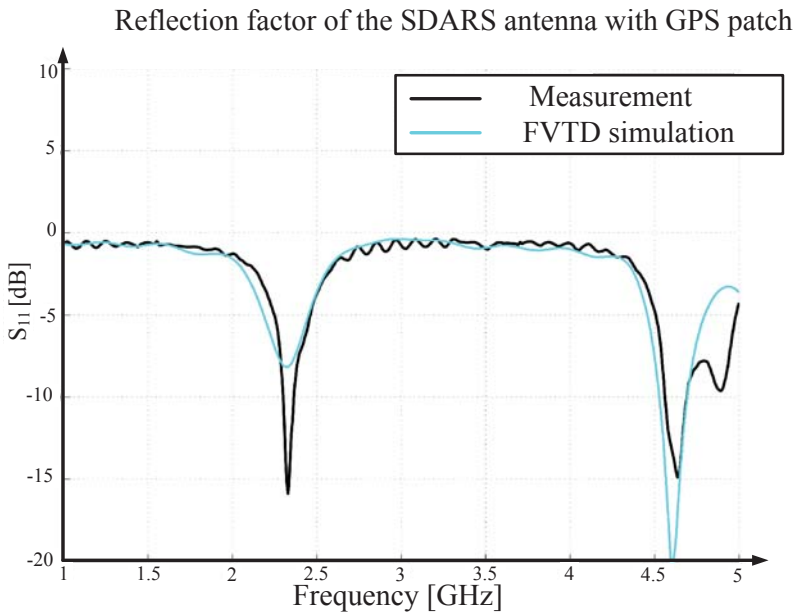

Figure 8.26: Validation of the FVTD simulation results of the SDARS antenna with GPS antenna.

Similar to the previous investigations, the UMTS antenna is soldered on a metallic plate according to the Figure 8.27 illustrating the antenna model and its appropriate simulation model.

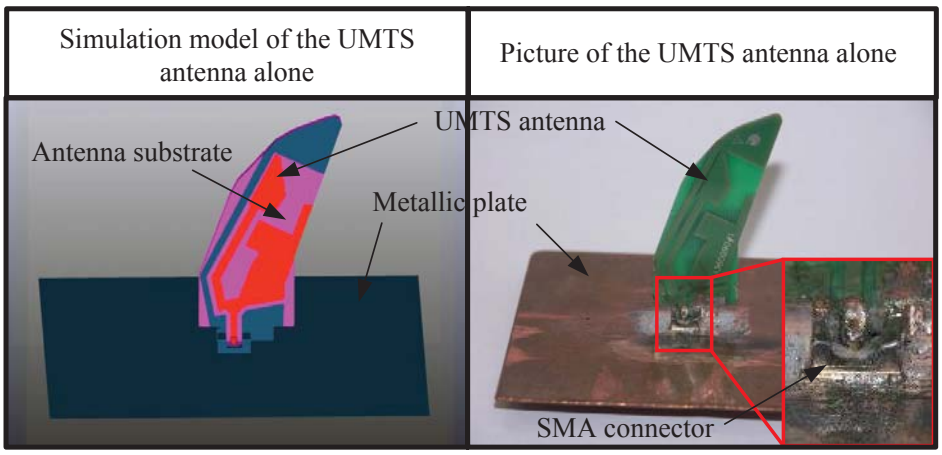

Figure 8.27: Picture and simulation model of the UMTS antenna.

Again, measured and simulated results illustrated in Figure 8.28 related to the antenna reflection factor agree satisfactorily in a wideband frequency range from 1 GHz to 5 GHz, where both curves show antenna resonances at the same frequency points or very close to each other. It should be noted that the value of the loss angle $\tan\delta$ of the antenna substrate was not available at the time of the simulation exercise. Therefore, this parameter was estimated. That could explain why at certain frequencies the simulated resonance level differs from the measured one.

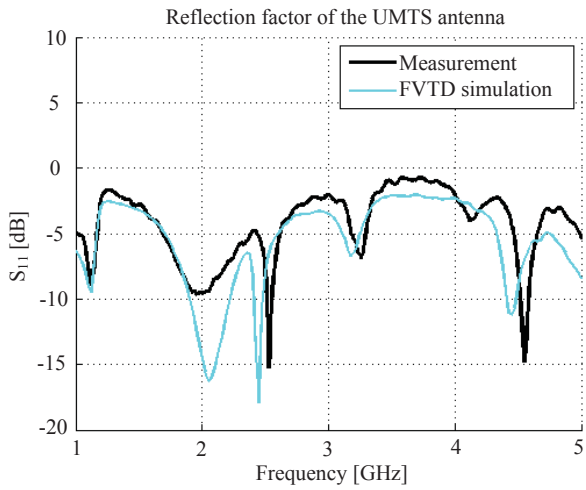

Figure 8.28: Validation of the FVTD simulation results of the UMTS antenna.

Table 8.1 shows simulation details of each executed simulation, where the number of the tetrahedra is directly related to the required simulation time. It should be noted that the last listed simulation model containing a very high number of tetrahedra was a first rough model and is shown in the table to exploit the modelling effect on the required simulation time. Hence, it is meaningful to spend more time to generate clean models with an acceptable number of tetrahedra that will be balanced during simulation.
Besides that, Table 8.1 gives the stability factor and the poorest tetrahedron parameter mentioned in Section 3.3.1, which describe the mesh quality of each simulation model. Empirically, to obtain reasonable simulation results, the stability factor and the poorest tetrahedron parameter have to be higher than 1% and 10%, respectively. If this rule is not respected, simulation accuracy could decrease.

Simulation model	Number of tetrahedra	Stability factor ζ [%]	Poorest tetrahedron parameter [%]	Simulation time [min]
Patch	766018	2.67	17.0	77
Bluetooth	632039	3.76	16.9	61
UMTS	1992953	4.00	10.3	1305
SDARS	874501	3.94	15.1	152
GPS	946908	1.34	14.7	380
SDARS+GPS	1200011	1.26	12.5	1100

Table 8.1: Simulation information for the results presented above.

Investigations have shown that the development of roof antenna systems requires to consider both the antenna cover, the ground plane of the roof antenna, and at least a small part of the car roof. These details shown in Figure 8.29 affect the antenna reception behaviour and cannot be neglected to achieve accurate results.

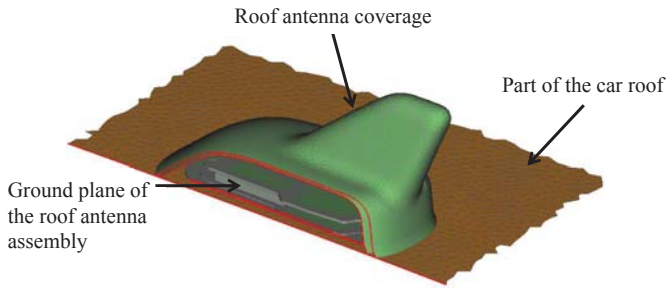

Figure 8.29: Cover and ground plane of the roof antenna assembly.

Figure 8.30 shows a simulation model of the roof antenna assembly consisting of a WLAN antenna, GPS antenna and UMTS antenna. The goal of this investigation is to see the effects on the UMTS antenna performance due to antennas placed in the immediate vicinity.

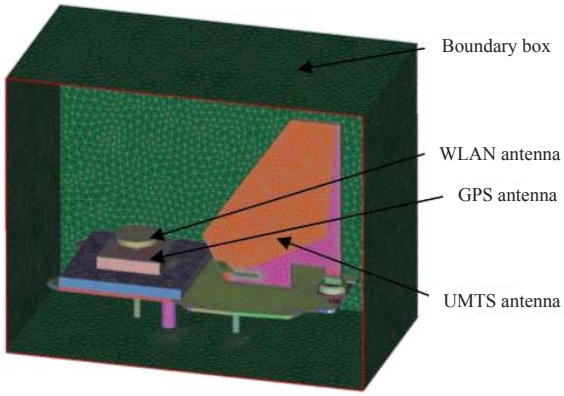

Figure 8.30: Simulation model of roof antenna system.

From the results shown in Figure 8.31 it can be seen that the coupling from the WLAN antenna (Port 2) to the UMTS antenna (Port 1) and from the coupling of the GPS antenna (Port 3) are negligible. This is desirable as the different services should not affect each other.

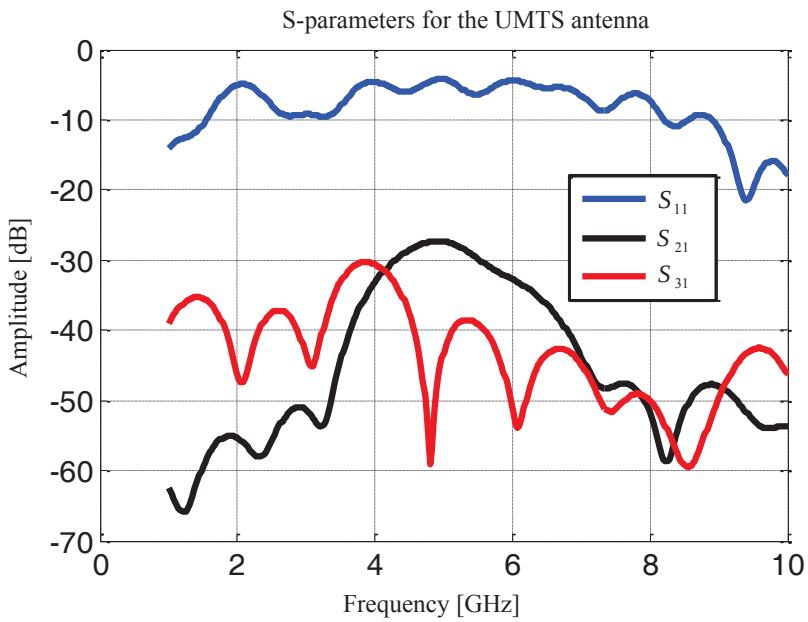

Figure 8.31: Results of the roof antenna sytem.

Also, development of the UMTS antenna can be performed without taking into account of the adjacent antennas to save simulation time. However, it is recommended in the last stage of development to consider all antennas including the ground plane and roof antenna cover as shown in Figure 8.29 for a realistic evaluation of the complete system.

One possibility to integrate the new wireless LAN antenna used for Car2X communication systems is to stack it on the GPS antenna. Figure 8.32 shows a simulation model of the wireless LAN antenna located in free space without taking into account of the adjacent antennas.

Figure 8.32: Wireless LAN antenna system.

Figure 8.33 illustrates the simulation model of the wireless LAN antenna by taking into account the GPS and SDARS antennas.

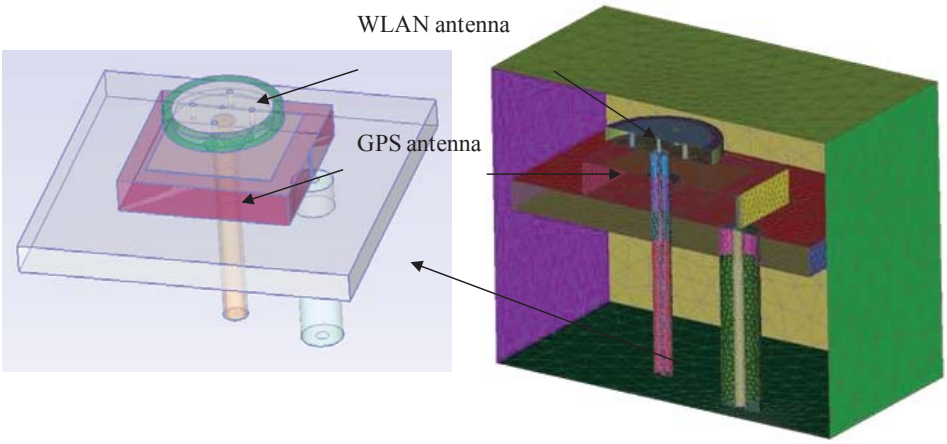

Figure 8.33: Wireless LAN and GPS antenna system.

Figure 8.34 shows a comparison of simulation results from the wireless LAN antenna in free space and by taking into account the GPS antenna and the ground plane. From the results below we can see how the reflection factor changes by placing the antenna on the existing GPS antenna.

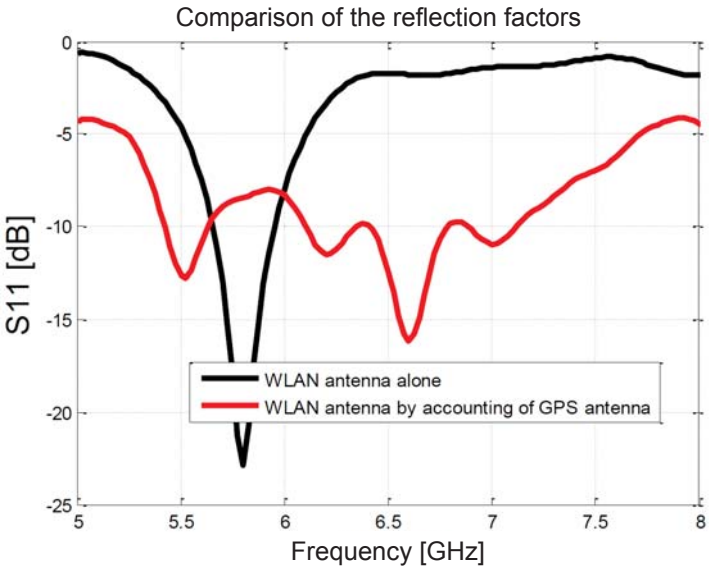

Figure 8.34: Wireless LAN and GPS antenna system results.

From these results, it can be seen how important it is to develop new antennas such as the wireless LAN antenna with consideration for other antennas in its vicinity. From the investigation results shown above, we can see that numerical approaches based on the finite volume method can provide a tool for the evaluation and development of wideband antenna systems for automotive applications. Hence, new challenges can be tackled by way of simulation in order to reduce the physical size of the antenna system. This helps to integrate the increasing number of antennas into the same allotted space while at the same time achieving a good compromise between system design and good reception quality for all available multimedia services.

9 Conclusion and Outlook

Due to the increasing number of car models and car configurations as well as the short development time, EM simulations are needed more than ever. The use of numerical simulation approaches is essential to ensure the best possible reception quality of the multiple automotive antennas installed in present-day vehicles, as presented in Chapter 1.
Optimized automotive antennas have to take into account several criteria as listed in Chapter 2.
Figure 9.1 gives an overview of the different simulation approaches applied in the virtual development process of automotive antennas.

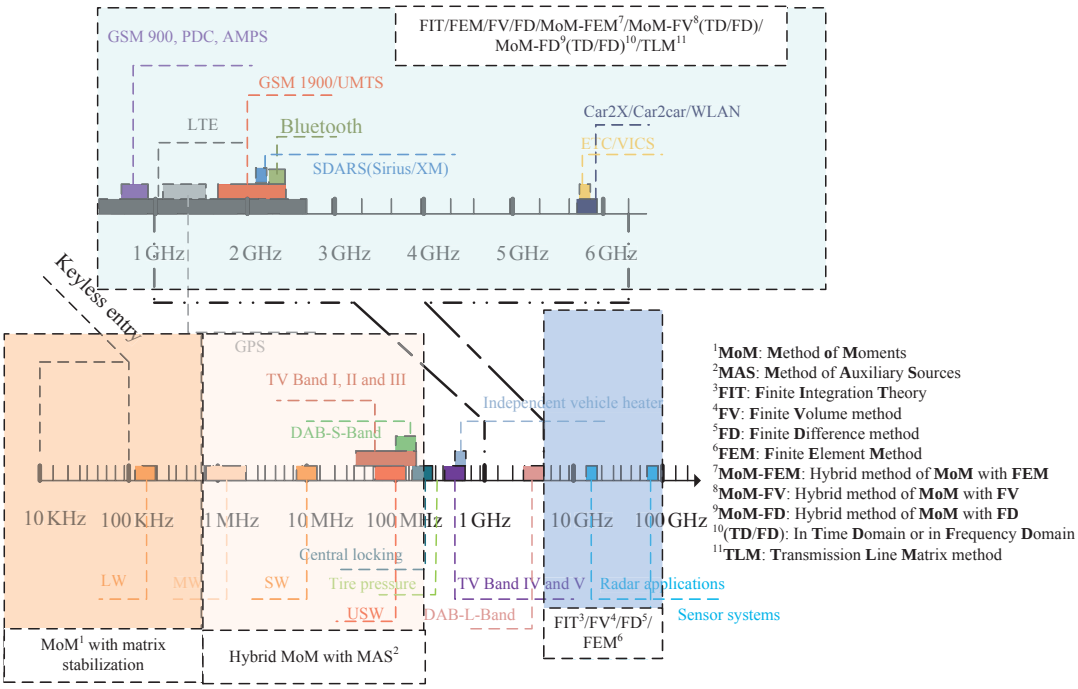

Figure 9.1: Numerical methods for RF automotive simulation.

The method of moments is one of the most popular simulation methods for automotive antenna simulations due to acceptable accuracy within a reasonable simulation time. The MoM taking into account the EFIE and MFIE formulations presented in Chapter 3 can be used in a low frequency range starting at 20 kHz such as for keyless entry or keyless go systems as shown in

Chapter 7. One challenge of the MoM applications in the treatment of glass antenna systems is to take into account the dielectric effect of sheet glass. Therefore, several approaches based on the MoM were developed to reflect the non negligible effect of the glass material. Three of the most used approaches for glass antenna simulations are described in Chapter 3. These numerical methods are validated by comparison with measurements as presented in Chapter 3 and Chapter 6. The hybrid MoM approach delivers with correct modelling of the simulation environment good results compared to measurements for both return loss and radiation pattern for glass antennas. Highly accurate simulation results can only be achieved if all measurement parameters are correctly modelled in the simulation framework such as the ground and the glass parameters. Geometry models of the car bodyshell affect the behaviour of glass antennas and should be taken into account for a correct simulation. Besides that, it can be assured that the best optimized automotive glass antenna in free space will be the best one when considered in its real environment. In the last stage of the automotive glass antenna development process, once the antenna is optimized in free space, one last measurement considering the complete antenna environment can be performed to check the simulation results. For very high frequency ranges, FIT, FV or FD could be applied to calculate antenna characteristics in a very high frequency range as for radar and sensor applications. In a frequency range from 1 GHz up to 5 GHz, it is recommended to take into account the influence of the car body. Simulation models can be quite large and require a long computation time. Therefore, computation time optimization methods described in Chapter 4 should be used to save computation time. In order to reduce the computation resources, hybrid methods based on MoM and FV, FEM or FD can be used [Jako 99; Brun 04; Pier 97; Alay 02; Thie 75; Geor 05].
Figure 9.2 gives an example of an antenna assembly mounted on the car roof.

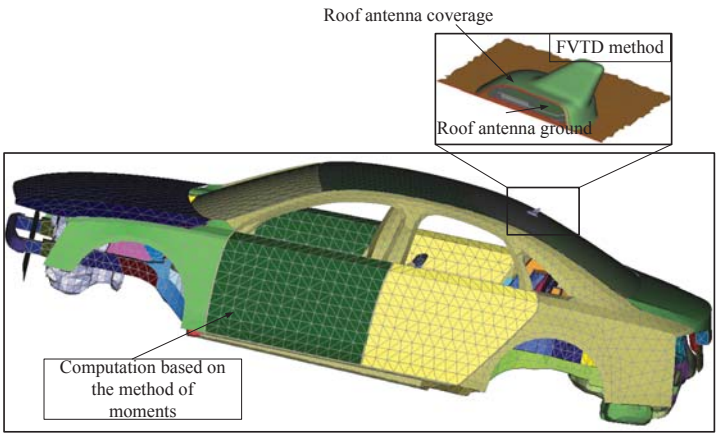

Figure 9.2: Hybrid method for calculating the roof antenna parameters taking into account the effect of the car body.

In order to obtain accurate results, new approaches could be investigated. The roof antenna could be approximated by the FVTD method and the influence of the car body can be considered by the MoM. In this way, it should be possible to give approaches covering all automotive antenna applications. Besides that, it is suitable to use channel simulations to predict the antenna behaviour in a real environment [Budd 11]. Such investigations could deliver more input information about the quality of the antenna diversity and positioning of new antenna concepts in future cars.

Bibliography

[Abou 98] R. Abou-Jaoude and E. K. Walton. "Numerical Modelling of On-Glass Conformal Automobile Antennas". *IEEE Transactions on Antennas and Propagation*, Vol. 46, No. 6, pp. 845–852, 1998.

[Alay 02] M. Alaydrus, V. Hansen, and T. F. Eibert. "Hybrid: Combining the Three-Dimensional Hybrid Finite Element Boundary Integral Technique for Planar Multilayered Media With the Uniform Geometrical Theory of Diffraction". *IEEE Transactions on Antennas and Propagation*, Vol. 50, No. 1, pp. 67–74, 2002.

[Alex 96] M. J. Alexander and M. J. Salter. "Low measurement uncertainties in the frequency range 30 MHz to 1 GHz using a calculable standard dipole antenna and national reference ground plane". *IEEE Proceedings Science Measurement and Technology*, Vol. 143, No. 4, pp. 221–228, 1996.

[Altm 71] J. Altmayer. *Automobile Windshield Antenna.* 1971. US Patent 3,599,214.

[Ande 88] M. K. Anderson. "Field-to-Wire Coupling from 1 to 18 GHz". *IEEE International Symposium on Electromagnetic Compatibility*, pp. 45–49, 1988.

[Ante 09] *Antennas and Accessories Catalog 200972010.* Rohde & Schwarz, 2009.

[Anto 05] A. Antoniou, J. Komyathy, J. Bench, and A. Emadi. "Modelling and simulation of various hybrid electric configurations of the high-mobility multi purpose wheeled vehicle (HMMWV)". *Vehicle Power and Propulsion*, pp. 507–514, September 2005.

[Auto 11] AutoCAD. "http://www.autodesk.de". 2011.

[Awad 78] K. H. Awadalla and T. S. M. MacLean. "Input Impedance of a Monopole Antenna at the Center of a Finite Ground Plane". *IEEE Transactions on Antennas and Propagation*, Vol. 26, No. 3, pp. 244–248, 1978.

[Bala 05] C. A. Balanis. *Antenna Theory Analysis And Design.* John Wiley & Sons, 2005.

[Bala 82] C. A. Balanis and D. DeCarlo. "Monopole Antenna Patterns on Finite Size Composite Ground Planes". *IEEE Transactions on Antennas and Propagation*, Vol. 30, No. 4, pp. 764–768, 1982.

[Bart 87] M. Barton and Z. J. Cendes. "New vector finite elements for three-dimensional magnetic field computation". *Journal of Applied Physics*, Vol. 61, pp. 3919–3921, 1987.

[Batc 01] J. C. Batchelor, R. J. Langley, and H. Endo. "On-glass mobile antenna performance modelling". *IEEE Proceedings on Microwaves, Antennas and Propagation*, Vol. 148, No. 4, pp. 233–238, 2001.

[Batt 02] S. Battermann and H. Garbe. "Effects of Realistic Groundplanes to NSA-measurements of Open Area Test Sites (OATS)". *Proceedings of the XXVIIth URSI General Assembly*, 2002.

[Batt 04] S. Battermann and H. Garbe. "Influence of the Ground Plane Geometry on the Normalized Site Attenuation of an OATS". *Antenna and Propagation Society International Symposium*, Vol. 1, pp. 503–506, 2004.

[Batt 05] S. Battermann and H. Garbe. "A New Measurement Method to Characterize Ground Planes". *International Symposium on Electromagnetic Compatibility*, Vol. 1, pp. 234–238, 2005.

[Bayr 09] Y. Bayram and J. L. Volakis. *Computational Methods for High Frequency Electromagnetic Interference*. VDM Verlag Dr. Müller, 2009.

[Boch 11] L. Bochenski. "Virtuelle Antennenentwicklung - Evaluierung auf FVTD basierender Simulations- Software und simulationsrelevanter Parameter". *Bachelor thesis - Fachhochschule Ingolstadt*, 2011.

[Bogd 02] F. G. Bogdanov, R. G. Jobava, and S. Frei. "About Evaluation of the Potential Integrals for Near Field Calculations in MoM Solution to EFIE for Triangulated Surfaces". *Proceedings of the 7th International Seminar/Workshop on Direct and Inverse Problems of Electromagnetic and Acoustic Wave Theory, DIPED*, October 2002.

[Bogd 04a] F. G. Bogdanov, R. G. Jobava, and S. Frei. "Scheme of Improving Accuracy of MoM Solutions Based on Analysing Boundary Condidtions Performance". *ATE Conference Proceedings*, pp. 217–224, May 2004.

[Bogd 04b] F. G. Bogdanov, R. G. Jobava, and S. Frei. "Estimating Accuracy of MoM Solutions on Arbitrary Triangulated 3-D Geometries Based on Examination of Boundary Conditions Performance and Accurate Derivation of Scattered Fields". *Journal of Electromagnetic Waves and Applications*, Vol. 18, No. 7, pp. 879–897, 2004.

[Bogd 05] F. G. Bogdanov, R. G. Jobava, P. Tsereteli, and S. Frei. "A Partitioned MoM Scheme for Treating EMC Problems on a Series of Geometries with a Predominant Common Part". *International Zurich Symposium*, 2005.

[Bogd 07] F. G. Bogdanov, R. G. Jobava, S. Frei, A. Gheonjian, E. Yavolovskaya, B. Huneke, and C. Lippert. "Enhanced MoM Scheme with Incorporation of General N-Port Networks in Application to Automotive EMC Problems". 2007.

[Bogd 09a] F. Bogdanov, D. Karkashadze, R. Jobava, A. Gheonjian, E. Yavolovskaya, and N. Bondarenko. "Hybrid MoM Scheme with Incorporation of Equivalent Glass Antenna Model in Application to Automotive EMC Problems". *Proceedings of the 20th International Zurich Symposium on Electromagnetic Compatibility*, pp. 217–220, January 2009.

[Bogd 09b] F. G. Bogdanov, R. G. Jobava, A. Gheonjian, E. A. Yavolovskaya, N. G. Bondarenko, T. N. Injgia, and S. Frei. "Development and Application of an Enhanced MoM Scheme with Integrated Generalized N-Port Networks". *Progress In Electromagnetics Research*, Vol. 7, pp. 135–148, 2009.

[Bogd 10] F. Bogdanov, R. Jobava, P. T. David Karkashadze, A. Gheonjian, E. Yavolovskaya, D. Schleicher, C. Ullrich, and H. Tazi. *New Trends and Developments in Automotive System Engineering.* www.intechweb.org, 2010.

[Boic 65] J. H. Boicey. *Automobile Windshield of Laminated Glass Having Embedded Antenna Wires.* 1965. US Patent 3,208,070.

[Bomm 09] C. Bommaraju. *Investigating Finite Volume Time Domain Methods in Computational Electromagnetics.* PhD thesis, Technische Universität Darmstadt, 2009.

[Bowl 06] N. Bowler. "Frequency-Dependence of Relative Permeability in Steel". *AIP Conference Proceedings*, Vol. 820, pp. 1269–1276, March 2006.

[Brak 98] E. Braken, D. Know-Sun, and Z. Y. Cendes. "S-Domain Methods for Simultaneous Time and Frequency Characterization of Electromagnetic Devices". *IEEE Transaction on Antenna and Propagation*, pp. 230–233, 1998.

[Bred 07] J. Bredemeyer, T. Kleine-Ostmann, T. Schrader, K. Münter, and J. Ritter. "Airborne field strength monitoring". *Advances in Radio Science*, Vol. 5, pp. 49–55, 2007.

[Bren 90] C. E. Brench. "Antenna Differences and their Influence on Radiated Emission Measurements". *IEEE International Symposium on Electromagnetic Compatibility*, pp. 440–443, 1990.

[Bros 03] J. Brose and H. Lindenmeier. "Optimized Reactive Port-Loads of a Multi-Antenna-System for Enhanced Diversity-Effectiveness". *ITG Fachbericht*, pp. 331–334, 2003.

[Bros 99] J. Brose and H. Lindenmeier. "Validierung der Berechnungsergebnisse für Mobilantennen". *Gemeinsame Tagung des U.R.S.I.-Landesausschusses der BRD und der ITG-Fachausschüsse 5.1, 7.5 und 8.4, Kleinheubach , Kleinheubacher Berichte*, Vol. 42, pp. 174–178, 1999.

[Brun 04] H.-D. Brüns, M. Sabielny, and H. S. D. Leugner. "Application and Limits of the MoM-PO-UTD Hybridization Technique". *IEEE International Symposium on Electromagnetic Compatibility, EMC*, Vol. 2, pp. 672–677, 2004.

[Budd 11] H. Buddendick. *Streuzentrenmodelle zur Simulation der Wellenausbreitung für automobile Radar- und Funksysteme*. PhD thesis, Technische Universität München, 2011.

[Capp 01] C. Capps. "Near Field or Far Field?". *EDN Magazine*, Vol. 8, No. 16, pp. 95–99, 2001.

[Case 88] J. P. Casey and R. Bansal. "Dielectrically loaded wire antennas". *IEEE Proceedings on Microwaves, Antennas and Propagation*, Vol. 135, No. 2, pp. 103–110, Apr. 1988.

[CATI 11] CATIA. "http://www.3ds.com/de/products/catia/welcome/". 2011.

[Cend 83] Z. J. Cendes, D. N. Shenton, and H. Shahnasser. "Magnetic field computation using triangulation and complementary finite element methods". *IEEE Transactions on Magnetics*, Vol. 19, pp. 2551–2554, 1983.

[Cend 91] Z. J. Cendes. "vector finite elements for electromagnetic field computation". *IEEE Transactions on Magnetics*, Vol. 27, pp. 3958–3966, 1991.

[Chan 77] Y. Chang and R. F. Harrington. "A Surface Formulation for Characteristic Modes of Material Bodies". *IEEE Transactions on Antennas and Propagation*, Vol. 25, No. 6, pp. 789–795, 1977.

[Chen 03] H.-F. Chen and K.-H. Lin. "A Numerical Analysis of Antenna Factor of Bilog Antennas for Normalized Site Attenuation and EMC Measurement". *IEEE International Symposium on Electromagnetic Compatibility*, Vol. 2, pp. 817–821, 2003.

[Chen 90] Q. Chen and D. R. Wilton. "Electromagnetic Scattering by Three-Dimensional Arbitrary Complex Material/Conducting Bodies". *Antennas and Propagation Society International Symposium (AP-S) "Merging Technologies for the 90's" – Digest*, Vol. 2, pp. 590–593, May 1990.

[Chew 90] W. C. Chew. *Waves and Fields in Inhomogeneous Media.* Van Nostrand Reinhold, New York, 1990.

[Clar 05] S. Clarke and U. Jakobus. "Dielectric Material Modelling in the MoM-Based Code *FEKO*". *IEEE Antennas and Propagation Magazine*, Vol. 47, No. 5, pp. 140–147, 2005.

[Clem 01] M. Clemens and T. Weiland. "Discrete Electromagnetism with the Finite Integration Technique". *Progress In Electromagnetics Research*, Vol. 32, pp. 65–87, 2001.

[Cler 65] J. Clerk-Maxwell. "A Dynamical Theory of the Electromagnetic Field". *Philosophical Transactions of the Royal Society of London*, pp. 459–512, 1865.

[Cros 01] R. L. Cross. *Some Magnetical Field Properties of Ferrite Rods Used for Small Ferrite Loaded Receiving Antennas Solved by the Moment Method.* Amateurradio WK00, 2001.

[CST 10] CST. "http://www.cst.com". 2010.

[Cui 00] T. J. Cui and W. C. Chew. "Accurate Model of Arbitrary Wire Antennas in Free Space, Above or Inside Ground". *IEEE Transactions on Antennas and Propagation*, Vol. 48, No. 4, pp. 482–493, Apr. 2000.

[Delg 89] H. J. Delgado, J. T. Williams, and S. A. Long. "Antenna Pattern Measurement Techniques for Infinite Ground Plane Simulation". *Antennas and Propagation Society International Symposium*, Vol. 1, pp. 339–342, 1989.

[Dema 88] J. Demarinis. "The Antenna Cable as a Source of Error in EMI Measurements". *IEEE International Symposium on Electromagnetic Compatibility*, pp. 9–14, 1988.

[Dode 10] D. Dodel and D. Häupler. *Satellitennavigation 2. Auflage.* Springer, 2010.

[Domi 92] H. Dominik. *Analyze elektromagnetischer Schirme mit der iterativen Momentenmethode.* PhD thesis, Technische Universität Carolo-Wilhelmina zu Braunschweig, Lünen, 1992.

[Dres 05] W. Dressel. *Modellierung von elektromagnetischen Strukturen mit Hilfe der TLM-Methode unter Verwendung statischer Untergitter.* PhD thesis, Technische Universität München, 2005.

[Eibe 03] T. F. Eibert. *Numerische Berechnungsverfahren von Antennen und Streuproblemen.* Lecture notes - Technische Universität Darmstadt, 2003.

[Eich 05] T. Eichner and S. Weber. "Automobilelektronik: Fokus Antennentechnologie". 2005.

[EMCo 09] EMCoS. "http://www.emcos.com/". 2009.

[FEKO 07] FEKO. "http://www.feko.info/". 2007.

[Fitz 88] R. G. Fitzgerrell. "Monopole Impedance and Gain Measurements on Finite Ground Planes". *IEEE Transactions on Antennas and Propagation*, Vol. 36, No. 3, pp. 431–439, 1988.

[Frei 06] S. Frei, R. Jobava, F. Bogdanov, and A. Gheonjian. "Schnelle Optimierungsuntersuchungen mit der Momentenmethode durch Zerlegung der Impedanzmatrix". *EMV Düsseldorf*, 2006.

[Frei 09] S. Frei. *Kfz-Bordnetze*. Lecture notes - Technische Universität Dortmund Arbeitsgebiet Bordsysteme, 2009.

[Fuji 94] K. Fujimoto and J. James. *Mobile Antenna Systems Handbook*. Artech House, 1994.

[Fume 05] C. Fumeaux. *An Introduction to the Finite-Volume Time-Domain Method (FVTD)*. ETH-Zentrum, 2005.

[Fume 06] C. Fumeaux, D. Baumann, and R. Vahldieck. "Finite-Volume Time-Domain Analysis of a Cavity-Backed Archimedean Spiral Antenna". *IEEE Transactions on Antennas and Propagation*, Vol. 54, pp. 844–851, 2006.

[Fume 07] C. Fumeaux, K. Sankaran, D. Baumann, and R. Vahldieck. "EM simulations with the Finite-Volume Time-Domain Method". *IFH Laboratory for Electromagnetic Fields and Microwave Electronics ETH Zurich*, 2007.

[Fume 08] C. Fumeaux. *The Finite-Volume Time-Domain Method (FVTD)*. Lecture notes - Institut für Feldtheorie und Höchstfrequenztechnik ETZ K95, ETH-Zentrum, 2008.

[Gave 94] J. D. Gavenda. "Near-Field Corrections to Site Attenuation". *IEEE Transactions on Electromagnetic Compatibility*, Vol. 36, No. 3, pp. 213–220, 1994.

[Gebe 03] O. Gebele. *EMV-Analyze beliebiger Leitungen über oberflächendiskretisierten metallischen Strukturen*. PhD thesis, Technische Universität Hamburg-Harburg, 2003.

[Geor 05] George, R. Jobava, P. Tsereteli, Z. S. Roman kvaratskhelia, and A. grachev. "Development of FEM/MoM Approach for Investigation of Vehicle Glass Antennas". *Technical Report for AUDI AG - I/EE-2*, 2005.

[Gheo 08] A. Gheonjian, F. G. Bogdanov, R. G. Jobava, and G. Sergia. "Validation of Planar Stratified Media Green Function Method for Simulation of Glass Antenna within EMC Studio". *Technical Report for AUDI AG - I/EE-2*, 2008.

[Gheo 09] A. Gheonjian. "Glass Antenna Construction in EMC Studio". *Technical Report for AUDI AG - I/EE-2*, 2009.

[Gheo 10] A. Gheonjian. "Calculation of Near Field in Volume and Visualization of results". *Technical Report for AUDI AG - I/EE-2*, 2010.

[Gheo 11a] A. Gheonjian. "Set of Tools for Vehicle Glass Antenna Model Construction in EMC Studio". *Technical Report for AUDI AG - I/EE-2*, 2011.

[Gheo 11b] A. Gheonjian. "Substantial Improvement of Procedure for Glass Antenna Model Construction in EMC Studio". *Technical Report for AUDI AG - I/EE-2*, 2011.

[Glis 80] A. W. Glisson and D. R. Wilton. "Simple and Efficient Numerical Methods for Problems of Electromagnetic Radiation and Scattering from Surfaces". *IEEE Transactions on Antennas and Propagation*, Vol. 28, No. 5, pp. 593–603, 1980.

[Gott 03] G. Gottwald. *Moderne Antennensysteme Intelligente Sende und Empfangstechnik im Kfz.* Vol. 246, Verlag Moderne Industrie, 2003.

[Goub 50] G. Goubau. "Surface Waves and Their Application to Transmission Lines". *Journal of Applied Physics*, Vol. 21, No. 11, pp. 1119–1128, November 1950.

[Grun 08] *Grundlage Auswertesoftware.* Neckartenzlingen, Germany, Apr. 2008.

[H 04] R. H. and M. Poole. *Ferrite Rod Antennas for HF.* R&D White Paper WH091, 2004.

[Harp 40] W. C. Harp. *Automobile Radio Antenna.* 1940. US Patent 2,210,289.

[Harr 61] R. F. Harrington. *Time-Harmonic Electromagnetic Fields.* McGraw-Hill Book Company, Inc., 1961.

[Harr 67] R. F. Harrington. "Matrix Methods for Field Problems". *Proceedings of the IEEE*, Vol. 55, No. 2, pp. 136–149, 1967.

[Harr 68] R. F. Harrington. *Field Computations by Moment Methods.* Macmillan Publishing Company, 1968.

[Harr 75] R. F. Harrington and J. Mautz. "An Impedance Sheet Approximation for Thin Dielectric Shells". *IEEE Transaction on Antenna and Propagation*, pp. 531–534, 1975.

[Harr 77] R. F. Harrington and J. R. Mautz. "H-Field, E-Field, and Combined Field Solutions for Bodies of Revolution". No. RADC-TR-77-109, 1977.

[Henk 07] H. Henke. *Elektromagnetische Felder Theorie und Anwendung.* Springer, 2007.

[Hira 98] M. Hirano, M. Takeuchi, T. Tomoda, and K. Nakano. "Keyless Entry System With Radio Card Transponder". *IEEE Transaction on Industrial Electronics*, Vol. 2, pp. 208–216, 1998.

[Hune 05] B. Huneke. "Optimierung numerischer Berechnungsmethoden für Kfz-Scheibenantennen durch messtechnische Bestimmung von Impedanzen und Fernfeldern". *Diplomarbeit - Fachhochschule Ingolstadt*, 2005.

[Iche 01] C. Icheln. *Methods for Measuring RF Radiation Properties of Small Antennas.* PhD thesis, Helsinki University of Technology, Espoo, Finland, 2001.

[Ishi 91] A. Ishimaru. *Electromagnetic Wave Propagation, Radiation, and Scattering.* Prentice-Hall International, Inc., 1991.

[Jako 95] U. Jakobus. *Erweiterte Momentenmethode zur Behandlung kompliziert aufgebauter und elektrisch grosser Streuprobleme.* PhD thesis, Institut für Hochfrequenztechnik der Universität Stuttgart, 1995.

[Jako 99] U. Jakobus. "Intelligente Kombination verschiedener numerischer Berechnungsverfahren zur effizienten Analyze elektromagnetischer Streuprobleme unter besonderer Berücksichtigung der Parallelverarbeitung". 1999.

[Jame 94] J. R. James, K. Fujimoto, K. Kagoshima, W. C. Y. Lee, K. Hirasawa, T. Taga, R. Mumford, Q. Balzano, H. K. Lindenmeier, L. Reiter, J. Hopf, T. Shiokawa, S. Ohmori, T. Teshirogi, and Y. Suzuki. *Mobile Antenna Systems Handbook.* Artech House, 1994.

[Java 09] I. Javakhishvili. *Novel MoM Based Techniques for Investigation of Vehicle Glass Antennas.* Master's thesis, Tbilisi State University, 2009.

[Joba 03a] R. Jobava, F. Bogdanov, A. Gheonjian, and S. Frei. "Analysis of Influence of Vehicle Bodyshell on the Characteristics of Wire Antennas Using a New MoM-based EM/EMC Solver". *IEEE Antennas and Propagation Society International Symposium, 22–27 June*, 2003.

[Joba 03b] R. Jobava, P. Tseretely, A. Radchenko, and F. Bogdanov. "Parallel Solvers of TriD". *EMCOS - www.emcos.com*, 2003.

[Joba 04] R. Jobava. "Antenna Cookbook for EMC-Calculations". *EMCOS - www.emcos.com*, 2004.

[Joba 06] R. Jobava and F. Bogdanov. "Development of Network parameters support in MoM". *Technical Report for AUDI AG - I/EE-2*, 2006.

[Joba 10] R. Jobava, F. Bogdanov, A. Gheonjian, E. Yavolovskaya, D. Karkashadze, P. Tsereteli, C. Ullrich, and H. T. Detlef Schleicher. "Recent Achievements in Computational Techniques Related to Automotive EMC simulations". *In 20th International Wroclaw Symposium on EMC, Wroclaw, Poland*, September 2010.

[Jung 04] B. H. Jung, T. K. Sarkar, Y.-S. Chung, M. Salazar-Palma, Z. Ji, and K. K. Seongman Jang. "Transient Electromagnetic Scattering from Dielectric Objects Using the Electric Field Integral Equation with Laguerre Polynomials as Temporal Basis Functions". *IEEE Transactions on Antennas and Propagation*, Vol. 52, No. 9, pp. 2329–2340, 2004.

[Kais 05] K. Kaiser. *Elekctromagnetic Compatibility Handbook*. CRC Press, 2005.

[Kark 04] K. Kark. *Antennen und Strahlungsfelder*. Vieweg, 2004.

[Karl 09] A. Karlsson. "Approximate Boundary Conditions for Thin Structures". *IEEE Transactions on Antennas and Propagation*, Vol. 57, No. 1, pp. 144–148, January 2009.

[Kell 62] J. B. Keller. "Geometrical Theory of Diffraction". *Journal of the Optical Society of America*, Vol. 52, No. 2, pp. 116–130, 1962.

[Kim 03] Y. Kim. *Development of Automobile Antenna Design and Optimization for FM/GPS/SDARS Applications*. PhD thesis, Ohio State University, 2003.

[Kimu 06] S. Kimura, J. Sato, and H. Uchida. *Antenna coil*. 2006. US Patent 7,095,381 B2.

[Kolu 02] B. M. Kolundzija and A. R. Djordjevic. *Electromagnetic Modelling of Composite Metallic and Dielectric Structures*. Artech House, 2002.

[Kone 05] T. Konefal, J. F. Dawson, A. C. Marvin, M. P. Robinson, and S. J. Porter. "A Fast Multiple Mode Intermediate Level Circuit Model for the Prediction of Shielding Effectiveness of a Rectangular Box Containing a Rectangular Aperture". *IEEE Transactions on Electromagnetic Compatibility*, Vol. 47, No. 4, pp. 678–691, 2005.

[Konr 07] R. Konrad. *Automobilelektronik - Eine Einführung für Ingenieure 2., Überarbeitete und erweiterte Auflage.* Vieweg & Sohn Verlag, 2007.

[Krum 94] M. Krumpholz. *Über die Grundlage der TLM-Methode.* PhD thesis, Lehrstuhl für Hochfrequentechnik der Technische Universität München, 1994.

[Kuli 09] S. Kulig. *Theoretische Elektrotechnik.* Lecture notes - Technische Universität Dortmund Lehrstuhl für elektrische Antriebe und Mechatronik, 2009.

[Kurz 08] P. Kurzweil, B. Frenzel, and F. Gebhard. *Physik Formelsammlung Für Ingenieure und Naturwissenschaftler.* Vieweg, 2008.

[Kwoc 10] A. Kwoczek. "Konzernforschung Fahrerinformationssysteme Security und Connectivity Volkswagen AG". *Submitted Patent*, 2010.

[Lee 07] B. Lee, C. Jung, B. Yu, K. Kong, N. Choi, F. H. Lee, S. Cho, M.-J. Park, and Y.-S. Chung. "Design concept of compact antenna for SDARS applications". *Electronics Letters*, Vol. 16, 2007.

[Lehn 10] G. Lehner. *Elektromagnetic Field Theory for Engineers and Physics.* Springer, 2010.

[Li 04] J.-Y. Li and L.-W. Li. "Electromagnetic Scattering by a Mixture of Conducting and Dielectric Objects: Analysis Using Method of Moments". *IEEE Transactions on Vehicular Technology*, Vol. 53, No. 2, pp. 514–520, 2004.

[Lin 76] J.-L. Lin, W. L. Curtis, and M. C. Vincent. "Electromagnetic Coupling to a Cable Through Apertures". *IEEE Transactions on Antennas and Propagation*, Vol. 24, No. 2, pp. 198–203, 1976.

[Lind 00] H. Lindenmeier, J. Hopf, and L. Reiter. *Antennendiversityanlage mit phasengeregelter Summation von Antennensignalen.* Planegg, 2000.

[Lind 83] K. Lindenmeier and L. Reiter. "Multipath reception in FM car radio receivers and antenna diversity by means of a distortion detector". *IEEE Antennas and Propagation Society International Symposium*, Vol. 21, pp. 187–190, May 1983.

[Lind 90] H. K. Lindenmeier, L. M. Reiter, J. F. Hopf, and A. J. Schwab. "Multiple FM Window Antenna System for Scanning Diversity with an Integrated Processor". *IEEE 40th Vehicular Technology Conference*, pp. 1–6, May 1990.

[Lind 92] H. K. Lindenmeier. "Multi Antenna Scanning". *IEEE Potentials*, Vol. 11, No. 1, pp. 36–39, 1992.

[Lind 96] S. Lindenmeier. *Finite Differenzen-Methoden zur Modellierung planarer Hochfrequenzschaltungen.* PhD thesis, Technische Universität München, May 1996.

[Lore 05] P. Lorenz, J. V. Vital, B. Biscontini, and P. Russer. "TLM-G-A Grid-Enabled Time-Domain Transmission-Line-Matrix System for the Analysis of Complex Electromagnetic Structures". *IEEE Transactions on Microwave Theory and Techniques*, Vol. 53, No. 11, pp. 3631–3637, 2005.

[Luo 09] F.-L. Luo, Ed. *Mobile Multimedia Broadcasting Standads Technology and Practice.* Springer, 2009.

[Maka 06] S. N. Makarov, S. D. Kulkarni, A. G. Marut, and L. C. Kempel. "Method of Moments Solution for a Printed Patch/Slot Antenna on a Thin Finite Dielectric Substrate Using the Volume Integral Equation". *IEEE Transactions on Antennas and Propagation*, Vol. 54, No. 4, pp. 1174–1184, Apr. 2006.

[Marh 02] R. J. Marhefka, B. A. Baertlein, M. Rao, and K. Prakah-Asante. "Modelling the Performance of Automotive Bumper Mounted Antennas". *IEEE Antennas and Propagation Society International Symposium*, Vol. 3, pp. 316–319, 2002.

[Marq 10] Marquardt. "http://www.marquardt.de/". 2010.

[Mart 05] A. J. Martin, A. R. Ruddle, and A. P. Duffy. "Comparison of Measured and Computed Local Electric Field Distributions Due to Vehicle-Mounted Antennas Using 2D Feature Selective Validation". *IEEE International Symposium on Electromagnetic Compatibility*, Vol. 1, pp. 290–295, 2005.

[Matt 01] P. Matthew N. O. Sadiku. *Numerical Techniques in Electromagnetics Second Edition.* CRC Press LLC, 2001.

[Matt 80] G. Matthaei, L. Young, and E. Jones. *Microwave Filters, Impedance-Matching Networks, and Coupling Structures. Artech Microwave Library*, Artech House Publishers, 1980.

[Maur 01] C. Mäurer. "Numerische Simulation Scheibenantenne – Untersuchung am ebenen Gittermodell". *EMSS*, 2001.

[Maur 06] C. Mäurer. "Vergleich verschiedener Modellierungsmethoden für Scheibenantennen". *EMSS*, 2006.

[Meek 98] D. Meeker. *Finite Element Method.* http://femm.foster-miller.net/wiki/HomePage, 1998.

[Mill 05] T. A. Milligan. *Modern Antenna Design.* IEEE and Wiley Interscience, 2005.

[Ober 06] H. S. Obermann, Ed. *Basiswissen der Elektro-, Digital- und Informationstechnik.* Vieweg, 2006.

[Orfa 04] S. J. Orfanidis. *Electromagnetic Waves and Antennas.* Rutgers University, 2004.

[Paul 94] C. R. Paul. *Analysis of Multiconductor Transmission Lines. Wiley Series in Microwave and Optical Engineering*, John Wiley & Sons, 1994.

[Petr 92] P. Petre and T. K. Sarkar. "A Planar Near-Field to Far-Field Transformation Using an Equivalent Magnetic Current Approach". *IEEE Antennas and Propagation Society International Symposium Digest*, Vol. 3, pp. 1534–1537, July 1992.

[Pier 97] L. Pierantoni, S. Lindenmeier, and P. Russer. "A Combination of Integral Equation Method and FD/TLM, Method for Efficient Solution of EMC Problems". *IEEE 27th European Microwave Conference*, Vol. 2, pp. 937–942, 1997.

[Pipe 02] S. Piperno, M. Remaki, and L. Fezoui. "A non diffusive Finite Volume Scheme for the Maxwell's Equations on Unstructured Meshes". *SIAM Journal Numerical Analysis. - Society for Industrial and Applied Mathematics*, Vol. 39, pp. 2089–2108, 2002.

[Popo 91] B. D. Popović. *CAD of Wire Antennas and Related Radiating Structures.* Research Studies Press, Taunton, Somerset, England, 1991.

[Povh 11] B. Povh. *Anschauliche Physik für Naturwissenschaftler.* Springer, 2011.

[Rabi 10] V. Rabinovch, N. Alexandrov, and B. Alkhateeb. *Automotive Antenna Design and Applications.* CRC Press, 2010.

[Rao 10] K. Rao, D. Kim, and J. Hwang. *Fast Fourier Transformation: Algorithms and Applications.* Springer, 2010.

[Rao 82] S. M. Rao, D. R. Wilton, and A. W. Glisson. "Electromagnetic Scattering by Surfaces of Arbitrary Shape". *IEEE Transactions on Microwave Theory and Techniques*, Vol. 30, No. 3, pp. 409–418, May 1982.

[Reif 11] K. Reif. *Bosch Autoelektrik und Autoelektronik Bordnetze, Sensoren und elektronische Systeme 6., Überarbeitete und erweiterte Auflage.* Vieweg & Teubner, 2011.

[Reit 99] L. Reiter, J. Hopf, and H. Lindenmeier. "Scanning diversity antenna system for motor vehicles". No. 6611677, 1999.

[Rich 08] J. A. Richards. *Radio Wave Propagation.* Springer, 2008.

[Rien 85] U. van Rienen and T. Weiland. "Triangular Discretization Method for the Evaluation of RF- Fields in Cylindrically Symmetric Cavities". *IEEE Transactions on Magnetics*, Vol. 21, pp. 2317–2320, 1985.

[Rien 99] U. van Rienen. "Finite Integration Technique on Triangular Grids Revisited". *Int. Journal of Numerical Modelling Electronic Networks, Devices and Fields, Spacial Issue*, Vol. 12, pp. 107–128, 1999.

[Rosl 08] S. Rosloniec. *Fundamental Numerical Methods for Electrical Engineering.* Springer, 2008.

[Roy 94] M. Roy and T. Fleissner. "RF Performance Optimization of a saw Based Transmitter for remote Keyless Entry System". *Ultrasonics Symposium*, 1994.

[Rudd 01] A. R. Ruddle, S. C. Pomeroy, and D. D. Ward. "Modelling the Installed Performance of Automotive Antennas Integrated with Vehicle Glazing". *IEEE Eleventh International Conference on Antennas and Propagation*, No. 2, pp. 732–735, Apr. 2001.

[Russ 00] P. Russer. "The Transmission Line Matrix Method". *Applied Computational Electromagnetics*, pp. 243–269, 2000.

[Russ 03] P. Russer. *Electromagnetics, Microwave Circuit and Antenna Design for Communications Engineering.* Artech House, 2003.

[Russ 08] P. Russer and U. Siart. *Time Domain Methods in Electromagnetics.* Springer, 2008.

[Sank 05] K. Sankaran. *Perfectly Matched Layer Boundary Condition for Maxwell Systems.* Laboratory for Electromgnetic Fields and Microwave Electronics (IFH), 2005.

[Sank 07] K. Sankaran. *Accurate Domain Truncation Techniques For Time-Domain Conformal Methods.* PhD thesis, Lecture notes - ETH Zürich, 2007.

[Sato 99] K. Sato, K. Nishikawa, Y. Nojima, and N. Suzuki. "Analysis of Electric Field Distribution near Car in Radio Remote Control System for Electric Equipment Installed in Car". *IEEE International Symposium on Electromagnetic Compatibility*, 1999.

[Saut 11] M. Sauter. *Grundkurs Mobile Kommunikationssysteme UMTS, HSPDA und LTE, GSM, GPRS und Wireless 4. Auflage.* Vieweg & Teubner, 2011.

[Schn 06] H. Schneider-Obermann, Ed. *Basiswissen der Elektro-, Digital- und Informationstechnik.* Vieweg & Sohn Verlag, 2006.

[schn 10] A. schneider. "Virtuelle Entwicklung von Keyless-Entry- und Keyless-Go-Systemen". *Diplomarbeit - Fachhochschule Ingolstadt*, 2010.

[Schw 07] A. J. Schwab and W. Kürner. *Elektromagnetische Verträglichkeit.* Springer, 2007.

[Slat 91] D. Slater. *Near Field Antenna Measurements.* Springer, 1991.

[Somm 09] A. Sommerfeld. "Über die Ausbreitung der Wellen in den Drahtlosen Telegraphie". *Ann. Phys*, Vol. 28, No. 16, pp. 665–736, 1909.

[Suga 07] K. Sugahara, H. Yamamoto, H. Ouchi, and Y. Nakano. "Numerical Analysis of Near-Field Magnetic Fields for Automobile Electronic Key Systems". *IEEE Transactions on Magnetics*, Vol. 8, pp. 3375–3379, 2007.

[Sun 01] D. K. Sun, J. F. Lee, and Z. J. Cendes. "Construction of nearly orthogonal Nedelec bases for rapid convergence with multilevel preconditioned solvers". *SIAM Journal on Scientific Computing*, Vol. 4, pp. 1053–1076, 2001.

[Taag 96] A. Taaghol and T. K. Sarkar. "Near-Field to Near-Far-Field Transformation for Arbitrary Near-Field Geometry, Utilizing an Equivalent Magnetic Current". *IEEE Transactions on Electromagnetic Compatibility*, Vol. 38, No. 3, pp. 536–542, 1996.

[Take 98] M. Takeuchi and K. Nakano. *Keyless entry system for looking and unlooking a vehicular lock device by a pocket portable radio signal transmitter.* 1998. US Patent 5,134,392.

[Talt 01] T. J. Talty, Y. Dai, and L. Lanctot. "Automotive Antennas: Trends and Future Requirements". *IEEE Antennas and Propagation Society International Symposium*, Vol. 1, pp. 430–433, 2001.

[Tazi 08] H. Tazi. "Untersuchung, Validierung und Optimierung von Berechnungsmethoden zur Störabstrahlung von Leitungsbündeln auf AM- und FM- Fahrzeugantennen". *Diplomarbeit - Technische Universität Dortmund*, 2008.

[Tazi 09] H. Tazi, C. Ullrich, J. Hippeli, and T. Eibert. "Simulation of Glass Antennas by Comparison of Three Approaches Based on the Method of Momdents". *Kleinheubacher Tagung, Miltenberg Germany*, 2009.

[Tazi 10a] H. Tazi, F. Bogdanov, and T. F. Eibert. "Application of the Equivalence Principle and the Multi Excitation Approach to Method of Moments for Optimization of Smart Entry Systems". *European Microwaves, Paris*, 2010.

[Tazi 10b] H. Tazi, F. Bogdanov, P. Tsereteli, and T. F. Eibert. "Matrix Partitioning of the Hybrid MoM and Modified Mirror Image Method to Calculate the Characteristics of Different Antennas Mounted in Windows of the Same Car Model". *In CNC/USNC/URSI National Radio Science Meeting, Toronto, Canada*, July 2010.

[Tazi 10c] H. Tazi, J. Hippeli, and T. F. Eibert. "Simulation Model of a Strip-line with Numerical Calculations Based on MoM for the Evaluation of the Glass Antenna Systems of Vehicles in LW/MW Frequency Range". *IEEE Antennas and Propagation International Symposium, Toronto, Canada*, July 2010.

[Tazi 10d] H. Tazi, C. Ullrich, and T. F. Eibert. "Integration der virtuellen Entwicklung der Antennensysteme im Entwicklungsprozess.". *In ITG-Workshop Automotive Antennen (WSAA 2010) in Ulm, Deutschland*, May 2010.

[Tazi 11a] H. Tazi and T. F. Eibert. "Approaches Based on the Method of Moments for Development of Glass Automotive Antennas". *In Asia Pacific Microwave Conference (APMC), Melbourne, Australia*, December 2011.

[Tazi 11b] H. Tazi and T. F. Eibert. "Virtual Development of Automotive Printed Antennas on Glass Based on Hybrid Method of Moments with Method of Auxiliary Sources". *In Asia Pacific Microwave Conference (APMC), Melbourne, Australia*, December 2011.

[Tazi 11c] H. Tazi, C. Ullrich, and T. F. Eibert. "Application of the Finite Volume Time Domain Method for Evaluation and Development of Wideband Automotive Antenna Systems". *In European Conference on Antennas and Propagation (EuCAP), Rome, Italy*, 2011.

[Thie 75] G. A. Thiele and T. H. Newhouse. "A Hybrid Technique for Combining Moment Methods with the Geometrical Theory of Diffraction". *IEEE Transactions on Antennas and Propagation*, Vol. 23, No. 1, pp. 62–69, 1975.

[Tipl 04] P. A. Tipler and G. Mosca. *Pysics for Scientists and Engineers (fifth edition)*. W. H. Freeman and Company New York, 2004.

[Titt 91] P. J. Tittensor and P. R. Sharples. "Mathematical Modelling of Heated Rear-Window Antennas". *ICAP 91, Seventh International Conference on Antennas and Propagation*, Vol. 2, pp. 954–956, Apr. 1991.

[Ullr 09] C. Ullrich. *Effiziente Simulationsmethoden fr die Optimierung von komplexen Fahrzeugantennensystemen.* PhD thesis, Technische Universität Mnchen, 2009.

[Ullr 10] C. Ullrich and H. Tazi. "Measurement Uncertainties in Automotive Antenna Measurements". *IEEE Antennas and Propagation International Symposium, Toronto, Canada*, July 2010.

[User 05] *User's Manual EMC Studio Version 6.3.* Tbilisi, Georgien, Apr. 2005.

[Vajn 09] S. Vajna, C. Weber, H. Bley, K. Zeman, and P. Hehenberger. *CAx für Ingenieure.* Springer, 2009.

[Voge 04] E. Voges. *Hochfrequenztechnik, 3. Auflage.* Hüthig, 2004.

[Vola 07] J. Volakis. *Antenna Engineering Handbook.* Mcgraw-Hill Professional, 2007.

[Vola 98] J. L. Volakis, C. K. Leo, and A. Chatterjee. *Finite Element Method Electromagnetics: Antennas, Microwave Circuits, and Scattering Applications.* IEEE Computer Soc. PR, 1998.

[Wang 90] T. Wang, R. F. Harrington, and J. R. Mautz. "Electromagnetic Scattering from and Transmission Through Arbitrary Apertures in Conducting Bodies". *IEEE Transactions on Antennas and Propagation*, Vol. 38, No. 11, pp. 1805–1814, 1990.

[Wang 91] J. J. H. Wang. *Generalized Moment Methods in Electromagnetics: Formulation and Computer Solution of Integral Equations.* John Wiley & Sons, Inc., 1991.

[Weil 77] T. Weiland. "Eine Methode zur Lösung der Maxwelli'schen Gleichungen für sechskomponentige Felder auf diskreter Basis". *AEÜ*, Vol. 31, pp. 116–120, 1977.

[Wern 06] M. Werner, Ed. *Nachrichten-Übertragungstechnik Analoge und digitale Verfahren mit modernen Anwendungen.* 2006.

[West 10] T. Westermann. *Modellbildung und Simulation mit einer Einführung in ANSYS.* Springer, 2010.

[Whee 47] H. A. Wheeler. "Fundamental Limitations of Small Antennas". *Proceeding Of The I.R.E.*, pp. 1479–1485, 1947.

[Whee 75] H. A. Wheeler. "Small Antennas". *IEEE Transactions on Antennas and Propagation*, Vol. 23, pp. 462–469, 1975.

[Wies 07a] W. Wiesbeck. *Ultra Breitbandige Antennen für Kommunikationstechnik und Navigation am Fahrzeug.* Forschungsverbung Medientechnik Südwest, 2007.

[Wies 07b] W. Wiesbeck and H. Lindenmeier. "Multimediafähige Antennensysteme für Kraftfahrzeuge". *HDT Seminar*, 2007.

[Wilt 02] D. R. Wilton. *Scattering*, Chap. Computational Methods, pp. 52–105. Academic Press, 2002.

[Wing 08] O. Wing. *Classical Circuit Theory*. Springer, 2008.

[Xue 04] Q. Xue, H. Wong, K. M. Shum, K. M. Luk, and C. H. Chan. "Active Receiving Antennas for Automotive Applications". *Antennas and Propagation Society International Symposium*, Vol. 2, pp. 1443–1446, 2004.

[Yarm 08] B. S. Yarman. *Design of Ultra Wideband Antenna Matching Networks*. Springer, 2008.

[Yavo 05] E. Yavolovskaya, A. Grachev, A. Gheonjian, and R. Jobava. "Glass FM antenna basic investigations". *Technical Report for AUDI AG - I/EE-2*, 2005.

[Yavo 08] E. Yavolovskaya, I. Oganezova, T. ljgia, A. Grachev, and A. Gheonjian. "Validation and Comparison of Methods for Simulation of Coupling to Glass Antenna". *Technical Report for AUDI AG - I/EE-2*, 2008.

[Zien 75] O. C. Zienkiewicz. *Methode der finiten Elemente*. Carl Hanser Verlag, 1975.